Dissertation zur Erlangung des Doktorgrades
der Fakultät für Chemie und Pharmazie
der Ludwig–Maximilians–Universität München

Photogeneration of reactive intermediates:
From initial quantum dynamics to chemical yields in solution

Sebastian Thallmair

aus

München, Deutschland

2015

Contents

Abstract

Bond cleavage and formation are key steps in chemistry and biochemistry. The present work investigates the generation of diphenylmethyl cations (Ph_2CH^+) via photoinduced bond cleavage of diphenylmethyl derivatives with a cationic or neutral leaving group. The resulting Ph_2CH^+ cations and its numerous derivatives serve as reference electrophiles for one of the most extensive reactivity scales covering 40 orders of magnitude. In chapter 1, the focus is on the initial bond cleavage of diphenylmethyltriphenylphosphonium ions ($Ph_2CH-PPh_3^+$) exhibiting a cationic leaving group. With the help of state-of-the-art quantum chemical and quantum dynamical methods, the reaction mechanism of the bond cleavage is revealed. Using a reduced model system, the potential energy surfaces can be calculated at the ONIOM level of theory along specially designed reactive coordinates. Two competing reaction channels emerge: a homolytic one in the S_1 state and a heterolytic one in the ground state. They are connected via an energetically accessible conical intersection which makes an efficient generation of the observed Ph_2CH^+ cations feasible. In contradiction with the experiment in polar or moderately polar solvents, quantum dynamical calculations for the isolated molecule reveal the formation of $Ph_2CH^\bullet$ radicals. While electrostatic solvent effects are negligible in this system, dynamic solvent effects emerge as being essential to explain the molecular mechanism.

Two methods with increasing complexity to describe the dynamic impact of the solvent environment are developed. The first approach, the dynamic continuum ansatz, treats the environment implicitly. It uses Stokes' law and the dynamic viscosity of the solvent in combination with quantum chemically and dynamically evaluated quantities to obtain the decelerating force exerted on the dissociating fragments. The ansatz does not require any fitting of parameters. The second method, the QD/MD approach, is based on an explicit treatment of the solvent surrounding. It combines molecular dynamics (MD) simulations of the reactant in a box of solvent molecules with quantum dynamics (QD) calculations of the reactant's dynamics. In this way, a more detailed microscopic picture of the molecular process can be derived taking into account individual arrangements of the solvent. Both methods unveil the crucial impact of the solvent cage on the bond cleavage mechanism. It hinders the free dissociation in the S_1 state and guides the molecular system to the conical intersection. QD simulations including the non-adiabatic coupling around the conical intersection show the formation of Ph_2CH^+ within $\sim 400\,fs$ which compares well with the initial rise of the cation absorption in the experiment.

Chapter 2 deals with the position of the counterion X^- in the ion pairs $Ph_2CH-PPh_3^+\ X^-$, $PhCH_2-PPh_3^+\ X^-$, and (p-CF_3-C_6H_4)$CH_2-PPh_3^+\ X^-$ in solution with X^- being Cl^-, Br^-, BF_4^-, and SbF_6^-. These structures are essential to clarify the role of oxidizable counterions like e.g. Cl^- during the initial bond cleavage in dichloromethane. The structures determined quantum chemically in dichloromethane show a similar counterion position than in the crystal. They are confirmed by the good accordance of the calculated and measured ^{1}H NMR shifts. The C(α)–H$\cdots$X$^-$ hydrogen bonds account for the pronounced counterion-dependent ^{1}H NMR shifts of the C(α)–H in CD_2Cl_2. The strong downfield shift of the signals increases according to $SbF_6^- < BF_4^- \ll Br^- < Cl^-$.

The last part (chapter 3) focuses on the secondary processes within a few picoseconds to several nanoseconds after the C-Cl bond cleavage in diphenylmethylchloride in solution. Initially, the neutral leaving group Cl leads mainly to the formation of radical pairs; only a minor fraction of ion pairs is generated in the beginning. A combined Marcus-Smoluchowski model is used to simulate the interplay between geminate recombination, diffusional separation, and electron

transfer of the radical and ion pair populations. The distance-dependent rates of the three processes together with broad distance-dependent population distributions faithfully reproduce the spectroscopically observed dynamics. The majority of Ph_2CH^+ cations is generated via electron transfer from the radical pairs. The detailed understanding of the secondary processes shows that a high Ph_2CH^+ cation yield can be expected if the radicals within a pair stay nearby for a long time to achieve an efficient electron transfer and if the resulting ions are separated fast to prevent geminate recombination.

Kurzfassung

Bruch und Bildung von Bindungen sind wesentliche Schritte in der Chemie und Biochemie. Die vorliegende Arbeit untersucht die Bildung von Diphenylmethylkationen (Ph_2CH^+) mittels photoinduziertem Bindungsbruch von Diphenylmethylderivaten mit kationischen oder neutralen Abgangsgruppen. Die entstehenden Ph_2CH^+ Kationen und ihre zahlreichen Derivate dienen als Referenzelektrophile für eine der weitreichendsten Reaktivitätsskalen, die 40 Größenordnungen abdeckt. In Kapitel 1 liegt der Fokus auf dem initialen Bindungsbruch von Diphenylmethyltriphenylphosphoniumionen ($Ph_2CH-PPh_3^+$), die eine kationische Abgangsgruppe aufweisen. Mit Hilfe modernster quantenchemischer und quantendynamischer Methoden wird der Reaktionsmechanismus aufgedeckt. Unter Verwendung eines reduzierten Modellsystems können die Potentialflächen auf ONIOM Niveau entlang eigens konstruierter reaktiver Koordinaten berechnet werden. Es zeigen sich zwei konkurrierende Reaktionskanäle: ein homolytischer im S_1 Zustand und ein heterolytischer im Grundzustand. Sie sind über eine energetisch zugängliche konische Durchschneidung verbunden, die eine effiziente Erzeugung der beobachteten Ph_2CH^+ Kationen ermöglicht. Im Widerspruch zum Experiment in polaren oder schwach polaren Lösungsmitteln zeigen quantendynamische Rechnungen der isolierten Moleküle die Bildung von $Ph_2CH^\bullet$ Radikalen. Während elektrostatische Lösungsmitteleffekte in diesem System zu vernachlässigen sind, sind dynamische Lösungsmitteleffekte ausschlaggebend, um die Reaktion zu erklären.

Es wurden zwei neue Methoden mit steigender Komplexität entwickelt, um den dynamischen Einfluss der Lösungsmittelumgebung zu beschreiben. Der erste Ansatz, der dynamische Kontinuumsansatz, behandelt die Umgebung implizit. Er nutzt das Gesetz von Stokes und die dynamische Viskosität des Lösungsmittels in Kombination mit quantenchemisch und -dynamisch berechneten Werten, um die Bremskraft, die auf die dissoziierenden Fragmente wirkt, zu erhalten. Der Ansatz benötigt keine Parameter, die angepasst werden müssten. Die zweite Methode, der QD/MD Ansatz, basiert auf einer expliziten Betrachtung der Lösungsmittelumgebung. Er kombiniert Moleklulardynamik (MD)-Simulationen des Edukts in einer Box von Lösungsmittelmolekülen mit Quantendynamik (QD)-Rechnungen der Eduktdynamik. Auf diese Weise kann ein detaillierteres mikroskopisches Bild abgeleitet werden, in dem individuelle Anordnungen der Lösungsmittelmoleküle berücksichtigt werden. Beide Methoden decken den entscheidenden Einfluss des Lösungsmittelkäfigs auf den Mechanismus des Bindungsbruchs auf. Er verhindert die freie Dissoziation im S_1 Zustand und führt das molekulare System zur konischen Durchschneidung. QD Simulationen unter Berücksichtigung der nicht-adiabatischen Kopplung rund um die konische Durchschneidung zeigen in guter Übereinstimmung mit dem initialen Anstieg der Kationenabsorption im Experiment die Bildung von Ph_2CH^+ nach $\sim 400\,\mathrm{fs}$.

Kapitel 2 behandelt die Position des Gegenions X^- in den Ionenpaaren $Ph_2CH-PPh_3^+\ X^-$, $PhCH_2-PPh_3^+\ X^-$ und $(p\text{-}CF_3\text{-}C_6H_4)CH_2-PPh_3^+\ X^-$ in Lösung, wobei X^- entweder Cl^-, Br^-, BF_4^- oder SbF_6^- ist. Diese Strukturen sind notwendig, um die Rolle oxidierbarer Gegenionen wie beispielsweise Cl^- während des initialen Bindungsbruchs zu klären. Die quantenchemisch bestimmten Strukturen in Dichlormethan zeigen die gleichen Gegenionpositionen wie im Kristall. Eine gute Übereinstimmung der berechneten und gemessenen ^1H NMR Verschiebungen bestätigt die Strukturen. Die $C(\alpha)-H\cdots X^-$ Wasserstoffbrückenbindungen erklären die ausgeprägt gegenionabhängigen ^1H NMR Verschiebungen der $C(\alpha)-H$ in CD_2Cl_2. Die starke Tieffeldverschiebung der Signale steigt gemäß $SbF_6^- < BF_4^- \ll Br^- < Cl^-$.

Der letzte Teil (Kapitel 3) konzentriert sich auf Sekundärprozesse innerhalb weniger Pikosekunden bis hin zu einigen Nanosekunden, die nach dem Bruch der C-Cl-Bindung in Diphenyl-

methylchlorid in Lösung aufteten. Zunächst führt die neutrale Abgangsgruppe Cl überwiegend zur Bildung von Radikalpaaren; lediglich ein kleiner Anteil von Ionenpaaren wird zu Beginn gebildet. Mit einem kombinierten Marcus-Smoluchowski-Model wird das Zusammenspiel zwischen geminater Rekombination, diffusiver Trennung und Elektronentransfer der Radikal- und Ionenpaarpopulation simuliert. Zusammen mit breiten abstandsabhängigen Populationsverteilungen reproduzieren die abstandsabhängigen Raten der drei Prozesse originalgetreu die spektroskopisch beobachtete Dynamik. Der Großteil der Ph_2CH^+ Kationen wird mittels Elektronentransfer aus den Radikalpaaren generiert. Das detaillierte Verständnis der Sekundärprozesse zeigt, dass eine hohe Ph_2CH^+ Ausbeute erwartet werden kann, wenn die Radikale innerhalb eines Paares lange nahe beeinander bleiben, um einen effizienten Elektrontransfer zu erreichen, und wenn die so gebildeten Ionen schnell getrennt werden, um geminate Rekombination zu verhindern.

List of publications

This thesis is based on the following five publications listed in chronological order. They are reprinted in the chapters 1 (**3–5**), 2 (**2**) and 3 (**1**).

1 C. F. Sailer, S. Thallmair, B. P. Fingerhut, C. Nolte, J. Ammer, H. Mayr, I. Pugliesi, R. de Vivie-Riedle, E. Riedle:
A Comprehensive Microscopic Picture of the Benzhydryl Radical and Cation Photogeneration and Interconversion through Electron Transfer.
ChemPhysChem **14**, 1423–1437 (2013).

2 J. Ammer, C. Nolte, K. Karaghiosoff, S. Thallmair, P. Mayer, R. de Vivie-Riedle, H. Mayr:
Ion-Pairing of Phosphonium Salts in Solution: C—H$\cdots$Halogen and C—H$\cdots\pi$ Hydrogen Bonds.
Chem. Eur. J. **19**, 14612–14630 (2013).

3 S. Thallmair, B. P. Fingerhut, R. de Vivie-Riedle:
Ground and Excited State Surfaces for the Photochemical Bond Cleavage in Phenylmethylphenylphosphonium Ions.
J. Phys. Chem. A **117**, 10626–10633 (2013).

4 S. Thallmair, M. Kowalewski, J. P. P. Zauleck, M. K. Roos, R. de Vivie-Riedle:
Quantum Dynamics of a Photochemical Bond Cleavage Influenced by the Solvent Environment: A Dynamic Continuum Approach.
J. Phys. Chem. Lett. **5**, 3480–3485 (2014).

5 S. Thallmair, J. P. P. Zauleck, R. de Vivie-Riedle:
Quantum Dynamics in an Explicit Solvent Environment: A Photochemical Bond Cleavage Treated with a Combined QD/MD Approach.
J. Chem. Theory Comput. **11**, 1987–1995 (2015).

Additional publications listed in chronological order:

6   S. Thallmair, W. Bauer, B. Weber:
         Strategies towards the Purposeful Design of Long-Range Ferromagnetic Ordering Due to
         Spin Canting.
         Polyhedron **28**, 1796–1801 (2009).

7   C. Gollub, M. Kowalewski, S. Thallmair, R. de Vivie-Riedle:
         Chemoselective Quantum Control of Carbonyl Bonds in Grignard Reactions Using Shaped
         Laser Pulses.
         Phys. Chem. Chem. Phys. **12**, 15780–15787 (2010).

8   T. M. Pfaffeneder, S. Thallmair, W. Bauer, B. Weber:
         Complete and Incomplete Spin Transitions in 1D Chain Iron(II) Compounds.
         New J. Chem. **35**, 691–700 (2010).

9   P. von den Hoff, S. Thallmair, M. Kowalewski, R. Siemering, R. de Vivie-Riedle:
         Optimal Control Theory – Closing the Gap Between Theory and Experiment.
         Phys. Chem. Chem. Phys. **14**, 14460–14485 (2012).

10   S. Thallmair, M. Kowalewski, B. P. Fingerhut, C. F. Sailer, R. de Vivie-Riedle:
         Molecular Wave Packet Dynamics Decelerated by Solvent Environment: A Theoretical
         Approach.
         in: Ultrafast Phenomena XVIII, M. Chergui, S. Cundiff, A. Taylor, R. de Vivie-Riedle, K.
         Yamanouchi (Eds.), *EPJ Web of Conferences* **41**, 05043 (2013).

11   S. Thallmair, R. Siemering, P. Kölle, M. Kling, M. Wollenhaupt, T. Baumert, R. de Vivie-
         Riedle:
         The Interplay of Nuclear and Electronic Motion in the Control of Molecular Processes: A
         Theoretical Perspective.
         in: Molecular Quantum Dynamics – From Theory to Applications, F. Gatti (Ed.),
         Springer, 2014, 213–248.

12   S. Thallmair, J. P. P. Zauleck, R. de Vivie-Riedle:
         Quantum Dynamics of Molecular Reactions Directed by Explicit Solvent Environment.
         in: Ultrafast Phenomena XIX, K. Yamanouchi, S. Cundiff, R. de Vivie-Riedle, M. Kuwata-
         Gonokami, L. S. DiMauro (Eds.), Springer Proceedings in Physics 162, Springer, 2015,
         373–377.

Introduction

Phototriggered processes play a fundamental role in chemistry as well as in biochemistry. They are an everyday occurrence in biology and natural synthesis. Examples from organic chemistry are electrocyclic reactions, sigmatropic rearrangements, cycloadditions, bond cleavage or isomerizations [1]. The latter are at the heart of molecular photoswitches which have been of growing interest in the past years [2–7]. Furthermore, polymerization reactions [8–10] as well as several specific named reactions in organic chemistry like e.g. the Photo-Friess rearrangement [11–14] or the Wolff rearrangement [14–17] can be initiated by light. Prominent events in biochemistry are the photosynthesis [18–25], the process of vision [26–29] or the formation of different photolesions of deoxyribonucleic acid (DNA) causing skin cancer [30–35]. Complex biomimetic reaction cascades may also involve photochemical steps to enable the formation of the desired natural product [36, 37].

During the last decades, a fruitful symbioses of experimental measurements of photochemical reactions and their theoretical descriptions paved the way for a better understanding of the underlying fundamental processes. Examples are ultrafast chemical reactions [6, 38–42], biochemical processes [25, 27, 32, 43] or biomimetic synthesis [37] among many others. Major technical progress in both areas contributed thereto. For real time observations of photochemical reactions the ability to generate ultrashort laser pulses on the low femtosecond time scale is a necessary tool [44–52]. First groundbreaking experiments by the group of Achmed H. Zewail lead to the awarding of the Nobel Prize in Chemistry to him in 1999 [53–56]. Nowadays, the tunability of laser pulses from the infrared (IR) to the ultraviolet (UV) region of the electromagnetic spectrum and variable observation times from femtoseconds up to microseconds and more offer a flexible tool to follow chemical reactions and to unravel excited state relaxation pathways [57–60]. Besides pump-probe spectroscopy also multidimensional spectroscopy contributes thereto [61–65].

From a theoretician's perspective, the development of suitable methods for the description of molecular processes is fundamental. Representative for the methodological progress are the Nobel Prizes in Chemistry of the years 1998 and 2013, which were awarded to John A. Pople and Walter Kohn for their development of computational methods in quantum chemistry and of density functional theory [66, 67] and to Martin Karplus, Micheal Levitt and Arieh Warshel for developing the quantum mechanics / molecular mechanics (QM/MM) method, a hybrid quantum chemical method [68–70]. The wave function based methods configuration interactions (CI), coupled cluster (CC), and complete active space self consistent field (CASSCF) as well as complete active space second-order perturbation theory (CASPT2) frequently are the methods of choice if electronically excited states are involved during the investigated reaction [71–76]. The time-dependent density functional theory (TDDFT) offers a computationally less demanding way to calculate excited states, but often the selection of the functional is crucial for the ordering of energetically closely lying electronic states [75–79]. The "our own n-layered integrated molecular orbital and molecular mechanics" (ONIOM) method provides a valuable way to also account for not directly involved molecular moieties during excited state calculations [80–84].

As chemical and biochemical reactions mainly take place in solution, the description of the reactant's environment additionally plays a crucial role. A computationally relatively economic treatment is connected with implicit solvation models which treat the solvent as a dielectric continuum and thus allow the consideration of electrostatic solvent effects [85–87]. Two prominent representatives are the polarizable continuum model (PCM) [86–88] and the conductor-

like screening model (COSMO) [86, 87, 89]. By far more computationally demanding is an explicit description of the solvent molecules which is possible for example with the QM/MM method [68–70, 90–92]. As the surrounding does not participate directly in the reaction, it is described on a lower level of theory than the reactive unit. Moreover, linear scaling methods provide an opportunity to increase the size of the QM region and thus to improve the accuracy of the theoretical calculations [93–96].

For the simulation of chemical reaction dynamics, time-dependent approaches are necessary. Naturally, this is more challenging in an electronically excited state than in the ground state. Reactive molecular dynamics (MD) simulations are computationally attractive but they require the determination of all necessary parameters in advance [97–101]. The advantage of semi-classical on-the-fly simulations is that the electronic Schrödinger equation is evaluated for each point in the configuration space reached by the trajectories. To obtain convergence for the overall reaction process often a vast number of trajectory calculations has to be performed. The availability of open source programs like NEWTON-X [102, 103] or the recently released SHARC [104, 105] facilitate the calculation of semi-classical dynamics at an appropriate level of theory. For excited states, multi reference methods like the multi reference configuration interactions (MRCI) or the CASSCF method are well-suited [106]. They additionally provide the possibility to perform non-adiabatic transitions between electronic states applying Tully's surface hopping [107–112]. The option to carry out excited state on-the-fly simulations using TDDFT provided by some quantum chemical program packages has to be treated with caution, as at this level of theory the description of conical intersections (CoIns) often involved along photochemical or photophysical relaxation pathways can be problematic. The most accurate possibility to describe photochemical reactions is provided by quantum dynamics (QD) calculations where also the wave packet character of the nuclei is preserved [113–116]. Electronic excitations by a laser pulse, coherent control studies [117, 118] or non-adiabatic processes like population transfer through CoIns [119, 120] can be described straightforwardly. A full-dimensional treatment of larger molecules, however, is nowadays still out of reach. In the case of bound potentials, the multi configuration time dependent Hartree (MCTDH) method offers an efficient way to include comparably many dimensions [121–123]. Nevertheless, for QD simulations, the knowledge of the decisive regions of the molecular configuration space and reactive coordinates connecting these regions are required beforehand. In chapter 1.1.2 an approach to optimally design adapted reactive coordinates is described.

The present work investigates the photogeneration of reactive carbocations – in particular diphenylmethyl cations (Ph_2CH^+) – by means of state-of-the-art quantum chemical and quantum dynamical calculations. Ph_2CH^+ and its numerous derivatives serve as reference electrophiles for one of the most extensive reactivity scales covering 40 orders of magnitude which is being developed by H. Mayr and coworkers [124–130]. A common way to generate the desired carbocations is photoexcitation of a precursor molecule [131, 132], e.g. diphenylmethylphosphonium ions or diphenylmethylhalides, resulting in a bond cleavage in the femto- to picosecond range [39, 133–136]. A subsequent reaction with a nucleophile can be followed spectroscopically at the prominent absorption band of the diphenylmethyl cations lying at $\sim 435\,\text{nm}$ in case of the unsubstituted Ph_2CH^+ [133, 137]. In this way, the reactivity of the pair of nucleophile and electrophile can be determined [126, 127, 132]. The bond cleavage can have either homolytic or heterolytic character. Both cases are observed for diphenylmethyl derivatives: the neutral diphenylmethylchloride (Ph_2CH-Cl) for instance shows homolytic bond cleavage which was already investigated theoretically as well as experimentally [82, 134, 136, 138]; the cationic diphenylmethyltriphenylphosphonium ions ($Ph_2CH-PPh_3^+$) exhibit heterolytic bond cleavage in case of an inert counterion [133, 139, 140]. The reaction mechanism of the cationic precursor $Ph_2CH-PPh_3^+$ is still an open question which will be addressed during the present work. Another question that will be answered in the following is the interconversion of the radical pair

to the ion pair subsequent to the initial bond cleavage of neutral precursors like Ph_2CH-Cl or Ph_2CH-Br [60].

The first part of this thesis considers $Ph_2CH-PPh_3^+$ ions containing a positively charged leaving group. They facilitate the generation of Ph_2CH^+ cations in polar as well as moderately polar solvents [132, 133]. The focus is on the molecular mechanism of the initial bond cleavage and in particular on the mechanic influence of the solvent environment – the dynamic solvent effects – on the ultrafast photochemical process. Thereto, a model system was set up and characterized which enabled the quantum chemical description of the full system $Ph_2CH-PPh_3^+$ using the ONIOM method. To perform QD simulations, adapted reactive coordinates were designed and the kinetic Hamiltonian was set up in these coordinates employing the G-matrix formalism [141–143]. As the investigated bond cleavage is an ultrafast process, the most relevant regions of the molecular configuration space can be described by a low-dimensional model being two-dimensional here. The simulations of the isolated molecules corresponding to the gas phase revealed the necessity to take the dynamic solvent effects into account while modeling the reaction dynamics. For this purpose, two different methods with increasing complexity have been developed: The first one, the dynamic continuum ansatz, describes the solvent environment implicitly. It uses Stokes' law and the dynamic viscosity of the solvent to describe the decelerating force exerted on the dissociating fragments. The second one, the QD/MD method, goes one step further and combines quantum dynamics and molecular dynamics for a more microscopic picture of the solvent cage based on its atomistic description. The MD simulations are used to provide information about the arrangement of the solvent molecules around the precursor. On the basis of these arrangements a solvent potential can be calculated and included into the QD simulations.

Another aspect in the surrounding of the $Ph_2CH-PPh_3^+$ ions is the respective counterion X^-. Ultrafast transient absorption measurements have shown that complex counterions like SbF_6^- or BF_4^- lead to the generation of carbocations while excitation of phosphonium salts with halides (e.g. Cl^-, Br^-) in dichloromethane is followed by radical formation [133, 134]. To unravel the role of the halides, the counterion has to be included in the theoretical treatment of the bond cleavage for which the geometry of the respective ion pair is decisive. The second chapter of the present work investigates the position of X^- within the ion pairs $Ph_2CH-PPh_3^+ \ X^-$, $PhCH_2-PPh_3^+ \ X^-$, and $(p\text{-}CF_3\text{-}C_6H_4)CH_2-PPh_3^+ \ X^-$ in solution. Thereto, quantum chemical calculations using density functional theory (DFT) were performed to optimize the structure of the ion pairs with X^- being Cl^-, Br^-, BF_4^-, and SbF_6^- in a continuum solvation model for dichloromethane. A subsequent comparison of the strongly counterion dependent ^1H nuclear magnetic resonance (NMR) shifts in solution confirmed the resulting structures which show hydrogen bondings comparable to the crystal structures.

The last part of the present thesis focuses on secondary processes emerging after the initial bond cleavage. A well-suited candidate for such a study is Ph_2CH-Cl, which exhibits mostly homolytic bond cleavage generating the radical pair $Ph_2CH^\bullet \ Cl^\bullet$. In comparison with the initial bond cleavage happening within $\sim 200\,fs$ in case of the Cl leaving group [134, 135], the secondary processes take place on a longer time scale. It ranges from a few picoseconds up to several nanoseconds. Two ubiquitous secondary processes are geminate recombination and diffusional separation. In the chosen example of Ph_2CH-Cl an additional process becomes evident: as the radical pair emerging from the initial bond cleavage is not the thermodynamically stable product in polar and moderately polar solvents, electron transfer from the $Ph_2CH^\bullet$ radical to the $Cl^\bullet$ radical generates the ion pair $Ph_2CH^+ \ Cl^-$. To describe all these interwoven processes, a combined Marcus-Smoluchowski model has been set up which is presented in chapter 3. It enables the simulation of the time-dependent behavior of the radical and ion pair populations in different solvents, which shows an excellent agreement with the transient absorption signals of $Ph_2CH^\bullet$ and Ph_2CH^+. Thus, the Marcus-Smoluchowski model allowed

to derive a detailed microscopic understanding of the secondary processes subsequent to the bond cleavage of diphenylmethylchloride. Beyond this, it gives new insights into the continuous distance-dependent population distributions of the radical and ion pairs which cannot be described using discrete species.

The present work opens a straightforward way to link the simulation of the ultrafast bond cleavage on the femto- to picosecond time scale and of the secondary processes in the pico- to nanosecond range. The two newly developed approaches to perform QD calculations taking the dynamic solvent effects into account provide ab initio information about the starting population distributions for the Marcus-Smoluchowski model. Hence, an overall simulation connecting all steps involved is feasible in the future.

1. Dynamic solvent effects using the example of the bond cleavage of diphenylmethyltriphenylphosphonium ions

In every day chemistry, solvents play an important role [144]. Their selection may be a crucial point during the design of a synthesis route [144, 145]. For example, the solubility of reactants or products depends on the solvent [145, 146]. Usually, electrostatic solvent effects are in the focus of such considerations. They may cause that certain reaction pathways experience different energetic stabilization in solution due to differences in the charge distribution along them [147–149]. In quantum chemistry, a number of methods with different complexity are available to describe these electrostatic solvent effects. In principle, two different ways to describe the solvent environment exist: The first type of approaches treats the solvent as a continuous medium with a specific solvent dependent dielectric constant ε_S. In the second type, the solvent molecules are modeled explicitly [85].

The PCM is one of the most common models for the description of an implicit solvation [86, 87, 150, 151]. At this, the total Hamiltonian $\hat{H}_{\mathrm{tot}}^{\mathrm{PCM}}$ reads

$$\hat{H}_{\mathrm{tot}}^{\mathrm{PCM}} \left[r_{\mathrm{M}}, Q_x \left(\vec{r}, \vec{r}' \right) \right] = \hat{H}_{\mathrm{M}} \left(r_{\mathrm{M}} \right) + \hat{H}_{\mathrm{MS}} \left[r_{\mathrm{M}}, Q_x \left(\vec{r}, \vec{r}' \right) \right], \tag{1.1}$$

with the molecular Hamiltonian $\hat{H}_{\mathrm{M}}$ and the Hamiltonian $\hat{H}_{\mathrm{MS}}$ describing the interactions of the solute M with the solvent S [87]. Note that both contributions to $\hat{H}_{\mathrm{tot}}^{\mathrm{PCM}}$ only depend on the degrees of freedom of the solute r_{M} and the solvent response functions $Q_x(\vec{r}, \vec{r}')$, where $\vec{r}$ and $\vec{r}'$ are position vectors. The degrees of freedom of the solvent molecules r_{S} are replaced by $Q_x(\vec{r}, \vec{r}')$, which only depend on a continuous solvent distribution. This is the main issue of the continuum models because it reduces the complexity of the problem significantly. The Hamiltonian $\hat{H}_{\mathrm{MS}}$ comprises the solvent reaction potential which in the original formulation of the PCM [88] only considered the electrostatic interaction between the solute and the solvent. Nowadays, additionally the steric repulsion and the dispersion interaction are described by $\hat{H}_{\mathrm{MS}}$ [86, 150, 152, 153]. The free energy of the solute in solution $G(M)$ contains the following contributions [86, 87, 150]:

$$G(M) = G_{\mathrm{cav}} + G_{\mathrm{el}} + G_{\mathrm{rep}} + G_{\mathrm{dis}} + G_{\mathrm{tm}}. \tag{1.2}$$

The energy necessary to form an empty cavity in the pure solvent, which has the shape of the solute M, is G_{cav}. It is calculated based on the geometry of M and of the solvent molecules [154, 155]. The second summand in eq. 1.2 contains the electrostatic energy i.e. on the one hand the complete molecular energy as well as the energy gain due to the electrostatic interaction between the solute and the solvent. The solvent response function to the electric field $\vec{E}(\vec{r})$ of the solute is the polarization $\vec{P}(\vec{r})$ of the solvent surrounding. In the simplest formulation of the PCM $\vec{P}(\vec{r})$ reads [86, 87]

$$\vec{P}(\vec{r}) = \frac{\varepsilon_S - 1}{4\pi} \vec{E}(\vec{r}), \tag{1.3}$$

where the solvent specific dielectric constant ε_S determines the strength of the polarization. The repulsion energy G_{rep} contains the steric interaction between the solute and its surrounding, and

the dispersion energy G_{dis} describes the dispersion contribution to $G(M)$. Both energy terms – G_{rep} and G_{dis} – are often combined to the van der Waals energy G_{vdW}. The last term in eq. 1.2 is the thermal motion contribution G_{tm} containing the energy of the thermal motion of the nuclei of the solvent molecules [86, 156].

The advantages of the implicit solvation within the PCM are not only applicable for quantum chemical calculations in the electronic ground state, but also for excited state calculations. In the framework of the PCM, the response of the solvent molecules to an electronic excitation of the solute can be partitioned in a fast and a slow part leading to a non-equilibrium situation. The fast response can be ascribed to the electrons adapting to the changed electronic structure of the solute while the slow response is due to the motion of the nuclei of the solvent molecules [157]. The possibility to distinguish between both makes the PCM an important tool for the simulation of vertical excitation energies and Stokes shifts in solution [158–161]. Nowadays, a large variety of molecular properties in solution like IR and Raman scattering intensities, NMR shifts, circular dichroism and vertical excitation energies are accessible with the help of the PCM [87, 162].

A more detailed way to describe the solvent environment around a solute is to model it explicitly [85, 92, 163]. Here the degrees of freedom of the solvent molecules are not omitted in the Hamiltonian:

$$\hat{H}_{\text{tot}}^{\text{expl}}(r_{\text{M}}, r_{\text{S}}) = \hat{H}_{\text{M}}(r_{\text{M}}) + \hat{H}_{\text{S}}(r_{\text{S}}) + \hat{H}_{\text{SS}}(r_{\text{S}}) + \hat{H}_{\text{MS}}(r_{\text{M}}, r_{\text{S}}), \quad\quad (1.4)$$

which then contains two additional terms compared to $\hat{H}_{\text{tot}}^{\text{PCM}}$ (cf. eq. 1.1): $\hat{H}_{\text{S}}(r_{\text{S}})$ describes the energy of the solvent molecules and $\hat{H}_{\text{SS}}(r_{\text{S}})$ the interaction energy of the solvent molecules among each other [87]. Since for the simulation of a solvent environment, a large amount of solvent molecules has to be included, the explicit approach is computationally more expensive compared to the implicit solvation. A quantum mechanical simulation of the whole system is nowadays still very demanding, thus usually the solvent molecules are described classically by a force field. However, linear scaling methods may enable to enlarge the quantum mechanically treated system to the innermost solvation shell [93–96]. Another aspect of the explicit approach is the requirement of averaging over the solvent coordinates. This is often done using MD or Monte-Carlo simulations [163]. The hybrid QM/MM method introduced by A. Warshel and M. Levitt enables to treat the solute or parts of the solute quantum chemically in a classically simulated environment [69, 70, 163, 164].

But solvent effects are not only restricted to static reactivity considerations where the electrostatic contributions are most important. Once a fast process brings the system off equilibrium, e.g. caused by an external trigger like a laser pulse, the dynamics of the solute are influenced immediately by the dynamics of its solvent surrounding. In the PCM the electrostatic solvent effects at the beginning of such a non-equilibrium situation can be taken into account as well as those in the final equilibrated state [86, 87, 159]. But the consideration of a time interval necessary for the equilibration can only be made using an explicit approach [165–167]. The obtained results can be compared to experimentally determined dynamic Stokes shifts which can be traced back to the solvent reorganization [165, 166, 168].

Beyond that, additional solvent effects can emerge for reactions with large structural changes like bond cleavage or formation. During these reactions, the solvent environment directly interacts with the molecular motion of the solute [169–173]. Its initial motion can be deviated along a path which is less blocked by solvent molecules and routes with smaller energy gradients can exert influence on the reaction process. Therefore, the dynamics of the solute are substantially affected by the forces induced by the solvent surrounding, hence its mechanic influence. These dynamic solvent effects are particularly important for ultrafast chemical reactions like photochemical bond cleavage. Here, the solute's fragments move apart from each other and strongly push into the solvent cage, which leads to a change of momentum.

From a theoreticians point of view, it is challenging to include these dynamic effects into simulations, especially into QD simulations. First successful realizations for photoinduced chemical processes have been demonstrated for the excited state bond cleavage of ICN, which was studied with classical MD methods. The setup of parametrized potentials [174] enabled I. Benjamin and K. R. Wilson to compare simulations in a Xe fluid with those for the gas phase [169]. They revealed that the dissociating molecular fragments are decelerated by the surrounding Xe atoms. Other groups observed a similar behavior in Ar [170, 171], water [172] and ethanol [173]. Moreover, S. E. Bradforth, I. Benjamin and coworkers reported the slowdown of rotationally hot CN$^\bullet$ radicals following the photodissociation [173, 175, 176]. By comparing MD simulations with transient pump-probe anisotropy measurements, it transpired that the rotational speed is reduced as a larger cavity is formed. In this cavity the CN$^\bullet$ radicals subsequently nearly freely rotate for several picoseconds.

Another experimentally extensively studied example is the photofragmentation dynamics of *para*-methyl substituted thiophenol and thioanisole. Transient pump-probe experiments were carried out in various solvents [177–179]. Observed differences of the behavior in the gas phase and in solution are traced back to the solvent cage, which hinders specific motions necessary to reach an active S_1/S_0-CoIn [178, 179]. A second aspect emphasizing the importance of the solvent cage are changes in the yield of different isomers observed after geminate recombination [177, 179]. So far, wave packet simulations of the dissociation process were performed only for the isolated molecules [180]. Here, additional QD calculations taking the solvent environment into account would improve the understanding of the microscopic reaction process.

In the 1970s, heavy ion physicists performed first quantum mechanical calculations on moving particles subject to viscous force [181–186]. One kind of approach used the expectation values of momentum and position together with a frictional constant for the calculation of the viscous force [181–184]. It combines the Schrödinger equation with the Langevin equation. W. Stocker and K. Albrecht introduced another approach which relies on the polar form of the wave function [186]. They finally used the phase of the wave function to calculate the frictional force.

The influence of rare gas matrices on the vibration of diatomics were investigated by femtosecond spectroscopy as well as quantum dynamical and semi-classical simulations [187–189]. In the simulations, the impact of the rigid rare gas cage on the stretching vibration was taken into account by a modulation of the potential energy curves [187].

In the focus of interest of the present thesis is the photochemistry of medium sized organic molecules that are used to generate carbocations in solution and to study these reactive intermediates [124–132]. To simulate the photoinduced bond cleavage of $Ph_2CH-PPh_3^+$ in solution, the mechanic impact of the solvent cage on the dissociating molecular fragments is crucial. During this thesis, two methods with increasing complexity to describe the dynamic impact of the solvent environment were developed. In the first approach, the dynamic solvent effects are included into quantum dynamical simulations in a continuum-like fashion realizing an implicit description of the environment. An explicit treatment of the solvent surrounding is the footing of the second method. The QD/MD approach combines QD and MD for a more microscopic picture of the solvent cage.

Both approaches are discussed in this chapter using the example of $Ph_2CH-PPh_3^+$. The chapter is structured as follows: In the first section 1.1 the quantum chemical description of the necessary potential energy surface (PES) of $Ph_2CH-PPh_3^+$ as well as the setup of the reactive coordinates adapted to the considered bond cleavage process are presented. It is followed by the dynamic continuum ansatz described in section 1.2. The QD/MD approach is then presented in section 1.3.

1.1. Quantum chemical characterization of the bond cleavage

For any investigation of the dynamics of a molecular system an appropriate method to characterize its time-independent properties is indispensable. Despite the reliability of the results, the required computational time is an important selection criterion [116,190]. In line with the second criterion is the dimensionality reduction for the QD simulations. Nowadays, a quantum dynamical treatment of a chemical problem like the investigated bond cleavage of Ph$_2$CH–PPh$_3^+$ in full dimensionality is still far out of reach [116,190]. In this section, the quantum chemical characterization of Ph$_2$CH–PPh$_3^+$ as well as the setup of specially designed reactive coordinates are discussed.

1.1.1. Ground and excited state surfaces for the model system phenylmethylphenylphosphonium ion

In the article "Ground and Excited State Surfaces for the Photochemical Bond Cleavage in Phenylmethylphenylphosphonium Ions" published in *The Journal of Physical Chemistry A* potential surfaces for the ground and excited states of the phenylmethylphenylphosphonium ion (PhCH$_2$–PH$_2$Ph$^+$) on the CASSCF and CASPT2 level of theory are presented [191]. The PhCH$_2$–PH$_2$Ph$^+$ is set up as a model system for the experimentally commonly employed Ph$_2$CH–PPh$_3^+$. Its appropriateness is shown by the comparison of excitation spectra of phosphonium ions with an increasing number of phenyl rings which were calculated at the second-order approximate coupled cluster (CC2) level of theory. On the basis of the model system PhCH$_2$–PH$_2$Ph$^+$, the following central statements can be made:

- The first and second excited singlet state are local π-π^* excitations on the phosphonium (S$_1$) and the methyl moiety (S$_2$). They are very close in energy and cannot be resolved in the experiment as they are broadened due to environmental effects. The third excited state S$_3$ which has charge transfer (CT) character is well separated. Any population transferred to the S$_2$ state can relax to the S$_1$ state through a S$_2$/S$_1$ CoIn close to the S$_2$ minimum in the Franck-Condon (FC) region.

- The excitation on the phosphonium moiety opens the preferred reaction path. Thus chemical modifications of the methyl moiety are clearly separated from the initiation of the bond cleavage process. The interaction of the S$_1$ with the CT state initiates a π^* to σ^* electron transfer which is followed by a σ to π electron transfer along the major reaction coordinate, the C1-P distance. Overall this leads to a homolytic bond cleavage in the S$_1$ state forming a radical pair (PhCH$_2^\bullet$ + PH$_2$Ph$^{\bullet +}$). In contrast, the ground state S$_0$ has a heterolytic character generating PhCH$_2^+$ + PH$_2$Ph.

- In the gas phase as well as in solution, the thermodynamically stable products are PhCH$_2^+$ + PH$_2$Ph. This is in good agreement with recent experimental studies [133,140]. But the bond cleavage in the S$_1$ state has homolytic character which is in clear disagreement with transient absorption measurements. They show the formation of Ph$_2$CH$^+$ after photoexcitation almost exclusively [133, 140]. The two competing reaction channels arise to be connected by a S$_1$/S$_0$ CoIn which is energetically reachable after the optical excitation following an angular coordinate. In principle, here the S$_1$ population can relax to the ground state, which is the heterolytic channel, but its efficiency has to be evaluated quantum dynamically.

The quantum chemical results for the model system PhCH$_2$–PH$_2$Ph$^+$ lay the foundation for the setup of the PESs for the full system Ph$_2$CH–PPh$_3^+$ in section 1.1.2 and the QD investigations discussed in the sections 1.2 and 1.3.

Hereafter, the article "Ground and Excited State Surfaces for the Photochemical Bond Cleavage in Phenylmethylphenylphosphonium Ions" published in *The Journal of Physical Chemistry A* is reprinted with permission from *J. Phys. Chem A*, **117**, 10626–10633 (2013); copyright 2013 American Chemical Society. Selected parts of the supporting information concerning the active space and the development of the orbital energies are reprinted in appendix A.

Ground and Excited State Surfaces for the Photochemical Bond Cleavage in Phenylmethylphenylphosphonium Ions

Sebastian Thallmair,[†,‡] Benjamin P. Fingerhut,[†,¶] and Regina de Vivie-Riedle*,[†]

[†]Department Chemie, Ludwig-Maximilians-Universität München, D-81377 München, Germany

[‡]Lehrstuhl für BioMolekulare Optik, Ludwig-Maximilians-Universität München, D-80538 München, Germany

Ⓢ *Supporting Information*

ABSTRACT: Photolytic bond cleavage is a well-established method to generate carbocations for organic synthesis. Changes in the leaving group have a large influence on the chemical yield. The underlying potential energy surfaces governing the initial process are mostly unknown. We provide potential energy surfaces of ground and excited states on the CASSCF/ CASPT2 level of theory for the charged precursor phenylmethylphenylphosphonium ion. We present the electronic and structural changes accompanying the excitation process and the subsequent bond cleavage. Inter-ring charge-transfer processes play a crucial role in the Franck–Condon region. Beyond the Franck–Condon region, competing reaction pathways emerge connected through conical intersections. The phenylmethylphenylphosphonium ion is used as a model system for the commonly used diphenylmethyltriphenylphosphonium ion. The appropriateness of the model is tested by CC2 calculations of the excitation spectrum.
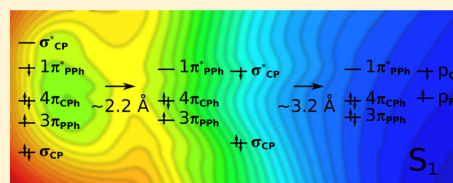
1. INTRODUCTION

Carbocations are well-studied reactive intermediates in organic chemistry and biochemistry. A convenient way to produce them is the photolytic bond cleavage demonstrated already for many compounds.[1−19] Especially in the case of diarylmethyl cations (Ar₂CH⁺), photolytic generation from charged Ar₂CH– X⁺ or neutral precursors Ar₂CH–X is frequently applied to study the kinetics of their reactions with nucleophiles.[2,4,8,10,15−18,20,21] While neutral precursors like Ar₂CH– Cl are well-suited to generate Ar₂CH⁺ in polar solvents like acetonitrile,[15,19] already in moderately polar solvents like dichloromethane the cations do not survive the first nanoseconds due to enhanced geminate recombination.[19] On the other hand, the chemical cation yield in moderately polar and nonpolar solvents is considerably higher for charged precursors.[14,16,18]

Here, we solely focus on charged precursors with the leaving group triphenylphosphine (PPh₃; see Scheme 1). Compared to diphenylmethylchloride (Ph₂CH–Cl), where the carbocations Ph₂CH⁺ are dominantely formed by electron transfer after homolysis,[17,19,22] the primary photoproducts are Ph₂CH⁺ and

Scheme 1. Reaction Scheme for the Photochemical Bond Cleavage in Diphenylmethyltriphenylphosphonium Ions Ph₂CH–PPh₃⁺ Where the Primary Photoproducts Are Ph₂CH⁺ and PPh₃

PPh₃, implying a heterolytic bond cleavage.[16] Additionally, the exchange of the Cl leaving group with PPh₃ introduces a second chromophore into the precursor. Both chromophores contain phenyl rings, and their excitations should be nearly degenerate. The question arises whether a preferred pathway exists or both chromophores participate in the bond cleavage process. For organic chemistry, the answer to this question is central because the stability of the carbocation is modified using different substituion patterns on the Ph₂CH moiety whereby the influence on the bond cleavage process is unclear.

To approach these questions, ab initio potential energy surfaces (PES) describing the path from the Franck–Condon (FC) region of the reactants to the products are necessary. Analytic potentials as used in former work on diphenylmethyl derivatives[11−13] are not appropriate. As shown in the prominent analytic potentials derived by Kim and Hynes for the ground state S_N1 reaction,[23] a priori assumptions on the process are needed for their construction. First ab initio PES for Ph₂CH–Cl[22,24] show significant deviations from the analytic potentials in use and the need for a multiconfigurational treatment. Although the PES are typically calculated in the gas phase, they contain important information about the formation of the primary photoproducts in solution. The neglect of the electrostatic influence of the solvent is justifiable as the actual dissociation takes place on a time scale faster than the solvent relaxation[22,24,25] and is supported by the strong potential gradient along the dissociation coordinate. Experimental evidence is given by recent measurements with high temporal
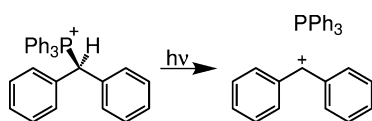
resolution.[22] In the case of a positively charged precursor, both dissociation channels, heterolytic as well as homolytic, yield one neutral and one positively charged fragment. Thus, only minor electrostatic solvent effects on the relative energies of the different channels are expected, and their neglect is even more justified than for the neutral precursors.

We concentrate our quantum chemical investigations on the optical excitation and the subsequent bond cleavage process. We performed coupled cluster calculations in the FC region for benchmarking the active space used to evaluate the PES along the reaction path on the CASSCF/MS-CASPT2 level of theory. In addition, we quantified the electrostatic solvent effect after full relaxation of the solvent environment. Besides the question of which chromophore plays the major role for the excitation, we investigate the mechanism of intramolecular charge transfer (CT) during the bond cleavage process. To be able to perform these calculations, we introduce a model system in section 2 that allows the application of highly correlated quantum chemical methods. After characterizing the key excited states (section 3), we examine the bond cleavage in section 4. Conical intersections (CoIn's) between both product channels are considered. They can be of particular importance because they allow for a fast nonradiative population transfer between electronic states.

2. CHOICE OF THE MODEL SYSTEM

2.1. Phenylmethylphenylphosphonium as a Model System for Diphenylmethyltriphenylphosphonium. The precursor diphenylmethyltriphenylphosphonium ion ($Ph_2CH-PPh_3^+$) is used to generate diphenylmethyl (benzhydryl, Ph_2CH^+) cations in polar as well as nonpolar solvents. It contains five phenyl rings (see Figure 1), two on the
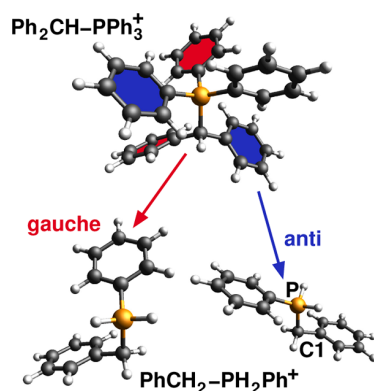
Figure 1. Optimized ground state geometry of the diphenylmethyl-triphenylphosphonium ion $Ph_2CH-PPh_3^+$ (top). Optimized ground state geometries of two different conformers of the phenyl-methylphenylphosphonium ion $PhCH_2-PH_2Ph^+$ (bottom). The gauche conformer is depicted on the left, and the anti conformer is depicted on the right.

benzhydryl moiety (Ph_2CH) and another three on the phosphonium moiety (PPh_3). This constellation allows local $\pi-\pi^*$ excitations either on the Ph_2CH or on the PPh_3 moiety as well as CT-type excitation from one moiety to the other. For the calculation of ground and excited states along the reaction coordinate of bond cleavage, a multiconfiguration method is required. We use the complete active space self-consistent field (CASSCF) method. For the complete precursor, CASSCF requires the consideration of six π-MOs of each phenyl ring and

the σ_{CP}- and σ_{CP}^*-MO of the C1–P bond, leading to an active space of 32 electrons in 32 orbitals. Due to the resulting $\sim 10^{18}$ configurations, these calculations are still out of reach. The C1–P bond is referred to as the C–P bond from hereon.

We designed a model system that preserves the main properties of $Ph_2CH-PPh_3^+$ but can be treated with highly correlated quantum chemical methods in an acceptable time span. Three of the phenyl rings, one on the benzhydryl moiety and two on the phosphonium moiety, are replaced by hydrogen atoms. The resulting phenylmethylphenylphosphonium ion $PhCH_2-PH_2Ph^+$ (see Figure 1) still includes the interplay between local $\pi-\pi^*$ excitations and CT excitation. The model is also supported by experimental studies showing that the replacement of a phenyl ring on the benzhydryl moiety is possible without changing the photochemical behavior.[14]

2.2. Quantum Chemical Methods. The quantum chemical calculations were performed with the program packages Gaussian09,[26] Molpro 2006.1,[27] and Turbomol V5.10.[28] We use DFT (B3LYP/6-31G(d)) to optimize geometries along the ground state minimum energy path (MEP). The description of the optical excitation and the subsequent bond cleavage process necessitates the consideration of several excited states and a multiconfiguration method. All PES were explored on the CASSCF(10,10)/6-31G(d) level of theory. For the one-dimensional PES, we included the dynamical electron correlation via multistate perturbation theory (MS-CASPT2).[29]

We restricted the active space to four π-MOs of each phenyl ring and the σ_{CP}- and σ_{CP}^*-MO of the C–P bond (see the Supporting Information (SI)). The eight π-MOs are essential for the excitation process and the initial charge exchange, whereas the bond cleavage process can only be described including the σ_{CP}- and σ_{CP}^*-MO of the C–P bond. The fully bonding and antibonding π-MOs are not contained in the active space to keep it manageable. Their influence on the relative energies is mostly taken into account by the MS-CASPT2 calculations. We checked the stability of the active space throughout the dissociation process. Figure S2 in the SI shows the active space along the dissociation coordinate at selected points. We verify the active space in the FC region by the approximate singles and doubles coupled cluster approach CC2.[30] It clearly shows that all major contributing configurations to the four lowest-lying singlet excited states are considered within the chosen active space. For the CC2 calculations, we used the def-SV(P) basis set,[31] the resolution-of-the-identity approach,[32] and a frozen core containing all 18 nonvalence orbitals of $PhCH_2-PH_2Ph^+$.

We also compared the CASSCF and MS-CASPT2 vertical excitation energies with CC2 results and evaluated the influence on the vertical excitation energies due to stepwise enlargement of the model system. For the description of an excited state bond cleavage process, the single reference method CC2 is not well-suited.[33]

3. MECHANISM OF OPTICAL EXCITATION

The first step in the photochemical generation of benzhydryl cations is the excitation of the precursor with a light pulse. Two classes of precursors are commonly used, uncharged precursors like Ph_2CH-Cl and charged precursors like $Ph_2CH-PPh_3^+$. In contrast to Ph_2CH-Cl where only one chromophore, the Ph_2CH moiety, exists, in $Ph_2CH-PPh_3^+$, the leaving group PPh_3 also acts as a chromophore. To classify the different optical excitation processes, we first identify the ground state

conformers of the model system PhCH$_2$–PH$_2$Ph$^+$ and then analyze the character of the excited singlet states in the FC region.

3.1. Ground State Geometries. The conformational search is performed on the DFT/B3LYP level of theory using a 6-31G(d) basis set. The ground state of PhCH$_2$–PH$_2$Ph$^+$ shows two different conformational isomers. The gauche conformer is a local minimum geometry, while the global minimum is the anti conformer (see Figure 1). The energy difference between the gauche and anti conformer is $\Delta G^0 = 6.9$ kJ/mol (0.071 eV), which can be ascribed to steric hindrance of the phenyl groups. The C–P bond length of both conformers is 1.84 Å. Because in the full system Ph$_2$CH–PPh$_3^+$ the phosphonium moiety contains three phenyl groups, both kinds of relative orientation of the phenyl rings are present. In the following discussions, we focus on the anti conformer. Therefore, we checked that the conformational influence of the gauche conformer on the barrier height in the first excited state S$_1$ along the ground state MEP is minor with an enlargement of $\Delta(\Delta E_{barrier}) = 0.014$ eV (see Table 1).

Table 1. Vertical Excitation Energies and Oscillator Strengths of PhCH$_2$–PH$_2$Ph$^+$ (anti Conformer) Calculated at the CASSCF(10,10), MS-CASPT2, and CC2 Levels of Theory at the Ground State Minimum Geometry[a]

	S$_1$	S$_2$	S$_3$
$\Delta E_{S_n \leftarrow S_0}^{CAS}$ [eV]	5.96	6.19	7.49
$f_{S_n \leftarrow S_0}^{CAS}$ [au]	0.030	0.0074	0.89
$\Delta E_{S_n \leftarrow S_0}^{MS\text{-}CASPT2}$ [eV]	5.24	5.34	6.36
$\Delta E_{S_n \leftarrow S_0}^{CC2}$ [eV]	5.11	5.17	5.68
$f_{S_n \leftarrow S_0}^{CC2}$ [au]	0.016	0.0034	0.59
$\Delta E_{barrier,min}^{MS\text{-}CASPT2}$ [eV]	0.155	0.168	
$\Delta E_{net\text{-}barrier}^{MS\text{-}CASPT2}$ [eV]	0.017	0.026	

[a]In addition, barrier heights along the bond cleavage coordinate are given at the MS-CASPT2 level of theory. As the minimum geometry, the DFT-optimized structure is used in all cases except for the $\Delta E_{barrier,min}^{MS\text{-}CASPT2}$ values. We listed the barrier heights with respect to the MEP in the corresponding excited state S$_n$ ($\Delta E_{barrier,min}^{MS\text{-}CASPT2}$). The net barriers relative to the FC point are also given ($\Delta E_{net\text{-}barrier}^{MS\text{-}CASPT2}$).

3.2. Key Excited Singlet States in the FC Region. On the basis of the optimized geometry of the anti conformer of PhCH$_2$–PH$_2$Ph$^+$, we calculated the three lowest excited singlet states using the CASSCF(10,10), MS-CASPT2, and CC2 levels of theory. The different excitation energies and oscillator strengths are given in Table 1. The two lowest excited states S$_1$ and S$_2$ are close in energy, with a gap of only 0.2–0.1 eV depending on the level of theory. The oscillator strength of the S$_1$ state is higher by a factor of 4–5 compared to the S$_2$ state. The third excited state S$_3$ is well-separated and lies about 1 eV above the S$_2$ state. Its oscillator strength is increased by a factor of 30–40 compared to the S$_1$ state.

Further information about the character of the excitations can be extracted from the electronic wave function. Figure 2 schematically shows the most important orbitals involved in the excitations leading to S$_1$ (blue), S$_2$ (magenta), and S$_3$ (cyan). The S$_1$ state corresponds to a local $3\pi_{PPh}$–$1\pi_{PPh}^*$ excitation of the phenyl ring on the PH$_2$Ph$^+$ leaving group. The second excited state S$_2$ corresponds to a local $4\pi_{CPh}$–$2\pi_{CPh}^*$ excitation on the phenyl ring of the methyl group (PhCH$_2$). The HOMO–LUMO ($6\pi_{CPh}$–$1\pi_{PPh}^*$) transition leads to the third
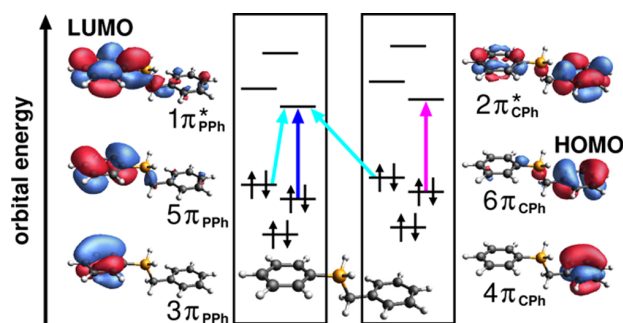
Figure 2. Schematic excitation scheme of PhCH$_2$–PH$_2$Ph$^+$. The most important contributions to the excitations in S$_1$ (blue), S$_2$ (magenta), and S$_3$ (cyan) are depicted together with the corresponding orbitals. The indices of the orbital designations specify if the phenyl ring is part of the methyl moiety (π_{CPh}) or the phosphine leaving group (π_{PPh}).

excited state S$_3$ and gives rise to its CT character. Nearly equivalent contributions to the electronic wave function come from the local $5\pi_{PPh}$–$1\pi_{PPh}^*$ transition on the PH$_2$Ph$^+$ group. At first glance, it is suprising that the HOMO–LUMO transition leads to a large energetic separation from S$_3$ to the S$_1$ and S$_2$ states (see Table 1). The reason can be explained straightforwardly by the enhanced electron–electron interaction accompanying the CT, whereby additional electron density is accumulated on the leaving group.

Figure 3 shows the relaxation of the first and second excited states on the CASSCF(10,10) level of theory. Along the relaxation coordinate of the S$_1$ state, which is localized on the PH$_2$Ph$^+$ moiety, the S$_1$ state is stabilized by 0.41 eV, and the energy gap between S$_1$ and S$_2$ increases. The second excited state S$_2$ is stabilized by 0.34 eV until it reaches its minimum
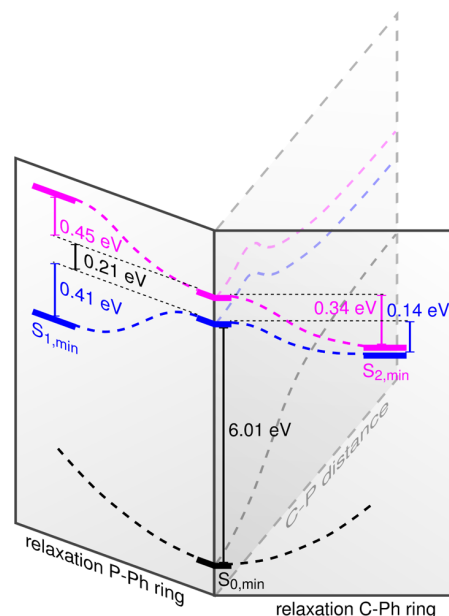
Figure 3. Relaxation of the first (blue) and second excited states (magenta) of PhCH$_2$–PH$_2$Ph$^+$ in the FC region. All minimum structures were optimized at the CASSCF(10,10) level of theory. The relaxation of the first excited state S$_1$ leads to an increase of the energy gap between S$_1$ and S$_2$, whereas at the S$_2$ minimum geometry, the S$_2$ becomes nearly degenerate with the S$_1$.

structure from the FC region. Here, contrary to the relaxation of the S_1 state, the energy gap between S_1 and S_2 decreases, and both states become nearly degenerate ($\Delta E^{CAS} = 0.004$ eV). We located a CoIn between S_1 and S_2 close to the minimum of the S_2 state (RMSD = 0.067 Å; see Table S3 in the SI). This strongly supports that the S_2 state population efficiently relaxes into the S_1 state and the actual dissociation process occurs via S_1. Additionally, the S_1 possesses a significantly larger oscillator strength (see Table 1).

When increasing the number of phenyl rings to approach the size of the full system $Ph_2CH-PPh_3^+$, the number of local $\pi-\pi^*$ transitions as well as CT excitations increases. We evaluate the influence of this enlargement on the ordering of the vertical excitation energies by CC2 calculations. Again, the ground state minimum geometries of $PhCH_2-PHPh_2^+$, $PhCH_2-PPh_3^+$, and $Ph_2CH-PPh_3^+$ were optimized using DFT/B3LYP. The calculated excitation spectra are summarized in Figure 4 and
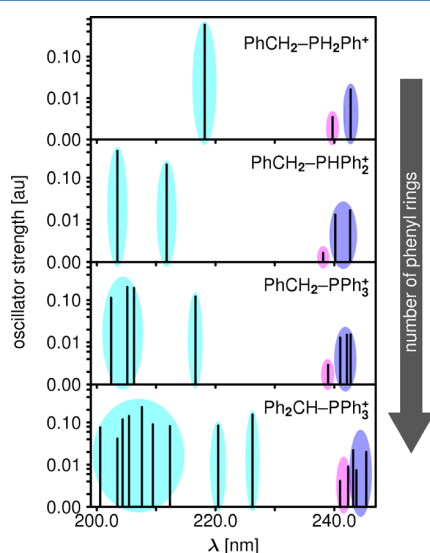
Figure 4. Calculated electronic transitions (CC2/def-SV(P)) for different phenylmethylphosphonium ions in the gas phase. The model system $PhCH_2-PH_2Ph^+$ is depicted on top. The number of phenyl rings increases top down. The transitions are highlighted depending on their character: local excitations on a phenyl ring of the phosphonium group (blue), local excitations on a phenyl ring of the methyl moiety (magenta), and CT excitations (cyan).

in Table S1 in the SI. The number of phenyl rings increases top down. The transitions are highlighted depending on their character: local excitations on a phenyl ring of the phosphonium group (blue), local excitations on a phenyl ring of the methyl moiety (magenta), and CT excitations (cyan).

The number of energetically low-lying local $\pi-\pi^*$ excitations (magenta and blue) corresponds to the number of phenyl rings present in the phosphonium ion. The observed ordering of the local excitations in the model system $PhCH_2-PH_2Ph^+$ remains unchanged, increasing the system size. All $\pi-\pi^*$ transitions on the phenyl rings of the phosphonium moiety are energetically slightly lower than the $\pi-\pi^*$ transitions on the phenyl rings of the methyl group. The slightly irregular pattern observed for the transition spectrum of the phosphonium moiety with increasing number of phenyl rings reflects the excitation from superposition states. Those are formed among the π orbitals with different weighting factors. The CT excitations (high-

lighted in cyan) stay well-separated from the local $\pi-\pi^*$ excitations by 0.33 eV for the full system (lowest panel in Figure 4) and 0.64 eV for $PhCH_2-PHPh_2^+$ (second panel in Figure 4). As expected, their number also increases top down. Again, the pattern can be ascribed to superposition states between the phenyl rings in the leaving group. Their formation is favored by the highly delocalized antibonding π^* orbitals. The individual lowest local excitation energies lower by the same amount ($\Delta(\Delta E^{CC2}_{S_1 \leftarrow S_0}) = 0.05$ eV) with increasing system size, nearly preserving the relative energy splitting between them ($Ph_2CH-PPh_3^+$, 0.063 eV/3.0 nm, compared to $PhCH_2-PH_2Ph^+$, 0.064 eV/3.0 nm). Thus, the calculated spectra show that the reduced model system is well-suited to describe the major optical properties of the full system in the FC region.

In the experimental ground state absorption spectrum of $Ph_2CH-PPh_3^+BF_4^-$ in acetonitrile, the first peak occurs at 277 nm and can be assigned to the local excitations. The individual transitions are significantly broadened and overlap quite strongly.[34] Thus, under experimental conditions, it is most likely not possible to address a single chromophore, but a mixture of both chromophores is excited. This special situation is the consequence of a leaving group containing phenyl rings. In the following section, we discuss the bond cleavage process after the optical excitation and address the question of which excitation provides the energetically preferred reaction path.

## 4. POTENTIAL ENERGY CURVES FOR GROUND AND EXCITED SINGLET STATES

4.1. One-Dimensional Potential Energy Cuts along the Ground State MEP for Bond Cleavage. On the basis of the ground state MEP along the C−P bond cleavage of $PhCH_2-PH_2Ph^+$, we calculated the potential energy curves of the ground state and the three lowest electronically excited singlet states using MS-CASPT2. All four singlet states show a distinct minimum, whereby the S_3 equilibrium is shifted toward a slightly longer bond length (see Figure 5 and Table S2 in the SI). Important for the photoinduced bond cleavage is the CT character of the S_3 state. Stabilization of the energetically unfavorable charge localization on the phosphonium moiety in the S_3 state is achieved during C−P bond elongation by charge
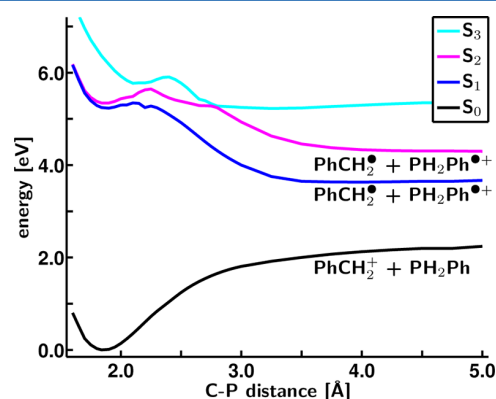
Figure 5. Potential energy curves for $PhCH_2-PH_2Ph^+$ along the ground state MEP for the C−P bond cleavage at the multistate single reference CASPT2 level of theory. In the dissociation limit, the ground state S_0 (black) leads to a heterolytic bond cleavage ($PhCH_2^+ + PH_2Ph$). The two lowest excited states S_1 (blue) and S_2 (magenta) lead to homolytic bond cleavage ($PhCH_2^{\bullet} + PH_2Ph^{\bullet+}$).

back transfer via the σ^*_{Cp} orbital and leads to the subsequent configuration exchange with S_2 and S_1, which show up as avoided crossings along the C−P coordinate. This exchange occurs shortly after the state minima in the FC region and introduces small barriers of 0.303 eV in the S_2 state at 2.25 Å and of 0.113 eV in the S_1 state at 2.10 Å. When the barrier heights are optimized in the corresponding excited state, they change to 0.168 eV in the S_2 state at 2.05 Å and 0.155 eV in the S_1 state at 2.05 Å. As the photoreaction starts at the FC point geometry and not in the S_1 or S_2 minimum, access energy is provided in the photochemical process. Taking this into account reduces the net barrier in the S_2 state to 0.026 eV and in the S_1 state to 0.017 eV. All values are summarizes in Table S5 in the SI. Together with the differences in the oscillator strength and the S_2/S_1 CoIn, these findings suggest that the excitation on the PH_2Ph moiety (S_1 state) opens the energetically preferred reaction path.

Further C−P bond elongation leads to significant stabilization of both the S_2 and the S_1 states accompanied by additional configuration changes until the final electronic character for the S_0, S_1, and S_2 states is reached in the dissociation limit. These can be followed in detail on the molecular orbital level. In Figure 6, we indicate the change in the electronic wave
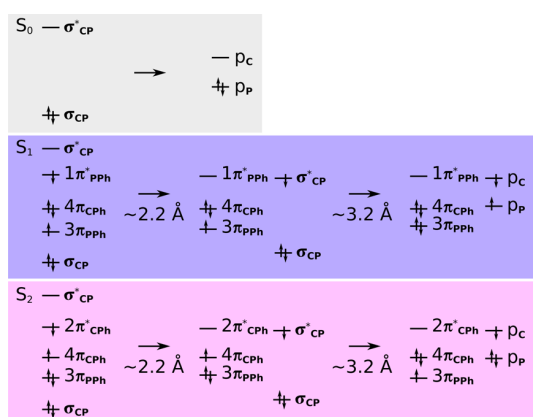
Figure 6. Schematic representation of the orbital occupation during the bond cleavage process in $PhCH_2–PH_2Ph^+$. In the ground state S_0, the formation of the p orbitals on the phosphorus and the carbon atoms from the σ_{CP} and σ^*_{CP} orbital is decisive. In the first (S_1) and second excited states (S_2), configuration exchanges from a π^* to the σ^*_{CP} orbital and thereafter in the occupied orbitals take place.

functions following the population of the most important orbitals in the active space. In the dissociation limit, the σ_{CP} orbital correlates with the p orbital p_P of the P atom, and the σ^*_{CP} orbital correlates with the p orbital p_C of the C atom. Thus, the final population of these orbitals distinguishes between heterolytic and homolytic bond cleavage.

In the ground state S_0, the bonding σ_{CP} orbital stays doubly occupied. It undergoes an adiabatic transformation from the molecular orbital to the atomic orbital and opens the heterolytic channel, leading to the carbocation $PhCH_2^+$. The orientation of the p_P orbital allows delocalization of the electron density over the whole leaving group by a linear combination with the $3\pi_{PPh}$ orbital. The same is true for the p_C orbital where the charge is correspondingly delocalized over the $PhCH_2$ moiety. The p_P orbital, the essential part of the HOMO, is inherently significantly lower in energy than the p_C orbital, the essential part of the LUMO, and thus compensates for the

electron−electron repulsion (ΔE^{HF}(LUMO−HOMO) = 5.5 eV).

In the excited singlet states, the situation is more complex. Due to the interaction with the S_3 state, the character of the first excited state S_1 changes from $3\pi_{PPh}1\pi^*_{PPh}$ to $3\pi_{PPh}\sigma^*_{CP}$ at a C−P distance of about 2.10−2.20 Å. This leads to the observed stabilization of the S_1 state and has been previously reported for comparable systems.[24,35] At a C−P bond length of 3.00−3.30 Å, a second CT happens, and one electron is transferred from the doubly occupied σ_{CP} orbital to the singly occupied $3\pi_{PPh}$ orbital. In the dissociation limit, σ_{CP} and σ^*_{CP} are now both occupied with one electron, and the S_1 state describes the homolytic bond cleavage leading to the formation of $PhCH_2^{\bullet}$. The formed radical pair consisting of a $PhCH_2^{\bullet}$ and a phosphonium radical cation is less stable than the photoproducts after heterolytic bond cleavage by 1.43 eV (MS-CASPT2 at a C−P distance of 5.00 Å; see Figure 5).

In the second excited state S_2, the process starts with a $\pi–\pi^*$ excitation on the $PhCH_2$ moiety. Again, the interaction with the S_3 state induces the first configuration exchange. It occurs from $4\pi_{CPh}2\pi^*_{CPh}$ to $4\pi_{CPh}\sigma^*_{CP}$ and at a C−P distance of about 2.10−2.30 Å, this time shifting the single electron from the $PhCH_2$ moiety to the σ^*_{CP} orbital. Like in the S_1 state, a second charge exchange happens, in this case between the two phenyl rings, and restores the charge balance. The electron hole in the $4\pi_{CPh}$ orbital of the CH_2Ph moiety is filled by an electron from the $5\pi_{PPh}$ orbital of the PH_2Ph moiety. In total, the bond cleavage is again homolytic.

Important differences to neutral precursors like $Ph_2CH–Cl$ exist. Both homolytic and heterolytic bond cleavage yield one positively charged and one uncharged fragment; the carbocation is the lowest product channel in the gas phase, and electrostatic solvent stabilization effects should be negligible. In order to confirm the latter proposition, implicit solvation by acetonitrile (polarizable continuum model, IEFPCM[36]) was included at the B3LYP/6-31G(d) level of theory. The energy gap between the heterolytic and the first homolytic channel shifts from 1.12 eV in the gas phase to 1.13 eV in acetonitrile. This confirms the minor importance of electrostatic solvent effects for charged precursors.
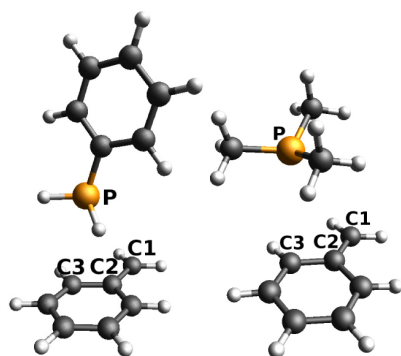
On the basis of the results presented so far, the following reaction process can be deduced. The optical excitations of the precursor molecule are local $\pi–\pi^*$ excitations mostly on the PH_2Ph moiety due to its higher oscillator strength. The small population transferred into the S_2 relaxes into the S_1 via a S_2/S_1 CoIn in the vincinity of the S_2 minimum. Thus, we expect that the excitation on the PH_2Ph moiety (S_1 state) opens the reaction path. After crossing the barrier, the system develops along the C−P distance coordinate. Because the barrier is roughly five times higher than that in the case of $Ph_2CH–Cl$,[24] the bond cleavage is expected to take substantially longer. This is in good agreement with the experimentally observed slower appearance on the low picosecond time scale of the photoproduct absorption signal for phosphonium leaving groups in solution.[16,34] Also in agreement with the experiment, we find the pair $PhCH_2^+$ + PH_2Ph to be the thermodynamically most stable products.

Along the one-dimensional potential energy cuts calculated for the ground state MEP, no hint for an avoided crossing between S_0 and S_1 is found. Consequently, only homolytic bond cleavage is possible, leading to a $PhCH_2^{\bullet}$ radical and a $PH_2Ph^{\bullet+}$ radical cation as direct photoproducts. Subsequent electron transfer from the $PhCH_2^{\bullet}$ radical to the $PH_2Ph^{\bullet+}$

radical cation could lead to the thermodynamically stable products $PhCH_2^+ + PH_2Ph$. However, in the transient broadband absorption spectrum of the complete system in solution, only the Ph_2CH^+ signature occurs and is stable on the nanosecond to microsecond time scale. No intermediate radical population has so far been observed. These experimental findings can only be explained by a crossing between S_0 and S_1, where the system can be transferred nonradiatively to the ground state. In principle, CoIn's allow such a fast population transfer between electronic states of benzhydryl compounds.[24] To locate them, additional coordinates are necessary.

4.2. Coupling between the Low-Lying Photoproduct Channels. The fast connection between the two lowest bond cleavage channels, producing either carbocations (S_0) or radicals (S_1), can only be provided by CoIn's. Possible interaction with triplet states would only open the homolytic channels. Indeed, we located an S_1/S_0 CoIn significantly below the FC point. For our model system $PhCH_2-PH_2Ph^+$, the structure of the S_1/S_0 CoIn of lowest energy is shown in Figure 7 (left). Here, the energy splitting between the ground state S_0

Table 2. Selected Geometry Parameters and Energies for the S_1/S_0 CoIn Structures of $PhCH_2-PH_2Ph^+$ and $PhCH_2-PMe_3^+$ and the Global S_1 Minimum of $PhCH_2-PH_2Ph^+$ Optimized at the CASSCF Level of Theory

	$PhCH_2-PH_2Ph^+$ S_1/S_0 CoIn$_{min}$	$PhCH_2-PMe_3^+$ S_1/S_0 CoIn$_{min}$	$PhCH_2-PH_2Ph^+$ S_1 minimum
d_{C1-P} [Å]	3.94	3.91	3.92
d_{C2-P} [Å]	3.54	3.85	3.52
d_{C3-P} [Å]	3.52	3.63	3.52
d_{C1-C2} [Å]	1.42	1.41	1.42
d_{C2-C3} [Å]	1.43	1.43	1.43
$\phi_{C1-C2-C3}$ [°]	121.0	121.4	121.1
$\varphi_{P-C1-C2}$ [°]	63.3	77.2	63.6
ϕ_{Ph-Ph} [°]	77.0		74.9
$E_{S_0}^{CAS}$ [H]	−840.918480	−728.490053	−840.918535
$E_{S_1}^{CAS}$ [H]	−840.918477	−728.490045	−840.918498
ΔE^{CAS} [cm^{-1}]	0.7	1.8	8.2

Figure 7. Optimized S_1/S_0 CoIn geometries of $PhCH_2-PH_2Ph^+$ (left) and $PhCH_2-PMe_3^+$ (right). The carbon atoms C1, C2, and C3 build the essential allylic C_3 subunit. Selected geometry parameters and energies for the CoIn structures are given in Table 2.
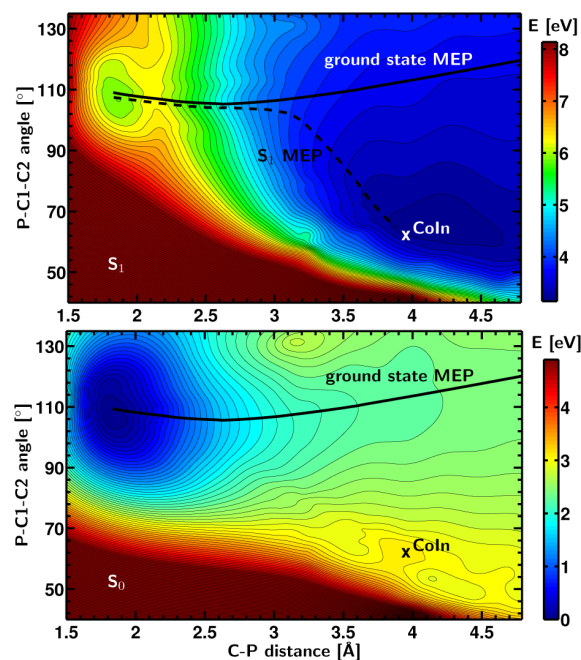
and S_1 is 0.7 cm^{-1} on the CASSCF level of theory. The position of the P atom is almost central above a C_3 subunit containing the methyl carbon atom (C1) as well as two carbon atoms from the phenyl group (C2 and C3). This structure is a generic motif often resulting in an energetic degeneracy between different electronic states.[24,37−40] The distances between the P atom and the C atoms of the C_3 subunit are in the range of 3.94−3.52 Å (see Table 2). The phenylphosphine is oriented nearly perpendicular to the benzyl moiety. The angle between both phenyl rings is $\phi_{Ph-Ph} = 77.0°$.

In the full system, the leaving group contains three phenyl groups, which makes such a perpendicular arrangement of one phenyl group impossible. In order to verify whether an S_1/S_0 CoIn is also observed with a symmetrically substituted leaving group, we optimized an S_1/S_0 CoIn with trimethylphosphine as the leaving group. The right side of Figure 7 shows the resulting geometry, which is very similar. The C−P distances lie between 3.91 and 3.63 Å (see Table 2). The energy difference of S_0 and S_1 is 1.8 cm^{-1} on the CASSCF level of theory.

From the geometry of the S_1/S_0 CoIn, the second coordinate necessary to reach the CoIn from the FC region can be derived directly. The second coordinate is the P−C1−C2 angle $\varphi_{P-C1-C2}$. Figure 8 displays the PES of the ground (bottom) and first excited states (top) along these two coordinates,

Figure 8. Two-dimensional PES of the ground state S_0 (bottom) and the first excited state S_1 (top) of $PhCH_2-PH_2Ph^+$. The solid black line indicates the direction of the ground state MEP shown in Figure 5, and the dashed black line shows the MEP of the first excited state S_1. In order to reach the marked CoIn, a motion along the P−C1−C2 angle $\varphi_{P-C1-C2}$ is necessary. The structures along the different MEPs as well as the CoIn geometry are fully relaxed. The geometries lying in between are linearly interpolated.

$\varphi_{P-C1-C2}$ and d_{C1-P}. The local minimum in the FC region is located at $\varphi_{P-C1-C2} = 110°$ and $d_{C1-P} = 1.86$ Å. The barrier in the S_1 state can be easily recognized. Initially, the energetically most favorable pathway follows the C−P distance. After the crossing of the barrier, a noticeable gradient exists along the second coordinate and points toward the minimum CoIn located at $\varphi_{P-C1-C2} = 63.3°$ and $d_{C1-P} = 3.94$ Å, which is very close to the global minimum of the S_1 state at $d_{C1-P} = 3.92$ Å

(see Table 2). This CoIn is energetically reachable; however, dynamical calculations have to clarify its efficiency.

5. CONCLUSIONS

Highly correlated quantum chemical studies for the photochemical bond cleavage in diphenylmethylphosphonium ions are presented. A model system ($PhCH_2-PH_2Ph^+$) preserving the main properties of the full system is introduced to enable the necessary multiconfigurational treatment for the PES along the reaction coordinates. We provide the PES on the CASSCF and the MS-CASPT2 level of theory. The two lowest excited singlet states in the model system correspond to local $\pi-\pi^*$ transitions. Compared with other well-studied benzhydryl derivatives,[3,8,10-13,19,22,24] the phosphonium leaving group offers a second chromophore and enhances the complexity of the excitation mechanism.

Our calculations show that the excitation on the PH_2Ph^+ moiety leads to the S_1 state, and the excitation on the $PhCH_2$ moiety leads to the S_2 state. The third excited state S_3 has CT character (see Figure 2) and corresponds to an excitation from the $PhCH_2$ moiety to the leaving group. The local excitations (S_1, S_2 states) are close in energy, while the CT state is well-separated. This situation does not change when the model system is extended to the full system. Only the excitation pattern within the separated transition manifolds becomes more complex. This can be explained by the increasing number of excitation pathways whose spectral positions reflect the possibility of different combinations of superposition states between the phenyl rings of the leaving group.

In the experiment, the local transitions are broadened due to environmental effects, both chromophores are excited, and possible dissociation pathways cannot be resolved. From the calculations, we can deduce the pathway from the FC region. Due to the five times larger oscillator strength of the S_1 state compared to the one of the S_2 state, the dissociation process starts mainly in the S_1 state. The system has to cross a small barrier along the dissociation coordinate. Any population transferred into the S_2 can relax via a CoIn to the S_1 dissociation path. We thus conclude that the excitation on the PH_2Ph moiety opens the preferred reaction path. The dissociation is mainly driven by the CT state, which enables the electron transfer from the π^* to the σ^* orbital. Our results show that there is a clear separation between the dissociation occurring via the leaving group and chemical modifications on the Ph_2CH moiety. Thus, dissociation and the stability of the carbocations can be controlled independently.

Along the bond cleavage coordinate, the ground state undergoes heterolysis, forming the carbocation as a thermodynamically stable product in the gas phase as well as in solution. This is in contrast to neutral benzhydryl derivatives[24] and in good agreement with the recent measurements.[16,34] The two lowest excited states undergo homolysis, leading to the benzhydryl radical. Thus, photochemical dissociation along the C−P distance can only produce benzhydryl radicals, which is in clear disagreement with the experiment that shows dominantly Ph_2CH^+ after the photoexcitation of $Ph_2CH-PPh_3^+$.[16,34] The connection between the FC region and the carbocation channel can be opened by a CoIn along a second coordinate. We located such a CoIn between the ground state and the first excited state, accessible following a bending motion of the phosphorus atom toward the phenyl ring of the $PhCH_2$ moiety. As this CoIn is located close to the S_1 minimum, a noticeable gradient points into its direction after

the barrier crossing in the FC region. The efficiency of this CoIn can only be clarified by dynamical calculations, which are in progress.

■ ASSOCIATED CONTENT

Ⓢ Supporting Information

Supplementary figures and tables, including the active space for CASSCF(10,10) calculations, the development of the active space for CASSCF(10,10) calculations, calculated electronic transitions (CC2/def-SV(P)) for different phosphonium ions in the gas phase, total energies calculated at the CASSCF-(10,10) level of theory, the C−P distance of the minimum geometries, development of orbital energies along the ground state MEP for the C−P bond cleavage, barrier heights calculated at the MS-CASPT2 level of theory, optimized geometries in *xyz*-format, and complete refs 26 and 27. This material is available free of charge via the Internet at http://pubs.acs.org.

■ AUTHOR INFORMATION

Corresponding Author
*E-mail: regina.de_vivie@cup.uni-muenchen.de. Phone: +49/(0)89/2180 77533.

Present Address
¶B.P.F.: Department of Chemistry, University of California, Irvine, California 92697-2025, United States.

Notes
The authors declare no competing financial interest.

■ REFERENCES

(1) Foster, B.; Gaillard, B.; Mathur, N.; Pincock, A. L.; Pincock, J. A.; Sehmbey, C. Substituent Effects on Homolytic versus Heterolytic Photocleavage of (1-Naphthylmethyl)trimethylammonium Chlorides. *Can. J. Chem.* **1987**, 65, 1599−1607.

(2) McClelland, R. A.; Kanagasabapathy, V. M.; Banait, N. S.; Steenken, S. Flash-Photolysis Generation and Reactivities of Triarylmethyl and Diarylmethyl Cations in Aqueous Solutions. *J. Am. Chem. Soc.* **1989**, 111, 3966−3972.

(3) Alonso, E. O.; Johnston, L. J.; Scaiano, J. C.; Toscano, V. G. Laser Flash Photolysis Studies of Carbocations Generated from (Naphthylmethyl)phosphonium Chlorides. *J. Am. Chem. Soc.* **1990**, 112, 1270−1271.

(4) Bartl, J.; Steenken, S.; Mayr, H.; McClelland, R. A. Photo-Heterolysis and -Homolysis of Substituted Diphenylmethyl Halides, Acetates, and Phenyl Ethers in Acetonitrile: Characterization of Diphenylmethyl Cations and Radicals Generated by 248-nm Laser Flash Photolysis. *J. Am. Chem. Soc.* **1990**, 112, 6918−6928.

(5) Alonso, E. O.; Johnston, L. J.; Scaiano, J. C.; Toscano, V. G. Laser Flash Photolysis Studies of the Formation and Reactivities of Phenyl(naphthyl)methyl Carbocations Generated from Phosphonium Salt Precursors. *Can. J. Chem.* **1992**, 70, 1784−1794.

(6) Imrie, C.; Modro, T. A.; Rohwer, E. R.; Wagener, C. C. P. Photolysis of (Arylmethyl)triphenylphosphonium Salts. Substituent, Counterion, and Solvent Effects on Reaction Products. *J. Org. Chem.* **1993**, 58, 5643−5649.

(7) Das, P. K. Transient Carbocations and Carbanions Generated by Laser Flash Photolysis and Pulse Radiolysis. *Chem. Rev.* **1993**, 93, 119−144.

(8) Hilborn, J. W.; MacKnight, E.; Pincock, J. A.; Wedge, P. J. Photochemistry of Substituted Benzyl Acetates and Benzyl Pivalates: A Reinvestigation of Substituent Effects. *J. Am. Chem. Soc.* **1994**, *116*, 3337−3346.

(9) Verbeek, J.-M.; Stapper, M.; Krijnen, E. S.; van Loon, J.-D.; Lodder, G.; Steenken, S. Photochemical Formation and Electrophilic Reactivities of Vinyl Cations. Influence of Substituents, Anionic Leaving Groups, Solvents, and Excitation Wavelength on Photoheterolysis and Photohomolysis of 1-(*p*-R-Phenyl)-2-(2,2′-biphenyldiyl)vinyl Halides. *J. Phys. Chem.* **1994**, *98*, 9526−9536.

(10) McClelland, R. A. Flash Photolysis Generation and Reactivities of Carbenium Ions and Nitrenium Ions. *Tetrahedron* **1996**, *52*, 6823−6858.

(11) Lipson, M.; Deniz, A. A.; Peters, K. S. Nature of the Potential Energy Surfaces for the S_N1 Reaction: A Picosecond Kinetic Study of Homolysis and Heterolysis for Diphenylmethyl Chlorides. *J. Am. Chem. Soc.* **1996**, *118*, 2992−2997.

(12) Peters, K. S. Nature of Dynamic Processes Associated with the S_N1 Reaction Mechanism. *Chem. Rev.* **2007**, *107*, 859−873.

(13) Peters, K. S. Dynamic Processes Leading to Covalent Bond Formation for S_N1 Reactions. *Acc. Chem. Res.* **2007**, *40*, 1−7.

(14) Ammer, J.; Mayr, H. Electrophilic Reactivity of the α,α-Dimethylbenzyl (Cumyl) Cation. *Macromolecules* **2010**, *43*, 1719−1723.

(15) Sailer, C. F.; Fingerhut, B. P.; Ammer, J.; Nolte, C.; Pugliesi, I.; Mayr, H.; de Vivie-Riedle, R.; Riedle, E. The First Picoseconds in the Life of Benzhydryl Cations: Ultrafast Generation and Chemical Reactions. *Ultrafast Phenomena XVII*; Chergui, M.; Jonas, D.; Riedle, E.; Schoenlein, R. W.; Taylor, A., Eds.; Oxford University Press: New York, 2011; pp 427−429.

(16) Ammer, J.; Sailer, C. F.; Riedle, E.; Mayr, H. Photolytic Generation of Benzhydryl Cations and Radicals from Quaternary Phosphonium Salts: How Highly Reactive Carbocations Survive Their First Nanoseconds. *J. Am. Chem. Soc.* **2012**, *134*, 11481−11494.

(17) Fingerhut, B. P.; Sailer, C. F.; Ammer, J.; Riedle, E.; de Vivie-Riedle, R. Buildup and Decay of the Optical Absorption in the Ultrafast Photo-Generation and Reaction of Benzhydryl Cations in Solution. *J. Phys. Chem. A* **2012**, *116*, 11064−11074.

(18) Ammer, J.; Nolte, C.; Mayr, H. Free Energy Relationships for Reactions of Substituted Benzhydrylium Ions: From Enthalpy over Entropy to Diffusion Control. *J. Am. Chem. Soc.* **2012**, *134*, 13902−13911.

(19) Sailer, C. F.; Thallmair, S.; Fingerhut, B. P.; Nolte, C.; Ammer, J.; Mayr, H.; de Vivie-Riedle, R.; Pugliesi, I.; Riedle, E. A Comprehensive Microscopic Picture of the Benzhydryl Radical and Cation Photo-Generation and Interconversion trough Electron Transfer. *Chem. Phys. Chem.* **2013**, *14*, 1423−1437.

(20) Mayr, H.; Bug, T.; Gotta, M. F.; Hering, N.; Irrgang, B.; Janker, B.; Kempf, B.; Loos, R.; Ofial, A. R.; Remennikov, G. Reference Scales for the Characterization of Cationic Electrophiles and Neutral Nucleophiles. *J. Am. Chem. Soc.* **2001**, *123*, 9500−9512.

(21) Mayr, H.; Ofial, A. R. Do General Nucleophilicity Scales Exist? *J. Phys. Org. Chem.* **2008**, *21*, 584−595.

(22) Sailer, C. F.; Krebs, N.; Fingerhut, B. P.; de Vivie-Riedle, R.; Riedle, E. Wavepacket Splitting in the First 100 fs Determines the Products from the Bond Cleavage of Diphenylmethylchloride. *EPJ Web Conf.* **2013**, *41*, 05042/1−05042/3.

(23) Kim, H. J.; Hynes, J. T. A Theoretical Model for S_N1 Ionic Dissociation in Solution. 1. Activation Free Energetics and Transition-State Structure. *J. Am. Chem. Soc.* **1992**, *114*, 10508−10528.

(24) Fingerhut, B. P.; Geppert, D.; de Vivie-Riedle, R. Ultrafast Dissociation Pathways of Diphenylmethyl Chloride to Generate Reactive Carbo Cations. *Chem. Phys.* **2008**, *343*, 329−339.

(25) Horng, M. L.; Gardecki, J. A.; Papazyan, A.; Maroncelli, M. Subpicosecond Measurements of Polar Solvation Dynamics: Coumarin 153 Revisited. *J. Phys. Chem.* **1995**, *99*, 17311−17337.

(26) Frisch, M. J.; Trucks, G. W.; Schlegel, H. B.; Scuseria, G. E.; Robb, M. A.; Cheeseman, J. R.; Scalmani, G.; Barone, V.; Mennucci,

B.; Petersson, G. A.; et al. *Gaussian 09*, revision A.02; Gaussian, Inc.: Wallingford, CT, 2009.

(27) Werner, H.-J.; Knowles, P. J.; Lindh, R.; Manby, F. R.; Schütz, M.; Celani, P.; Korona, T.; Rauhut, G.; Amos, R. D.; Bernhardsson, A.; et al. *MOLPRO*, version 2006.1, a Package of Ab Initio Programs; 2006.

(28) Ahlrichs, R.; Bär, M.; Häser, M.; Horn, H.; Kölmel, C. Electronic Structure Calculations on Workstation Computers: The Program System Turbomole. *Chem. Phys. Lett.* **1989**, *162*, 165−169.

(29) Werner, H.-J. Third-Order Multireference Perturbation Theory: The CASPT3Method. *Mol. Phys.* **1996**, *89*, 645−661.

(30) Christiansen, O.; Koch, H.; Jørgensen, P. The Second-Order Approximate Coupled-Cluster Singels and Doubles Model CC2. *Chem. Phys. Lett.* **1995**, *243*, 409−418.

(31) Schäfer, A.; Horn, H.; Ahlrichs, R. Fully Optimized Contracted Gaussian Basis Sets for Atoms Li to Kr. *J. Chem. Phys.* **1992**, *97*, 2571−2577.

(32) Hättig, C.; Weigend, F. CC2 Excitation Energy Calculations on Large Molecules Using the Resolution of the Identity Approximation. *J. Chem. Phys.* **2000**, *113*, 5154−5161.

(33) Pabst, M.; Köhn, A.; Gauss, J.; Stanton, J. F. A Worrisome Failure of the CC2 Coupled-Cluster Method when Applied to Ozone. *Chem. Phys. Lett.* **2010**, *495*, 135−140.

(34) Sailer, C. F.; Singh, R. B.; Ammer, J.; Riedle, E.; Pugliesi, I. Encapsulation of Diphenylmethyl Phosphonium Salts in Reverse Micelles: Enhanced Bimolecular Reaction of the Photofragments. *Chem. Phys. Lett.* **2011**, *512*, 60−65.

(35) Lan, Z.; Domcke, W.; Vallet, V.; Sobolewski, A. L.; Mahapatra, S. Time-Dependent Quantum Wave-Packet Description of the ^{1}ps* Photochemistry of Phenol. *J. Chem. Phys.* **2005**, *122*, 224315/1−224315/13.

(36) Scalmani, G.; Frisch, M. J. Continuous Surface Charge Polarizable Continuum Models of Solvation. I. General Formalism. *J. Chem. Phys.* **2010**, *132*, 114110/1−114110/15.

(37) Bernardi, F.; Olivucci, M.; Robb, M. A.; Tonachini, G. Can a Photochemical Reaction Be Concerted? A Theoretical Study of the Photochemical Sigmatropic Rearrangement of But-1-ene. *J. Am. Chem. Soc.* **1992**, *114*, 5805−5812.

(38) Wilsey, S.; Houk, K. N.; Zewail, A. H. Ground- and Excited-State Reactions of Norbornene and Isomers: A CASSCF Study and Comparison with Femtosecond Experiments. *J. Am. Chem. Soc.* **1999**, *121*, 5772−5786.

(39) Wilsey, S.; Houk, K. N. H/Allyl and Alkyl/Allyl Conical Intersections: Ubiquitous Control Elements in Photochemical Sigmatropic Shifts. *J. Am. Chem. Soc.* **2000**, *122*, 2651−2652.

(40) Rossi, A. R.; Wang, Y.; Wiberg, K. B. Excited States and Photochemistry of Bicyclo[1.1.0]butane. *J. Phys. Chem. A* **2009**, *113*, 1686−1695.

1.1.2. Setting up the potential surfaces for the full system

With the knowledge from section 1.1.1 at hand, the PESs for the full system Ph$_2$CH–PPh$_3^+$ can be calculated. On their basis QD simulations can clarify the relevance of the localized CoIn for the photochemical bond cleavage of Ph$_2$CH–PPh$_3^+$. First, the design of the reactive coordinates for the bond cleavage of Ph$_2$CH–PPh$_3^+$ will be discussed. Before that, however, a brief introduction to the G-matrix formalism will be given. It is used to express the kinetic Hamiltonian and demands preconditions of the used coordinates which have to be kept in mind during designing the reactive coordinates.

The G-matrix formalism

The time evolution of the molecular system is described by the time-dependent Schrödinger equation

$$i\hbar \frac{\partial}{\partial t}\Psi(x,t) = \hat{H}_x \Psi(x,t)$$
$$= \left(\hat{T}_x + \hat{V}_x \right) \Psi(x,t). \tag{1.5}$$

with the Hamiltonian $\hat{H}_x$ being the sum of the kinetic operator $\hat{T}_x$ and the potential operator $\hat{V}_x$. Eq. 1.5 is set up in Cartesian coordinates $\{x\}$. For a more appropriate description of chemical reactions it is common to transform the Schrödinger equation into internal coordinates $\{q\}$ [113, 143]. The transformation of the multiplicative operator $\hat{V}_x$ into $\hat{V}_q$ is trivial. This is not the case for the kinetic part $\hat{T}_x$ of the Hamiltonian

$$\hat{T}_x = -\frac{\hbar^2}{2} \sum_{i=1}^{3N} \frac{1}{m_i} \frac{\partial^2}{\partial x_i^2} \tag{1.6}$$

with the masses m_i and the total number of atoms N. Especially if the chosen internal coordinates include angles the transformation is challenging because they describe a non-linear motion. The G-matrix formalism introduced by B. Podolsky [141] opens a way to reformulate the kinetic operator $\hat{T}_x$ in internal coordinates. The coordinate transformation can be formulated with the help of the matrix elements $\left(J^{-1}\right)_{ri}$ of the inverse of the Jacobian matrix $\mathbf{J}$

$$q_r = \sum_{i=1}^{3N} \left(J^{-1}\right)_{ri} x_i \qquad \text{with} \quad \left(J^{-1}\right)_{ri} = \frac{\partial q_r}{\partial x_i}. \tag{1.7}$$

Using the Jacobian determinant $j = \det |\mathbf{J}|$ the kinetic operator $\hat{T}_q$ can be formulated in internal coordinates [142, 143, 192]:

$$\hat{T}_q = -\frac{\hbar^2}{2} \sum_{r=1}^{3N} \sum_{s=1}^{3N} j^{-\frac{1}{2}} \frac{\partial}{\partial q_r} \left[j G_{rs} \frac{\partial}{\partial q_s} j^{-\frac{1}{2}} \right]. \tag{1.8}$$

The elements G_{rs} of the G-matrix are calculated according to

$$G_{rs} = \sum_{i=1}^{3N} \frac{1}{m_i} \frac{\partial q_r}{\partial x_i} \frac{\partial q_s}{\partial x_i}. \tag{1.9}$$

In principle, the Jacobian determinant j as well as the G-matrix $\mathbf{G}$ are position-dependent. Assuming that the change of j with respect to $\{q\}$ is negligible compared to the position dependence of $\mathbf{G}$, eq. 1.8 can be simplified [192–194]:

$$\hat{T}_q \simeq -\frac{\hbar^2}{2} \sum_{r=1}^{3N} \sum_{s=1}^{3N} \frac{\partial}{\partial q_r} \left[G_{rs} \frac{\partial}{\partial q_s} \right]. \tag{1.10}$$

In practice, if the matrix elements $\left(J^{-1}\right)_{ri}$ are unknown, $\mathbf{G}$ is usually calculated via its inverse $\mathbf{G}^{-1}$ [192–194], which has the following elements [195]:

$$\left(G^{-1}\right)_{rs} = \sum_{i=1}^{3N} m_i \frac{\partial x_i}{\partial q_r} \frac{\partial x_i}{\partial q_s}. \tag{1.11}$$

To yield the inverse elements, the partial derivatives are reversed, which makes them much easier to be calculated compared to the normal G-matrix elements G_{rs} because it is possible to use the finite differences method [196]. The molecular system can be displaced slightly along the internal coordinates and the actual atomic positions can be written in Cartesian coordinates. After fulfilling the Eckart conditions [197] which provide the three rotational and three translational degrees of freedom being omitted in internal coordinates, the elements of $\mathbf{G}^{-1}$ can be calculated [193, 194]. To fulfill the Eckart conditions, a method proposed by A. Y. Dymarsky and K. N. Kudin is used [198–200]. Subsequent inversion of $\mathbf{G}^{-1}$ yields the desired G-matrix $\mathbf{G}$.

So far, the derivation of the G-matrix is formulated for the complete $(3N-6)$ dimensional internal coordinate space plus the rotational and translational degrees of freedom. If a reduced number of internal coordinates is used for the calculation of $\mathbf{G}$ – as it is often the case – the matrix can be blocked leading to the following structure [201]:

$$\mathbf{G} = \begin{pmatrix} \mathbf{G}_{\text{active}} & \mathbf{G}_{\text{coupling}} \\ \mathbf{G}_{\text{coupling}} & \mathbf{G}_{\text{inactive}} \end{pmatrix}, \tag{1.12}$$

with $\mathbf{G}_{\text{active}}$ being the block of the considered, active coordinates, $\mathbf{G}_{\text{inactive}}$ the one with the not considered, inactive coordinates and the coupling block $\mathbf{G}_{\text{coupling}}$. Assuming no coupling between the active and inactive coordinates, it is sufficient to calculate the inverse of $\mathbf{G}_{\text{active}}$, as the diagonal blocks of the matrix can be inverted separately.

Finally, let us take a look on the preconditions necessary to apply the G-matrix method. The first two are that the internal coordinates $\{q\}$ are linearly independent [143, 195] and that the coordinate transformation is bijective [192]. The common set of $(3N-6)$ internal coordinates, which is used to specify a molecular geometry in the Z-matrix format, namely distances, angles and dihedral angles [85, 202, 203], is usually chosen in a way that they are linearly independent. In case of $\{q\}$ containing linear combinations of these distances, angles or dihedral angles, they have to be defined in a way that they are linearly independent. The second precondition is ensured by considering the rotational and translational degrees of freedom via fulfillment of the Eckart conditions. A third precondition of more technical nature is a smooth behavior of the atomic movements along the internal coordinates. This is in general the case as long as single internal coordinates are used. However, for a better and more adapted description of the investigated process often relaxed PESs are employed. It leads to more intricate atomic movements because the effective internal coordinates become more complex due to the relaxation process. If the constrainedly optimized geometries for the relaxed PES show too big differences in the relaxed coordinates, these effective internal coordinates become pronged. Immediately problems arise during the calculation of the G-matrix because the derivatives in eq. 1.11 are not continuous any more. A conceivable scenario could be the sudden change of a dihedral angle during a relaxed scan of an angular coordinate. One way to omit these problems is to describe the behavior of the relaxation by a function depending on the main single internal coordinate [194], as it is described in the next section.

Design of the reactive coordinates

For the quantum dynamical treatment of high-dimensional problems like the investigated bond cleavage of $Ph_2CH-PPh_3^+$, the number of considered coordinates has to be significantly reduced

[116, 190]. The $(3N - 6)$ internal degrees of freedom of a system with N atoms have to be decreased to about $2 - 4$ if reactive processes with non-harmonic potentials are in the focus. The investigated bond cleavage is an ultrafast process, thus the most relevant regions of the molecular configuration space can be described by a low-dimensional model. Consequently, the question arises to find the few possible coordinates – in the present work two – that are ideally adapted to the investigated chemical reaction.

Due to the nature of a bond cleavage it is obvious to chose the C1-P distance r as one of these reactive coordinates (see fig. 1.1 b)). The aim of the QD calculations is to test whether the localized S$_1$/S$_0$ CoIn enables a fast population transfer from the S$_1$ state to the ground state, which would lead to an efficient and fast formation of carbocations. In the previous section 1.1.1, it was shown that an angular motion additional to r leads to the localized CoIn depicted in fig. 1.1 a) [191]. To optimally define an internal coordinate of the system which directly points toward the CoIn, a dummy atom X is placed in the structure of PhCH$_2$−PH$_2$Ph$^+$ at the CoIn. It lies in the plain spanned by the three C atoms of the allyl moiety important for the CoIn [138, 204, 205] in such a way that the vector pointing from X to the P atom is orthogonal to the allyl plain. Hence the second coordinate is the P-C1-X angle ϕ depicted in fig. 1.1 b).
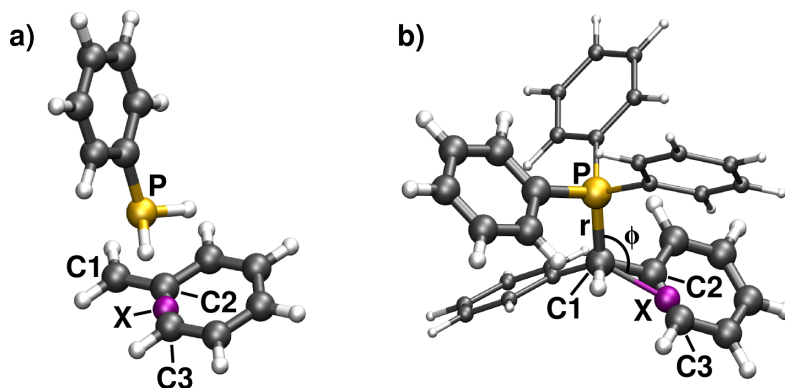

Figure 1.1.: **a)** Optimized geometry of the S$_1$/S$_0$ CoIn of the model system PhCH$_2$−PH$_2$Ph$^+$. The dummy atom X is positioned in the plain spanned by the three C atoms of the allyl moiety C1, C2 and C3 in such a way that the vector pointing from X to the P atom is orthogonal to the allyl plain. **b)** Optimized structure of Ph$_2$CH−PPh$_3^+$ in its electronic ground state with the dummy atom X and the two chosen coordinates for the QD simulations: the C1-P distance r and the P-C1-X angle ϕ. For the ONIOM calculations, the thicker drawn phenyl rings constitute the high-level system while the thinner drawn phenyl rings are only contained in the low-level system.

Of course these two internal coordinates by themselves only describe the most apparent structural changes during the bond cleavage and toward the geometry of the CoIn. Especially along r important relaxation processes take place in the background, primarily in the carbon backbone of the diphenylmethyl (Ph$_2$CH) moiety. The major contribution stems from the sp^3 to sp^2 rehybridization at the central methyl carbon atom and the bond length changes associated therewith. Fig. 1.2 a) illustrates the structural changes of the Ph$_2$CH moiety (red: unrelaxed, cyan: relaxed). The aim is to describe the PES including these background relaxations by designing a combined coordinate. For this purpose, first the energetic stabilization and the structural differences associated with the relaxation are analyzed. Then the crucial contributions (being discussed in detail in the following) are included into the corresponding coordinates to improve the description of the PES. In order not to introduce artifacts into the G-matrix, the background relaxation is described by functions which were fitted to the course of the changing coordinates along the ground state minimum energy path (MEP) for the bond cleavage.
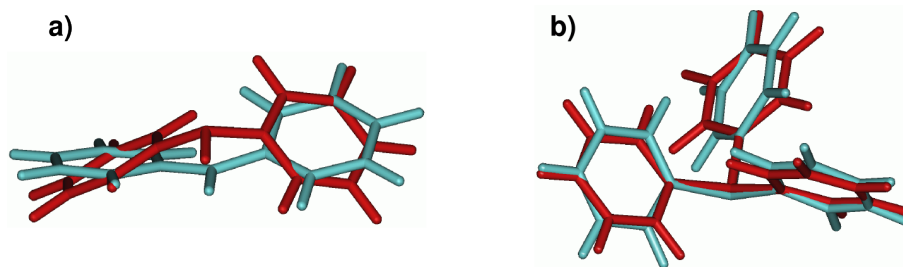
Figure 1.2.: Unrelaxed (red) and relaxed (cyan) geometry of **a)** the Ph_2CH^+ and **b)** the PPh_3 moiety. The change in hybridization from sp^3 to sp^2 at the central C1 atom of the Ph_2CH^+ can be easily recognized whereas the major differences concerning PPh_3 are rotations of the phenyl rings.

To quantify the overall relaxation energy for the bond cleavage in the ground state S_0 the C1-P bond was cleaved heterolytically [191]. The energy difference between an unrelaxed and a relaxed structure is the respective relaxation energy. Their sum for both fragments, Ph_2CH^+ and PPh_3, is 1.97 eV at the DFT level of theory (functional B3LYP/basis set 6-31g(d)). Thereof 15 % (0.30 eV) stem from the relaxation of the PPh_3 moiety while the Ph_2CH^+ accounts for 85 % (1.68 eV). The root-mean-square deviation (RMSD) between the unrelaxed and the relaxed structures are 0.46 Å for PPh_3 and 0.72 Å for Ph_2CH^+ [198]. At first glance, the difference of the RMSD values of less than a factor of two seems to be astonishing compared to the more than fivefold difference of the relaxation energies. But a closer look at the nature of the structural changes in both fragments explains these observations. The geometry relaxation of PPh_3 leads to rotations of the phenyl rings (see fig. 1.2 b)) which result in a relatively small energetic stabilization. In contrast thereto the most important geometry change in Ph_2CH^+ is the sp^3 to sp^2 rehybridization, as already mentioned. It is accompanied by a much larger energetic stabilization due to the steeper PES along this motion.

As the geometry changes of Ph_2CH^+ are more important for the relaxation energy than the ones of PPh_3, the focus for the inclusion of the structural relaxation lies on the carbon backbone of the Ph_2CH^+ moiety along r. In good approximation the relaxation is independent of the angle ϕ. Along the S_0 MEP for the bond cleavage the internal coordinates of the Ph_2CH fragment have been analyzed. After projection on the C1-P distance r, the courses of the most strongly varying coordinates were fitted depending on r. In detail, they are:

- The height d_{py} of the pyramid built by the central methyl carbon atom C1 of the Ph_2CH moiety, the two linked carbon atoms C2 and C8 as well as the linked H atom (for the atom numbering of the Ph_2CH moiety see fig. 1.3). The top is the central methyl C1

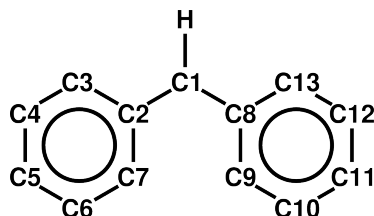
Figure 1.3.: Structural formula of the Ph_2CH moiety illustrating the numbering of the carbon atoms. The view is taken from the position of the P atom which means that at the CoIn the PPh_3 leaving group is located above the allylic subunit formed by the carbon atoms C1, C2 and C3. For the sake of clarity the aromatic hydrogen atoms are omitted.

atom [194]. As a consequence, the height decreases with increasing sp^2 hybridization of the methyl C1. Its course is fitted with a sigmoid function:

$$d_{\mathrm{py}}(r) = a \left(\frac{1}{1 + \exp(-b(r - r_0))} - 1 \right). \tag{1.13}$$

- The distance between the C1 atom and its neighboring atoms shortens due to the higher s orbital character in the sp^2 hybrid orbitals compared to the sp^3 case. The C1-C2 bond length modification is fitted with the following sigmoid function:

$$d_{\mathrm{C1\text{-}C2}}(r) = c \frac{1}{1 + \exp(-d(r - r_0))} - e. \tag{1.14}$$

The C1-C8 bond length modification is fitted with eq. 1.14 as well, whereas the C1-H distance change was neglected as it amounts only 0.015 Å.

- The angles enclosed by the bonds around C1, namely the C1-C2, the C1-C8, and the C1-H bond also change along the MEP. The course of α_{C2C1H}, α_{C2C1C8} as well as α_{HC1C8} is fitted with the sigmoid function given in eq. 1.14.

- During the sp^3 to sp^2 rehybridization the relative orientation between the two planes of the phenyl rings changes. To mimic this reorientation, first of all the angle $\alpha_{\mathrm{ph\text{-}C1C8}}$ between the C3C5C7 plane and the C1-C8 bond has to be fitted according to eq. 1.14. The second parameter necessary to adapt is the angle between the normal vectors of both phenyl ring planes C3C5C7 and C8C10C12. It is done using the following function:

$$\alpha_{\mathrm{ph\text{-}ph}}(r) = f \exp\left(-gr\right) + \alpha_{\mathrm{ph\text{-}ph}}^{\infty}. \tag{1.15}$$

Here the angle $\alpha_{\mathrm{ph\text{-}ph}}^{\infty}$ is set to the value of the optimized Ph$_2$CH$^+$ without further being fitted.

The position of the PPh$_3$ leaving group along the MEP in the ground state is defined by three coordinates. Two of them are chosen as reactive coordinates, r and ϕ. The third coordinate – the dihedral angle β_{LG} – is defined between P, C1, X, and C3. Its change along the MEP is fitted with the function:

$$\beta_{\mathrm{LG}}(r) = \ln \left(\frac{\exp(-h(r - r_0))}{1 + \exp(-h(r - r_0))} \right) + \beta_{\mathrm{LG}}^{\mathrm{CoIn}}. \tag{1.16}$$

To optimally reach the geometry of the CoIn in the two-dimensional space, $\beta_{\mathrm{LG}}^{\mathrm{CoIn}}$ takes the value of 90° which is the required value due to the definition of the dummy atom X.

Tab. 1.1 provides an overview of the fitted parameters. All relative errors lie well below 0.1 (see last column of tab. 1.1). Fig. 1.4 shows the course of d_{py} (black circles) along the MEP projected on the C1-P distance r as well as the fitted function (red line; eq. 1.13). The larger r, the lower the height d_{py} gets, reflecting the rehybridization from sp^3 to sp^2. Around $r = 4.0 - 4.5$ Å the methyl C1 atom is almost fully planarized. In the optimized Ph$_2$CH$^+$, d_{py} takes a value of $5 \cdot 10^{-5}$ Å.

coordinate	fit function	fit parameters	relative error
d_{py}	eq. 1.13	$a = (-0.649 \pm 0.005)\,\text{Å}$	0.007
		$b = (2.15 \pm 0.02)\,\text{Å}^{-1}$	0.010
		$r_0 = (2.280 \pm 0.009)\,\text{Å}$	0.004
$d_{\text{C1-C2}}$	eq. 1.14	$c = (-0.168 \pm 0.003)\,\text{Å}$	0.02
		$d = (2.07 \pm 0.05)\,\text{Å}^{-1}$	0.02
		$r_0 = (2.17 \pm 0.02)\,\text{Å}$	0.008
		$e = (1.586 \pm 0.003)\,\text{Å}$	0.002
$d_{\text{C1-C8}}$	eq. 1.14	$c = (-0.192 \pm 0.003)\,\text{Å}$	0.02
		$d = (2.17 \pm 0.04)\,\text{Å}^{-1}$	0.02
		$r_0 = (2.09 \pm 0.02)\,\text{Å}$	0.008
		$e = (1.609 \pm 0.003)\,\text{Å}$	0.002
α_{C2C1H}	eq. 1.14	$c = (12.4 \pm 0.6)\,^{\circ}$	0.05
		$d = (3.6 \pm 0.3)\,\text{Å}^{-1}$	0.07
		$r_0 = (2.06 \pm 0.03)\,\text{Å}$	0.014
		$e = (102.3 \pm 0.5)\,^{\circ}$	0.005
α_{C2C1C8}	eq. 1.14	$c = (33 \pm 1.4)\,^{\circ}$	0.04
		$d = (2.16 \pm 0.08)\,\text{Å}^{-1}$	0.04
		$r_0 = (1.88 \pm 0.04)\,\text{Å}$	0.02
		$e = (98 \pm 1.4)\,^{\circ}$	0.014
α_{HC1C8}	eq. 1.14	$c = (12.6 \pm 0.7)\,^{\circ}$	0.05
		$d = (3.6 \pm 0.3)\,\text{Å}^{-1}$	0.08
		$r_0 = (2.05 \pm 0.03)\,\text{Å}$	0.02
		$e = (102.0 \pm 0.6)\,^{\circ}$	0.006
$\alpha_{\text{ph-C1C8}}$	eq. 1.14	$c = (-80 \pm 3)\,^{\circ}$	0.04
		$d = (1.83 \pm 0.08)\,\text{Å}^{-1}$	0.05
		$r_0 = (2.14 \pm 0.05)\,\text{Å}$	0.02
		$e = (94 \pm 3)\,^{\circ}$	0.03
$\alpha_{\text{ph-ph}}$	eq. 1.15	$f = (3.8 \pm 0.2) \cdot 10^2\,^{\circ}$	0.06
		$g = (1.24 \pm 0.03)\,\text{Å}^{-1}$	0.03
β_{LG}	eq. 1.16	$h = (-16.7 \pm 1.1)\,\text{Å}^{-1}$	0.07
		$r_0 = (3.45 \pm 0.08)\,\text{Å}$	0.02

Table 1.1.: Fitted parameters of the fit functions given in eqs. $1.13 - 1.16$ to describe the relaxation of the carbon backbone of the Ph_2CH moiety and the dihedral angle β_{LG} of the PPh_3 leaving group along the MEP for the bond cleavage in the ground state. The last column specifies the relative error of the fitted parameters.
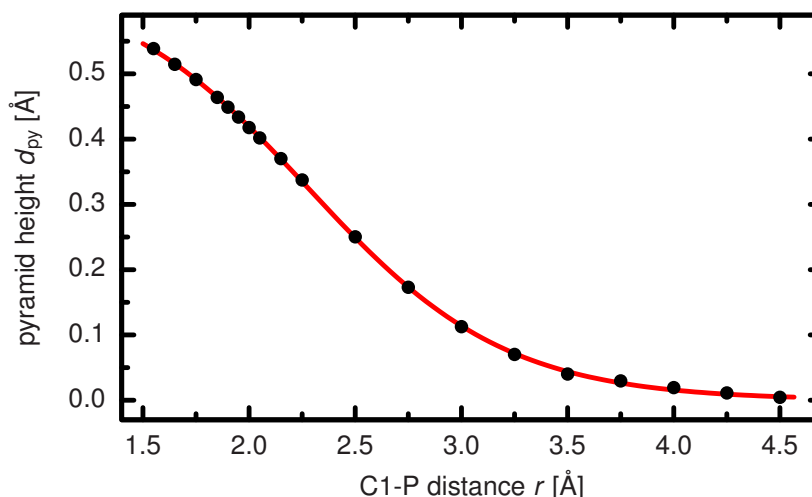
Figure 1.4.: Course of the height d_{py} (black circles) of the pyramid defined by the atoms C1, C2, C8 and H (see fig. 1.3) along the ground state MEP for the bond cleavage in $Ph_2CH-PPh_3^+$ projected to the C1-P distance r. The red line depicts the fit function (eq. 1.13) using the parameters listed in tab. 1.1.

With the parametrization of the most important geometrical changes at hand, the relaxed structure of the Ph_2CH moiety can be reconstructed at an arbitrary point of the two-dimensional coordinate space (r, ϕ). To guarantee a proper reconstruction, the order in which the fitted internal coordinates are adapted to the desired value is important [194]. The procedure starting from the S_0 minimum geometry is visualized in fig. 1.5. After loading the S_0 minimum geometry, the desired C1-P distance r determines the adjustment of the background relaxation. First, the distances between the methyl C1 atom and both phenyl rings d_{C1-C2} and d_{C1-C8} are adjusted, followed by the pyramidalization of C1 (d_{py}). Then the angles enclosed by the bonds around C1 (C1-C2, C1-C8, and C1-H) are brought into line. Thereby it is sufficient to adapt only two of the three angles, i.e. α_{C2C1H} and α_{HC1C8} in the present case. Note that now it is not useful to take the cross product of both arms enclosing the actual angle as rotational axis because then the rotation would affect the pyramidalization. Instead, an iterative procedure can be applied employing the normal vector of the C2-C8-H plain as rotational axis if C1 is located in the origin. The next step is to match the relative orientation of both phenyl rings which is realized via $\alpha_{ph-C1C8}$ and α_{ph-ph}. Again, both angles are leveled using an iterative procedure. To adjust $\alpha_{ph-C1C8}$ the left phenyl ring in fig. 1.3 is rotated with $\overline{C1C2}$ as rotational axis. In the case of α_{ph-ph} the right phenyl ring is rotated around the $\overline{C1C8}$ axis. Before finally the PPh_3 moiety can be positioned according to r, ϕ and β_{LG}, the RMSD between the relaxed and the loaded Ph_2CH moiety has to be minimized [198].

To quantify the achieved amount of relaxation or rather the amount of relaxation energy covered by the parametrization of the backbone motion of the Ph_2CH moiety along the MEP the energy difference between the unrelaxed and the via parametrization adapted structure is calculated. The value is then compared to the relaxation energy of the optimized structure. The covered relaxation energy is 1.56 eV which is 93 % of the 1.68 eV achieved by optimization. The RMSD between the via parametrization adapted and the optimized structure is 0.087 Å corresponding to a covered proportion of 88 %. Note that the remaining proportion of the RMSD is higher than the one of the relaxation energy. This means that the energetically most important backbone motions are included in the parametrization process. The covered fraction of the total relaxation energy of both fragments is still 79 %. The reason is that the amount of the PPh_3 leaving group is not reduced.

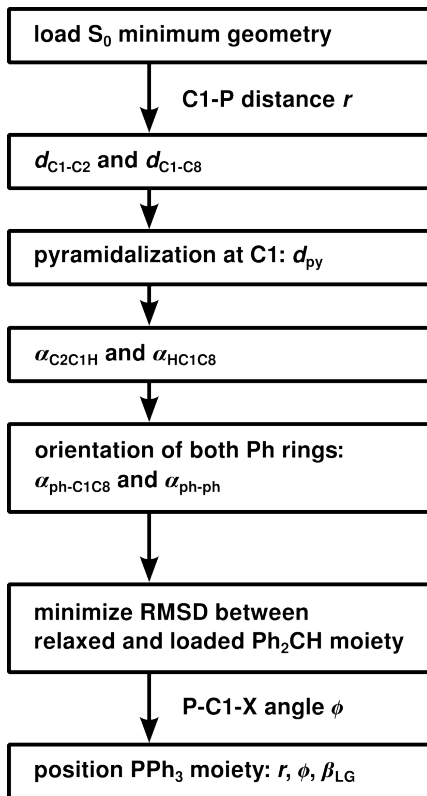Figure 1.5.: Flowchart for the construction of $Ph_2CH-PPh_3^+$ at an arbitrary point of the two-dimensional coordinate space (r, ϕ). After loading the S_0 minimum geometry, the carbon backbone of the Ph_2CH moiety is relaxed using the parametrization given in tab. 1.1. Finally, the PPh_3 moiety is positioned after minimization of the RMSD between the relaxed and the loaded Ph_2CH fragment.

Shape of the G-matrix elements

The two designed reactive coordinates are well-suited for quantum dynamical simulations of the photoinduced bond cleavage of $Ph_2CH-PPh_3^+$. On their basis the elements of the G-matrix can be calculated as described in the beginning of section 1.1.2. Fig. 1.6 illustrates the shape of the three matrix elements G_{rr}, $G_{r\phi}$ and $G_{\phi\phi}$. Both off-diagonal elements $G_{r\phi}$ and $G_{\phi r}$ are identical because **G** is symmetric. As expected, G_{rr} and $G_{\phi\phi}$ have a positive sign (cf. eq. 1.9). In contrast, the coupling element $G_{r\phi}$ has a negative sign in the majority of the depicted range.

The matrix element G_{rr} shown in a) is small for $r < 2\,\text{Å}$. In the range of $2\,\text{Å} \leq r \leq 4\,\text{Å}$ three maxima appear which become more pronounced with increasing P-C1-X angle ϕ. The first maximum is the highest, the second one has the broadest shape. The strong variation of G_{rr} in this range is due to the background relaxation of the Ph_2CH fragment which is included in the r coordinate [194]. For $r > 4\,\text{Å}$ this background motion is diminished and G_{rr} becomes constant as then r is a linear coordinate in the Cartesian coordinate space.

The off-diagonal element $G_{r\phi}$ specifies the kinetic coupling between the coordinates r and ϕ (see fig. 1.6 b)). Its absolute value is smaller by a factor of 5 compared to G_{rr}. In the area of $2\,\text{Å} \leq r \leq 4\,\text{Å}$ two minima occur which again become more pronounced for larger ϕ values. For $r > 4\,\text{Å}$, $G_{r\phi}$ approaches zero ($|G_{r\phi}| < 10^{-7}$ au) meaning that the kinetic coupling decreases.

The second diagonal element $G_{\phi\phi}$ shown in fig. 1.6 c) is smaller by about a factor of 10 compared to G_{rr}. For $r < 3\,\text{Å}$ it is faintly structured showing two maxima for $\phi > 100\,°$,
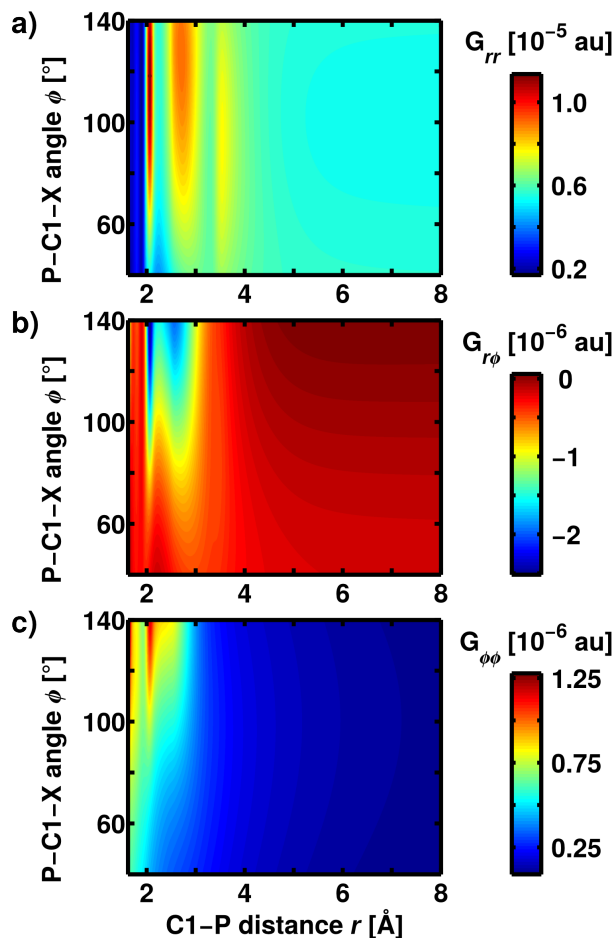
Figure 1.6.: G-matrix elements for the two-dimensional coordinate space $\{r, \phi\}$. The first diagonal element G_{rr} is depicted in **a)**, the off-diagonal element $G_{r\phi}$ in **b)**, and the second diagonal element $G_{\phi\phi}$ in **c)**. As the matrix is symmetric, both off-diagonal elements $G_{r\phi}$ and $G_{\phi r}$ are identical.

whereof one fades out for smaller ϕ. Outside of $r = 4\,\text{Å}$, the matrix element $G_{\phi\phi}$ levels off below 10^{-7} au.

ONIOM potential energy surfaces

The G-matrix elements presented in the last paragraph are the crucial part of the kinetic Hamiltonian $\hat{T}_q$ given in eq. 1.10. To perform QD calculations, additionally the potential operator $\hat{V}_q$ is required. Here, the molecular PESs of $Ph_2CH–PPh_3^+$ were calculated at the ONIOM level of theory [74, 80, 81, 83, 206]. To this, the molecule has to be divided in two parts – the model and the real system – which are treated at a different level of theory; the model system at a high quantum chemical level, the real system at a lower one. In the model or high-level system the crucial part of the investigated process takes place while the additional part of the real or low-level system plays a subordinated role. Nevertheless it should not be neglected. The overall energy of the system is calculated according to

$$E^{\text{ONIOM}} = E_{\text{model}}^{\text{high}} - E_{\text{model}}^{\text{low}} + E_{\text{real}}^{\text{low}} \,, \tag{1.17}$$

with $E_{\text{model}}^{\text{high}}$ and $E_{\text{model}}^{\text{low}}$ being the high- and low-level energy of the model system and $E_{\text{real}}^{\text{low}}$ the low-level energy of the real system [80, 206]. For the reduction of the real system to obtain the

model system, bonds have to be cut. The eliminated moieties have to be replaced by single atoms to avoid open valences. Usually, hydrogen atoms are used. As the bond length changes from a C-C to a C-H single bond, it has to be scaled. Here, the scaling parameters of 0.709 for a C-C bond and of 0.754 for a P-C bond are taken from reference [207].

At the ONIOM level of theory, not only ground state energies can be calculated but also excitation energies. In principle, this can be done by taking the difference of the ONIOM energies of the ground state $E_{S_0}^{ONIOM}$ and the ith excited state $E_{S_i}^{ONIOM}$ [81, 83]:

$$\Delta E_{S_i \leftarrow S_0}^{ONIOM} = E_{S_i}^{ONIOM} - E_{S_0}^{ONIOM} \ . \tag{1.18}$$

This would require three excited state calculations, one at the high level of theory (e.g. CASSCF) for the model system and two at the lower level of theory (e.g. TDDFT) for the model and the real system. In cases where the excitation can be assumed to be limited to the model system, it is sufficient to just perform the high level of theory calculation for the model system [81, 83]. This leads to the constraint low-level state (CLS) approximation

$$E_{S_i}^{ONIOM} \approx E_{S_i}^{ONIOM,CLS} = E_{model,S_i}^{high} - E_{model,S_0}^{low} + E_{real,S_0}^{low} \ , \tag{1.19}$$

which results in a substantial gain in computing time as just one excited state calculation has to be performed. Hence, the excitation energy using the CLS approximation can be estimated to be the excitation energy of the model system [81, 83]:

$$\Delta E_{S_i \leftarrow S_0}^{ONIOM} \approx \Delta E_{S_i \leftarrow S_0}^{ONIOM,CLS} = \Delta E_{model,S_i \leftarrow S_0}^{high}. \tag{1.20}$$

Due to the resulting saving of computing time, the CLS approximation has a high attractiveness and is used for the calculation of the potential energy surfaces of $Ph_2CH-PPh_3^+$ in the present work. The high-level calculations at the CASSCF(10,10) level of theory [191] were performed using the program package Molpro 2012 [208], for the low-level calculations (DFT, functional M06-2X [209, 210]) the program package Gaussian 09 was employed [211]. Throughout all calculations the double-ζ basis set 6-31G(d) was used [212–214]. Fig. 1.1 b) illustrates the subdivision of $Ph_2CH-PPh_3^+$ into the model system $PhCH_2-PH_2Ph^+$, which only contains the thicker drawn parts, and the real system. To receive the model system, the omitted thinner drawn phenyl rings are replaced by hydrogen atoms. In chapter 1.1.1 the appropriateness of the model system was demonstrated by the comparison of excitation spectra of phosphonium ions with an increasing number of phenyl rings calculated at the CC2 level of theory [191].

The resulting PES for the ground state S_0 and the first excited state S_1 are depicted in fig. 1.7. The horizontal axis is the C1-P distance r, the vertical axis the P-C1-X angle ϕ. The minimum of the ground state is located at $r = 1.9$ Å and $\phi = 125°$ (see fig. 1.7 a)). The first excited state exhibits a local minimum next to the FC point recognizable in fig. 1.7 b). A small barrier separates this FC minimum from the dissociative area of the S_1 PES. A large gradient mainly in r direction leads to a gain of potential energy of about 2.5 eV during the dissociation process.

The global minimum of the S_1 surface lies in the vicinity of a S_1/S_0 CoIn. Its presence within the PES confirms the success of the reactive coordinate choice because the angular coordinate ϕ was chosen in a way that the CoIn is included in the two-dimensional coordinate space. The CoIn is located at $r = 2.9$ Å and $\phi = 75°$, the point of minimal energy difference ($\Delta E = 0.085$ eV) between S_1 and S_0 at the ONIOM level of theory. The structure of the marked S_1/S_0 CoIn is presented in fig. 1.8 and is similar to the S_1/S_0 CoIn optimized for the model system $PhCH_2-PH_2Ph^+$ which was described in chapter 1.1.1 [191]. Again, the P atom is positioned over an allylic C_3 subunit containing the carbon atoms C1, C2 and C3. Such an allylic subunit is a generic motif which often induces a CoIn [138, 191, 204, 205]. Comparing the geometry of the CoIn of $PhCH_2-PH_2Ph^+$ and the one for the full system $Ph_2CH-PPh_3^+$, two major
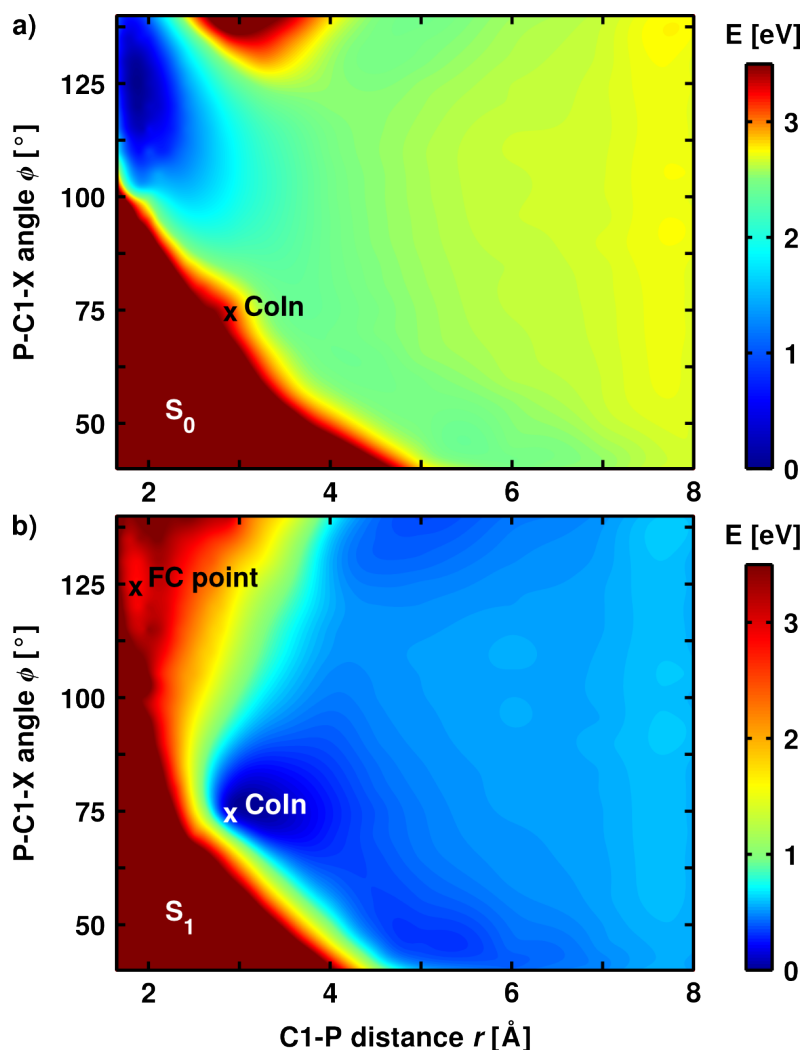
Figure 1.7.: Molecular PESs of $Ph_2CH-PPh_3^+$ calculated at the ONIOM level of theory. **a)** The ground state potential has its minimum at $r = 1.9\,\text{Å}$ and $\phi = 125\,°$. **b)** The S_1 potential shows a local minimum in the FC region. Its global minimum lies next to the S_1/S_0 CoIn at $r = 2.9\,\text{Å}$ and $\phi = 75\,°$. Note that the minimum of each surface is set to zero separately.

differences attract attention. First, in the case of $PhCH_2-PH_2Ph^+$, both phenyl rings are almost perpendicular. They enclose an angle of $77\,°$ (see chapter 1.1.1). Fig. 1.8 illustrates that due to steric reasons this does not occur for $Ph_2CH-PPh_3^+$. Secondly, the C1-P distance is shortened by about $1\,\text{Å}$ which might be traced back to the increased interaction between the π orbitals of the phenyl rings because their alignment is more parallel enabling a significantly better overlap.

Non-adiabatic coupling along the reactive coordinates

With the G-matrix $\mathbf{G}(r,\phi)$ and the molecular potential $V_q(r,\phi)$ at hand, the behavior of $Ph_2CH-PPh_3^+$ in its first excited state S_1 can be simulated quantum dynamically. In order to verify the importance of the discussed S_1/S_0 CoIn for the photochemical bond cleavage, the population transfer enabled by the CoIn has to be incorporated in the QD simulations. Thereto, a non-adiabatic correction is necessary in the usual time-dependent Schrödinger equation (eq. 1.5), because the action of the kinetic operator of the nuclei $\hat{T}_x$ on the electronic

wave function is not negligible in the vicinity of a CoIn [119, 120, 215, 216]. The strategy for the calculation of the non-adiabatic correction was to perform the quantum chemical calculations for the optimized S_1/S_0 CoIn of the model system $PhCH_2-PH_2Ph^+$ and to shift the non-adiabatic coupling thereon to the CoIn on the ONIOM potential. Using atomic units [71], the time-dependent Schrödinger equation for the nuclear wave functions $\Psi_{1,x}$ and $\Psi_{2,x}$ of two electronic states including the non-adiabatic correction reads [119, 120]:

$$i\frac{\partial}{\partial t}\begin{pmatrix}\Psi_{1,x}\\\Psi_{2,x}\end{pmatrix} = \left\{\begin{pmatrix}\hat{T}_x & \hat{K}_{12,x}\\-\hat{K}_{12,x} & \hat{T}_x\end{pmatrix}+\begin{pmatrix}\hat{V}_{1,x} & 0\\0 & \hat{V}_{2,x}\end{pmatrix}\right\}\begin{pmatrix}\Psi_{1,x}\\\Psi_{2,x}\end{pmatrix}, \tag{1.21}$$

with the non-adiabatic coupling term $\hat{K}_{12,x}$ being defined as

$$\hat{K}_{12,x} = -\sum_{i=1}^{3N}\frac{1}{m_i}\left(f_{12,x}^{(i)}\frac{\partial}{\partial x_i}+\frac{1}{2}g_{12,x}^{(i)}\right). \tag{1.22}$$

It contains the first- and second-order non-adiabatic coupling matrix elements (NACMEs) $f_{12,x}^{(i)}$ and $g_{12,x}^{(i)}$ which depend on the electronic wave functions $\Phi_{1,x}$ and $\Phi_{2,x}$:

$$f_{12,x}^{(i)} = \left\langle\Phi_{1,x}\left|\frac{\partial}{\partial x_i}\Phi_{2,x}\right.\right\rangle \text{ and} \tag{1.23}$$

$$g_{12,x}^{(i)} = \left\langle\Phi_{1,x}\left|\frac{\partial^2}{\partial x_i^2}\Phi_{2,x}\right.\right\rangle. \tag{1.24}$$

Often the second-order NACME $g_{12,x}^{(i)}$ is neglected as it is usually much smaller than $f_{12,x}^{(i)}$ [119, 120]. However, a simple elimination of $g_{12,x}^{(i)}$ in eq. 1.22 results in a non-hermitian Hamiltonian in eq. 1.21. To avoid its non-hermiticity, $g_{12,x}^{(i)}$ can be disassembled in a hermitian part $h_{12,x}^{(i)}$ and a non-hermitian remainder [119, 120]:

$$g_{12,x}^{(i)} = h_{12,x}^{(i)} + \frac{\partial}{\partial x_i}f_{12,x}^{(i)}$$
$$= \left\langle\frac{\partial}{\partial x_i}\Phi_{1,x}\left|\frac{\partial}{\partial x_i}\Phi_{2,x}\right.\right\rangle + \frac{\partial}{\partial x_i}f_{12,x}^{(i)}. \tag{1.25}$$

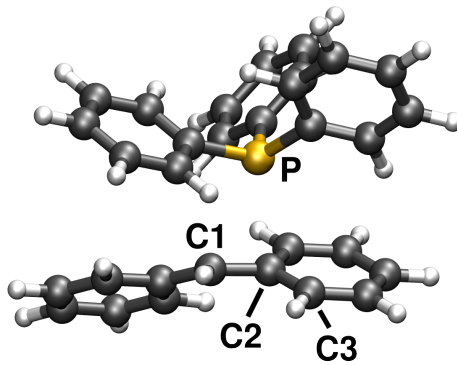Figure 1.8.: Structure of the S_1/S_0 CoIn of the full system $Ph_2CH-PPh_3^+$ at $r = 2.9\,\text{Å}$ and $\phi = 75°$ (cf. fig. 1.7). Like in the model system $PhCH_2-PH_2Ph^+$, the P atom is located above the allylic C_3 subunit constituted by C1, C2 and C3.

If only $h_{12,x}^{(i)}$ is omitted, the hermiticity of the Hamiltonian is maintained. It results in the following approximated non-adiabatic coupling term:

$$\hat{K}_{12,x} \approx \hat{K}'_{12,x} = -\sum_{i=1}^{3N} \frac{1}{m_i} \left(f_{12,x}^{(i)} \frac{\partial}{\partial x_i} + \frac{1}{2} \left(\frac{\partial}{\partial x_i} f_{12,x}^{(i)} \right) \right), \tag{1.26}$$

which describes the population transfer between both electronic states in eq. 1.21.

In the preceding sections of this chapter, the transformation of the potential and the kinetic operator – $\hat{V}_x$ and $\hat{T}_x$ – from Cartesian to internal coordinates as well as the design of the selected reactive internal coordinates r and ϕ were discussed. To apply the time-dependent Schrödinger equation 1.21 in internal coordinates $\{q\}$, the non-adiabatic coupling term $\hat{K}'_{12,x}$ in eq. 1.26 has to be transformed, too. This can be done with the help of the matrix elements $\left(J^{-1} \right)_{si} = \frac{\partial q_s}{\partial x_i}$ of the inverse Jacobian matrix (cf. eq. 1.7) and leads to

$$\begin{aligned}
\hat{K}'_{12,q} &= -\sum_{s=1}^{3N} \sum_{i=1}^{3N} \frac{1}{m_i} \left(f_{12,x}^{(i)} \frac{\partial q_s}{\partial x_i} \frac{\partial}{\partial q_s} + \frac{1}{2} \left(\frac{\partial q_s}{\partial x_i} \frac{\partial}{\partial q_s} f_{12,x}^{(i)} \right) \right) \\
&= \sum_{s=1}^{3N} \left(\tilde{f}_{12,q}^{(s)} \frac{\partial}{\partial q_s} + \frac{1}{2} \left(\frac{\partial}{\partial q_s} \tilde{f}_{12,q}^{(s)} \right) \right).
\end{aligned} \tag{1.27}$$

Note that here the transformed NACME $\tilde{f}_{12,q}^{(s)}$ already includes the masses m_i and the negative sign [119]:

$$\tilde{f}_{12,q}^{(s)} = -\sum_{i=1}^{3N} \frac{1}{m_i} f_{12,x}^{(i)} \frac{\partial q_s}{\partial x_i}. \tag{1.28}$$

With eq. 1.28 at hand, the transformation of $f_{12,x}^{(i)}$, which can be calculated analytically by standard quantum chemistry program packages, can be performed. In the case of known matrix elements $\left(J^{-1} \right)_{si}$, the transformation is straightforward. But in the present example of the S$_1$/S$_0$ CoIn of PhCH$_2$−PH$_2$Ph$^+$ this does not apply. In order to be able to transform $f_{12,x}^{(i)}$ into $\tilde{f}_{12,q}^{(s)}$, the assumption has to be made that in the vicinity of the CoIn the background motion linked to the reactive coordinates is negligible. This is justifiable, as at the CoIn, the C1-P distance takes a value of $r = 3.94$ Å (see section 1.1.1) which is already quite large. In this distance range the rehybridization from sp^3 to sp^2 which is the main source of background relaxation has already mostly taken place (see fig. 1.4 and reference [194]). Thus r and ϕ are purely defined by the position vectors $\vec{P}$, $\vec{C1}$ and $\vec{X}$ of the respective atoms:

$$r = \left| \vec{P} - \vec{C1} \right| \quad \text{and}$$

$$\phi = \arccos \left(\frac{\left(\vec{P} - \vec{C1} \right) \cdot \left(\vec{X} - \vec{C1} \right)}{\left| \vec{P} - \vec{C1} \right| \left| \vec{X} - \vec{C1} \right|} \right), \tag{1.29}$$

and the transformation according to eq. 1.28 is feasible.

The first-order NACME $f_{12,x}^{(i)}$ around the optimized S$_1$/S$_0$ CoIn of PhCH$_2$−PH$_2$Ph$^+$ were calculated at the CASSCF(10,10) level of theory using Molpro 2012 [208]. Fig. 1.9 illustrates the course of the PESs in the vicinity of the CoIn. The tilted shape of the CoIn in the $\{r, \phi\}$ space is clearly recognizable. On the ground state surface (lower potential) the gradient pointing in the direction of the bond cleavage – i.e. toward larger r values – is considerably larger than the one leading to the S$_0$ minimum of the reactant. This emphasizes the potential importance of the CoIn for the carbocation formation which will be verified in section 1.2.
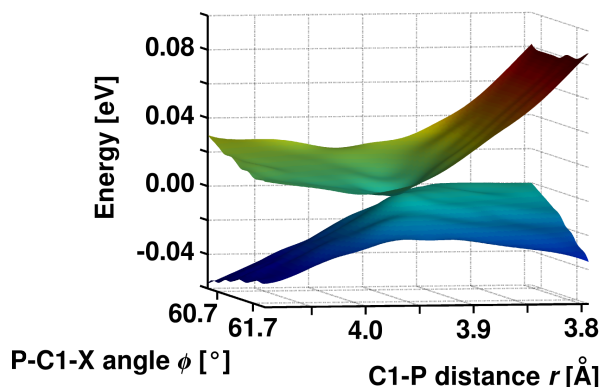
Figure 1.9.: Potential surfaces of the ground state and the first excited state of $PhCH_2-PH_2Ph^+$ in the vicinity of the optimized CoIn calculated at the CASSCF(10,10) level of theory. The tilted shape of the CoIn is clearly visible.

Fig. 1.10 shows the transformed NACMEs $\tilde{f}_{12,r}$ (a)) and $\tilde{f}_{12,\phi}$ (b)) of the high-level system $PhCH_2-PH_2Ph^+$. They are already shifted to the CoIn in the full system $Ph_2CH-PPh_3^+$ at $r = 2.9\,\text{Å}$ and $\phi = 75\,°$. The coupling is strongly localized to a very small area around the CoIn in the considered two-dimensional coordinate space. A comparable spatial size is found for the NACMEs of a CoIn in the diphenylmethyl derivative Ph_2CH-Cl with chlorine as leaving group [82]. A comparison of the size of both elements $\tilde{f}_{12,r}$ and $\tilde{f}_{12,\phi}$ reveals that the coupling in r direction is about three times stronger than the one in ϕ direction.
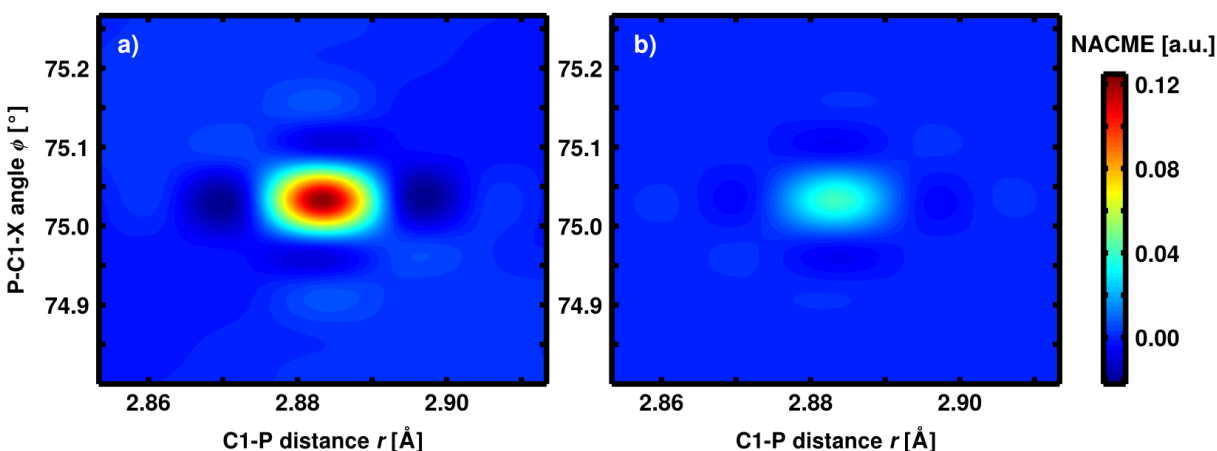

Figure 1.10.: Non-adiabatic coupling matrix elements **a)** $\tilde{f}_{12,r}$ and **b)** $\tilde{f}_{12,\phi}$ already shifted to the CoIn in the full system $Ph_2CH-PPh_3^+$ at $r = 2.9\,\text{Å}$ and $\phi = 75\,°$. An alternative representation can be found in fig. 4 (top row) of reference [217] which is reprinted in section 1.2.

1.2. Implicit treatment of the dynamic solvent effects: The dynamic continuum ansatz

On the basis of the results presented in section 1.1.2, the bond cleavage of $Ph_2CH-PPh_3^+$ can be investigated quantum dynamically. To reproduce the experimentally observed product formation, an appropriate description of the dynamic solvent effects discussed at the beginning

of chapter 1 is indispensable. This and the next chapter deal with two different methods to incorporate the dynamic solvent effects in QD simulations, which constitute the main part of the present thesis.

In the article "Quantum Dynamics of a Photochemical Bond Cleavage Influenced by the Solvent Environment: A Dynamic Continuum Approach" published in *The Journal of Physical Chemistry Letters* QD simulations of the bond cleavage are presented [217]. The G-matrix method (cf. section 1.1.2) together with a Chebychev propagation scheme [218] are employed to propagate the nuclear ground state wave function on the S_1 PES (see fig. 1.7 b)). The vibrational ground state wave function $v = 0$ was calculated using the relaxation method [219]. Besides QD calculations for the isolated molecule corresponding to the gaseous environment, a new method is introduced which allows for the description of dynamic solvent effects. The key statements of the article are:

- In the gas phase, the wave packet evolving on the S_1 potential of $Ph_2CH–PPh_3^+$ after photoexcitation misses the localized S_1/S_0 CoIn due to the large gradient along r. It is mainly accelerated in the r direction and remains in the first excited state leading to the formation of the radical pair $Ph_2CH^\bullet + PPh_3^{\bullet+}$ [191], which is in clear contradiction to the experimental observations in different organic solvents like acetonitrile (MeCN) or dichloromethane [133].

- The dynamic solvent effects exerted on the molecular system can be described in the quantum mechanical formalism by means of an additional potential $\hat{V}_{\text{dec}}(\Psi)$ in the Hamiltonian:

$$\hat{H}(\Psi) = \hat{T}_{\text{nuc}} + \hat{V}_{\text{mol}} + \hat{V}_{\text{dec}}(\Psi), \tag{1.30}$$

with $\hat{T}_{\text{nuc}}$ being the kinetic operator of the nuclei and $\hat{V}_{\text{mol}}$ the molecular electronic PES, and resulting in a non-linear Schrödinger equation. $\hat{V}_{\text{dec}}$ is based on the frictional force F_{dec} experienced by the dissociating fragments, which is calculated using the dynamic viscosity of the solvent η [220] together with Stokes' law [217, 221]. Integration of F_{dec} yields the
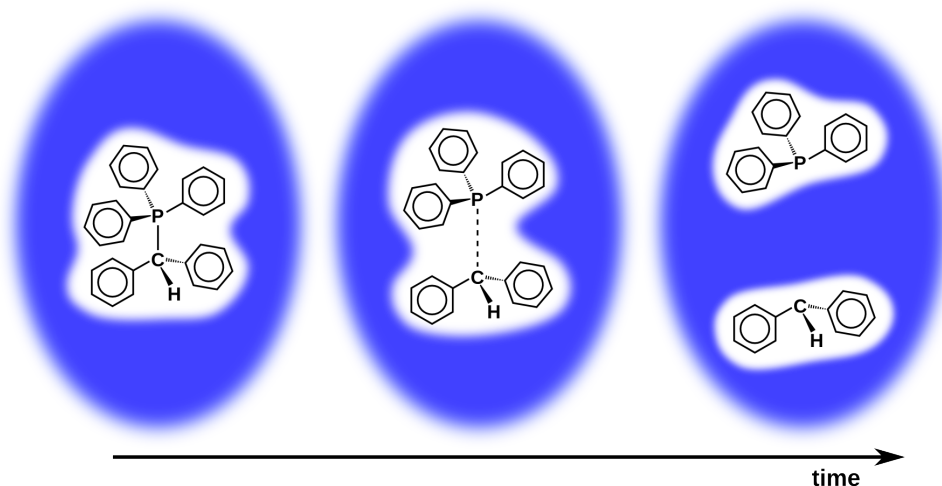

Figure 1.11.: Schematic representation of the implicit solvent surrounding during the bond cleavage of $Ph_2CH–PPh_3^+$. The necessary deformation of the white solvent cavity can be recognized from left to right. This deformation results in a deceleration of the molecular fragments which is described by the dynamic continuum ansatz in the quantum dynamical context.

decelerating potential $\hat{V}_{\text{dec}}$:

$$\hat{V}_{\text{dec}}(r) = -\int_0^r F_{\text{dec}}(r')dr'. \tag{1.31}$$

The newly developed dynamic continuum ansatz treats the solvent surrounding in an implicit way and exclusively relies on quantum chemical and quantum mechanical quantities as well as the experimentally determined dynamic viscosity. Thus no fitting of parameters is required.

- Fig. 1.11 shows the implicit solvent environment and illustrates the necessity of deforming the solvent cavity during the bond cleavage. The solvent surrounding decelerates the wave packet and opens a way to explore the small gradient pointing toward the S_1/S_0 CoIn. Here, the branching between both product channels – the homolytic or heterolytic one – takes place.

- If the NACMEs presented in section 1.1.2 are included into the QD simulations, the necessary time interval for the generation of Ph_2CH^+ is revealed. It takes about 400 fs until their formation through the CoIn occurs. This is in good agreement with the sub-picosecond initial rise of the carbocation signal observed in recent pump-probe measurements [133].

The QD simulations including the dynamic solvent effects and the NACMEs revealed the reaction mechanism for the ultrafast photochemical bond cleavage of $Ph_2CH-PPh_3^+$. In the following, the article "Quantum Dynamics of a Photochemical Bond Cleavage Influenced by the Solvent Environment: A Dynamic Continuum Approach" published in *The Journal of Physical Chemistry Letters* is reprinted with permission from *J. Phys. Chem. Lett.* **5**, 3480–3485 (2014); copyright 2014 American Chemical Society.

Quantum Dynamics of a Photochemical Bond Cleavage Influenced by the Solvent Environment: A Dynamic Continuum Approach

Sebastian Thallmair,[†,‡] Markus Kowalewski,[†,§] Julius P. P. Zauleck,[†] Matthias K. Roos,[†] and Regina de Vivie-Riedle*[,†]

[†]Department Chemie, Ludwig-Maximilians-Universität München, D-81377 München, Germany
[‡]Lehrstuhl für BioMolekulare Optik, Ludwig-Maximilians-Universität München, D-80538 München, Germany

Ⓢ *Supporting Information*

ABSTRACT: In every day chemistry, solvents are used to influence the outcome of chemical synthesis. Electrostatic effects stabilize polar configurations during the reaction and in addition dynamic solvent effects can emerge. How the dynamic effects intervene on the ultrafast time scale is in the focus of this theoretical study. We selected the photoinduced bond cleavage of $Ph_2CH–PPh_3^+$ for which the electrostatic interactions are negligible. Elaborate ultrafast pump–probe studies already exist and serve as a reference. We compared quantum dynamical simulations with and without environment and noticed the necessity to model the influence of the solvent cage on the reactive motions of the solute. The frictional force induced by the dynamic viscosity of the solvent is implemented in the quantum mechanical formalism with a newly developed approach called the dynamic continuum ansatz. Only when the environment is included are the experimentally observed products reproduced on the subpicosecond time scale.

SECTION: Liquids; Chemical and Dynamical Processes in Solution

$\hat{H}(\Psi) = \hat{H}_0 + \hat{V}_{dec}(\Psi)$

V_{el}

V_{dec}

without V_{dec} → homolysis

with V_{dec} → heterolysis
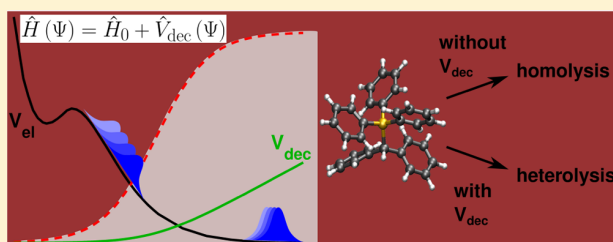
Solvents play an important role in chemistry.[1] Their polarity and viscosity can change the reaction outcome and rate. The electrostatic contributions become effective when reactants and products possess different dipole moments.[2−4] Here, also the reorientation of the solvent has to be considered if it happens on a similar time scale as the reaction.[5−7] Independent of the presence of electrostatic interactions, dynamic solvent effects may arise that directly interfere with the intramolecular motion. Possible scenarios are photoinduced bond cleavage or formation where ultrafast large amplitude motions occur. The corresponding changes in the molecular structure cause modifications in the shape and volume of the solute's cavity. The surrounding molecules have to be displaced to enable the molecular deformation. This caging effect becomes important, especially, when bulky molecular fragments are involved. For theoretical studies the challenge is to include this effect in the simulations.

Successful realizations were demonstrated for the photo-dissociation of ICN studied with classical molecular dynamics methods. Benjamin and Wilson used parametrized potentials to simulate the excited state dynamics and showed that the dissociating fragments are decelerated by the surrounding Xe fluid compared to the gas phase.[8] Similar observations were also reported for other solvents.[9−11] Additionally, the slowdown of the rotationally hot $CN^•$ radicals subsequent to photo-dissociation can be observed. Comparison of classical molecular dynamics simulations with transient pump–probe anisotropy measurements shows that the rotation of the $CN^•$ radicals is

decelerated until a larger cavity is formed.[8,12,13] In their enlarged cage, $CN^•$ radicals rotate nearly freely for several picoseconds even in room temperature liquids.[14]

We present an ansatz that incorporates the frictional force from the surrounding solvent cage in the quantum mechanical formalism directly based on the time-dependent Schrödinger equation. It opens a straightforward way to keep the wave packet character to describe the electronic excitation by a laser pulse for coherent control studies[15] in solution and for nonadiabatic processes like population transfer through a conical intersection (CoIn). First quantum mechanical investigations on moving particles that are subject to viscous force were done in the 1970s in heavy ion physics.[16−20] Different approaches using expectation values of the momentum and position[16,17] as well as the phase of the wave function[20] were employed. The effect of rare gas matrices on vibrating diatomics were studied by femtosecond spectroscopy and quantum dynamics simulations.[21]

Our interest lies in photoinduced molecular bond cleavage in organic molecules that generates short-lived reactive inter-mediates. For these reactions we will demonstrate that already on the short femtosecond time scale the dynamic solvent effect becomes important. Phosphonium salts like $Ph_2CH–PPh_3^+\ X^-$

containing diphenylmethyltriphenylphosphonium (Ph$_2$CH—PPh$_3^+$) ions are commonly used for the photogeneration of diphenylmethyl cations (Ph$_2$CH$^+$) as intermediates in polar and moderately polar solvents like acetonitrile or dichloromethane[22] (see Scheme 1). Experimental investigations using

Scheme 1. Reaction Scheme for the Photochemical Bond Cleavage in Diphenylmethyltriphenylphosphonium Ions Ph$_2$CH—PPh$_3^{+a}$
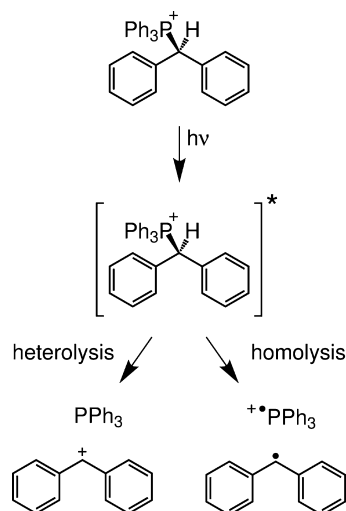
^{a}The dissociation character of the ground state is heterolytic leading to the photoproducts Ph$_2$CH$^+$ and PPh$_3$; the first and second excited state have homolytic character generating Ph$_2$CH$^\bullet$ and PPh$_3^{\bullet+}$.

ultrafast broadband transient absorption spectroscopy demonstrated that, with nonoxidizable counterions X$^-$ (e.g., BF$_4^-$ or SbF$_6^-$), diphenylmethyl cations are formed almost exclusively.[23] Quantum chemical studies revealed that, after a local $\pi-\pi^*$ excitation on the leaving group PPh$_3$ and the crossing of a small barrier in the first excited state S$_1$, the C1—P bond cleavage can take place.[24] In the dissociation limit, the S$_1$ state describes the homolytic bond cleavage leading to the formation of a radical pair Ph$_2$CH$^\bullet$ and PPh$_3^{\bullet+}$ (Scheme 1, right channel), whereas in the ground state S$_0$ the desired Ph$_2$CH$^+$ cations (and PPh$_3$) are built after heterolytic bond cleavage (Scheme 1, left channel). An energetically reachable CoIn was identified, which connects both product channels.[24] Additional to the primary dissociation coordinate, the C1—P distance, an angular coordinate is necessary to reach the CoIn (see Figure 1). Thus, the static quantum chemical results suggest that a wave packet evolving along the dissociation coordinate has to reach the CoIn where the excited state population could be efficiently transferred to the ground state to generate the experimentally observed diphenylmethyl cations.[23]

In order to clarify the reaction mechanism and the role of the CoIn, we first performed quantum dynamical calculations (for details, see Supporting Information (SI)) on the two-dimensional potential energy surface (PES) of the S$_1$ state, spanned by the two coordinates identified as essential to describe the reaction (see Figure 1). Figure 2 shows the time evolution of the wave packet at selected times after a large part of the wave packet has crossed the barrier in the Franck−Condon (FC) region. The other fraction of the wave packet stays in the local S$_1$-minimum behind the barrier. The black and white isolines illustrate snapshots at 170 and 290 fs after starting the
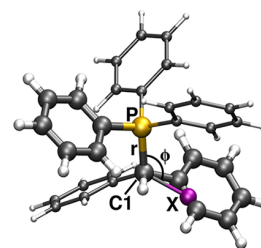
Figure 1. Optimized geometry of Ph$_2$CH−PPh$_3^+$. For the calculation of the potential energy surface used in the quantum dynamical simulations, the ONIOM method is employed (see SI). The thicker part of Ph$_2$CH−PPh$_3^+$ shows the high-level system PhCH$_2$−PH$_2$Ph$^+$ of the ONIOM calculations; the thinner drawn phenyl rings are only contained in the low-level system Ph$_2$CH−PPh$_3^+$ and are replaced by hydrogen atoms in the high-level system. The coordinates considered in our quantum dynamical calculations are the C1−P distance r and the angle ϕ between the atoms P, C1 and the dummy atom X, which is introduced to optimally define the angle ϕ.
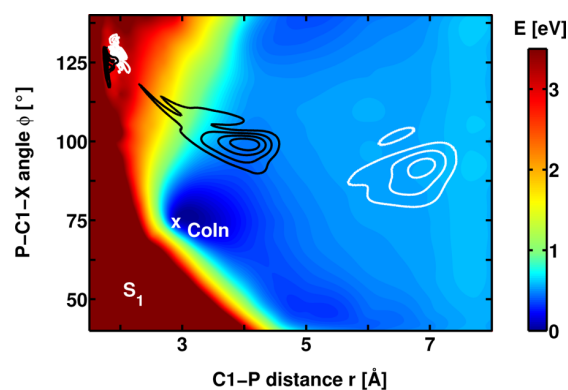
Figure 2. Potential energy surface of the first excited state S$_1$ of Ph$_2$CH−PPh$_3^+$ together with dissociating wave packets. Two snapshots are taken at 170 fs (black isolines) and 290 fs (white isolines) after starting the propagation in the FC region. The wave packet clearly misses the CoIn at a C1−P distance r of 2.9 Å and a P−C1−X angle ϕ of 75°.

propagation in the FC region. Evidently the wave packet misses the CoIn, although it lies close to the global minimum of the S$_1$ - PES. As the gradient in the r direction is larger than the one in the ϕ direction the vibrational wave packet is mainly accelerated in the r direction. The dissociation occurs in the S$_1$ state and radical pairs are formed after a homolytic bond cleavage. This is clearly in contrast to the experimentally observed heterolytic process.[23] As both dissociation channels have one positively charged fragment, electrostatic solvent effects change neither the energetics of the reaction nor the energetic order of the dissociation channels.[24] Only due to its dynamic impact the solvent is expected to play a decisive role.

We developed a dynamic continuum ansatz that treats the solvent environment in a continuum-like fashion and can be applied when no charges are generated during the reaction. Its decelerating effect is described in the quantum mechanical formalism by means of an additional potential term $\hat{V}_{dec}$ (Ψ) in the Hamiltonian. $\hat{V}_{dec}$ (Ψ) is constructed from a nonconservative force, which depends on the wave function Ψ. Thus, the Hamiltonian is expressed as the sum of the operators for the kinetic energy of the nuclei ($\hat{T}_{nuc}$), the potential energy ($\hat{V}_{el}$), and the decelerating potential ($\hat{V}_{dec}$ (Ψ)):

Letter

$$\hat{H}(\Psi) = \hat{H}_0 + \hat{V}_{dec}(\Psi)$$
$$= \hat{T}_{nuc} + \hat{V}_{el} + \hat{V}_{dec}(\Psi) \qquad (1)$$

The sum of $\hat{T}_{nuc}$ and $\hat{V}_{el}$ is the molecular Hamiltonian $\hat{H}_0$. The negative gradient of $\hat{V}_{dec}(\Psi)$ reflects the decelerating frictional force $\overrightarrow{F}_{dec}$ originating from the surrounding solvent molecules. The time evolution of the wave function Ψ of the system is described by the following nonlinear time-dependent Schrödinger equation:

$$i\hbar\frac{\partial}{\partial t}\Psi = (\hat{H}_0 + \hat{V}_{dec}(\Psi))\Psi \qquad (2)$$

In the chosen example Ph$_2$CH–PPh$_3^+$ the bond cleavage process is decelerated. From an atomistic viewpoint, the velocity at which both fragments move apart from each other decreases. The decelerating frictional force $\overrightarrow{F}_{dec}$ is not constant along the C1–P distance r. It is negligible as long as the solute's cavity is not deformed but becomes gradually important with the increase of the cavity. The information how the cavity changes can be obtained by calculating its surface area along the reaction coordinate with the GEPOL algorithm[25,26] as implemented in Gaussian09.[27] Figure 3a shows the cavity
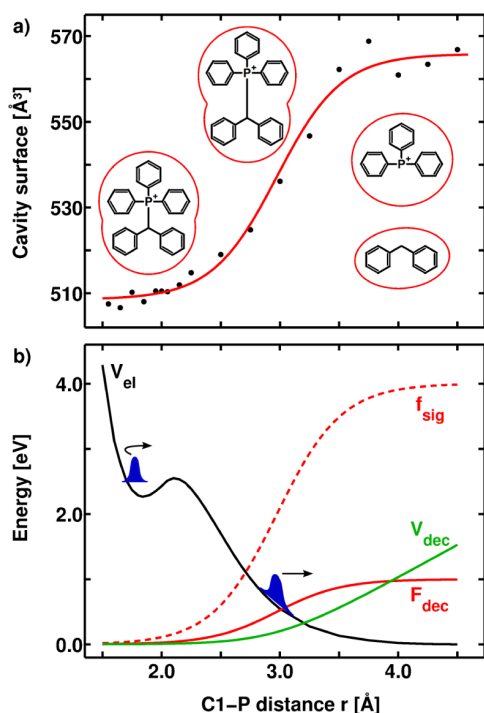
Figure 3. (a) Cavity surface area of the solute Ph$_2$CH–PPh$_3^+$ in acetonitrile (black dots) depending on the C1–P distance calculated for a polarized continuum model. The solid red line shows the fitted sigmoid function f_{sig}. The structural formula illustrates that the cavity surface area increases along the dissociation coordinate until it reaches a constant value when both fragments have separated cavities. (b) Discrimination between a locally trapped (left) and a dissociating part of a wave packet (right) in a molecular potential V_{el} (solid black line) with the help of the sigmoid shape function f_{sig} (dashed red line). The solid red line illustrates the decelerating force $F_{dec}(r,t)$; the solid green line illustrates the decelerating potential $V_{dec}(r,t)$ as a function of the C1–P distance, shown for a specific time t during the propagation. The energy axis relates solely to the molecular potential $\hat{V}_{el}$.

surface area (black dots) as a function of r. Around the FC point it stays almost constant. However, with growing r it increases until a constant value is reached when both fragments are separated. The change of the cavity surface can be fitted with a sigmoid function $f_{sig}(r)$ (red solid line in Figure 3a). The step of $f_{sig}(r)$ indicates the onset of the dynamic solvent effect. Its position is determined by r_s; its slope by a_s (see eq 3). When the sigmoid function reaches its plateau, the maximum force $\overrightarrow{F}_0(t)$ at time t is experienced by the system (for the detailed definition of $\overrightarrow{F}_0(t)$ see eq 4). The product of $\overrightarrow{F}_0(t)$ and $f_{sig}(r)$ yields the decelerating force $\overrightarrow{F}_{dec}(r,t)$ which depends on the position along the coordinate r and on the time t:

$$\overrightarrow{F}_{dec}(r, t) = \overrightarrow{F}_0(t)f_{sig}(r)$$
$$= \overrightarrow{F}_0(t)\frac{1}{1 + \exp(-a_s(r - r_s))} \qquad (3)$$

Accordingly, $\overrightarrow{F}_{dec}(r, t)$ is zero for $r \ll r_s$, and the wave packet evolves solely under the influence of the molecular potential. Around r_s, the force $\overrightarrow{F}_{dec}(r,t)$ increases until it reaches its maximum value $\overrightarrow{F}_0(t)$ and the wave packet is decelerated. $\overrightarrow{F}_0(t)$ is proportional to the expectation value of the velocity $\langle\overrightarrow{v}_r(t)\rangle$ of the wave packet along r at which the fragments move apart from each other. A simple model for the frictional force $\overrightarrow{F}_0(t)$ in a viscous medium is given by Stokes' law

$$\overrightarrow{F}_0(t) = -\gamma\langle\overrightarrow{v}_r(t)\rangle$$
$$= -6\pi\eta R_{eff}\langle\overrightarrow{v}_r(t)\rangle, \qquad (4)$$

with the experimentally determined dynamic viscosity of the solvent η[28] and the effective radius R_{eff}. The latter takes into account that the momentum along the dissociation coordinate r is equally partitioned between the fragments and that they have different radii R_i and masses m_i:

$$R_{eff} = \frac{R_1 m_2 + R_2 m_1}{m_1 + m_2} \qquad (5)$$

In this sense, R_{eff} combines the forces acting on both particles, which have to be calculated individually according to conservation of momentum and Stokes' law.

The radii R_i for the fragments are obtained from quantum chemistry by mapping their cavity volume to the volume of a sphere whose radius then corresponds to R_i. Integration of $-\overrightarrow{F}_{dec}(r, t)$ over r yields the decelerating potential $V_{dec}(r,t)$. In a one-dimensional case, the vector $\overrightarrow{F}_{dec}(r, t)$ becomes scalar: $\overrightarrow{F}_{dec}(r,t) \rightarrow F_{dec}(r,t)$. As $F_0(t)$ is independent of r, it can be moved outside the integral:
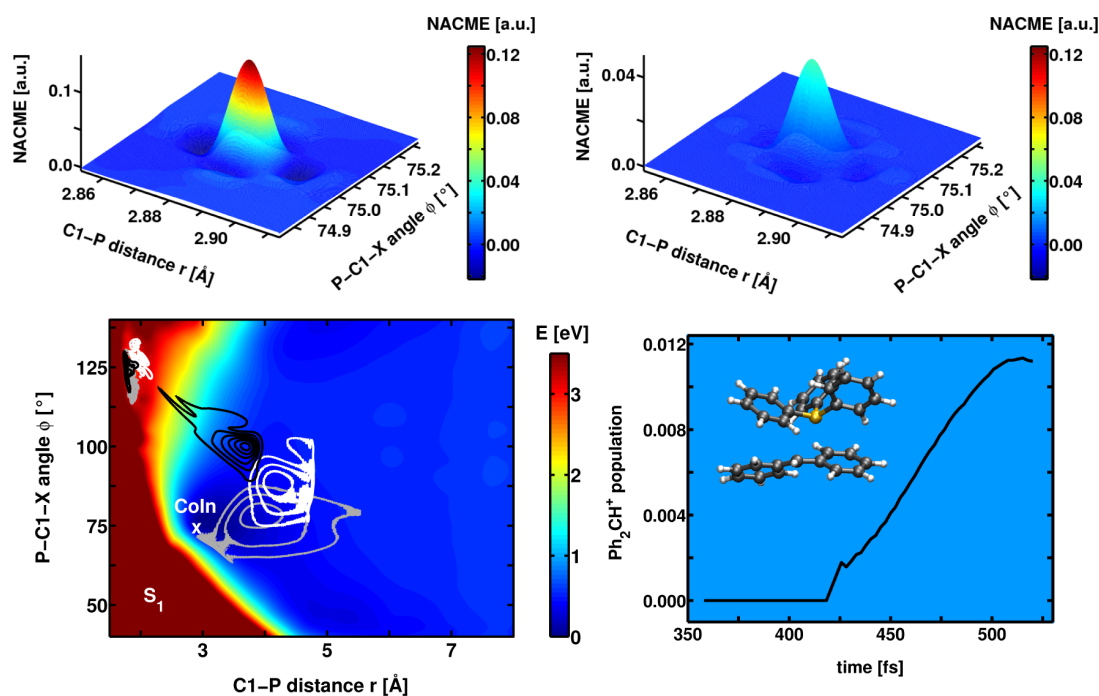
Figure 4. Nonadiabatic coupling matrix elements $\langle \Psi_0 | (\partial)/(\partial r) | \Psi_1 \rangle$ (top, left) and $\langle \Psi_0 | (\partial)/(\partial \phi) | \Psi_1 \rangle$ (top, right) for the investigated CoIn in the high-level system PhCH$_2$–PH$_2$Ph$^+$. Potential energy surface of the first excited state S$_1$of Ph$_2$CH–PPh$_3^+$ together with dissociating wave packets propagated with the dynamic continuum ansatz (bottom, left). Three snapshots are taken at 170 fs (black isolines), 290 fs (white isolines) and 390 fs (gray isolines) after starting the propagation in the FC region. In contrast to Figure 2, the wave packet is decelerated and reaches the CoIn with the ground state. Product population of the ground state that was transferred through the CoIn and evolves toward longer bond length, leading to the formation of Ph$_2$CH$^+$ cations (bottom, right). The inlay shows the geometry of Ph$_2$CH–PPh$_3^+$ at the CoIn.

$$V_{dec}(r, t) = -\int_0^r F_{dec}(r') \, dr'$$

$$= -F_0(t) \int_0^r \frac{1}{1 + \exp(-a_s(r' - r_s))} \, dr'$$

$$= -F_0(t) \left[-\frac{1}{a_s} \ln\left(\frac{\exp(-a_s(r' - r_s))}{1 + \exp(-a_s(r' - r_s))} \right) \right]_0^r$$

(6)

Therefore, $V_{dec}(r,t)$ has the shape of the antiderivative of the sigmoid function with the slope $-F_0(t)$ as shown in Figure 3, panel b (green solid line).

The dissociation dynamics can be divided in three central steps, which are reflected in the sigmoid function. When the wave packet is in the FC region, the dynamics are not influenced by the solvent. Later when the wave packet is split at the barrier along the dissociation coordinate as depicted in panel b of Figure 3, only the part of the wave packet that moves toward larger bond length and passes the step of $f_{sig}(r)$ is decelerated by the solvent cage. Thus, only the velocity of the outer part of the wave packet contributes to $F_0(t)$. This case is ensured by shaping the wave packet with the sigmoid function $f_{sig}(r)$ before calculating the velocity $\langle v_{r,out}(t) \rangle$ of the outer part:

$$\langle v_{r,out}(t) \rangle = \frac{1}{\mu_r} \frac{\langle f_{sig}(r)\Psi(r, \phi, t) | \hat{p}_r | f_{sig}(r)\Psi(r, \phi, t) \rangle}{\langle f_{sig}(r)\Psi(r, \phi, t) | f_{sig}(r)\Psi(r, \phi, t) \rangle}$$

(7)

with the reduced mass μ_r. According to the sigmoid function $f_{sig}(r)$ the decelerating force $F_{dec}(r, t)$ then converges to the

maximum force $F_0(t)$ for large values of r. As the wave packet is slowed down $F_0(t)$ decreases until no friction is experienced by the system. Accordingly, the decelerating potential $V_{dec}(r, t)$ flattens until it vanishes.

The limit of our dynamic continuum ansatz is given by the representability of the momentum distribution by its respective expectation value for the considered process. The approach can straightforwardly be extended to higher dimensions. However, it should be noted that the decelerating potential $V_{dec}(r_1, r_2, ...)$ has to be the antiderivative of all the force functions $\overrightarrow{F_{dec,i}}(r_1, r_2...)$, with i being an enumerator for the number of forces included in the model. This is fulfilled automatically as long as the force functions along different coordinates only depend on that respective coordinate, i.e., $\overrightarrow{F_{dec,i}}(r_1, r_2...) = F_{dec,i}(r_j)\vec{e}_j$, with $\vec{e}_j$ being the unit vector in the r_j direction. Once the forces become interdependent, this is not generally the case, and there might not exist a single potential that accounts for all the desired forces.

The dynamic continuum ansatz is suited for our example of the photochemical bond cleavage of Ph$_2$CH–PPh$_3^+$. The quantum dynamical calculations without environment (see Figure 2) have shown that the dominant direction of motion is the r direction because its gradient is larger than the one along ϕ. As shown in eq 4, the maximum force $\overrightarrow{F_0}(t)$ along a coordinate is proportional to the corresponding expectation value of the velocity. Thus, the decelerating force in ϕ direction is of minor importance, and we confine the dynamic effects of the solvent to the r direction.

Figure 4 (bottom, left) shows the PES of the S_1 state together with three exemplary snapshots of the dissociating wave packet under the influence of the environment. The snapshots are taken at 170 fs (black isolines), 290 fs (white isolines) and 390 fs (gray isolines) after starting the propagation in the FC region. Compared to the dynamics without solvent (see Figure 2) slight differences are already observable for the wave packet at 170 fs (black). The dynamic solvent effect becomes more pronounced as the propagation evolves. At 290 fs the wave packet has slowed down significantly along the r direction and starts moving under the influence of the gradient toward the CoIn, which is close to the global S_1 minimum. Simultaneously, a broadening of the wave packet is observed, as a minor part keeps a small momentum toward the dissociation S_1 channel, while the major part approaches the CoIn. The CoIn is reached for the first time at 390 fs.

In order to observe the population transfer through the CoIn, we calculated the nonadiabatic coupling around the CoIn optimized in the high-level system $PhCH_2-PH_2Ph^+$ at the CASSCF(10,10) level of theory.[24] Figure 4 (top row) shows the nonadiabatic coupling matrix elements $\langle \Psi_0|(\partial/\partial r)|\Psi_1\rangle$ (left) and $\langle \Psi_0|(\partial/\partial\phi)|\Psi_1\rangle$ (right). $\langle \Psi_0|(\partial/\partial r)|\Psi_1\rangle$ is about 3 times larger than $\langle \Psi_0|(\partial/\partial\phi)|\Psi_1\rangle$. Both matrix elements enter into our adiabatic implementation of the quantum dynamics on coupled PES.[29] After coupling through the CoIn, we observe a branching of the wave packet toward the ground state minimum or toward the dissociation channel correlated to the Ph_2CH^+ formation. The increase in the Ph_2CH^+ population is depicted in Figure 4, bottom right. We observe a population rise until about 500 fs, which compares well with the fast initial rise of the Ph_2CH^+ transient absorption signal on the subpicosecond time scale.[23] Geminate recombination as well as diffusional separation occur on a longer time scale and could be treated with an augmented Smoluchowski-type diffusion method.[3]

In summary, we have shown that the dynamic effects of the solvent play a decisive role during the photochemical bond cleavage process in diphenylmethyltriphenylphosphonium ions ($Ph_2CH-PPh_3^+$). We presented an ansatz that treats these effects in a continuum-like fashion within the quantum mechanical formalism. The ansatz does not require fitting of parameters and solely relies on quantum mechanically and dynamically evaluated quantities as well as on the experimentally determined dynamic viscosity of the solvent. The solvent cage decelerates the dissociating wave packet and gives it the opportunity to follow the small gradient toward the CoIn where the branching between diphenylmethyl radicals ($Ph_2CH^\bullet$) radicals and Ph_2CH^+ cations takes place. Only with the solvent environment included is the passage through the CoIn possible and the experimentally observed Ph_2CH^+ cations are formed.

The presented dynamic continuum ansatz is general for any bond cleavage process as the coordinate describing the separation of two fragments is the most essential for this important type of chemical reaction. Its range of application can be extended further to the most general situation of wave packet splitting along multiple reaction pathways. Specially designed shape functions can ensure that the diverse solvent effects experienced along the individual reaction channels are correctly reflected in the simulations. Typical examples are small organic cyclic molecules, like cyclohexadiene, furane and the DNA bases, where the excited state population can relax via photophysical or photochemical channels exhibiting different velocities and structural changes. As long as the expectation value of the momentum of the considered parts of the wave packet is meaningful for the molecular process, the presented dynamic continuum ansatz is applicable.

■ COMPUTATIONAL METHODS

The potential energy surface of $Ph_2CH-PPh_3^+$ was calculated with the "our own n-layered integrated molecular orbital and molecular mechanics (ONIOM)" method. The thicker drawn part of $Ph_2CH-PPh_3^+$ in Figure 2 indicates the high-level system calculated at the CASSCF(10,10) level of theory with the program package Molpro;[30] the thinner phenyl rings are only contained in the low-level system. It is calculated at the DFT (M06-2X) level of theory using Gaussian09.[27] Throughout all calculations, the basis set 6-31G(d) was employed. The major relaxation processes along the dissociation coordinate r are included in the PES. That is the change of the sp^3 to sp^2 hybridization at the C1 atom of the methyl group and the rotation of the phenyl rings and bond length changes, which come along with the lowering of the hybridization. The nonadiabatic couplings were calculated analytically at the CASSCF(10,10) level of theory for the optimized CoIn in the high-level system $PhCH_2-PH_2Ph^+$, and the projected nonadiabatic coupling matrix elements were shifted to the point of minimal energy difference between S_1 and S_0 on the ONIOM potential at $r = 2.9$ Å and $\phi = 75°$. An energetic comparison of the critical points at the MS-CASPT2 level of theory can be found in the SI. The energetic shifts are too small to change the observed reaction channels and the derived mechanism.

For the quantum dynamical simulations, a homemade program was employed that solves the time-dependent Schrödinger equation on a spatial grid using the Chebychev propagation scheme[31] and the G-matrix method for the kinetic operator $\hat{T}$[32–34] (for details see SI). The vibrational ground state wave function $\upsilon = 0$ for the electronic ground state S_0 was placed on the S_1 PES. It was shifted slightly to shorter C1−P distance to ensure that the main part of the wave packet crosses the barrier next to the FC region. This is necessary because the minimal barrier[24] is not included in the two-dimensional coordinate space. To include it a third coordinate would be needed, which would increase the simulation time drastically.

■ ASSOCIATED CONTENT

ⓢ Supporting Information

Details about the quantum dynamical simulations, figures of the S_1 PES of $Ph_2CH-PPh_3^+$ and the G-matrix elements, potential energies of the critical points at the MS-CASPT2 level of theory as well as geometries in xyz-format are available in the online version of this article. This material is available free of charge via the Internet at http://pubs.acs.org/.

■ AUTHOR INFORMATION

Corresponding Author
*E-mail: regina.de_vivie@cup.uni-muenchen.de.
Present Address
§(M.K.) Department of Chemistry, University of California, Irvine, California 92697−2025, USA

Notes
The authors declare no competing financial interest.

■ ACKNOWLEDGMENTS

■ REFERENCES

(1) Reichardt, C.; Welton, T. *Solvents and Solvent Effects in Organic Chemistry*; Wiley-VCH Verlag GmbH & Co. KGaA: Weinheim, Germany, 2011.

(2) Melo, A.; Alfaia, A. J. I.; Reis, J. C. R.; Calado, A. R. T. Unusual Solvent Effect on a S_N2 Reaction. A Quantum-Mechanical and Kinetic Study of the Menshutkin Reaction between 2-Amino-L-methylbenzimidazole and Iodomethane in the Gas Phase and in Acetonitrile. *J. Phys. Chem. B* **2006**, *110*, 1877−1888.

(3) Sailer, C. F.; Thallmair, S.; Fingerhut, B. P.; Nolte, C.; Ammer, J.; Mayr, H.; de Vivie-Riedle, R.; Pugliesi, I.; Riedle, E. A Comprehensive Microscopic Picture of the Benzhydryl Radical and Cation Photo-Generation and Interconversion through Electron Transfer. *ChemPhysChem* **2013**, *14*, 1423−1437.

(4) Struebing, H.; Ganase, Z.; Karamertzanis, P. G.; Siougkrou, E.; Haycock, P.; Piccione, P. M.; Armstrong, A.; Galindo, A.; Adjiman, C. S. Computer-Aided Molecular Design of Solvents for Accelerated Reaction Kinetics. *Nat. Chem.* **2013**, *5*, 952−957.

(5) Stratt, R. M.; Maroncelli, M. Nonreactive Dynamics in Solution: The Emerging Molecular View of Solvation Dynamics and Vibrational Relaxation. *J. Phys. Chem.* **1996**, *100*, 12981−12996.

(6) Nibbering, E.; Elsaesser, T. Probing Solvation Dynamics with Femtosecond Vibrational Spectroscopy. *Appl. Phys. B: Lasers Opt.* **2000**, *71*, 439−441.

(7) Rosspeintner, A.; Lang, B.; Vauthey, E. Ultrafast Photochemistry in Liquids. *Annu. Rev. Phys. Chem.* **2013**, *64*, 247−271.

(8) Benjamin, I.; Wilson, K. R. Proposed Experimental Probes of Chemical Reaction Molecular Dynamics in Solution: ICN Photodissociation. *J. Chem. Phys.* **1989**, *90*, 4176−4197.

(9) Krylov, A. I.; Gerber, R. B. Photodissociation of ICN in Solid and in Liquid Ar: Dynamics of the Cage Effect and of Excited-State Isomerization. *J. Chem. Phys.* **1994**, *100*, 4242−4252.

(10) Amatatsu, Y.; Morokuma, K. A Theoretical Study on the Photochemical Reaction of ICN in Liquid Ar. *Chem. Phys. Lett.* **1995**, *245*, 469−474.

(11) Winter, N.; Chorny, I.; Vieceli, J.; Benjamin, I. Molecular Dynamics Study of the Photodissociation and Photoisomerization of ICN in Water. *J. Chem. Phys.* **2003**, *119*, 2127−2143.

(12) Moskun, A. C.; Jailaubekov, A. E.; Bradforth, S. E.; Tao, G.; Stratt, R. M. Rotational Coherence and a Sudden Breakdown in Linear Response Seen in Room-Temperature Liquids. *Science* **2006**, *311*, 1907−1911.

(13) Rivera, C. A.; Winter, N.; Harper, R. V.; Benjamin, I.; Bradforth, S. E. The Dynamical Role of Solvent on the ICN Photodissociation Reaction: Connecting Experimental Observables Directly with Molecular Dynamics Simulations. *Phys. Chem. Chem. Phys.* **2011**, *13*, 8269−8283.

(14) Moskun, A. C.; Bradforth, S. E. Photodissociation of ICN in Polar Solvents: Evidence for Long Lived Rotational Excitation in Room Temperature Liquids. *J. Chem. Phys.* **2003**, *119*, 4500−4515.

(15) von den Hoff, P.; Thallmair, S.; Kowalewski, M.; Siemering, R.; de Vivie-Riedle, R. Optimal Control Theory - Closing the Gap Between Theory and Experiment. *Phys. Chem. Chem. Phys.* **2012**, *14*, 14460−14485.

(16) Albrecht, K. A New Class of Schrödinger Operators for Quantized Friction. *Phys. Lett. B* **1975**, *56*, 127−129.

(17) Hasse, R. W. On the Quantum Mechanical Treatment of Dissipative Systems. *J. Math. Phys.* **1975**, *16*, 2005−2011.

(18) Kostin, M. Friction and Dissipative Phenomena in Quantum Mechanics. *J. Stat. Phys.* **1975**, *12*, 145−151.

(19) Hasse, R. W. Approaches to Nuclear Friction. *Rep. Prog. Phys.* **1978**, *41*, 1027−1101.

(20) Stocker, W.; Albrecht, K. A Formalism for the Construction of Quantum Friction Equations. *Ann. Phys.* **1979**, *117*, 436−446.

(21) Ibrahim, H.; Héjjas, M.; Fushitani, M.; Schwentner, N. Phase Sensitive Control of Vibronic Guest-Host Interaction: Br_2 in Ar Matrix. *J. Phys. Chem. A* **2009**, *113*, 7439−7450.

(22) Ammer, J.; Mayr, H. Photogeneration of Carbocations: Applications in Physical Organic Chemistry and the Design of Suitable Precursors. *J. Phys. Org. Chem.* **2013**, *26*, 956−969.

(23) Ammer, J.; Sailer, C. F.; Riedle, E.; Mayr, H. Photolytic Generation of Benzhydryl Cations and Radicals from Quaternary Phosphonium Salts: How Highly Reactive Carbocations Survive Their First Nanoseconds. *J. Am. Chem. Soc.* **2012**, *134*, 11481−11494.

(24) Thallmair, S.; Fingerhut, B. P.; de Vivie-Riedle, R. Ground and Excited State Surfaces for the Photochemical Bond Cleavage in Phenylmethylphenylphosphonium Ions. *J. Phys. Chem. A* **2013**, *117*, 10626−10633.

(25) Pascual-Ahuir, J. L.; Silla, E. GEPOL: An Improved Description of Molecular Surfaces. I. Building the Spherical Surface Set. *J. Comput. Chem.* **1990**, *11*, 1047−1060.

(26) Pascual-Ahuir, J. L.; Silla, E.; Tuñon, L. GEPOL: An Improved Description of Molecular Surfaces. III. A New Algorithm for the Computation of a Solvent-Excluding Surface. *J. Comput. Chem.* **1994**, *15*, 1127−1138.

(27) Frisch, M. J.; Trucks, G. W.; Schlegel, H. B.; Scuseria, G. E.; Robb, M. A.; Cheeseman, J. R.; Scalmani, G.; Barone, V.; Mennucci, B.; Petersson, G. A. et al. *Gaussian 09*, revision A.02; Gaussian, Inc.: Wallingford, CT, 2009.

(28) Kuchling, H. *Taschenbuch der Physik*, 20th ed.; Carl Hanser Verlag: München, Germany, 2010.

(29) Hofmann, A.; de Vivie-Riedle, R. Adiabatic Approach for Ultrafast Quantum Dynamics Mediated by Simultaneously Active Conical Intersections. *Chem. Phys. Lett.* **2001**, *346*, 299−304.

(30) Werner, H.-J.; Knowles, P. J.; Knizia, G.; Manby, F. R.; Schütz, M.; Celani, P.; Korona, T.; Lindh, R.; Mitrushenkov, A.; Rauhut, G. et al. MOLPRO, version 2012.1, A Package of Ab Initio Programs, 2012.

(31) Tal-Ezer, H.; Kosloff, R. An Accurate and Efficient Scheme for Propagating the Time Dependent Schrödinger Equation. *J. Chem. Phys.* **1984**, *81*, 3967−3971.

(32) Wilson Jr., E. B.; Decius, J. C; Cross, P. C. *Molecular Vibrations*; McGraw-Hill: New York, 1955.

(33) Schaad, L.; Hu, J. The Schrödinger Equation in Generalized Coordinates. *J. Mol. Struct: THEOCHEM* **1989**, *185*, 203−215.

(34) Kowalewski, M.; Mikosch, J.; Wester, R.; de Vivie-Riedle, R. Nucleophilic Substitution Dynamics: Comparing Wave Packet Calculations with Experiment. *J. Phys. Chem. A* **2014**, *118*, 4661−4669.

1.3. Quantum dynamics in an explicit solvent environment: A combined QD/MD approach

So far, the solvent was treated in an implicit way by the dynamic continuum ansatz using Stokes' law, the dynamic viscosity as well as the expectation value of the velocity to calculate the frictional force acting on the reactant's dynamics [217, 221]. To further improve its treatment, the solvent cage can be described explicitly. In this section, the article "Quantum Dynamics in an Explicit Solvent Environment: A Photochemical Bond Cleavage Treated with a Combined QD/MD Approach" published in the *Journal of Chemical Theory and Computation* is presented [222], which introduces a new QD/MD approach to take into account the effects of the solvent cage on the bond cleavage. Thereby the solvent MeCN is treated by MD simulations with the program package Gromacs [223–225]. Randomly selected snapshots from the MD trajectories give an averaged picture of the atomistic solvent surrounding of the reactant, again $Ph_2CH\text{–}PPh_3{}^+$. As in the previous section 1.2, the time-dependent behavior of the reactant in its first excited state S_1 is modeled quantum dynamically on a spatial grid spanned by the two reactive coordinates r and ϕ (see section 1.1.2). Fig. 1.12 illustrates the new QD/MD approach. The interaction between the dissociating molecular fragments and the solvent molecules is again described by an additional potential term $\hat{V}_{\text{solv}}$ in the Hamiltonian:

$$\hat{H} = \hat{T}_{\text{nuc}} + \hat{V}_{\text{mol}} + \hat{V}_{\text{solv}}. \tag{1.32}$$

But in the present approach it explicitly contains the quantum chemically calculated interaction energy E_{sf} between each of the two fragments (the diphenylmethyl radical ($Ph_2CH^\bullet$) and $PPh_3^{\bullet+}$) and each MeCN molecule along the two-dimensional spatial grid spanned by r and ϕ [226]:

$$\hat{V}_{\text{solv}} = \sum_{i=1}^{N_{\text{solv}}} \sum_{j=1}^{N_{\text{frag}}} E_{\text{sf}} \left(q_1^{ij}, q_2^{ij}, q_3^{ij}, \ldots, q_6^{ij} \right), \tag{1.33}$$

with N_{frag} and N_{solv} being the number of fragments and solvent molecules respectively. The six degrees of freedom $\left\{ q_1^{ij}, q_2^{ij}, q_3^{ij}, \ldots, q_6^{ij} \right\}$ describe the relative orientation of one fragment and one solvent molecule in the three-dimensional space. The central results obtained in connection with the new combined QD/MD approach are:

- The MD simulations of the solvent cannot only be used for the description of the environment of the reactant, but also to rate the coordinates $\left\{ q_1^{ij}, q_2^{ij}, q_3^{ij}, \ldots, q_6^{ij} \right\}$ with respect to
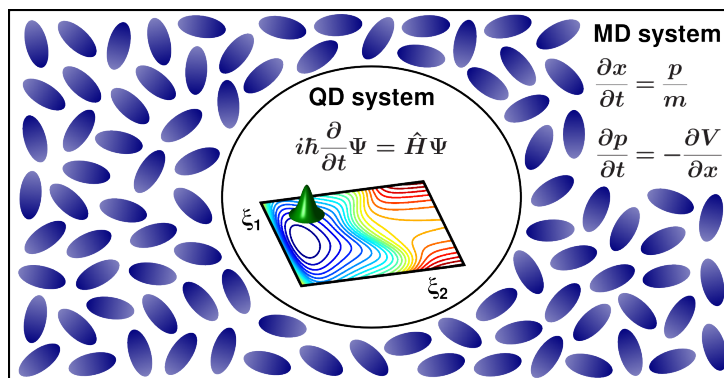

Figure 1.12.: Schematic illustration of the QD/MD approach. The solvent environment is described classically by MD simulations, the time-dependent behavior of the reactant within the solvent box is modeled quantum dynamically.

their importance for the solvent-fragment interaction energy E_{sf}. The coordinates themselves are then utilized to set up a quantum chemical database for the interaction energy to permit the calculation of the solvent potential.

- The sums of the molecular ONIOM potential V_{mol} (see fig. 1.7 b)) and the solvent potential V_{solv} of the respective snapshots reveal that two limiting cases concerning the possible reaction channels are possible. In the first case, one reaction channel is accessible, which leads toward the S_1/S_0 CoIn. In the second case, two different reaction pathways are evident. One thereof again pointing toward the CoIn while the other one opens a dissociative way in the S_1 state. The first case occurs about two time more often than the second one.

- The averaged picture from 50 different solvent configurations shows that after 1200 fs 83 % of the excited state population leaving the FC region is guided to the CoIn where the formation of the experimentally observed Ph_2CH^+ cations takes place. The remaining 17 % explores the dissociation channel in the S_1 state leading to radical pair formation.

Altogether, the explicit QD/MD approach leads to a more detailed microscopic picture of the influence of the solvent environment on the bond cleavage process in comparison with the dynamic continuum ansatz. In the presented example of $Ph_2CH-PPh_3{}^+$, it confirms the results of the dynamic continuum ansatz. Furthermore, it reveals the two different reaction pathways and clarifies the higher relevance of the one leading to the CoIn.

On the following pages the article "Quantum Dynamics in an Explicit Solvent Environment: A Photochemical Bond Cleavage Treated with a Combined QD/MD Approach" published in the *Journal of Chemical Theory and Computation* is reprinted with permission from *J. Chem. Theory Comput.* **11**, 1987-1995 (2015); copyright 2015 American Chemical Society. The supporting information is reprinted in appendix B.

Article

pubs.acs.org/JCTC

Quantum Dynamics in an Explicit Solvent Environment: A Photochemical Bond Cleavage Treated with a Combined QD/MD Approach
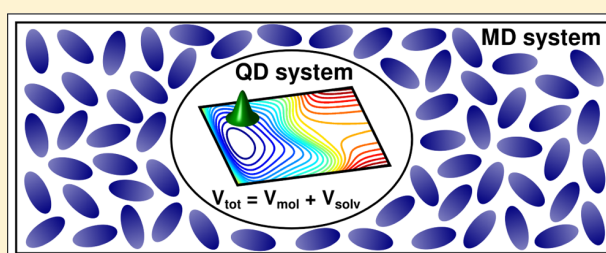
Sebastian Thallmair,[†,‡] Julius P. P. Zauleck,[†] and Regina de Vivie-Riedle*,[†]

[†]Department Chemie, Ludwig-Maximilians-Universität München, D-81377 München, Germany
[‡]Lehrstuhl für BioMolekulare Optik, Ludwig-Maximilians-Universität München, D-80538 München, Germany

Ⓢ *Supporting Information*

ABSTRACT: In quantum chemistry methods to describe environmental effects on different levels of complexity are available in the common program packages. Electrostatic effects of a solvent for example can be included in an implicit or explicit way. For chemical reactions with large structural changes additional mechanical effects come into play. Their treatment within a quantum dynamical context is a major challenge, especially when excited states are involved. Recently, we introduced a method that realizes an implicit description. Here, we present an approach combining quantum dynamics and molecular dynamics. It explicitly incorporates the solvent environment, whereby the electrostatic as well as the dynamic effects are captured. This new method is demonstrated for the ultrafast photoinduced bond cleavage of diphenylmethylphosphonium ions (Ph$_2$CH–PPh$_3^+$), a common precursor to generate reactive carbocations in solution.

1. INTRODUCTION

Solvents are an important aspect of every day chemistry.[1] While they are often only the reaction medium and do not participate directly in product formation, their electrostatic influence can stabilize or destabilize certain reaction pathways depending on the charge distribution along them.[2,3] In addition, dynamic effects of the solvent environment can emerge.[4,5] The solvent molecules directly interact with the molecular motion of the solute. In the case of ultrafast reactions like photochemical bond cleavage, where strong changes of the molecular structure occur, dynamic solvent effects are particularly important. The solute's fragments, moving apart, push into the solvent cage, and their initial motion is hindered. This can deviate their motion along a path less blocked by solvent molecules, and routes toward smaller energy gradients can come into play. In this way, the dynamics of the molecular system are substantially affected by the forces induced by the solvent cage and hence by its mechanical influence.

From a theoreticians point of view, the challenge is to treat the dynamic solvent effects during quantum dynamics (QD) simulations of photoinduced processes. A solution to treat this caging effect within the quantum mechanical framework in a continuum-like fashion was found recently.[5] The approach uses Stokes' law and the dynamic viscosity of the solvent to include the frictional force exerted on the molecular motion into the QD simulations. It was shown that the deceleration due to the environment is crucial for describing product formation during the bond cleavage of Ph$_2$CH–PPh$_3^+$. Another possibility for investigating the dynamic effect of the solvent environment is

to perform molecular dynamics (MD) simulations of the reactant in a box of solvent molecules. For photoinduced bond cleavage in ICN, parametrized potentials are available to simulate the excited state dynamics and to compare the gas phase with the behavior in different fluids, e.g., Xe,[6] Ar,[7,8] or H$_2$O.[9] Moskun et al. derived a microscopic picture of the rotational deceleration of CN$^\bullet$ radicals after photochemical bond cleavage in liquid Ar by comparing classical MD simulations and transient pump−probe anisotropy measurements.[10]

Here, we present a new method that includes an explicit, atomistically modeled solvent environment in QD simulations on quantum chemical potential surfaces. The method is demonstrated for QD on a regular grid, which offers high flexibility in its applications. We use the photoinduced bond cleavage of Ph$_2$CH–PPh$_3^+$ as an example. The selected solvent, acetonitrile (MeCN), does not react with the solute or its photoproducts. MD simulations are used to evaluate the solvent environment and to deduce the minimum number of coordinates required to describe the interaction between solvent and solute by means of a statistical analysis. The resulting solute solvent interaction energy is then calculated for each point of the ab initio potentials based on a quantum chemically precalculated database. Quantum dynamics are performed for many solvent arrangements, and their average leads to the overall picture of the bond cleavage.

This article is structured as follows: The description of our new QD/MD approach and the statistical rating of the coordinates for the solute solvent interaction are given in Section 2. This is followed by a brief summary of the computational details of the calculations (Section 3). The application of the QD/MD method to the photochemical bond cleavage of $Ph_2CH-PPh_3^+$ and the discussion of the results are presented in Section 4.

2. INCLUDING THE EXPLICIT ENVIRONMENT INTO QUANTUM DYNAMICS

2.1. Calculation of the Solvent Potential. Our new QD/MD approach combines QD with an atomistic modeling of the solvent environment. The surrounding of the reactant enters the QD via an additional potential term $\hat{V}_{solv}$ in the Hamiltonian, comparable to the dynamic continuum ansatz.[5] $\hat{V}_{solv}$ contains the interaction energy between the reactant and its ambient solvent molecules. Thus, the Hamiltonian $\hat{H}$ encompasses the operators for the kinetic energy of the nuclei ($\hat{T}_{nuc}$), the molecular potential energy ($\hat{V}_{mol}$), and the solvent potential ($\hat{V}_{solv}$)

$$\hat{H} = \hat{T}_{nuc} + \hat{V}_{mol} + \hat{V}_{solv}$$

$$= \hat{T}_{nuc} + \hat{V}_{tot} \tag{1}$$

The sum of $\hat{V}_{mol}$ and $\hat{V}_{solv}$ is the total potential $\hat{V}_{tot}$. The time evolution of the wave function Ψ of the system is described by the time-dependent Schrödinger equation

$$i\hbar \frac{\partial}{\partial t}\Psi = (\hat{T}_{nuc} + \hat{V}_{mol} + \hat{V}_{solv})\Psi \tag{2}$$

The solvent potential $\hat{V}_{solv}$ is the sum of all individual interaction energies E_{sf} between the N_{solv} solvent molecules and the reactant described by the wave function Ψ. Consistent with a standard force field, $\hat{V}_{solv}$ is described by two-body interactions. The reactant is partitioned into N_{frag} fragments, which, approximately, do not change their shape during the process. They are chosen to reflect the chemistry of the system, which means separation or reordering of the fragments model the major structural changes during the reaction. Each fragment contributes to $\hat{V}_{solv}$

$$\hat{V}_{solv} = \sum_{i=1}^{N_{solv}} \sum_{j=1}^{N_{frag}} E_{sf}(q_1^{ij}, q_2^{ij}, q_3^{ij}, ..., q_6^{ij}) \tag{3}$$

E_{sf} depends on the relative orientation of the considered pair of solvent molecule i and fragment j and is a function of six degrees of freedom q_n^{ij} with $n \in \{1, 2, ..., 6\}$, i.e., one distance and five angular coordinates (Figure 1). This is the number necessary to describe the relative orientation of two three-dimensional objects in a three-dimensional space. Each object requires three noncollinear rotational axes (R_{A1}, R_{A2}, R_{A3} and R_{B1}, R_{B2}, R_{B3}) which can be chosen arbitrarily. If one axis of each object is collinear with the connecting vector between both centers of mass, which is the case for R_{A2} and R_{B2} in Figure 1, then one redundant degree of freedom can be removed. In addition, the distance between the centers of mass is necessary. Thus, altogether, six degrees of freedom fully describe the relative orientation of the solvent molecule i and the fragment j and constitute the orientation space.

The potential landscape for the arrangement of the solvent environment around a solute is very flat and has a large number
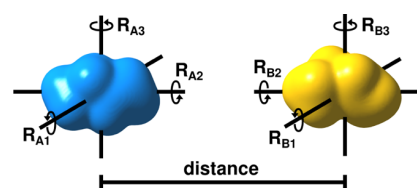

Figure 1. Illustration of the coordinates necessary to describe the relative orientation of two three-dimensional objects in three-dimensional space. One of the two rotational axis, R_{A2} and R_{B2}, can be left out if they are collinear with the connecting vector of both objects. Altogether, six degrees of freedom describe the relative orientation of both objects.

of energetically accessible regions around local minima at room temperature. This makes it nearly impossible to optimize a representative number of configurations around a medium-sized molecule. A convenient way to cover the thermodynamically accessible configuration space is to perform MD simulations of the reactant in a box of solvent molecules. From these, a sufficiently large number of snapshots along the trajectories represents the surrounding solvent. The MD simulations should be carried out for the reactant in its electronic ground state. This is also reasonable for the initial setting of the excited state dynamics, especially if ultrashort laser pulses are used for excitation. On this time scale, the nuclei of the solvent molecules cannot react to the electronic changes of the solute.[11,12] For each snapshot of the MD trajectories, the solvent potential V_{solv} has to be calculated, which is then used for a QD simulation. In addition, the QD simulations require the potential energy surfaces V_{mol} of the reactant, which are set up on a grid of selected coordinates. The Hamiltonian in eq 1 allows the setup in full dimensions; in our working example, we will follow the reaction in specially designed reactive coordinates ξ_i. For each grid point, the interaction energy E_{sf} between reactant and solvent molecules is evaluated in the six-dimensional orientation space by reading the current structure of the reactant and placing it at the respective position in the solvent box for the given snapshot (Figure 2). To include not only the steric, i.e., mechanical, but also electrostatic effects of the solvent, E_{sf} is calculated quantum chemically. The sum of all E_{sf} yields the solvent potential V_{solv} for this grid point (eq 3). This procedure is repeated for the whole grid, leading to a V_{solv} mapped to the coordinate space of the potential energy surface V_{mol}. The sum of both yields the total potential V_{tot} for the reaction in solution. To permit the quantum chemical calculation of E_{sf}, we precalculate the interaction between the reactant and one solvent molecule for all possible relative orientations on a regular space grid in the six-dimensional orientation space. The energy for any arbitrary orientation is then obtained by interpolation.

The QD calculations are carried out on all thus-constructed V_{tot} individually. The average of all QD simulations reflects the impact of the solvent surrounding on the investigated process. It is calculated by summation of the absolute squares of the propagated wave functions Ψ_i using the different solvent potentials of the N_{snap} snapshots

$$|\Psi_{av}|^2 = \frac{1}{N_{snap}} \sum_{i=1}^{N_{snap}} |\Psi_i|^2 \tag{4}$$

An important issue to consider is the ratio of the time scales for the motion of the reactant and the motion of the solvent
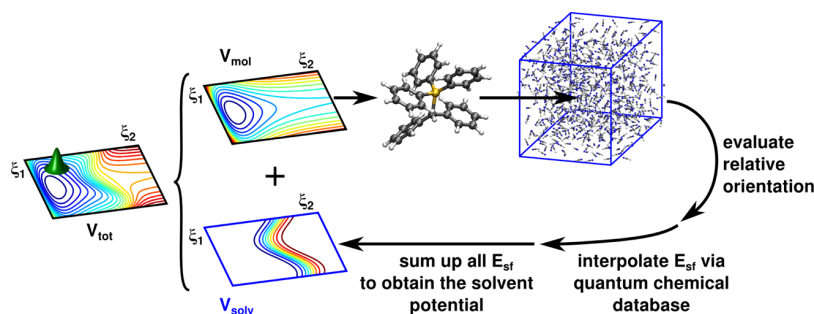
Figure 2. Flowchart visualizing the procedure to calculate the solvent potential V_{solv} based on the reactive coordinates ξ_i of the ab initio molecular potential V_{mol}. For all combinations of ξ_1 and ξ_2, a solute molecule is placed into the cavity in the solvent box, the relative orientation between the solvent molecules and the fragments is evaluated, and E_{sf} is interpolated via the quantum chemical database. Finally, all E_{sf} are summed for each (ξ_1, ξ_2) to yield V_{solv}, which is then added to V_{mol}. The resulting V_{tot} is used for the QD simulations.

molecules. In general, three different scenarios are possible: Either the molecular reaction is much faster than the motion of the solvent molecules or vice versa or the dynamics of both systems happens on a comparable time scale. In the first two cases, one can take advantage of the separation of time scales. In case one, the position of the solvent molecules at the beginning of the molecular reaction is decisive for the whole process and, as a first approximation, the solvent motion is negligible. This is the case for ultrafast photoinduced processes on the hundreds of femtoseconds time scale, like photochemical bond cleavage[5,13−15] or photoisomerization.[16,17] In the second case, one can average over the solvent dynamics. Thus, only one solvent potential V_{solv} is experienced by the reactant. In the third case, when both dynamics are comparably fast, no separation of time scales is possible and both systems have to be propagated in parallel. An example for this case are vibrationally mediated processes involving ladder climbing[18,19] or bimolecular processes in the ground state.[20]

2.2. Evaluating the Coordinates Relevant for the Relative Orientation of Solvent and Fragment. The MD simulations can be used not only to take the snapshots needed for a statistical solvent description but also to facilitate rating the five rotational axes with regard to their importance for the interaction energy E_{sf}. The decisive criterion for their rating is the standard deviation σ_{q_n} of the probability distribution of E_{sf} for each coordinate q_n. The larger σ_{q_n}, the more important is the coordinate q_n. Note that the standard deviation depends on the temperature T, as each MD simulation sketches a Boltzmann distribution. Thus, the obtained rating is valid only for the given temperature T.

The standard deviation σ_{q_n} for a chosen coordinate q_n can be calculated starting from the empirical distribution function $F_m(q_n)$ for a random sample of m elements[21]

$$F_m(q_n) = \frac{1}{m} \sum_{i=1}^{m} 1\{q_{ni} \leq q_n\} \tag{5}$$

with q_{ni} being the coordinate values from the random sample. $F_m(q_n)$ is the fraction of the m elements of the sample that fulfill the condition $q_{ni} \leq q_n$. For the case of an infinite sample size, the derivative of $F_m(q_n)$ is the probability distribution $P(q_n)$

$$P(q_n) = \frac{\partial}{\partial q_n} F_m(q_n) \tag{6}$$

With the integral $\int_{q_0}^{q_0+\Delta q} P(q_n)\,dq_n$, the probability for q_n to take a value within the interval $[q_0; q_0 + \Delta q]$ can be evaluated. The probability distribution $P(q_n)$ is Boltzmann distributed, as it is extracted from an MD simulation at a particular temperature T

$$P(q_n) = \frac{1}{Z_{q_n}} \exp\left(-\frac{E_{sf}(q_n)}{k_B T}\right) \tag{7}$$

with $1/Z_{q_n}$ being the normalization factor and Z_{q_n} the canonical partition function. The usual degeneracy factor is not present in eq 7 because, first, it is already included due to the explicit dependence of E_{sf} on the coordinate q_n, which compensates for orientations with the same E_{sf} value. Second, all coordinate-dependent degeneracies can be removed beforehand by ensuring that each orientation is uniquely defined in the orientation space. To obtain $E_{sf}(q_n)$, we take the logarithm of eq 7. As for the coordinate rating, we are interested only in the relative variation of $E_{sf}(q_n)$ along q_n and not in the absolute values, the expression can be simplified by shifting $E_{sf}(q_n)$ by $\ln(Z_{q_n})\,k_B T$

$$\begin{aligned} E'_{sf}(q_n) &= E_{sf}(q_n) + \ln(Z_{q_n})\,k_B T \\ &= -\ln(P(q_n))k_B T \end{aligned} \tag{8}$$

Equation 8 provides an elegant way to obtain the potential landscape for the interaction energy $E'_{sf}(q_n)$ from the MD simulation without explicit calculation. The accessibility of the different energy states depends on the temperature. Thus, the next step is the transformation of $E'_{sf}(q_n)$ into the probability distribution $P(E'_{sf})$. The probability that a specific energy state is occupied is given by the Boltzmann distribution, where the density of states $n(E'_{sf})$ takes the place of the degeneracy factor

$$P(E'_{sf}) = \frac{1}{Z_{E'_{sf}}} \exp\left(-\frac{E'_{sf}}{k_B T}\right) n(E'_{sf}) \tag{9}$$

with $Z_{E'_{sf}}$ being the canonical partition function. The density of states is the sum of the reciprocal absolute gradients of $E'_{sf}(q_n)$ at all values of q_n for which $E'_{sf}(q_n) = E'_{sf}$ multiplied by $N(q_n)$

$$n(E'_{sf}) = \sum_{E'_{sf}(q_n)=E'_{sf}} \left| \frac{\partial E'_{sf}(q_n)}{\partial q_n} \right|^{-1} N(q_n) \tag{10}$$

$N(q_n)$ is a coordinate-dependent degeneracy factor. For the spherical coordinates, as used here to describe the relative

orientation between the fragments and the solvent, the factor takes into account the different accessible surface areas of a sphere depending on the polar angle.

Figure 3a shows an exemplary probability distribution $P(q_n)$ along an angular coordinate q_n. Following eq 8, we extract the
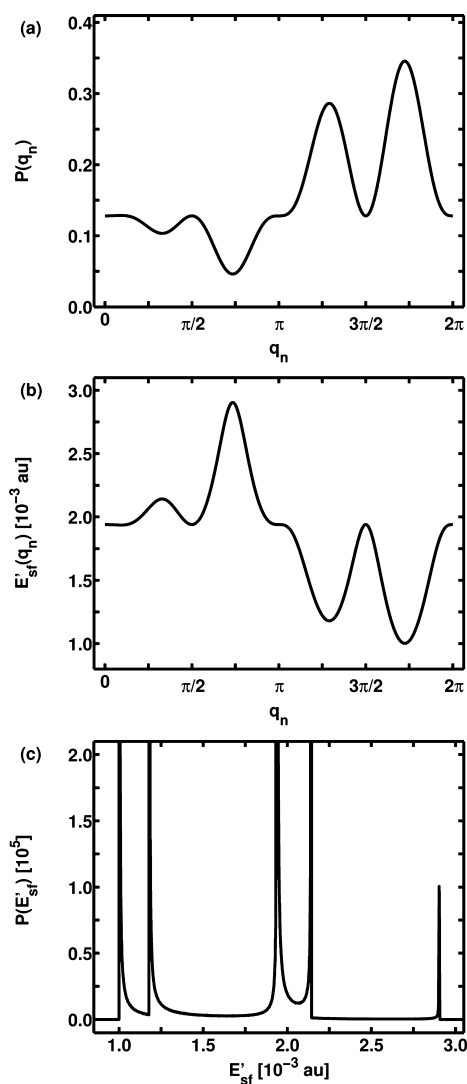
Figure 3. (a) Probability distribution $P(q_n)$ along an angular coordinate q_n. (b) $E'_{sf}(q_n)$ along q_n calculated from $P(q_n)$ at a temperature of $T = 298$ K according to eq 8. As expected, the maxima in the probability distribution $P(q_n)$ correspond to minima in $E'_{sf}(q_n)$. (c) Probability distribution for the energy $P(E'_{sf})$ resulting from $E'_{sf}(q_n)$ depicted in (b) at $T = 298$ K determined according to eq 9.

underlying $E'_{sf}(q_n)$ (Figure 3b). As expected, the maxima in $P(q_n)$ correspond to minima in $E'_{sf}(q_n)$. The probability distribution $P(E'_{sf})$ is calculated from eq 9 and depicted in Figure 3c. It shows the typical structure of a density of states. The stationary points of $E'_{sf}(q_n)$ lead to the poles of $P(E'_{sf})$ due to the reciprocal absolute gradient in eq 10. The broader the energy range of $P(E'_{sf})$, the larger the standard deviation σ_{q_n} gets. In Figure 3c, the most relevant range is from 1×10^3 to 2.2×10^3 au. With the expectation value of the energy $\overline{E'_{sf}}$

$$\overline{E'_{sf}} = \int_{-\infty}^{\infty} E'_{sf} \cdot P(E'_{sf}) \, dE'_{sf} \tag{11}$$

finally, the standard deviation σ_{q_n} can be calculated as the square root of the variance $\mathrm{Var}(E'_{sf})$

$$\sigma_{q_n} = \sqrt{\mathrm{Var}(E'_{sf})} = \sqrt{\int_{-\infty}^{\infty} (E'_{sf} - \overline{E'_{sf}})^2 P(E'_{sf}) \, dE'_{sf}} \tag{12}$$

3. COMPUTATIONAL DETAILS

For all MD simulations, the program package Gromacs[22,23] (version 3.3.2) was used. The solute $Ph_2CH-PPh_3^+$ was described by the all-atom version of the OPLS (optimized potentials for liquid simulations) force field.[24] The atomic charges were determined quantum chemically (DFT, M06-2X, 6-31G(d)) with the program package Gaussian09.[25] For the liquid MeCN, force field parameters developed by Edwards et al.[26] were used that reproduced the viscosity of MeCN well.[27] We used a cubic simulation box with an edge length of 40 Å containing 709 MeCN molecules. The time evolution was calculated using a time step of 1 fs. The temperature was kept constant at 298 K by a Berendsen thermostat. After propagating the system for 10 ps while monitoring the temperature to ensure successful equilibration, snapshots were taken every 200 fs.

The interaction energy E_{sf} between a fragment and a MeCN molecule was evaluated quantum-chemically at the DFT (M06-2X, 6-31G(d)) level of theory with the program package Gaussian09.[25] The molecular potential $\hat{V}_{mol}$ of $Ph_2CH-PPh_3^+$ was calculated with the our own n-layered integrated molecular orbital and molecular mechanics (ONIOM) method.[28−30] The high-level system (thicker drawn part of $Ph_2CH-PPh_3^+$ in Figure 4, top) was calculated at the CASSCF(10,10) level of theory with the program package Molpro;[31] the low-level system additionally contains the thinner phenyl rings and is calculated at the DFT (M06-2X) level of theory using Gaussian09.[25] Throughout all calculations, the basis set 6-31G(d) was employed. This approach was already employed and tested in ref 5. The coordinates for the quantum dynamical calculations are the C1−P distance r and the angle ϕ between the atoms P, C1, and the dummy atom X, which is introduced to ensure that the conical intersection (CoIn) lies in the coordinate space. Along the dissociation coordinate r, which describes the distance between the phosphorus atom P and the carbon atom C1 (Figure 4, top), the potential energy surface accounts for the major relaxation processes. Those are given by the lowering of the hybridization from sp^3 to sp^2 at the C1 atom of the methyl group as well as the rotation of the phenyl rings and bond length changes.

The quantum dynamical simulations were carried out by a homemade program that solves the time-dependent Schrödinger equation on a spatial grid using the Chebychev propagation scheme[32] and the G-matrix method for the kinetic operator $\hat{T}$[33−35] (for details, see the Supporting Information). At the beginning of the propagation, the vibrational ground state wave function $v = 0$ of the electronic ground state S_0 was placed on the S_1 state. It was shifted slightly to a shorter C1−P distance to ensure that the main part of the wave packet crosses the barrier next to the Franck−Condon (FC) region in the gas phase. This is necessary because the two-dimensional coordinate space does not include the minimal barrier.[36] To include it, a third coordinate would be required, which would lead to an enormous increase in the simulation time.

4. BOND CLEAVAGE OF $PH_2CH-PPH_3^+$ IN AN EXPLICIT SOLVENT ENVIRONMENT

Our interest lies in the photochemistry of medium-sized organic molecules, in particular in photoinduced dissociative processes. A well-suited example for the significance of the dynamic solvent effect is the bond cleavage of $Ph_2CH-PPh_3^+$ in MeCN[4,5] for which we apply our new QD/MD approach. Salts like $Ph_2CH-PPh_3^+X^-$ are common precursors for the generation of diphenylmethyl cations (Ph_2CH^+) as intermediates in polar and moderately polar solvents (Figure 4).[37]
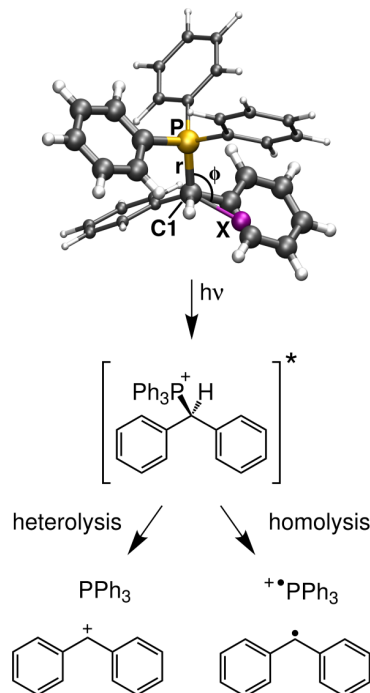

Figure 4. Reaction scheme for the photochemical bond cleavage in diphenylmethyltriphenylphosphonium ions $Ph_2CH-PPh_3^+$. The ground state has heterolytic dissociation character, leading to Ph_2CH^+ and PPh_3 as photoproducts; the character of the first and second excited state is homolytic, generating $Ph_2CH^\bullet$ and $PPh_3^{\bullet+}$. The optimized geometry of $Ph_2CH-PPh_3^+$ is depicted at the top. The potential energy surface used in the quantum dynamical simulations is calculated at the ONIOM level of theory. The high-level system $PhCH_2-PH_2Ph^+$ of the ONIOM calculations contains the thicker drawn part of $Ph_2CH-PPh_3^+$; in the low-level system $Ph_2CH-PPh_3^+$, the thinner drawn phenyl rings are taken into account additionally. The coordinates for the quantum dynamical calculations are the C1−P distance r and the angle ϕ between the atoms P, C1, and the dummy atom X, which is introduced to ensure that the CoIn lies in the coordinate space.

Ultrafast broadband transient absorption experiments revealed that almost exclusively diphenylmethyl cations are formed if the counterion X^- is nonoxidizable (e.g., BF_4^- or SbF_6^-).[38] Quantum chemical investigations showed that after a local $\pi-\pi^*$excitation on the PPh_3 moiety the C1−P bond cleavage can take place by crossing a small barrier in the first excited state S_1.[36] In the dissociation limit, the S_1 state leads to the formation of a radical pair $Ph_2CH^\bullet$ and $PPh_3^{\bullet+}$ (homolytic bond cleavage), whereas in the ground state S_0, the desired Ph_2CH^+ cations and PPh_3 are generated (heterolytic bond cleavage). QD simulations clarified that for the bond cleavage

in $Ph_2CH-PPh_3^+$ ions the dynamic solvent effect is essential. By including the frictional force of the solvent implicitly, we were able to explain the experimentally observed initial product formation on the several hundreds of femtoseconds time scale.[4,5,38] The applied dynamic continuum ansatz combines Stokes' law with the dynamic viscosity of the solvent to model the deceleration by the solvent cage.[5] This enables the system to reach a CoIn, which connects both product channels and allows the fast generation of Ph_2CH^+ cations.[5]

The presented QD/MD approach goes one step further and includes an atomistic modeling of the solvent cage. Here, the MeCN solvent cage is obtained from MD simulations, during which the methyl group of MeCN is treated as a united atom.[26] If the bending is neglected, then MeCN can be treated as linear. One advantage of this simplification is that the number of coordinates in the orientation space can be reduced to five if one of the rotational axes of MeCN is selected to be collinear with the molecular axis. During the QD calculations, the positions of the solvent molecules around the solute $Ph_2CH-PPh_3^+$ are frozen, as in scenario one (introduced in Section 2.1). This is legitimized by the fact that the bond cleavage takes place within 200−300 fs and is faster than the motion of the solvent molecules in the thermodynamic equilibrium. Thus, the initially experienced solvent potential V_{solv} is crucial for the time evolution of the wave packet, although the shape of the solvent cage will change during the reaction process.

The five coordinates $|\vec{r}_{sf}|$, α_s, α_f, β_s, and β_f to describe E_{sf} in the orientation space are presented in Figure 5. $|\vec{r}_{sf}|$ is the
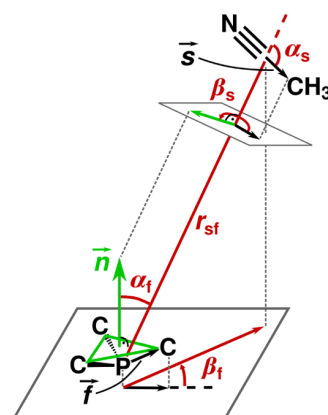
Figure 5. Definition of the five coordinates r_{sf}, α_s, α_f, β_s, and β_f describing the relative orientation of one MeCN and the PPh_3 moiety. For the sake of simplicity, only the C atoms of the phenyl rings that are bound to the P atom are shown; the remaining atoms are omitted.

length of the connecting vector between the center of mass of MeCN and the central atom of the two fragments: the P atom in the case of PPh_3 and the methyl C atom for Ph_2CH. The remaining four coordinates are angles describing the rotation of the fragment (α_f, β_f) and of the solvent (α_s, β_s). In detail, α_f specifies the angle between $\vec{r}_{sf}$ and the normal vector $\vec{n}$ of the plane (green triangle) defined by the three C atoms attached to the P atom. It is defined in the interval $[0;\pi]$. β_f characterizes the rotation of the PPh_3 fragment around $\vec{n}$. To this, we use the auxiliary vector $\vec{f}$, which points from the P atom to one C atom. β_f is then defined as the angle (counterclockwise) between the projections of the vectors $\vec{r}_{sf}$ and $\vec{f}$ into the

C−C−C plane. The angle β_f takes values between $[0;2\pi[$. α_s is the angle between $\overrightarrow{r_{sf}}$ and the vector $\vec{s}$, which points from the center of mass of MeCN to its methyl group. The angle α_s is defined in the interval $[0;\pi]$. β_s indicates the rotation of MeCN around $\overrightarrow{r_{sf}}$ and is defined in the interval $[0;2\pi[$. It is calculated projecting the vectors $\vec{s}$ and $\vec{n}$ into a plane perpendicular to $\overrightarrow{r_{sf}}$. The angle between these projected vectors (again in counterclockwise direction) is β_s. For the second fragment, Ph$_2$CH, generated in the bond cleavage, the methyl C atom replaces the P atom and one atom of the C−C−C plane is exchanged by the H atom. The selected coordinates are orthogonal and guarantee that each position in the orientation space is uniquely defined by one coordinate quintuple.

In the next step, the importance of the five coordinates for the interaction energy E_{sf} has to be evaluated. The significance of the distance coordinate is obvious; the rating of the four angular coordinates has to be determined according to the standard deviations σ_{q_n}. For this, 2500 snapshots along MD trajectories were analyzed. The orientations of all MeCN molecules with a maximum distance of 8.0 Å between the two nearest atoms of the fragment and the solvent molecule were calculated. Beyond 8.0 Å, no influence of the structure of the solute on the solvent orientation was observed. As E_{sf} depends on all five coordinates, orientational effects along one coordinate can be compensated by another one. This happens when the preferred value for one coordinate depends systematically on the value of one or more other coordinates. To ensure that no compensation of orientations occurs for the tested coordinate, we divided the interval of the remaining angular coordinates in half and compared the shape of the obtained probability distributions $P(q_n)$ of both parts with each other and the initial shape. If they are similar enough, then no further dividing is necessary; if they are not, then the procedure is repeated for both halves. When convergence of the shape is reached in step i, the $(i-1)$th partitioning is used to calculate the m related standard deviations $\sigma_{q_n}^j$ for the m resulting intervals with $j \in \{1, 2, ..., m\}$. The standard deviation σ_{q_n} for the whole domain of definition is calculated via the average of the variances $(\sigma_{q_n}^j)^2$ weighted by the proportion of elements N_j/N_0 in the interval j according to

$$\sigma_{q_n} = \sqrt{\sum_{j=1}^{m} \frac{N_j}{N_0}(\sigma_{q_n}^j)^2} \tag{13}$$

where N_j is the number of elements in the interval j and $N_0 = \sum_{j=1}^{m} N_j$ (for details, see the Supporting Information). As the probability distributions are quite noisy, a comparison of the raw data is difficult. Thus, $P(q_n)$ was smoothed by applying a low-pass Butterworth filter before being normalized. Additionally, we calculated the integral of the absolute difference of the normalized probability distributions to check that the absolute deviations are not too large. All values were below 12% (for details, see the Supporting Information).

The values of the standard deviations σ_{q_n} along the four angular coordinates calculated following eq 13 are given in Table 1. Their values are between 7.21×10^{-5} and 2.71×10^{-4} au. In general, the ones for the PPh$_3$ moiety are slightly larger than the ones for Ph$_2$CH. This could be due to the less sterically demanding H atom that replaces one phenyl ring, which leads to a flatter potential around the H atom and thus

Table 1. Standard Deviation σ_{q_n} of the Interaction Energy between the Molecular Fragment and MeCN along the Four Angular Coordinates α_s, β_s, α_f, and β_f

fragment	σ_{α_s} (au)	σ_{β_s} (au)	σ_{α_f} (au)	σ_{β_f} (au)
PPh$_3$	1.58×10^{-4}	7.61×10^{-5}	1.62×10^{-4}	2.71×10^{-4}
Ph$_2$CH	1.28×10^{-4}	7.21×10^{-5}	1.03×10^{-4}	1.34×10^{-4}

reduces the standard deviation in the probability distributions $P(E_{sf})$. We carefully checked the influence of the filtering process on the values of σ_{q_n}. They change slightly, but the observed trends are fairly robust.

For the PPh$_3$ moiety, σ_{β_s} has the smallest value. The other values are at least twice as large; the largest one is observed for σ_{β_f}. A similar picture is obtained for the Ph$_2$CH moiety. Here also, σ_{β_s} has the smallest value. Since for both fragments σ_{β_s} has the smallest value, β_s is the least important coordinate for the interaction energy E_{sf}. As the E_{sf} values entering the QD simulations are evaluated quantum chemically, the reduction of its degrees of freedom from $n = 5$ to $n = 4$ leads to a significant reduction in computational time. Thus, the solvent potential $\hat{V}_{solv}(r,\phi)$ is approximated as

$$\hat{V}_{solv}(r, \phi)$$
$$= \sum_{i=1}^{N_{solv}} \sum_{j=1}^{2} E_{sf}\left(\left|\overrightarrow{r_{sf}^{ij}}(r, \phi)\right|, \alpha_s^{ij}(r, \phi), \alpha_f^{ij}(r, \phi), \beta_f^{ij}(r, \phi)\right) \tag{14}$$

We calculated $V_{solv}(r,\phi)$ for 50 snapshots of the MD trajectories with a time interval of 200 fs between the snapshots and simulated the bond cleavage process quantum dynamically for each of the obtained V_{tot}. For reference, we show the molecular potential $V_{mol}(r,\phi)$ of the first excited state S$_1$ without any solvent influence in Figure 6. The FC point is
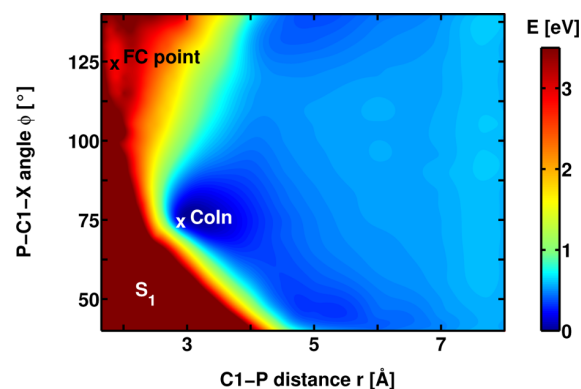
Figure 6. Molecular potential V_{mol} of the first excited state S$_1$ of Ph$_2$CH−PPh$_3^+$ calculated at the ONIOM (CASSCF(10,10)/M06-2X/6-31G(d)) level of theory. The potential is shown up to a C1−P distance of $r = 8.0$ Å to clarify that V_{mol} has no barrier along the r direction.

located at a C1−P distance of $r = 1.87$ Å and a P−C1−X angle of $\phi = 125°$, the S$_0$/S$_1$ CoIn at $r = 2.9$ Å and $\phi = 75°$,[5] and the global S$_1$ minimum next to the S$_0$/S$_1$ CoIn.

The left column of Figure 7 depicts two selected MD snapshots. The solute Ph$_2$CH−PPh$_3^+$ is drawn in a space-filling representation; the MeCN solvent molecules are shown in a ball and stick representation. The white ball represents the
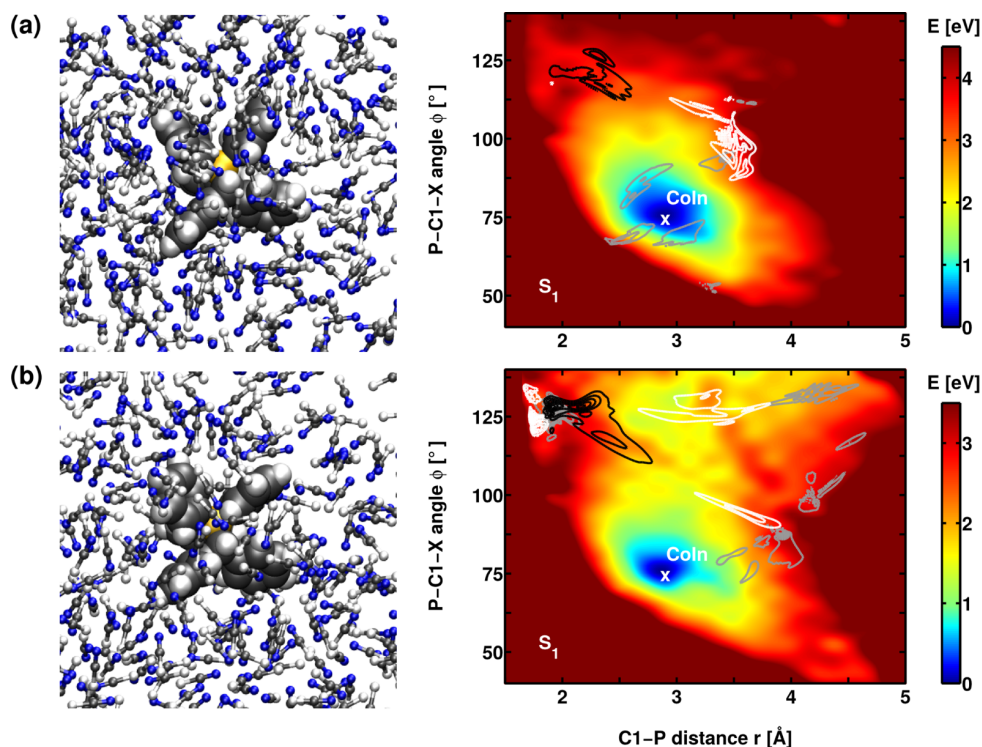
Figure 7. Two selected snapshots of Ph$_2$CH−PPh$_3^+$ in a box of MeCN taken from the MD simulation (left column). The solute Ph$_2$CH−PPh$_3^+$ is drawn in a space-filling representation; the MeCN solvent molecules are shown in a ball and stick representation. The white ball represents the methyl group, the gray one the C atom and the blue one the N atom. The corresponding total potentials $V_{tot}(r,\phi)$ are depicted in the right column together with three snapshots of the propagated wave packets. For (a), they are taken at 90 fs (black isolines), 180 fs (white isolines), and 240 fs (gray isolines), and for (b), at 90 fs (black isolines), 160 fs (white isolines), and 240 fs (gray isolines) after starting the propagation in the FC region. In the total potential V_{tot} shown in (a), the whole wave packet explores the channel toward the global minimum and oscillates around the CoIn. In contrast, the wave packet in V_{tot} depicted in (b) splits and explores both offered dissociation pathways.

methyl group, the gray one the C atom and the blue one the N atom. The right column of Figure 7 shows the total potential V_{tot} of the first excited state S$_1$ for the depicted solvent arrangements together with three snapshots from the wave packet evolution. The snapshots in Figure 7a are taken at 90 fs (black isolines), 180 fs (white isolines), and 240 fs (gray isolines), and in Figure 7b, at 90 fs (black isolines), 160 fs (white isolines), and 240 fs (gray isolines) after starting the propagation in the FC region of the S$_1$ state.

First, we focus on the two resulting V_{tot}, which exhibit significant differences in their topography. The solvent potential generates a barrier at large C1−P distances of approximately $r = 3.5$ Å, where the dissociating fragments approach the solvent cage. This leads to the steep rise of the total potential, which is not present in the purely molecular potential V_{mol} (Figure 6). The first V_{tot} (Figure 7a, right) has one valley pointing toward the CoIn. In contrast, the second V_{tot} (Figure 7b, right) offers two reaction channels. One points toward the CoIn, and the other one leads away from the CoIn. These examples represent the two limiting cases found in the 50 snapshots taken from the MD trajectories. The first case occurs about two times more often than the second.

The quantum dynamics of the bond cleavage is visualized by the selected snapshots from the wave packet propagation. In Figure 7a, the wave packet leaves the FC area about 90 fs after the propagation has been started (black isolines). Subsequently, it hits the potential barrier of the solvent cage at about $r = 3.7$ Å and $\phi = 100°$ (white isolines). Then, it evolves toward the

CoIn and oscillates back and forth around the global minimum of V_{tot}. The time evolution of the wave packet in the second solvent arrangement (Figure 7b) differs fundamentally. After 90 fs, a part of the wave packet crosses the barrier in the FC region and moves toward a larger C1−P distance (black isolines). Compared to the propagation in Figure 7a, a significant fraction stays in the FC minimum. The part overcoming the barrier already reveals a splitting toward the two reaction channels. At 160 fs, the branching of the wave packet is completed (white isolines). The upper fraction moves toward larger ϕ values and dissociates in the first excited state, leading to the formation of radicals (gray isolines). The lower part hits the potential barrier at around $r = 4.0$ Å and $\phi = 90°$ and is guided toward the CoIn with the ground state.

The two examples demonstrate the importance of the individual arrangement of the solvent cage. It has a significant impact on the direction in which the wave packet evolves and whether a splitting occurs. The second reaction channel opens when no solvent molecules hinder the motion of the reactant along that channel. This situation can be captured only by a microscopic description of the solvent environment, as provided by our QD/MD ansatz.

For an overall picture of the bond cleavage, we averaged the wave packet propagations for the 50 different environments according to eq 4. As we found convergence in the population dynamics, 50 snapshots proved to be a sufficiently large number (for details, see the Supporting Information). To analyze the population distribution, we separated the two-dimensional

potentials in three areas. They correspond to the FC region ($r \leq 2.1$ Å and $\phi > 105°$; gray rectangle in the inset of Figure 8),
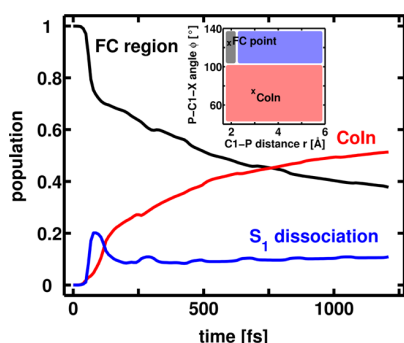
Figure 8. Population dynamics for the QD simulation of the bond cleavage of $Ph_2CH-PPh_3^+$ averaged over 50 different solvent arrangements taken from MD trajectories. The population in the FC region (black line) is located in the gray rectangle in the inset, the population in the S_1 dissociation area (blue line) in the blue rectangle, and the population around the CoIn (red line) in the red rectangle.

the dissociation channel in the S_1 state ($r > 2.1$ Å and $\phi > 105°$; blue rectangle), and the area around the CoIn ($\phi \leq 105°$; red rectangle). To start the propagation, the vibrational ground state wave function $v = 0$ is transferred to the S_1 state. Accordingly, the population in the FC region is one at $t = 0$ fs (black line). Within the first 70 fs, 30% of the population leave the FC region with an initial momentum along the r direction, observable in the sudden increase of population in the S_1 dissociation channel (blue line). At about 100 fs, the averaged wave packet is deflected toward the CoIn. Correspondingly, the population now increases in this area (red line). This increase continues moderately while the S_1 dissociation channel stays constant. After 1200 fs, the population is distributed as follows: 40% is still located in the FC region, 10% dissociated in the first excited state, and 50% reached the CoIn, from where the population can relax to the ground state[5,36] to form the experimentally observed Ph_2CH^+ cations. The explicit treatment of the solvent provides a passage toward the CoIn similar to the results from the dynamic continuum ansatz.[5] Furthermore, it captures the individual arrangements of the solvent cage and, based on this, reveals the formation of different reaction channels.

5. SUMMARY AND CONCLUSIONS

We presented our newly developed QD/MD method to include the explicit solvent environment in reactive QD simulations. The method merges MD simulations of the reactant in a box of solvent molecules with QD calculations of the reactant's dynamics. The interaction between the QD system and the solvent molecules is incorporated in the Hamiltonian for the QD calculations. The interaction energy E_{sf} between the reactant and a solvent molecule depends on their relative orientation, which, in general, can be described by six degrees of freedom q_n with $n \in \{1, 2, ..., 6\}$ in the orientation space. We showed that MD trajectories also provide the necessary information to calculate the standard deviation σ_{q_n} of the interaction energy $E_{sf}(q_n)$ as a decisive criterion for rating the coordinates q_n. With this procedure, the least relevant degrees of freedom can be eliminated to reduce the

computational cost for the precalculation of the quantum chemical database.

To demonstrate the impact of the solvent cage treated explicitly with our new QD/MD approach, we chose the photoinduced bond cleavage of $Ph_2CH-PPh_3^+$. It has been shown that consideration of dynamic solvent effects during the quantum dynamical simulation of the process is crucial to explain the experimentally observed heterolytic bond cleavage generating Ph_2CH^+ cations.[5,38] We performed MD simulations of one $Ph_2CH-PPh_3^+$ in a box of MeCN. The rating of the coordinates in the orientation space led to four necessary coordinates: the distance coordinate r_{sf} and three angular coordinates α_s, α_f, and β_f. With them, we calculated the solvent potential $V_{solv}(r,\phi)$ for 50 snapshots of the MD simulations and performed QD simulations for each of the obtained total potentials $V_{tot}(r,\phi)$. The solvent cage hinders the free dissociation in the S_1 state. In the microscopic description, two different dissociation channels emerged. One leads to dissociation in the S_1 state and homolytic bond cleavage, and the other one leads to a S_0/S_1 CoIn, where the system can relax to the ground state, which has heterolytic dissociation character. The average over all QD simulations gives the overall picture of the photoinduced bond cleavage. 83% of the excited state population that leaves the FC region approaches the CoIn, where the formation of Ph_2CH^+ cations can take place. The remaining 17% pass through the second dissociation channel of the homolytic bond cleavage. Thus, our new QD/MD approach provides a passage toward the CoIn similar to the results from the dynamic continuum ansatz[5] and explains the experimental observations for the initial product formation.[38] Compared to the dynamic continuum ansatz, it goes one step further and gives a more detailed microscopic picture of the whole process. It allows for the description of different reaction channels reflecting the individual arrangements of the solvent cage. Furthermore, the flexibility of the solvent cage with temperature and solvent composition can be modeled.

The presented results demonstrate encouragingly that a combination of MD and QD simulations is an appropriate tool to describe photoinduced ultrafast molecular processes in a complex environment. The next step for future development is the inclusion of the feedback of the QD system on the motion of the classically treated solvent molecules. This will further broaden the application range to reactions where the dynamics of the reactant and solvent are on a comparable time scale.

■ ASSOCIATED CONTENT

ⓢ Supporting Information

Details of the quantum dynamical simulations, the partitioning of the coordinates in the orientation space to calculate the probability distributions $P(q_n)$, the convergence of the population dynamics, a qualitative comparison of the required computing time, and geometries in *xyz* format. This material is available free of charge via the Internet at http://pubs.acs.org.

■ AUTHOR INFORMATION

Corresponding Author
*E-mail: regina.de_vivie@cup.uni-muenchen.de.

Journal of Chemical Theory and Computation   `Article`

■ REFERENCES

(1) Reichardt, C.; Welton, T. *Solvents and Solvent Effects in Organic Chemistry*; Wiley-VCH: Weinheim, Germany, 2011.

(2) Sailer, C. F.; Thallmair, S.; Fingerhut, B. P.; Nolte, C.; Ammer, J.; Mayr, H.; de Vivie-Riedle, R.; Pugliesi, I.; Riedle, E. *ChemPhysChem* **2013**, *14*, 1423−1437.

(3) Struebing, H.; Ganase, Z.; Karamertzanis, P. G.; Siougkrou, E.; Haycock, P.; Piccione, P. M.; Armstrong, A.; Galindo, A.; Adjiman, C. S. *Nat. Chem.* **2013**, *5*, 952−957.

(4) Thallmair, S.; Kowalewski, M.; Fingerhut, B.; Sailer, C.; de Vivie-Riedle, R. *EPJ Web Conf.* **2013**, *41*, 05043−1−05043−3.

(5) Thallmair, S.; Kowalewski, M.; Zauleck, J. P. P.; Roos, M. K.; de Vivie-Riedle, R. *J. Phys. Chem. Lett.* **2014**, *5*, 3480−3485.

(6) Benjamin, I.; Wilson, K. R. *J. Chem. Phys.* **1989**, *90*, 4176−4197.

(7) Krylov, A. I.; Gerber, R. B. *J. Chem. Phys.* **1994**, *100*, 4242−4252.

(8) Amatatsu, Y.; Morokuma, K. *Chem. Phys. Lett.* **1995**, *245*, 469−474.

(9) Winter, N.; Chorny, I.; Vieceli, J.; Benjamin, I. *J. Chem. Phys.* **2003**, *119*, 2127−2143.

(10) Moskun, A. C.; Jailaubekov, A. E.; Bradforth, S. E.; Tao, G.; Stratt, R. M. *Science* **2006**, *311*, 1907−1911.

(11) Horng, M. L.; Gardecki, J. A.; Papazyan, A.; Maroncelli, M. *J. Phys. Chem.* **1995**, *99*, 17311−17337.

(12) Caricato, M.; Mennucci, B.; Tomasi, J.; Ingrosso, F.; Cammi, R.; Corni, S.; Scalmani, G. *J. Chem. Phys.* **2006**, *124*, 124520-1−124520-13.

(13) Moskun, A. C.; Bradforth, S. E. *J. Chem. Phys.* **2003**, *119*, 4500−4515.

(14) Sailer, C. F.; Krebs, N.; Fingerhut, B. P.; de Vivie-Riedle, R.; Riedle, E. *EPJ Web Conf.* **2013**, *41*, 05042-1−05042-3.

(15) Cui, G.; Thiel, W. *Angew. Chem., Int. Ed.* **2013**, *52*, 433−436.

(16) Nenov, A.; Cordes, T.; Herzog, T. T.; Zinth, W.; de Vivie-Riedle, R. *J. Phys. Chem. A* **2010**, *114*, 13016−13030.

(17) Weingart, O.; Lan, Z.; Koslowski, A.; Thiel, W. *J. Phys. Chem. Lett.* **2011**, *2*, 1506−1509.

(18) Gollub, C.; Kowalewski, M.; Thallmair, S.; de Vivie-Riedle, R. *Phys. Chem. Chem. Phys.* **2010**, *12*, 15780−15787.

(19) von den Hoff, P.; Thallmair, S.; Kowalewski, M.; Siemering, R.; de Vivie-Riedle, R. *Phys. Chem. Chem. Phys.* **2012**, *14*, 14460−14485.

(20) Fingerhut, B. P.; Sailer, C. F.; Ammer, J.; Riedle, E.; de Vivie-Riedle, R. *J. Phys. Chem. A* **2012**, *116*, 11064−11074.

(21) Bronstein, I. N.; Semendjajew, K. A.; Musiol, G.; Mühlig, H. *Taschenbuch der Mathematik*, 7th ed.; Wissenschaftlicher Verlag Harri Deutsch GmbH: Frankfurt am Main, Germany, 2008.

(22) Lindahl, E.; Hess, B.; van der Spoel, D. *J. Mol. Model.* **2001**, *7*, 306−317.

(23) van der Spoel, D.; Lindahl, E.; Hess, B.; Groenhof, G.; Mark, A. E.; Berendsen, H. J. C. *J. Comput. Chem.* **2005**, *26*, 1701−1718.

(24) Jorgensen, W. L.; Maxwell, D. S.; Tirado-Rives, J. *J. Am. Chem. Soc.* **1996**, *118*, 11225−11236.

(25) Frisch, M. J.; Trucks, G. W.; Schlegel, H. B.; Scuseria, G. E.; Robb, M. A.; Cheeseman, J. R.; Scalmani, G.; Barone, V.; Mennucci, B.; Petersson, G. A.; Nakatsuji, H.; Caricato, M.; Li, X.; Hratchian, H. P.; Izmaylov, A. F.; Bloino, J.; Zheng, G.; Sonnenberg, J. L.; Hada, M.; Ehara, M.; Toyota, K.; Fukuda, R.; Hasegawa, J.; Ishida, M.; Nakajima, T.; Honda, Y.; Kitao, O.; Nakai, H.; Vreven, T.; Montgomery, J. A., Jr.; Peralta, J. E.; Ogliaro, F.; Bearpark, M.; Heyd, J. J.; Brothers, E.; Kudin, K. N.; Staroverov, V. N.; Kobayashi, R.; Normand, J.; Raghavachari, K.; Rendell, A.; Burant, J. C.; Iyengar, S. S.; Tomasi, J.; Cossi, M.; Rega, N.; Millam, J. M.; Klene, M.; Knox, J. E.; Cross, J. B.; Bakken, V.; Adamo, C.; Jaramillo, J.; Gomperts, R.; Stratmann, R. E.; Yazyev, O.; Austin, A. J.; Cammi, R.; Pomelli, C.; Ochterski, J. W.; Martin, R. L.; Morokuma, K.; Zakrzewski, V. G.; Voth, G. A.; Salvador, P.; Dannenberg, J. J.; Dapprich, S.; Daniels, A. D.; Farkas, O.; Foresman, J. B.; Ortiz, J. V.; Cioslowski, J.; Fox, D. J. *Gaussian 09*, revision A.02; Gaussian, Inc.: Wallingford, CT, 2009.

(26) Edwards, D. M.; Madden, P. A.; McDonald, I. R. *Mol. Phys.* **1984**, *51*, 1141−1161.

(27) Mountain, R. D. *J. Chem. Phys.* **1997**, *107*, 3921−3923.

(28) Svensson, M.; Humbel, S.; Froese, R. D. J.; Matsubara, T.; Sieber, S.; Morokuma, K. *J. Phys. Chem.* **1996**, *100*, 19357−19363.

(29) Bearpark, M. J.; Larkin, S. M.; Vreven, T. *J. Phys. Chem. A* **2008**, *112*, 7286−7295.

(30) Fingerhut, B. P.; Oesterling, S.; Haiser, K.; Heil, K.; Glas, A.; Schreier, W. J.; Zinth, W.; Carell, T.; de Vivie-Riedle, R. *J. Chem. Phys.* **2012**, *136*, 204307.

(31) Werner, H.-J.; Knowles, P. J.; Knizia, G.; Manby, F. R.; Schütz, M.; Celani, P.; Korona, T.; Lindh, R.; Mitrushenkov, A.; Rauhut, G.; Shamasundar, K. R.; Adler, T. B.; Amos, R. D.; Bernhardsson, A.; Berning, A.; Cooper, D. L.; Deegan, M. J. O.; Dobbyn, A. J.; Eckert, F.; Goll, E.; Hampel, C.; Hesselmann, A.; Hetzer, G.; Hrenar, T.; Jansen, G.; Köppl, C.; Liu, Y.; Lloyd, A. W; Mata, R. A.; May, A. J.; McNicholas, S. J.; Meyer, W.; Mura, M. E.; Nicklass, A.; O'Neill, D. P.; Palmieri, P.; Peng, D.; Pflüger, K.; Pitzer, R.; Reiher, M.; Shiozaki, T.; Stoll, H.; Stone, A. J.; Tarroni, R.; Thorsteinsson, T.; Wang, M. *MOLPRO*, version 2012.1, 2012.

(32) Tal-Ezer, H.; Kosloff, R. *J. Chem. Phys.* **1984**, *81*, 3967−3971.

(33) Wilson, E. B., Jr.; Decius, J. C.; Cross, P. C. *Molecular Vibrations*; McGraw-Hill: New York, USA, 1955.

(34) Schaad, L.; Hu, J. *J. Mol. Struct.: THEOCHEM* **1989**, *185*, 203−215.

(35) Kowalewski, M.; Mikosch, J.; Wester, R.; de Vivie-Riedle, R. *J. Phys. Chem. A* **2014**, *118*, 4661−4669.

(36) Thallmair, S.; Fingerhut, B. P.; de Vivie-Riedle, R. *J. Phys. Chem. A* **2013**, *117*, 10626−10633.

(37) Ammer, J.; Mayr, H. *J. Phys. Org. Chem.* **2013**, *26*, 956−969.

(38) Ammer, J.; Sailer, C. F.; Riedle, E.; Mayr, H. *J. Am. Chem. Soc.* **2012**, *134*, 11481−11494.

2. A second issue concerning the surrounding: The position of the counterion

In the previous chapter, the solvent environment of the reactant $Ph_2CH-PPh_3^+$ exhibited to have a vast influence on the dynamics of the photochemical bond cleavage. A second issue within the surrounding of the $Ph_2CH-PPh_3^+$ ion is its respective counterion X^-. In general, the considered phosphonium ions can be crystallized with different counterions, e.g. SbF_6^-, BF_4^-, Cl^- or Br^- [132, 133, 227]. Besides their different size, these counterions have a strongly varying oxidation potential. State-of-the-art broadband transient absorption measurements exposed the susceptibility of the bond cleavage for the kind of counterion X^- present [133]. Complex, hardly oxidizable counterions like SbF_6^- or BF_4^- lead to the generation of carbocations in polar and moderately polar solvents while excitation of phosphonium salts with comparably easily oxidizable halides as Cl^- or Br^- in moderately polar solvents – e.g. dichloromethane – is followed by radical formation. While SbF_6^- or BF_4^- are expected to spectate at the bond cleavage not having the ability to participate, the halides are suggested to take part at the reaction. Ammer et al. suspect that a single electron transfer from the counterion to the excited phosphonium ion is the crucial step for the observed radical formation in case of X^- being a halide [133]. An additional point that attracted attention is the degree of ion pairing – hence the distance to the counterion – which can influence the product formation.

The first question to address is the location of the counterion X^- within the ion pair $Ph_2CH-PPh_3^+$ X^- in solution. The article "Ion-Pairing of Phosphonium Salts in Solution: C—H···Halogen and C—H···π Hydrogen Bonds" published in *Chemistry – A European Journal* provides an extensive study of ion pairs of the phosphonium ions $Ph_2CH-PPh_3^+$, $PhCH_2-PPh_3^+$, and $(p\text{-}CF_3\text{-}C_6H_4)CH_2-PPh_3^+$ in the crystal as well as in solution [227]. The ^1H NMR shifts of the $C(\alpha)$–H protons of the phosphonium ions in CD_2Cl_2 display a strong counterion dependence. The positions of the counterions in the crystal as well as in solution were determined by X-ray analysis of the crystals and quantum chemical calculations respectively. To obtain the solution structures, the ion pairs were optimized at the DFT level of theory (functional M06-2X [209, 210]) employing the program package Gaussian 09 [211]. The electrostatic solvent effects were taken into account by the integral equation formalism variant of the PCM [160, 228, 229]. To confirm the optimized structures, the calculation of ^1H NMR shifts was conducted using the functional WP04 [230, 231]. The optimized structures revealed that the position of the counterion in solution is the same as in the crystal. The central statements drawn in the article are:

- The strong downfield shift of the ^1H NMR signals of the $C(\alpha)$–H protons for the ion pairs $Ph_2CH-PPh_3^+$ X^-, $PhCH_2-PPh_3^+$ X^-, and $(p\text{-}CF_3\text{-}C_6H_4)CH_2-PPh_3^+$ X^- in comparison to the free phosphonium ions increases according to $SbF_6^- < BF_4^- \ll Br^- < Cl^-$. For the less bulky phosphonium ions $PhCH_2-PPh_3^+$ and $(p\text{-}CF_3\text{-}C_6H_4)CH_2-PPh_3^+$ the ion pairing with BPh_4^- leads to a slight upfield shift. These observations contradict earlier interpretations which mostly traced the differences of the ^1H NMR shifts back to the upfield shift due to the phenyl ring current of the BPh_4^- anions [232]. The calculated ^1H NMR shifts of the $C(\alpha)$–H as well as the aromatic protons in CD_2Cl_2 compare well with the experimental results and confirmed the calculated solution structures of the ion pairs. The ^1H NMR shift calculations of the free unpaired phosphonium ions opened up

the opportunity to investigate the pure counterion effect with respect to an unaffected reference. The theoretical calculations supported the ascription of the strong counterion dependence of the ^{1}H NMR shifts back to the deshielding of the protons by the counterions X^- except for BPh_4^-.

- Both structures – in the crystal as well as in solution – indicate $C(\alpha)$–H$\cdots X^-$ hydrogen bonds, which prove to account for the pronounced counterion-dependent ^{1}H NMR shifts of the $C(\alpha)$–H in CD_2Cl_2. Their strength increases in the order $BPh_4^- < SbF_6^- < BF_4^- < Br^- < Cl^-$ which corresponds to the order of the increasing downfield shift. Besides this, a rise of the $C(\alpha)$–H acidity also results in an increase of the hydrogen bond strength.

- With regard to the IR frequencies of the $C(\alpha)$–H stretch vibration a red shift is observed experimentally for the halides which form strong hydrogen bonds while a blue shift occurs in case of the weak hydrogen bond acceptors SbF_6^- and BF_4^-.

The knowledge of the solution geometries of the examined ion pairs lays the foundation for a future theoretical investigation of the counterion influence during the photochemical bond cleavage. If an inert counterion like SbF_6^- and BF_4^- is employed, the electronic states of the phosphonium ions are not perturbed by the presence of the counterion. In contrast thereto, the interaction with oxidizable anions like Cl^- or Br^- might induce a change in the electronic structure which entails the different photochemical behavior observed in CH_2Cl_2.

On the next pages the article "Ion-Pairing of Phosphonium Salts in Solution: C—H$\cdots$Halogen and C—H$\cdots\pi$ Hydrogen Bonds" published in *Chemistry – A European Journal* is reprinted with permission from *Chem. Eur. J.* **19**, 14612–14630 (2013); copyright 2013 John Wiley and Sons. The contribution within the framework of the present work comprises the performance of all quantum chemical calculations – i.e. the optimization of the ion pairs $Ph_2CH-PPh_3^+$ X^-, $PhCH_2-PPh_3^+$ X^-, and $(p\text{-}CF_3\text{-}C_6H_4)CH_2-PPh_3^+$ X^- with X^- being Cl^-, Br^-, BF_4^-, and SbF_6^- followed by the calculation of the ^{1}H NMR shifts for all optimized structures, both at the DFT level of theory – and their interpretation with respect to the experimental observations. The theoretical results are presented in particular on the pages $14619-14624$ (pages $60-65$ in the pagination of this work) and in the tables 6, 9, 10, and 11 as well as in figure 7.

CHEMISTRY
A EUROPEAN JOURNAL

ChemPubSoc
Europe

Ion-Pairing of Phosphonium Salts in Solution:
C−H···Halogen and C−H···π Hydrogen Bonds

Johannes Ammer,* Christoph Nolte, Konstantin Karaghiosoff,* Sebastian Thallmair, Peter Mayer, Regina de Vivie-Riedle, and Herbert Mayr[a]

Abstract: The ^{1}H NMR chemical shifts of the C(α)−H protons of arylmethyl triphenylphosphonium ions in CD_2Cl_2 solution strongly depend on the counteranions X^-. The values for the benzhydryl derivatives $Ph_2CH−PPh_3^+X^-$, for example, range from $\delta_H = 8.25$ ($X^- = Cl^-$) over 6.23 ($X^- = BF_4^-$) to 5.72 ppm ($X^- = BPh_4^-$). Similar, albeit weaker, counterion-induced shifts are observed for the *ortho*-protons of all aryl groups. Concentration-dependent NMR studies show that the large shifts result from the deshielding of the protons by the anions, which decreases in the order $Cl^- > Br^- \gg BF_4^- > SbF_6^-$. For the less bulky derivatives $PhCH_2−PPh_3^+X^-$, we also find C−H···Ph interactions between C(α)−H and a phenyl group of the BPh_4^- anion, which result in upfield NMR chemical shifts of the C(α)−H protons. These interactions could also be observed in crystals of $(p\text{-}CF_3\text{-}C_6H_4)CH_2−PPh_3^+BPh_4^-$. However, the dominant effects causing the counterion-induced shifts in the NMR spectra are the C−H···X^- hydrogen bonds between the phosphonium ion and anions, in particular Cl^- or Br^-. This observation contradicts earlier interpretations which assigned these shifts predominantly to the ring current of the BPh_4^- anions. The concentration dependence of the ^{1}H NMR chemical shifts allowed us to determine the dissociation constants of the phosphonium salts in CD_2Cl_2 solution. The cation–anion interactions increase with the acidity of the C(α)−H protons and the basicity of the anion. The existence of C−H···X^- hydrogen bonds between the cations and anions is confirmed by quantum chemical calculations of the ion pair structures, as well as by X-ray analyses of the crystals. The IR spectra of the Cl^- and Br^- salts in CD_2Cl_2 solution show strong red-shifts of the C−H stretch bands. The C−H stretch bands of the tetrafluoroborate salt $PhCH_2−PPh_3^+BF_4^-$ in CD_2Cl_2, however, show a blue-shift compared to the corresponding BPh_4^- salt.

Keywords: crystal structure · hydrogen bonds · ion pairs · NMR spectroscopy · solution structure
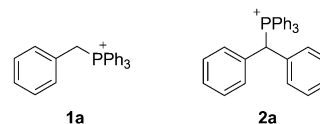
Introduction

Hydrogen bonds involving C−H donors have attracted considerable interest in the last two decades,[1–3] and only recently it became generally recognized that, in many cases, these interactions have to be classified as moderate or even strong hydrogen bonds.[4]

The C(α)−H protons of alkyl triphenylphosphonium salts are particularly acidic[5,6] so that C(α)−H···X^- hydrogen bonds between the phosphonium ion and its counterion X^- should be quite favorable. The importance of such hydrogen bonds in crystals as well as in solutions of phosphonium halides was already demonstrated in a 1964 report that received only little attention.[7] For example, the CH_2 stretching vibrations of $PhCH_2−PPh_3^+Cl^-$ (**1a**Cl^-, Scheme 1) in chloroform solution (2853 and 2780 cm^{-1}) are red-shifted ($\Delta\bar{\nu} \approx -80$ cm^{-1}) compared with those of the corresponding BPh_4^- salt (2937 and 2857 cm^{-1}). Likewise, the CH_2 signals in the ^{1}H NMR spectrum of **1a**Cl^- were reported to be shifted downfield relative to those of **1a**BPh_4^- ($\Delta\delta_H \approx +0.4$ ppm in CH_3CN).[7] Spectral shifts as those observed for **1a**Cl^- are classical criteria for a hydrogen bond.[8]

Schiemenz and co-workers have collected an enormous wealth of data on ^{1}H NMR spectra of phosphonium salts and found analogous trends, that is, that the α protons of phosphonium ions in chloroform or dichloromethane solution generally undergo upfield shifts of up to $\Delta\delta_H \approx -3$ ppm when the counterion is exchanged from halide to BPh_4^-.[9,10] Similar results were found for other onium salts.[11–15] According to these reports, the interaction between the onium ions and "normal" inorganic anions such as halide ions plays only a minor role and is related to the phenomenon of solvation.[9] Instead, the large upfield shifts in the BPh_4^- salts (e.g., $\Delta\delta_H = -1.41$ ppm for **1a**BPh_4^- compared to **1a**Br^- in

[a] Dr. J. Ammer, Dr. C. Nolte, Prof. Dr. K. Karaghiosoff, S. Thallmair, Dr. P. Mayer, Prof. Dr. R. de Vivie-Riedle, Prof. Dr. H. Mayr
Ludwig-Maximilians-Universität München, Butenandtstrasse 5–13
81377 München (Germany)
Fax: (+49)89-2180-77398
E-mail: Johannes.Ammer@cup.uni-muenchen.de
        Konstantin.Karaghiosoff@cup.uni-muenchen.de

Supporting information for this article is available on the WWW under http://dx.doi.org/10.1002/chem.201204561.

Scheme 1. Structures of the phosphonium ions **1a** and **2a**.

WILEY
ONLINE LIBRARY

FULL PAPER

CD$_2$Cl$_2$)[9] were rationalized to be predominantly caused by the ring current of the BPh$_4^-$ anion's phenyl rings, which reside above the C(α)$-$H protons of the phosphonium ion due to Coulomb attraction between the two ions.[9,10,16,17] Based on this effect, many applications of the BPh$_4^-$ anion as shift reagent in NMR spectroscopy have been described.[9,11–15,18]

One of the examples used by Schiemenz to illustrate the usefulness of the "BPh$_4^-$ effect" was the possibility to determine $^2J_{H,P}$ for the α proton of Ph$_2$CH$-$PPh$_3^+$ (**2a**).[9] This could not be achieved in the absence of BPh$_4^-$ due to the overlap of the C(α)$-$H signals with the aromatic protons in the NMR spectra of the corresponding halide salts. In the course of our studies of phosphonium salts as precursors for the photogeneration of carbocations,[19,20] we required knowledge about the ion pairing of the phosphonium salt **2a**X$^-$ in solution. Much to our surprise, our data clearly showed that the C(α)$-$H protons of **2a**BPh$_4^-$ do not experience any significant ring current effect in CD$_2$Cl$_2$ solution. Considering the relevance of phosphonium ion/anion interactions in crystal engineering,[21] anion recognition,[22] salt-based solvent systems,[23,24] photochemistry,[19,20,25] structure determination,[10,26] and organic synthesis,[27,28] we decided to carry out a more detailed investigation of the ion pairing in **2a**X$^-$ and related phosphonium salts.

NMR Spectroscopy

^{1}H NMR Signals for the C(α)$-$H protons of phosphonium salts in CD$_2$Cl$_2$ solution

Benzhydryl triphenylphosphonium salts (2a X$^-$): Ion pairing of the salts Ph$_2$CH$-$PPh$_3^+$ X$^-$ (**2a**X$^-$) in CD$_2$Cl$_2$ solution is

evident from the fact that the NMR spectra of **2a** depend on the counterion X$^-$ (Table 1). The most obvious effect is the large change of the ^{1}H NMR chemical shifts ($\Delta\delta_H =$ + 2.53 ppm) for the C(α)$-$H protons (CHP$^+$) when X$^-$ is varied from BPh$_4^-$ via SbF$_6^-$, BF$_4^-$, and Br$^-$ to Cl$^-$ (Table 1).

Figure 1 shows that the δ_H values of the C(α)$-$H protons of **2a**BPh$_4^-$ in CD$_2$Cl$_2$ are almost independent of the salt concentration ($\delta_H \approx 5.78$ ppm, Table 2). Moreover, the values for **2a**BPh$_4^-$ differ by only 0.2 ppm or less from those of **2a**SbF$_6^-$. These observations clearly rule out any significant influence of the ring current of the BPh$_4^-$ anions' phenyl rings on the chemical shifts of the C(α)$-$H protons of **2a**, as suggested by Schiemenz.[9]

At concentrations of [**2a**X$^-$] > 0.02 M, the δ_H values of the C(α)$-$H protons of **2a**X$^-$ with X$^-$ = Cl$^-$, Br$^-$, BF$_4^-$, or SbF$_6^-$ reach plateaus (Figure 1) and we can conclude that at
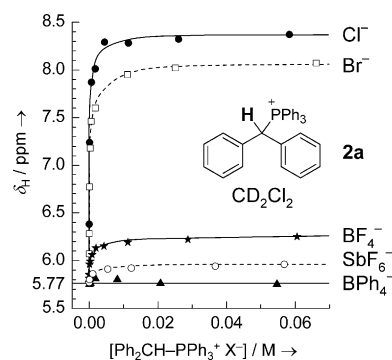
Figure 1. Concentration-dependent ^{1}H NMR (600 MHz, 27°C) chemical shifts δ_H of the benzylic C(α)$-$H protons of **2a**X$^-$ with different counteranions X$^-$ = Cl$^-$ (●), Br$^-$ (□), BF$_4^-$ (★), SbF$_6^-$ (○), or BPh$_4^-$ (▲) in CD$_2$Cl$_2$.

Table 1. ^{31}P NMR (162 MHz), ^{1}H NMR (400 MHz), and ^{13}C NMR (100 MHz) data for the phosphonium ion **2a** in CD$_2$Cl$_2$. Data for **2a**X$^-$ were determined at concentrations where the phosphonium salts exist as ion pairs.

Salt	P$^+$ δ_P [ppm]	CHP$^+$ δ_H [ppm] ($^2J_{H,P}$ [Hz])	$^1J_{H,C}$[a] [Hz]	o-CHPh$_2$ δ_H [ppm]	m-CHPh$_2$ δ_H [ppm]	p-CHPh$_2$ δ_H [ppm]	o-PPh$_3$ δ_H [ppm]	m-PPh$_3$ δ_H [ppm]	p-PPh$_3$ δ_H [ppm]
2aCl$^-$	22.1	8.25 (18.3)	131.3	7.55–7.60[b]	7.20–7.30[b]	7.20–7.30[b]	7.79–7.84	7.55–7.60[b]	7.72–7.77
2aBr$^-$	22.1	8.10 (18.0)	131.1	7.53–7.61[b]	7.21–7.31[b]	7.21–7.31[b]	7.74–7.79[b]	7.53–7.61[b]	7.74–7.79[b]
2aBF$_4^-$	21.8	6.23 (17.4)	130.2	7.19–7.22	7.28–7.33	7.35–7.40	7.43–7.49	7.59–7.65	7.81–7.85
2aSbF$_6^-$	21.7	5.98 (17.2)	129.3	7.15–7.17	7.30–7.34	7.38–7.44[b]	7.38–7.44[b]	7.61–7.66	7.82–7.87
2aBPh$_4^-$	21.6	5.72 (17.1)	128.7	7.05–7.10	7.27–7.36[c]	7.39–7.47	7.27–7.36[c]	7.55–7.62	7.79–7.86
"free" **2a**[d]	–[e]	5.77 (17.0)	–[e]	7.09–7.11	7.33–7.37[b]	7.42–7.45	7.33–7.37[b]	7.62–7.65	7.85–7.89
Δ(Cl$^-$)[f]	+0.6	**+2.53 (+1.2)**	+2.6	~ +0.50	~ –0.07	~ –0.18	~ +0.50	~ ±0	~ –0.08

Salt	CHP$^+$ δ_C [ppm] ($^1J_{C,P}$ [Hz])	i-CHPh$_2$ δ_C [ppm] ($^2J_{C,P}$ [Hz])	o-CHPh$_2$ δ_C [ppm] ($^3J_{C,P}$ [Hz])	m-CHPh$_2$ δ_C [ppm] ($^4J_{C,P}$ [Hz])	p-CHPh$_2$ δ_C [ppm] ($^5J_{C,P}$ [Hz])	i-PPh$_3$ δ_C [ppm] ($^1J_{C,P}$ [Hz])	o-PPh$_3$ δ_C [ppm] ($^2J_{C,P}$ [Hz])	m-PPh$_3$ δ_C [ppm] ($^3J_{C,P}$ [Hz])	p-PPh$_3$ δ_C [ppm] ($^4J_{C,P}$ [Hz])
2aCl$^-$	45.3 (41.8)	134.3 (4.0)	131.7 (6.9)	129.4 (1.5)	129.0 (2.7)	119.2 (82.3)	135.7 (9.2)	130.3 (12.3)	135.2 (3.1)
2aBr$^-$	45.9 (42.3)	134.1 (4.0)	131.6 (6.8)	129.5 (1.7)	129.2 (2.5)	119.0 (82.4)	135.7 (9.3)	130.3 (12.4)	135.3 (3.1)
2aBF$_4^-$	49.6 (43.9)	132.9 (4.1)	131.1 (6.6)	130.0 (1.7)	129.9 (2.6)	118.3 (82.5)	135.3 (9.1)	130.8 (12.4)	135.9 (3.1)
2aSbF$_6^-$	50.5 (44.2)	132.6 (4.2)	130.9 (6.6)	130.1 (1.8)	130.0 (2.5)	118.1 (82.7)	135.2 (9.1)	130.8 (12.4)	136.0 (3.1)
2aBPh$_4^-$	51.3 (44.3)	132.3 (4.2)	130.8 (6.6)	130.25 (1.7)	130.32 (2.5)	117.9 (82.6)	135.2 (9.1)	131.0 (12.2)	136.3 (3.1)
Δ(Cl$^-$)[f]	**–6.0 (–2.5)**	+2.0 (–0.2)	+0.9 (+0.3)	–0.8 (–0.2)	–1.3 (+0.2)	+1.3 (–0.3)	+0.5 (+0.1)	–0.7 (+0.1)	–1.1 (±0)

[a] $^1J_{H,C}$ determined from ^{13}C satellites in the ^{1}H NMR (600 MHz) spectra. [b] Two signals superimposed. [c] Superimposed with o-protons of BPh$_4^-$. [d] ^{1}H NMR (600 MHz) spectrum of a 2.13×10^{-5} M solution of **2a** SbF$_6^-$ in CD$_2$Cl$_2$. At this concentration, the phosphonium salt predominantly exists in the form of the free (unpaired) ions. [e] Not available. [f] Difference between **2a** Cl$^-$ and **2a** BPh$_4^-$ (the latter has virtually the same ^{1}H NMR spectrum as "free" **2a**).

Table 2. Concentration-dependent ^1H NMR chemical shifts δ_H (600 MHz) for $C(\alpha)-H$ and dissociation constants K_D [M] of **2a** X^- with different counterions X^- in CD_2Cl_2.

Salt	[2aX⁻]/M	δ_H [ppm]	$x_{paired,exptl}$	K_D[a] [M]	$x_{paired,calcd}$[b]
2a BPh₄⁻	1.75×10^{-5}	5.80	–	–	
	1.03×10^{-4}	5.75	–		
	4.07×10^{-4}	5.76	–		
	1.76×10^{-3}	5.81	–		
	8.25×10^{-3}	5.80	–		
	2.08×10^{-2}	5.76	–		
	5.47×10^{-2}	5.75	–		
	average δ_H	**5.78**			
2a SbF₆⁻	2.13×10^{-5}	5.77	0.00		0.03
	1.07×10^{-4}	5.80	0.16		0.13
	1.02×10^{-3}	5.86	**0.47**	6×10^{-4}	(0.47)
	5.44×10^{-3}	5.91	0.74		0.72
	1.23×10^{-2}	5.92	0.79		0.80
	3.68×10^{-2}	5.94	0.89		0.88
	5.68×10^{-2}	5.96	1.00		0.90
2a BF₄⁻	2.12×10^{-5}	5.81	0.08		0.08
	4.22×10^{-5}	5.85	0.17		0.14
	1.03×10^{-4}	5.96	0.40		0.26
	3.36×10^{-4}	5.99	**0.46**	2.2×10^{-4}	(0.46)
	8.91×10^{-4}	6.06	0.60		0.61
	2.01×10^{-3}	6.13	0.75		0.72
	4.26×10^{-3}	6.15	0.79		0.80
	1.13×10^{-2}	6.19	0.88		0.87
	2.87×10^{-2}	6.22	0.94		0.92
	6.06×10^{-2}	6.25	1.00		0.94
2a Br⁻	1.81×10^{-5}	6.07	0.13		0.17
	3.58×10^{-5}	6.28	0.22		0.26
	1.03×10^{-4}	6.77	**0.43**	7.6×10^{-5}	(0.43)
	3.04×10^{-4}	7.18	0.61		0.61
	6.09×10^{-4}	7.46	0.73		0.70
	1.83×10^{-3}	(7.6)[c]	0.80		0.82
	1.12×10^{-2}	7.95	0.95		0.92
	2.51×10^{-2}	8.02	0.98		0.95
	6.62×10^{-2}	8.07	1.00		0.97
2a Cl⁻	2.31×10^{-5}	6.38	0.23		0.32
	1.00×10^{-4}	7.24	**0.57**	3.4×10^{-5}	(0.57)
	7.13×10^{-4}	7.87	0.81		0.81
	1.76×10^{-3}	8.01	0.86		0.87
	4.45×10^{-3}	8.29	0.97		0.92
	1.14×10^{-2}	8.28	0.97		0.95
	2.61×10^{-2}	8.32	0.98		0.96
	5.83×10^{-2}	8.37	1.00		0.98

[a] K_D derived from the data for phosphonium salt concentrations where $x_{paired,exptl} \approx 0.5$. [b] Calculated using K_D from this table. [c] Superimposed with signals of aryl protons.

$Ph_2CH-PPh_3^+$ ions (**2a**). The determination of the K_D values listed in Table 2 will be discussed below.

Benzyl triphenylphosphonium salts (1a,bX⁻): It was already noted by Schiemenz and co-workers, that the "BPh₄⁻ effect" decreases with steric shielding.[9,10] For that reason, we also tested the "BPh₄⁻ effect" in sterically less hindered systems and investigated the concentration-dependent effects of the counteranions on the ^1H NMR chemical shifts δ_H (600 MHz, CD_2Cl_2) of the $C(\alpha)-H$ protons of the benzyl triphenylphosphonium ions $PhCH_2-PPh_3^+$ (**1a**) and the 4-(trifluoromethyl)benzyl triphenylphosphonium ions $(p\text{-}CF_3\text{-}C_6H_4)CH_2-PPh_3^+$ (**1b**) (Tables S1 and S2 in the Supporting Information). Figure 2a and b illustrate the data.
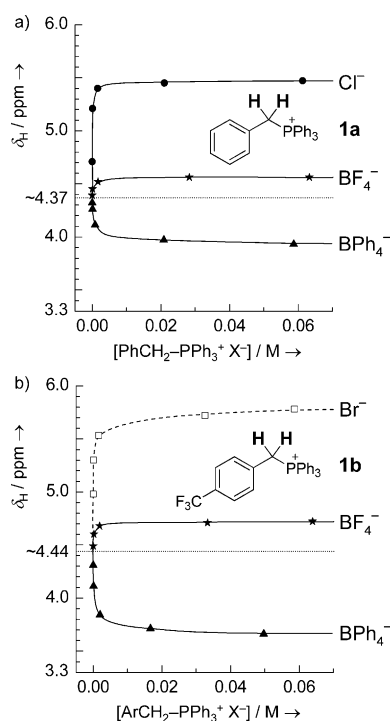
Figure 2. Concentration-dependent ^1H NMR (600 MHz, 27 °C) chemical shifts δ_H of the benzylic $C(\alpha)-H$ protons of a) **1a** X^- or b) **1b** X^- with different counteranions $X^- = Cl^-$ (●), Br^- (□), BF_4^- (★), or BPh_4^- (▲) in CD_2Cl_2.

these concentrations we observe ion pairs almost exclusively. Literature NMR spectra of phosphonium salts in CD_2Cl_2 or $CDCl_3$ solution, which were recorded under typical conditions of NMR measurements, can thus be expected to characterize the ion pairs.

At lower concentrations ($<5\times10^{-3}$ M), the chemical shifts of the $C(\alpha)-H$ protons of **2a** X^- with all investigated anions except BPh_4^- decrease markedly and approach δ_H of the tetraphenylborate salt (Figure 1). Finally, at a concentration of 2.13×10^{-5} M, the chemical shift of the $C(\alpha)-H$ proton of **2a** SbF_6^- reaches a value of $\delta_H = 5.77$ ppm (Table 2), which is identical to δ_H observed for **2a** BPh_4^-. We can therefore assume that this δ_H value corresponds to the unpaired

The phosphonium halides **1a** Cl^- and **1b** Br^-, as well as the tetrafluoroborates **1a,b** BF_4^-, show similar behavior as the corresponding benzhydryl triphenylphosphonium salts **2a** X^-. In the concentration range [**1a,b** X^-] ≥ 0.02 M, the δ_H values of the $C(\alpha)-H$ protons are virtually constant and we can conclude that the phosphonium halides and tetrafluoroborates predominantly exist as ion pairs under these conditions (Figure 2). At lower concentrations ($<5\times10^{-3}$ M), the δ_H values decrease: For 2×10^{-5} M solutions of the tetrafluoroborate salts, we determined chemical shifts of $\delta_H = 4.39$ (**1a** BF_4^-) and 4.49 ppm (**1b** BF_4^-) for the $C(\alpha)-H$ protons (Tables S1 and S2 in the Supporting Information).

Ion-Pairing of Phosphonium Salts in Solution

FULL PAPER

The C(α)$-$H protons of the tetraphenylborate salts **1a,b** BPh$_4^-$, however, show the opposite effect: Their chemical shifts are also virtually constant (**1a** BPh$_4^-$: 3.95 ppm; **1b** BPh$_4^-$: 3.68 ppm) at concentrations ≥ 0.02 M, but *increase* with decreasing concentration until they reach the value of $\delta_H = 4.32$ ppm (**1a** BPh$_4^-$) or 4.31 ppm (**1b** BPh$_4^-$) at concentrations of 2×10^{-5} M (Figure 2).

Thus, the δ_H values of the C(α)$-$H protons of **1a** X$^-$ with different counteranions X$^-$ approach a common value of $4.32 < \delta_H < 4.39$ ppm at low concentrations of **1a** X$^-$, and we can estimate $\delta_{H,unpaired} \approx 4.37$ ppm for the C(α)$-$H protons of the free benzyl triphenylphosphonium ion **1a**. Analogously, $4.31 < \delta_H < 4.49$ ppm at low concentrations of **1b** X$^-$ leads to an estimate of $\delta_{H,unpaired} \approx 4.44$ ppm for the C(α)$-$H protons of free **1b**.

The knowledge of δ_H for the unpaired phosphonium ions **1a,b** allows us to directly compare the magnitude of the "BPh$_4^-$ effect" with the influence of C(α)$-$H···halide hydrogen bonding. The large difference between the C(α)$-$H protons of the ion pairs **1a** Cl$^-$ and **1a** BPh$_4^-$ ($\Delta\delta_H = +1.54$ ppm) is mostly due to the deshielding effect of Cl$^-$, whereas the shielding effect of BPh$_4^-$ contributes less than 30% to the observed $\Delta\delta_H$. The smaller deshielding effects of the "normal" anions X$^- = Cl^-$ and BF$_4^-$ on the C(α)$-$H protons of **1a** (e.g., $\Delta\delta_H \approx +1.0$ ppm for **1a** Cl$^-$ relative to unpaired **1a**) compared to those for the analogous benzhydryl derivatives **2a** X$^-$ (e.g., $\Delta\delta_H \approx +2.5$ ppm for **2a** Cl$^-$ relative to unpaired **2a**) are explained by the statistical factor of two C(α)$-$H protons in **1a** (vs one in **2a**) and the lower C(α)$-$H acidity of **1a** (pK_a 17.6 in DMSO)[6] compared to that of **2a** (p$K_a \approx 9$ in DMSO estimated from the correlation equation published in ref. [5] and pK_a 30.6 for Ph$_2$CH$_2$[29]).

The *p*-CF$_3$ substituent decreases the pK_a value of the phosphonium salt **1b** in DMSO to 14.6, compared to pK_a 17.6 for the parent compound **1a**,[6] which results in stronger C$-$H···X$^-$ hydrogen bonds in the **1b** X$^-$ ion pairs. Accordingly, Figure 2b shows comparably large downfield shifts for the C(α)$-$H protons in the **1b** Br$^-$ and **1b** BF$_4^-$ ion pairs. The "BPh$_4^-$ effect" also increases with the C(α)$-$H acidity: The upfield shift of $\Delta\delta_H \approx -0.78$ ppm for the C(α)$-$H protons of **1b** that results from ion pairing with the BPh$_4^-$ ion is almost twice as large as the upfield shift of $\Delta\delta_H \approx -0.44$ for **1a** BPh$_4^-$ (Figure 2). The relative magnitudes of the "ordinary anion" effects and the "BPh$_4^-$ effect" in **1b** X$^-$ are therefore similar to those in the parent compounds **1a** X$^-$.

Correlation with ΔG_t^0 (H$_2$O$\rightarrow$CH$_3$CN) of the anions X$^-$: Figures 1 and 2 show that the deshielding of the C(α)$-$H protons in the **2a** X$^-$ and **1a,b** X$^-$ ion pairs increases in the order SbF$_6^-$ < BF$_4^-$ < Br$^-$ < Cl$^-$. An anion's ability to act as hydrogen bond acceptor is related to its single free ion energy of transfer ΔG_t^0 (H$_2$O $\rightarrow$ CH$_3$CN),[30] since a large contribution to the transfer energy is the loss of the HO$-$H···X$^-$ hydrogen bonds to the good hydrogen-bond donor H$_2$O. Figure 3 illustrates that the chemical shifts δ_H for the
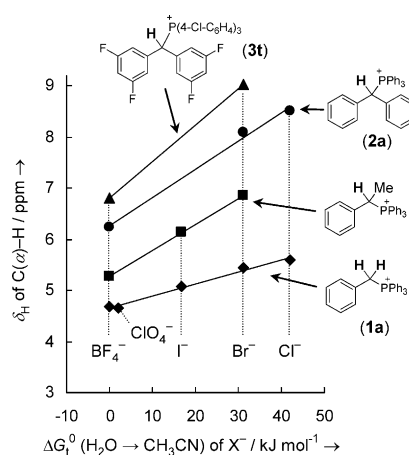
Figure 3. Plot of the ^{1}H NMR chemical shifts δ_H for the C(α)$-$H in arylmethyl triarylphosphonium salts (ion pairs) with different counter-anions X$^-$ in CD$_2$Cl$_2$ (**2a**, **3t**) and CDCl$_3$ (other salts) against the single free ion energies of transfer ΔG_t^0 (H$_2$O$\rightarrow$CH$_3$CN) of the anions X$^-$. The points for **1a** BPh$_4^-$ and **2a** BPh$_4^-$ deviate from the correlation (not shown). See Table S3 in the Supporting Information for numeric values and references.

C(α)$-$H protons of **2a** X$^-$ and other arylmethyl phosphonium salts in CD$_2$Cl$_2$ or CDCl$_3$ correlate linearly with ΔG_t^0 (H$_2$O $\rightarrow$ CH$_3$CN) of the anions.

Other NMR signals of the phosphonium ions in CD$_2$Cl$_2$ solution

Besides the large change in δ_H for the C(α)$-$H protons, Tables 1 and 3 also show the effect of the counter-anion X$^-$ on other ^{31}P NMR, ^{1}H NMR, and ^{13}C NMR signals of **2a** and **1a** in CD$_2$Cl$_2$.

Benzhydryl triphenylphosphonium salts (2a X$^-$): The excellent agreement between the ^{1}H NMR chemical shifts of 2.13×10^{-5} M **2a** SbF$_6^-$ and the concentration-independent ^{1}H NMR chemical shifts of **2a** BPh$_4^-$ (Table 1) corroborates the assumption that **2a** SbF$_6^-$ mostly exists in the form of the free ions at this concentration. Pairing with the Cl$^-$ anion polarizes the bond between α-C and α-H ($\Delta\delta_H = +2.53$ ppm, $\Delta\delta_C = -6.0$ ppm), while the effect on the phosphorus atom is rather small ($\Delta\delta_P = +0.6$ ppm). The coupling constant $^1J_{H,C} = 128.7$ Hz for C(α)$-$H of **2a** BPh$_4^-$ is typical for sp^3 carbons,[31] and increases slightly in the presence of the hydrogen-bond acceptor Cl$^-$ ($\Delta^1J_{H,C} = +2.6$ Hz). A slight increase of $^1J_{H,C}$ by a few Hz was previously observed for other C$-$H···X hydrogen bonds and may result from the additional electric field component along the C$-$H bond in the presence of the hydrogen-bond acceptor.[32] The ^1J and ^2J coupling constants between C(α)$-$H and P change by $\Delta^1J_{C,P} = -2.5$ and $\Delta^2J_{H,P} = +1.2$ Hz, respectively.

The *ortho*-protons of the phenyl groups are also deshielded substantially ($\Delta\delta_H \approx +0.50$ ppm), especially if one considers that the effect of the Cl$^-$ anion is averaged over six *o*-PPh$_3$ or four *o*-CHPh$_2$ protons. Other effects are small: The *iso*- and *ortho*-carbons are also deshielded slightly ($\Delta\delta_C \approx$

Table 3. ^{31}P NMR (162 MHz), ^{1}H NMR (400 MHz), and ^{13}C NMR (100 MHz) data for the phosphonium ion **1a** in CD$_2$Cl$_2$. Data for **1a** X$^-$ were determined at concentrations where the phosphonium salts exist as ion pairs.

Salt	P$^+$ δ_P [ppm]	CH$_2$P$^+$ δ_H [ppm] ($^2J_{H,P}$ [Hz])	$^1J_{H,C}$[a] [Hz]	o-CH$_2$Ph δ_H [ppm]	m-CH$_2$Ph δ_H [ppm]	p-CH$_2$Ph δ_H [ppm]	o-PPh$_3$ δ_H [ppm]	m-PPh$_3$ δ_H [ppm]	p-PPh$_3$ δ_H [ppm]
1aCl$^-$	23.1	5.42 (14.7)	134.6	7.07–7.10	7.14–7.18	7.24–7.29	7.70–7.76	7.60–7.66	7.77–7.82
1aBF$_4^-$	22.2	4.56 (14.1)	134.2	6.91–6.94	7.20–7.25	7.31–7.36	7.48–7.54	7.65–7.71	7.84–7.88
"free" **1a**[b]	–[c]	4.39 (14.0)	–[c]	6.87–6.89	7.25–7.28	7.38–7.41	7.43–7.46	7.68–7.72	7.89–7.92
"free" **1a**[d]	–[c]	4.32 (14.0)	–[c]	6.85–6.89[e]	7.26–7.28	7.38–7.44[f]	7.38–7.44[f]	7.68–7.71	7.89–7.92
1aBPh$_4^-$	21.6	3.94 (13.8)	133.9	6.73–6.76	7.21–7.28[f]	7.34–7.39	7.21–7.28[f]	7.57–7.62	7.79–7.84
Δ(Cl$^-$)[g]	–[c]	**+1.03 (+0.7)**	–[c]	~ **+0.20**	~ –0.10	~ –0.13	~ **+0.29**	~ –0.07	~ –0.10
Δ(BPh$_4^-$)[h]	–[c]	**–0.38 (–0.2)**	–[c]	~ **–0.12**	≤ –0.05	~ –0.05	~ **–0.16**	~ –0.10	~ –0.09

Salt	CH$_2$P$^+$ δ_C [ppm] ($^1J_{C,P}$ [Hz])	i-CH$_2$Ph δ_C [ppm] ($^2J_{C,P}$ [Hz])	o-CH$_2$Ph δ_C [ppm] ($^3J_{C,P}$ [Hz])	m-CH$_2$Ph δ_C [ppm] ($^4J_{C,P}$ [Hz])	p-CH$_2$Ph δ_C [ppm] ($^5J_{C,P}$ [Hz])	i-PPh$_3$ δ_C [ppm] ($^1J_{C,P}$ [Hz])	o-PPh$_3$ δ_C [ppm] ($^2J_{C,P}$ [Hz])	m-PPh$_3$ δ_C [ppm] ($^3J_{C,P}$ [Hz])	p-PPh$_3$ δ_C [ppm] ($^4J_{C,P}$ [Hz])
1aCl$^-$	31.2 (46.9)	128.1 (8.5)	131.9 (5.6)	129.4 (3.3)	129.0 (3.9)	118.5 (85.8)	135.0 (9.8)	130.6 (12.6)	135.5 (3.0)
1aBF$_4^-$	31.5 (49.0)	127.0 (8.5)	131.5 (5.5)	129.8 (3.2)	129.6 (3.8)	117.6 (86.1)	134.6 (9.7)	130.9 (12.6)	136.1 (3.1)
1aBPh$_4^-$	31.7 (49.0)	126.5 (8.4)	131.4 (5.4)	129.8 (3.2)	129.7 (3.8)	117.1 (86.4)	134.4 (9.7)	131.0 (12.6)	136.2 (3.0)
Δ(total)[i]	–0.5 (**–2.1**)	+1.6 (–0.1)	+0.5 (+0.2)	–0.4 (–0.1)	–0.7 (+0.1)	+1.4 (–0.6)	+0.6 (+0.1)	–0.4 (±0)	–0.7 (±0)

[a] $^1J_{H,C}$ determined from ^{13}C satellites in the ^{1}H NMR (600 MHz) spectra. [b] Determined from ^{1}H NMR (600 MHz) spectrum of a 2.08×10^{-5} M solution of **1a** BF$_4^-$ in CD$_2$Cl$_2$. [c] Not available. [d] Determined from ^{1}H NMR (600 MHz) spectrum of a 1.75×10^{-5} M solution of **1a** BPh$_4^-$ in CD$_2$Cl$_2$. [e] Superimposed with p-protons of BPh$_4^-$. [f] Two signals superimposed. [g] "Ordinary anion effect": Difference between **1a**Cl$^-$ ion pairs and free ions (2.08×10^{-5} M **1a** BF$_4^-$). [h] "BPh$_4^-$ effect": Difference between **1a** BPh$_4^-$ ion pairs and free ions (1.75×10^{-5} M **1a** BPh$_4^-$). [i] Difference between **1a**Cl$^-$ and **1a**BPh$_4^-$.

+0.5 to +2 ppm) in the presence of Cl$^-$, while the *meta*- and *para*-positions of the aromatic rings are slightly shielded ($\Delta\delta_H \approx 0$ to –0.18 ppm, $\Delta\delta_C \approx$ –0.7 to –1.3 ppm). The effects of Br$^-$, BF$_4^-$, and SbF$_6^-$ on the NMR signals of **2a** are similar but less pronounced.

Benzyl triphenylphosphonium salts (1a X$^-$): Table 3 includes two sets of ^{1}H NMR data for the free PhCH$_2$–PPh$_3^+$ ion (**1a**), one determined from a 2.08×10^{-5} M solution of **1a** BF$_4^-$, the other from a 1.75×10^{-5} M solution of **1a** BPh$_4^-$. Again, the good agreement between the two data sets confirms the assignment to the unpaired phosphonium ion **1a**.

Ion-pairing affects the ^{1}H NMR signals of **1a**Cl$^-$ in a similar way as those of the corresponding benzhydryl triphenylphosphonium ions (**2a**): The C(α)–H protons experience the largest deshielding ($\Delta\delta_H \approx$ +1.03 ppm, $\Delta^2J_{H,P} \approx$ +0.7 Hz); a smaller but still significant deshielding effect is observed for the *ortho*-protons of the PPh$_3$ group ($\Delta\delta_H \approx$ +0.29 ppm) and the o-protons of the benzyl group ($\Delta\delta_H \approx$ +0.20 ppm). The *meta*- and *para*-protons of PPh$_3$ and benzyl are slightly shielded ($\Delta\delta_H \approx$ –0.07 to –0.13 ppm).

The same protons which experience a deshielding by pairing with Cl$^-$ are shielded in the **1a** BPh$_4^-$ ion pairs (Table 3): $\Delta\delta_H \approx$ –0.38 ppm for C(α)–H, $\Delta\delta_H \approx$ –0.16 and $\approx$ –0.12 ppm for the *ortho*-protons of the PPh$_3$ and benzyl groups, respectively. The changes in the chemical shifts of the other protons are in the same direction and of the same magnitude ($\Delta\delta_H \approx$ –0.08 to –0.11 ppm) as in **1a**Cl$^-$.

The ^{31}P NMR signals ($\Delta\delta_P \approx$ +1.5 ppm when going from **1a** BPh$_4^-$ to **1a**Cl$^-$) and the ^{13}C NMR signals of **1a**, including those of C(α), vary only little with the counteranion X$^-$ (Table 3).

NMR Signals of the anions X$^-$ in CD$_2$Cl$_2$ solution

Figure 4a shows the ^{19}F NMR (376 MHz) spectrum of **2a** BF$_4^-$ in CD$_2$Cl$_2$ at a concentration where the salt exists as ion pairs (6×10^{-2} M). We observed a 1:1:1:1 quartet ($^1J_{F,B} \approx$ 1.2 Hz) at $\delta_F = -152.0$ ppm for the main isotopomer, ^{11}BF$_4^-$ ($I = \frac{3}{2}$ for the ^{11}B nucleus), together with the unresolved signal for the ^{10}B ($I = 3$) isotopomer about 0.05 ppm further downfield. The corresponding signal of the boron atom in the ^{11}B NMR (128 MHz) spectrum is at $\delta_B = -2.0$ ppm.

The ^{19}F NMR is sensitive enough so that we could also determine the fluorine chemical shift of the BF$_4^-$ anion at a concentration of 2×10^{-5} M, where **2a** BF$_4^-$ exists as free ions in CD$_2$Cl$_2$ (Figure 4b). Under these conditions, the signal for the main isotopomer is found at $\delta_F \approx -153.4$ ppm, which is upfield by $\Delta\delta_F \approx -1.4$ ppm compared to the paired **2a** BF$_4^-$ salt.

Figure 4c and d show the heteronuclear NMR spectra of a ca. 6×10^{-2} M solution of **2a** SbF$_6^-$ in CD$_2$Cl$_2$. The antimony isotopes ^{121}Sb ($I = \frac{5}{2}$) and ^{123}Sb ($I = \frac{7}{2}$) have similar natural abundances and comparable magnetogyric ratios ($\gamma = 6.4435 \times 10^7$ and 3.4892×10^7 rad T^{-1} s^{-1}, respectively).[33] The ^{19}F NMR spectrum of **2a** SbF$_6^-$ in CD$_2$Cl$_2$ (Figure 4c) thus features two superimposed signals at $\delta_F = -123.6$ ppm: a sextet with $^1J_{F,Sb} \approx$ 1950 Hz for ^{121}SbF$_6^-$ and an octet with $^1J_{F,Sb} \approx$ 1020 Hz for ^{123}SbF$_6^-$. The ratio of the $^1J_{F,Sb}$ coupling constants of the two isotopomers corresponds to the ratio of the magnetogyric ratios of the antimony isotopes (i.e., the reduced coupling constants, which are proportional to $^1J_{F,Sb}/\gamma_{Sb}$, are the same for both isotopomers). The coupling constant of $^1J_{Sb,F} \approx$ 1960 Hz is also found in the ^{121}Sb NMR (65 MHz) spectrum, in which five lines of the septet at $\delta_{Sb} \approx 86.2$ ppm are observed (Figure 4d). Due to the broadness of the signal, we could not detect the ^{19}F NMR signal of
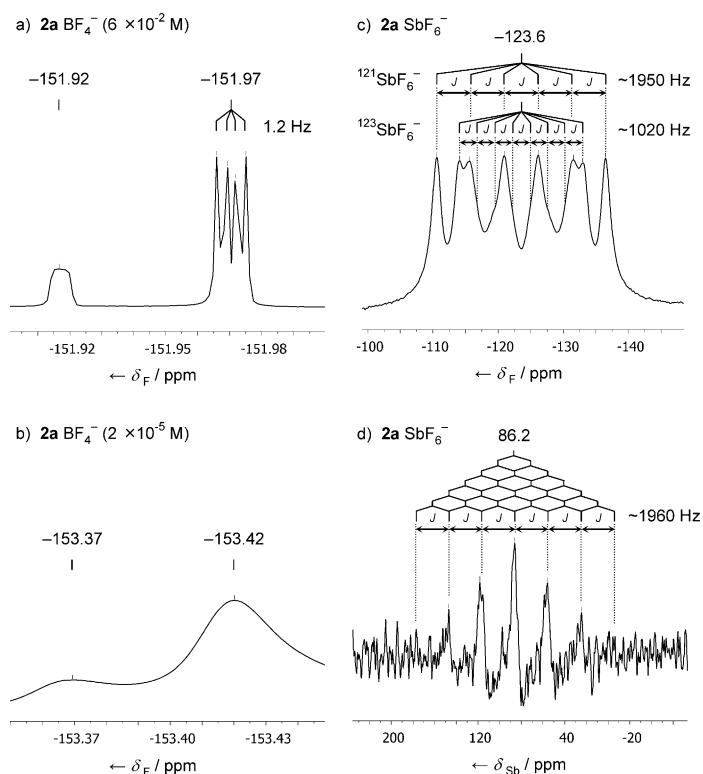
Ion-Pairing of Phosphonium Salts in Solution

FULL PAPER

a) **2a** BF$_4^-$ (6 ×10^{-2} M)

−151.92   −151.97

1.2 Hz

-151.92   -151.95   -151.98

← δ_F / ppm

b) **2a** BF$_4^-$ (2 ×10^{-5} M)

−153.37   −153.42

-153.37   -153.40   -153.43

← δ_F / ppm

c) **2a** SbF$_6^-$

−123.6

^{121}SbF$_6^-$ J J J J J J   ~1950 Hz

^{123}SbF$_6^-$ ~1020 Hz

-100   -110   -120   -130   -140

← δ_F / ppm

d) **2a** SbF$_6^-$ 86.2

J J J J J J J   ~1960 Hz

200   120   40   -20

← δ_{Sb} / ppm

Figure 4. Left: ^{19}F NMR spectra (376 MHz) of **2a** BF$_4^-$ in CD$_2$Cl$_2$ at concentrations of a) 6×10^{-2} M, or b) 2×10^{-5} M. Right: c) ^{19}F NMR spectrum (376 MHz) and d) ^{121}Sb NMR spectrum (65 MHz) of **2a** SbF$_6^-$ in CD$_2$Cl$_2$ (ca. 0.06 M).

2a SbF$_6^-$ at lower concentrations, where the salt is mostly unpaired.

The NMR data for the BF$_4^-$ and SbF$_6^-$ anions shown in Figure 4 a,c,d indicate a very high symmetry of the anions despite the fact that these spectra were recorded under conditions where the phosphonium salts predominantly exist as ion pairs. This indicates that all fluorine atoms are equivalent on the NMR time scale. The interaction between the BF$_4^-$ anion and the phosphonium ion **2a** can only be noticed by the slight downfield shift of the signal by $\Delta\delta_F \approx -1.4$ ppm, which indicates the averaged effect over four fluorine atoms.

We also had a closer look at the NMR data of the BPh$_4^-$ anions in concentrated solutions of **1a,b** BPh$_4^-$ in CD$_2$Cl$_2$. However, the ^{11}B, ^{1}H, and ^{13}C NMR signals of the BPh$_4^-$ anion in the phosphonium salts **1a,b** BPh$_4^-$ in CD$_2$Cl$_2$ do not differ significantly from those of the free BPh$_4^-$ ions or those of **2a** BPh$_4^-$ which does not show any "BPh$_4^-$ effect" (Table S4 in the Supporting Information).

Dissociation constants of the phosphonium salts in CD$_2$Cl$_2$

The large differences between the C(α)−H proton chemical shifts of the unpaired phosphonium ions (e.g., $\delta_{H,unpaired} = 5.77$ ppm for **2a**) and the paired phosphonium ions ($\delta_{H,paired}$ = maximum δ_H for the α proton measured at the highest concentration of the salts; see Tables 2, S1, and S2)

allow us to derive the mole fractions of the paired phosphonium ions, $x_{paired,exptl}$ [Eq. (1)].

$$x_{paired,exptl} = \frac{\delta_H - \delta_{H,unpaired}}{\delta_{H,paired} - \delta_{H,unpaired}} \qquad (1)$$

At phosphonium salt concentrations where $x_{paired,exptl} \approx 0.5$, we estimated the dissociation constants K_D (M) for **1a,b**X$^-$ and **2a**X$^-$ in CD$_2$Cl$_2$ as defined by Equation (2) in which [R$_4$P$^+$X$^-$]$_0$ is the total salt concentration. The resulting values are listed in Table 4.

$$K_D = \frac{[R_4P^+]_{unpaired} \cdot [X^-]_{unpaired}}{[R_4P^+X^-]_{paired}} = \frac{(1 - x_{paired,exptl})^2}{x_{paired,exptl}} \cdot [R_4P^+X^-]_0 \qquad (2)$$

Table 4. Dissociation constants K_D [M] for phosphonium salts **1a,b**X$^-$ and **2a**X$^-$ with different counter-anions X$^-$ in CD$_2$Cl$_2$.

X$^-$	ΔG_{acid}[a] [kcal mol^{-1}]	ΔG_t^{0}[b] [kJ mol^{-1}]	K_D[c] [M] **1a**X$^-$	**1b**X$^-$	**2a**X$^-$
BPh$_4^-$	—[d]	−32.8	2.5×10^{-4}	1.1×10^{-4}	[e]
SbF$_6^-$	256	—[d]	[f]	[f]	6×10^{-4}
BF$_4^-$	288	(~0)[g]	(1×10^{-4})	(5×10^{-5})	2.2×10^{-4}
Br$^-$	315	31.3	[f]	2.9×10^{-5}	7.6×10^{-5}
Cl$^-$	324	42.1	6.8×10^{-5}	[f]	3.4×10^{-5}
pK_a for C(α)−H in DMSO:			17.6[h]	14.6[h]	(~9)[i]

[a] Calculated ΔG_{acid} (298 K) for deprotonation of the conjugate acids HX in the gas phase.[34] [b] Single free ion energies of transfer ΔG_t^0 (H$_2$O → CH$_3$CN, 25 °C) for the anions X$^-$.[30] [c] Dissociation constants in CD$_2$Cl$_2$ based on δ_H of the C(α)−H protons; this work. [d] Not available. [e] No effect of X$^-$ on δ_H of the C(α)−H protons. [f] Not determined. [g] For BF$_4^-$, $\Delta G_t^0 \approx 0$ was estimated.[35] [h] From ref. [6]. [i] Estimated from the correlation equation published in ref. [5] and pK_a 30.6 for Ph$_2$CH$_2$.[29]

With this method, more reliable values of K_D can be obtained than by evaluating K_D from all investigated solutions, which also include those in which paired or non-paired species are highly dominating. The mole fractions of unpaired ions $x_{paired,calcd}$ calculated from these K_D values are in fair agreement with the experimental values $x_{paired,exptl}$ (Tables 2, S1, S2). The K_D values for **1a,b** BF$_4^-$ are only rough estimates, as the effect of ion pairing on δ_H is small for these salts ($\Delta\delta_H \approx 0.17$ to 0.23 ppm for C(α)−H protons) and we cannot determine $\delta_{H,unpaired}$ for the unpaired ions **1a,b** very accurately.

The dissociation constants K_D determined in this manner decrease in the order SbF$_6^-$ > BF$_4^-$ > Br$^-$ > Cl$^-$ (Table 4). Thus, the degree of association of the phosphonium salts increases with the deshielding of the C(α)−H protons in the respective ion pairs (SbF$_6^-$ < BF$_4^-$ < Br$^-$ < Cl$^-$). In agreement with the higher C(α)−H acidity of **1b** compared with **1a**,[6] the dissociation constants K_D for all **1b**X$^-$ salts are smaller than those for the corresponding **1a**X$^-$ salts (e.g., K_D of **1b** Br$^-$ is already smaller than that of **1a** Cl$^-$ although

J. Ammer, K. Karaghiosoff et al.

Cl^- is more basic than Br^-) (Table 4). Since **2a** has an even higher $C(\alpha)-H$ acidity than **1b**, one might also expect lower dissociation constants K_D for **2a**X^- than for **1b**X^-. On the contrary, the K_D values for **2a**X^- are higher than for **1b**X^- (Table 4), that is, the salts **2a**X^- dissociate more readily. The reason for this may be a combination of steric hindrance and a statistical effect due to the fact that there is only one $C(\alpha)-H$ proton in the benzhydryl derivatives **2a**X^- but two in the benzyl derivatives **1b**X^-.

It should be noted, however, that the differences in K_D are rather small, and all K_D values are in the same order of magnitude as previously reported for benzhydrylium, tritylium, pyrylium, and tetraalkylammonium salts in CH_2Cl_2.[36]

Effect of the solvent: ^1H NMR Signals for α protons of **2a** in CD_3CN solution

In CD_3CN, variation of the counteranion X^- has a much smaller effect on the ^1H NMR chemical shifts of $C(\alpha)-H$ of **2a** X^- than in CD_2Cl_2. As in CD_2Cl_2, the δ_H values for **2a**BPh_4^- do not vary with the concentration ($\delta_H = 6.27$ ppm, Figure 5). The very similar δ_H for **2a**BF_4^- and **2a**SbF_6^- suggest that these compounds are also mostly unpaired at concentrations of $\sim 1 \times 10^{-2}$ M in CD_3CN.

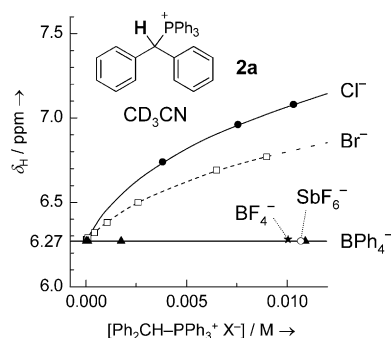Figure 5. Concentration-dependent ^1H NMR (600 MHz, 27 °C) chemical shifts δ_H of the benzylic $C(\alpha)-H$ protons of **2a**X^- with different counteranions $X^- = Cl^-$ (●), Br^- (□), BF_4^- (★), SbF_6^- (○), or BPh_4^- (▲) in CD_3CN.

The chemical shifts of $\delta_H \leq 6.29$ ppm determined for the $C(\alpha)-H$ protons of **2a** Br^- in CD_3CN at concentrations $\leq 1 \times 10^{-4}$ M indicate that ion pairing is negligible in this concentration range (Table S5 in the Supporting Information). At larger concentrations, the phosphonium halides do form ion pairs to some extent. However, the δ_H values of the phosphonium halides in CD_3CN do not reach a plateau in the concentration range where **2a** Br^- is soluble in CD_3CN ($< 1 \times 10^{-2}$ M). Therefore, we cannot estimate the degree of ion pairing or the dissociation constants K_D in CD_3CN from the NMR data.

Effect of $C(\alpha)-H$ acidity: Substituent effects on the NMR spectra of phosphonium salts
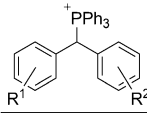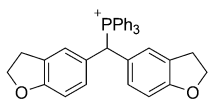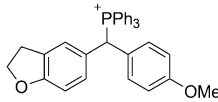
In a series of benzhydryl triphenylphosphonium salts $Ar_2CH-PPh_3^+$ X^- (**2**X^-) with different Ar groups, the acidities of the $C(\alpha)-H$ groups increase with the electron-withdrawing character of the substituents on the benzhydryl moiety. The series of substituted benzhydryl triphenylphosphonium tetrafluoroborates **2a–t**BF_4^- (Table 5), which we required for our laser flash photolysis experiments,[19] can thus be employed to study the interaction between $C(\alpha)-H$ and BF_4^- as a function of $C(\alpha)-H$ acidity.

The NMR data for the **2a–t**BF_4^- ion pairs in CD_2Cl_2 solution are collected in Table 5, where the salts **2a–t**BF_4^- are arranged according to the sums of their substituents' σ^- parameters.[37] We use the σ^- parameters as a measure for the $C(\alpha)-H$ acidities of the phosphonium ions here, because the pK_a values of **2a–t**BF_4^- are not available and the pK_a values of the closely related benzyl triphenylphosphonium salts in DMSO have been shown to correlate with the σ^- parameters of the benzyl substituents.[6] The ^1H NMR chemical shifts of the $C(\alpha)-H$ protons increase from $\delta_H \approx 6.04$ to ≈ 6.80 ppm when the substituents of the benzhydryl group are varied from electron-donating (**2b**) to strongly electron-withdrawing (**2s** or **2t**). Figure S1 in the Supporting Information displays a moderate correlation of δ_H for the $C(\alpha)-H$ protons of **2**BF_4^- with the sums of the σ^- parameters.

If the observed increase of δ_H of the $C(\alpha)-H$ protons and the less pronounced concomitant variations in δ_C of the $C(\alpha)$ atom and δ_P of the phosphorus atom (Table 5) are linked with stronger interactions with the BF_4^- anion, one should also observe the effect in the ^{19}F NMR spectra of the BF_4^- ions. Indeed, the ^{19}F NMR chemical shifts for $^{11}BF_4^-$ increase from $\delta_F \approx -152.2$ to ≈ -150.4 ppm when going from **2b** BF_4^- to **2t**BF_4^- (Figure 6 and Table 5). Thus, the greater the $C(\alpha)-H$ acidity of the phosphonium ion **2**, the larger the upfield shift $\Delta\delta_F$ for the BF_4^- anion due to the increasing strength of ion pairing with the phosphonium ion. The increasing $C(\alpha)-H$ acidity from **2a**BF_4^- ion pairs to **2t**BF_4^- ion pairs causes approximately the same shifts in the ^1H and ^{19}F NMR signals ($\Delta\delta_H \approx +0.45$ ppm and $\Delta\delta_F \approx +1.6$ ppm) as going from the free ions **2a** and BF_4^- to the **2a**BF_4^- ion pairs ($\Delta\delta_H \approx +0.46$ ppm and $\Delta\delta_F \approx +1.4$ ppm) (Figure 6). In analogous series of neutral benzhydryl derivatives such as benzhydryl halides, substituent variations induce considerably smaller changes of δ_H for the $C(\alpha)-H$ protons in the other direction (see Figure S1 in the Supporting Information).

Moreover, the α protons of the *unpaired* benzyl triphenylphosphonium ions $PhCH_2-PPh_3^+$ (**1a**) and $p-(CF_3)-C_6H_4-CH_2-PPh_3^+$ (**1b**) have very similar δ_H values despite the differing substitution patterns (see Tables S1 and S2 in the Supporting Information). All these observations suggest that the variations in δ_H of the benzhydryl methine protons observed for the ion pairs of the differently substituted benzhydryl triphenylphosphonium tetrafluoroborates **2**BF_4^-

Ion-Pairing of Phosphonium Salts in Solution

FULL PAPER

Table 5. Selected NMR data for triphenylphosphonium tetrafluoroborates **2a–t**BF$_4^-$ in CD$_2$Cl$_2$ solution under conditions where the phosphonium salts exist as ion pairs.

Salt	R^1	R^2	Σσ^{-}[a]	P$^+$−C(α)−H δ$_H$ [ppm] ($^2J_{H,P}$ [Hz])	δ$_C$ [ppm] ($^1J_{C,P}$ [Hz])	δ$_P$ [ppm]	^{11}BF$_4^-$[b] δ$_F$ [ppm] ($^1J_{F,B}$ [Hz])
ion pairs							
2bBF$_4^-$			—[c]	6.04 (17.2)	49.1 (42.8)	20.5	−152.2 (—[d])
2cBF$_4^-$			—[c]	6.04 (17.2)	48.9 (43.1)	20.6	−152.3 (—[d])
2dBF$_4^-$	*p*-OMe	*p*-OMe	−0.52	6.15 (17.3)	48.2 (43.2)	20.8	−152.1 (—[d])
2eBF$_4^-$	*p*-OMe	*p*-Me	−0.43	6.08 (17.2)	48.9 (43.5)	21.0	−152.4 (1.0)
2fBF$_4^-$	*p*-OMe	*p*-OPh	−0.36	6.18 (17.4)	48.4 (43.5)	21.0	−152.1 (1.1)
2gBF$_4^-$	*p*-Me	*p*-Me	−0.34	6.04 (17.2)	49.4 (43.6)	21.1	−152.3 (1.1)
2hBF$_4^-$	*p*-OMe	H	−0.26	6.20 (17.2)	48.9 (43.5)	21.3	−152.1 (1.1)
2iBF$_4^-$	*p*-Me	H	−0.17	6.20 (17.4)	49.1 (43.8)	21.5	−152.2 (1.1)
2jBF$_4^-$	*p*-OPh	H	−0.10	6.31 (17.4)	48.6 (43.8)	21.5	−151.8 (1.1)
2kBF$_4^-$	*p*-F	*p*-F	−0.06	6.49 (17.7)	47.3 (44.7)	21.9	−151.3 (—[d])
2lBF$_4^-$	*p*-F	H	−0.03	6.40 (17.5)	48.1 (44.3)	21.9	−151.5 (1.2)
2aBF$_4^-$	H	H	0.00	6.23 (17.4)	49.6 (43.9)	21.8	−152.0 (1.2)
2mBF$_4^-$	*m*-F	H	0.34	6.39 (17.5)	48.5 (44.5)	22.0	−151.6 (1.1)
2nBF$_4^-$	*p*-Cl	*p*-Cl	0.38	6.48 (17.7)	47.4 (44.6)	21.8	−151.2 (1.2)
2oBF$_4^-$	*p*-CF$_3$	H	0.65	6.53 (17.7)	48.4 (44.7)	22.1–22.2	−151.4 (1.2)
2pBF$_4^-$	*m,m'*-F$_2$	H	0.68	6.51 (17.5)	47.9 (45.1)	22.2	−151.4 (1.2)
2qBF$_4^-$	*m*-F	*m*-F	0.68	6.52 (17.6)	47.7 (45.0)	22.3	−151.1 (1.2)
2rBF$_4^-$	*m,m'*-F$_2$	*m*-F	1.02	6.61 (17.6)	47.1 (45.6)	22.5	−150.8 (1.3)
2sBF$_4^-$	*p*-CF$_3$	*p*-CF$_3$	1.30	6.80 (17.8)	47.5 (45.3)	22.4–22.5	−150.7 (—[d])
2tBF$_4^-$	*m,m'*-F$_2$	*m,m'*-F$_2$	1.36	6.68 (17.6)	46.6 (46.2)	22.6	−150.4 (1.3)
"free" ions							
2a[e,g]	H	H	0.00	5.77 (17.0)	—[c]	—[c]	−
BF$_4^-$[f,g]	−	−	−	−	−	−	−153.4 (—[d])

[a] From ref. [37]. [b] Isotopomer signal for ^{10}BF$_4^-$ downfield by $\Delta\delta_F < +0.1$ ppm. [c] Not available. [d] Not resolved. [e] Determined from ^{1}H NMR (600 MHz) spectrum of a 2.13×10^{-5} M solution of **2a** SbF$_6^-$ in CD$_2$Cl$_2$. [f] Determined from ^{19}F NMR (376 MHz) spectrum of a ~2×10^{-5} M solution of **2a** BF$_4^-$ in CD$_2$Cl$_2$. [g] At the employed concentrations, the salts predominantly exist in the form of the free (unpaired) ions.
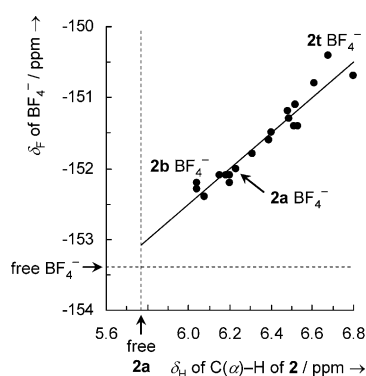
Figure 6. Correlation of ^{19}F NMR (376 MHz) chemical shifts δ_F of the BF$_4^-$ anions versus the ^{1}H NMR (400 MHz) chemical shifts δ_H of the C(α)−H protons of the phosphonium ions **2** in the ion pairs **2a–t**BF$_4^-$ in CD$_2$Cl$_2$ ($\delta_F = 2.51\delta_H - 167.54$; $R^2 = 0.9299$). The dashed lines show the chemical shifts of the free ions **2a** and BF$_4^-$.

The C(α)−H acidities of the benzhydryl triarylphosphonium ions Ar$_2$CH−PAr$_3^+$X$^-$ are also affected by variation of the PAr$_3$ moiety. Table S6 in the Supporting Information illustrates that the δ_H values for the C(α)−H protons for the tris(4-chlorophenyl)phosphonium salts Ar$_2$CH−P(*p*-Cl-C$_6$H$_4$)$_3^+$BF$_4^-$ (**3**BF$_4^-$) are 0.15 to 0.48 ppm higher and the δ_F values for the BF$_4^-$ anion are 0.7 to 2.1 ppm higher than for the corresponding triphenylphosphonium salts Ar$_2$CH−PPh$_3^+$BF$_4^-$ (**2**BF$_4^-$). Thus, electron-withdrawing substituents in the triphenylphosphonium group have analogous effects on δ_H and δ_F as substituents in the benzhydryl group.

mainly result from the different interactions of the methine protons with the BF$_4^-$ anions.

Calculations and X-ray Analyses

To learn more about the structure of the phosphonium salt ion pairs in solution, we will now compare the NMR data with the results of quantum chemical calculations as well as with the C−H···X$^-$ interactions in the crystals. The structural

features in solution and in the crystals resemble each other and will therefore be discussed together for each compound.

Strong hydrogen bonds are characterized by short H···X⁻ distances and C−H···X⁻ angles close to 180°, but there are no clear cut-off criteria to decide whether a C−H···X⁻ contact should be considered as a hydrogen bond. According to the latest IUPAC definition of the hydrogen bond,[8] weak hydrogen bonds may also be longer than the sum of the van der Waals radii, and the angle of a hydrogen bond "should preferably be above 110°". In the calculated solution structures, as well as in the crystal structures, we have considered all H···X⁻ distances up to 2.90 Å, and also added some notable longer contacts, the most important of which are shown as dashed lines in the Figures. Particularly short (shorter than the sum of the van der Waals radii)[38] or close to linear contacts (C−H···X⁻ angle ≥ 160°) are indicated by bold type in the Tables listing the lengths and angles of the C−H···X⁻ contacts.

Benzhydryl triphenylphosphonium salts (2a X⁻)

Calculated structures in CH₂Cl₂ solution: The solution-phase structures of the salts **2a** X⁻ in dichloromethane (Figure 7a–d) were determined by DFT calculations on the M06-2X 6-31+G(d,p) level of theory with a polarizable continuum model to describe the effect of the solvent.[39–43] The solution structure of the BPh₄⁻ salt was not calculated due to the large size of the ions. Table 6 lists the distances and angles of the C−H···X⁻ contacts in the ion pairs.

Crystal structures: Crystal structures of salts of the Ph₂CH−PPh₃⁺ cation (**2a**) have not been described previously. In this work, we have therefore determined the crystal structures of the same salts **2a** X⁻ which we have investigated in solution. Only **2a** BPh₄⁻ crystallizes as very long thin needles, and we could not obtain single crystals of sufficient size in all three dimensions to determine the structure of this salt by X-ray diffraction. In each of the crystal structures, the phosphonium ions have many C−H···X⁻ interactions with one particular anion and fewer contacts with other anions (Figure 7e–h). The solid state structures thus resemble the 1:1 ion pairs which are present in solution (Figure 7a–d). Table 7 lists the distances and angles of the closest C−H···X⁻ contacts in the crystals.

Benzhydryl triphenylphosphonium chloride (2a Cl⁻): The calculated structure of **2a** Cl⁻ in CH₂Cl₂ (Figure 7a) shows two strong hydrogen bonds between the Cl⁻ anion and the C(α)−H and one o-PPh₃ proton (H19···Cl distance 2.44 Å and C19−H19···Cl angle 176°; H2···Cl distance 2.52 Å and C2−H2···Cl angle 176°) (Table 6). The positioning of the chloride anion near the C(α)−H and o-PPh₃ protons is further stabilized by two weaker hydrogen bonds to o-CPh₂ protons of both phenyl rings of the benzhydryl group (H31···Cl distance 2.81 Å and C31−H31···Cl angle 147°; H25···Cl distance 3.13 Å and C25−H25···Cl angle 140°).

These interactions seem to be so favorable that they are also found in the crystal (Figure 7e), which shows two short contacts between Cl⁻ and the C(α)−H as well as one o-CPh₂ proton (H19···Cl distance 2.49 Å and C19−H19···Cl angle 166°; H31···Cl distance 2.82 Å, C31−H31···Cl angle 147°), but a significantly longer distance between the Cl⁻ anion and the o-PPh₃ proton (H2···Cl distance 3.00 Å and C2−H2···Cl angle 161°) (Table 7). The packing of the molecules is controlled by additional C−H···Cl⁻ hydrogen bonds involving some of the *meta*- and *para*-protons of the PPh₃ group, resulting in a different orientation of the phenyl groups compared to the solution structure. Particularly strong is the C−H···Cl⁻ interaction for one of the p-PPh₃ protons (H10···Cl distance 2.58 Å and C10−H10···Cl angle 171°). Thus, the distances and angles for the two shortest C−H···Cl⁻ interactions in crystals of **2a** Cl⁻ come very close to the typical values of O−H···Cl⁻ hydrogen bonds.[3]

Benzhydryl triphenylphosphonium bromide (2a Br⁻): The calculated structure of the **2a** Br⁻ ion pair in CH₂Cl₂ (Figure 7b) closely resembles that of the chloride (Figure 7a); only the distances between the hydrogen (or carbon) atoms and the halide ion are longer by 0.1 to 0.2 Å (Table 6).

Again, a similar motif is found in the **2a** Br⁻ crystal (Figure 7f and Table 7): The strongest interactions between cation and anion are the hydrogen bonds between the Br⁻ anion and the C(α)−H and o-PPh₃ protons (H7···Br distance 2.90 Å and C7−H7···Br angle 172°; H6···Br distance 2.85 Å, C6−H6···Br angle 167°), as well as the interaction of one m-PPh₃ proton with a second bromide anion (H16···Br distance 2.81 Å and C16−H16···Br angle 151°). Weaker interactions are observed between Br⁻ and the o-CHPh₂ protons as well as another o-PPh₃ proton, but these are already in the same range as the interactions between Br⁻ and various phenyl protons of further surrounding phosphonium ions (≥ 3.0 Å).

Benzhydryl triphenylphosphonium tetrafluoroborate (2a BF₄⁻): In the calculated structure of **2a** BF₄⁻ in CH₂Cl₂ solution (Figure 7c), the C(α)−H (H19) as well as one o-PPh₃ (H12) and one o-CPh₂ proton (H31) show bifurcated hydrogen bonds with two of the fluorine atoms (F2 and F3) (Table 6). Additionally, the o-PPh₃ proton (H12) has a third C−H···F−BF₃⁻ interaction with a third fluorine atom (F1), and the second phenyl group of the benzhydryl moiety also shows one contact between o-CPh₂ (H25) and F−BF₃⁻ (F3).

In the **2a** BF₄⁻ crystal, all fluorine atoms of the BF₄⁻ anion exhibit multifurcated hydrogen bonds to several surrounding phosphonium ions. The usual pattern of close interactions between the anion and the C(α)−H proton (H19), one o-PPh₃ (H12), and one o-CPh₂ proton (H31) is also found (Figure 7g and Table 7), but it differs a bit from the calculated structure in solution. Again, the shortest contact is the C(α)−H···F−BF₃⁻ interaction (H19···F2 distance 2.23 Å and C19−H19···F2 angle 158°), but in the crystal, only the o-PPh₃ proton (H12) shows bifurcated hydrogen bonds, while the other interactions are directed towards only one of the fluorine atoms. The fourth close C−H···F−

Ion-Pairing of Phosphonium Salts in Solution

FULL PAPER

calculated structures in solution

X-ray structures of the crystals

Symmetry codes:
[c] −1+x, y, z
[e] 0.5−x, −0.5+y, 0.5−z
[g] −0.5+x, 0.5−y, −0.5+z

[x] Selected distances (Å)
and angles (°) for C(α):
C19−P1: 1.851(3)
C19−C26: 1.522(4)
C19−C20: 1.537(4)
P1−C19−C26: 114.1(2)
P1−C19−C20: 112.0(2)
C20−C19−C26: 114.5(2)

Symmetry codes:
[e] 0.5+x, 1.5−y, 0.5+z
[l] 0.5+x, 0.5+y, z
[i] x, 1−y, −0.5+z
[h] x, 1+y, z

[x] Selected distances (Å)
and angles (°) for C(α):
C7−P1: 1.833(5)
C7−C30: 1.536(7)
C7−C8: 1.553(7);
P1−C7−C30: 114.0(3)
P1−C7−C8: 112.8(3)
C8−C7−C30: 112.3(4)

Symmetry codes:
[a] x, 1−y, 0.5+z
[b] 0.5+x, 1.5−y, 0.5+z
[g] 0.5+x, 1.5−y, 0.5+z
[h] x, 1−y, −0.5+z
[e] x, −1+y, z

[x] Selected distances (Å)
and angles (°) for C(α):
C19−P1: 1.855(4)
C19−C26: 1.530(5)
C19−C20: 1.541(4)
P1−C19−C26: 113.8(2)
P1−C19−C20: 111.9(2)
C20−C19−C26: 112.1(3)

Symmetry codes:
[g] −0.5+x, 0.5−y, 0.5+z
[c] 1.5−x, −0.5+y, 0.5−z
[j] −0.5+x, 0.5−y, −0.5+z
[a] 0.5−x, −0.5+y, 0.5−z
[e] −1+x, y, z

[x] Selected distances (Å)
and angles (°) for C(α):
C13−P1: 1.863(5)
C13−C14: 1.536(7)
C13−C20: 1.519(7)
P1−C13−C14: 115.1(3)
P1−C13−C20: 110.0(3)
C20−C13−C14: 115.8(4)

Figure 7. a)–d) Calculated structures of Ph$_2$CH−PPh$_3$$^+$ X$^−$ (**2a**X$^−$) ion pairs in CH$_2$Cl$_2$ solution: a) **2a**Cl$^−$, b) **2a**Br$^−$, c) **2a**BF$_4$$^−$, d) **2a**SbF$_6$$^−$. The numbering corresponds to the atom numbers in the crystal structures. e)–h) X-ray structures of the salts Ph$_2$CH−PPh$_3$$^+$ X$^−$ (**2a**X$^−$): e) **2a**Cl$^−$, f) **2a**Br$^−$, g) **2a**BF$_4$$^−$, h) **2a**SbF$_6$$^−$. All C−H⋯X$^−$ contacts with d(H⋯X$^−$) ≤ 2.90 Å are shown as orange lines, selected longer contacts are indicated by dashed lines. For C−H⋯X$^−$ bond lengths and angles, see Tables 6 and 7.

Table 6. Calculated distances and angles of C−H···X⁻ contacts in Ph₂CH−PPh₃⁺ X⁻ (**2a** X⁻) ion pairs in CH₂Cl₂ solution.

Salt	Donor[a]	Acceptor[a]	d(C−H)	d(H···X⁻) [Å]	d(C···X⁻) [Å]	∡(C−H···X⁻) [°]
2a Cl⁻	H19 (α-H)	Cl1	1.1022	**2.44**	3.54	**176**
	H2	Cl1	1.0907	**2.52**	3.61	**176**
	H31	Cl1	1.0881	**2.81**	3.77	147
	H21	Cl1	1.0869	3.13	4.02	140
2a Br⁻	H7 (α-H)	Br1	1.1021	**2.64**	3.74	**177**
	H6	Br1	1.0901	**2.68**	3.77	**178**
	H25	Br1	1.0877	**2.93**	3.92	152
	H13	Br1	1.0869	3.24	4.14	141
2a BF₄⁻	H19 (α-H)	F2	1.0968	**2.30**	3.24	142
	H19 (α-H)	F3		**2.20**	3.23	156
	H12	F2	1.0861	**2.25**	3.29	158
	H12	F1		**2.38**	3.29	140
	H12	F3		2.66	3.56	140
	H31	F2	1.0863	2.57	3.32	126
	H31	F3		2.71	3.63	142
	H25	F3	1.0857	2.57	3.32	125
2a SbF₆⁻	H13 (α-H)	F4	1.0977	**2.28**	3.28	151
	H13 (α-H)	F5		**2.44**	3.37	141
	H2	F4	1.0860	2.74	3.45	122
	H2	F5		**2.30**	3.36	165
	H2	F2		**2.42**	3.19	126
	H3	F2	1.0848	2.66	3.30	117
	H21	F5	1.0865	2.59	3.34	126
	H21	F3		**2.44**	3.50	**165**
	H15	F4	1.0852	**2.54**	3.22	120

[a] See Figure 7 for numbering of atoms.

Table 7. Distances and angles of C−H···X⁻ contacts in crystals of Ph₂CH-PPh₃⁺ X⁻ (**2a** X⁻).

Salt	Donor[a]	Acceptor[a]	Code[a]	d(H···X⁻) [Å]	d(C···X⁻) [Å]	∡(C−H···X⁻) [°]
2a Cl⁻	H19 (α-H)	Cl1	–	**2.49(3)**	**3.444(3)**	**166(2)**
	H31	Cl1	–	**2.82**	3.654(3)	147
	H2	Cl1	–	3.00	3.913 (3)	**161**
	H21	Cl1	–	3.20	3.900(3)	132
	H10	Cl1	e	**2.58**	3.526(3)	**171**
	H5	Cl1	c	**2.76**	3.573(3)	144
	H11	Cl1	g	**2.81**	3.526(3)	133
2a Br⁻	H7 (α-H)	Br1	–	**2.90**	3.894(5)	**172**
	H6	Br1	–	**2.85**	3.781(5)	**167**
	H13	Br1	–	3.19	4.000(5)	144
	H25	Br1	–	3.14	4.024(5)	156
	H24[b]	Br1	–	3.68	4.491(5)	146
	H16	Br1	e	**2.81**	3.672(6)	151
	H20	Br1	l	3.02	3.915(6)	158
	H22	Br1	i	3.05	3.734(5)	131
	H23	Br1	i	3.22	3.828(5)	123
	H28	Br1	h	3.38	4.267(5)	156
2a BF₄⁻	H19 (α-H)	F2	e	**2.23**	3.218(4)	158
	H18	F2	e	2.59	3.340(4)	136
	H12	F2	e	**2.53**	3.329(4)	141
	H12	F1	e	2.80	3.450(4)	127
	H31	F2	e	2.73	3.423(4)	130
	H23	F1	a	**2.44**	3.259(4)	144
	H24	F2	a	2.84	3.643(5)	143
	H3	F2	b	**2.54**	3.467(3)	**164**
	H3	F4	b	2.67	3.236(4)	119
	H4	F4	b	2.70	3.247(4)	117
	H8	F3	g	**2.56**	3.482(5)	**163**
	H14	F3	g	2.59	3.527(4)	**170**
	H14	F4	g	2.62	3.192(4)	119
	H15	F4	g	2.60	3.179(5)	120
	H16	F1	h	**2.29**	3.221(4)	**167**
	H17	F3	h	2.62	3.357(4)	135
	H28	F4	–	**2.48**	3.407(4)	**164**
2a SbF₆⁻	H13 (α-H)	F4	a	2.67	3.505(5)	151
	H13 (α-H)	F5	a	2.84	3.683(5)	153
	H2	F5	a	**2.42**	3.372(6)	**178**
	H2	F2	a	2.72	3.293(5)	120
	H3	F2	a	2.60	3.234(5)	125
	H21[b]	F3	a	3.16	4.096(5)	**169**
	H25	F1	e	2.85	3.561(6)	133
	H19	F1	e	2.58	**3.074(5)**	113
	H29	F3	e	2.74	3.208(5)	111
	H31	F2	–	2.59	3.265(5)	129
	H30	F2	–	2.80	3.365(6)	119
	H10	F5	g	2.66	3.373(6)	132
	H11[b]	F5	g	2.95	3.511(6)	119
	H8	F3	c	**2.50**	**3.097(6)**	121
	H9	F3	c	**2.53**	**3.114(6)**	120
	H4	F4	j	**2.54**	3.374(6)	147
	H5	F6	j	2.76	3.571(6)	144

[a] See Figure 7 for numbering of atoms and symmetry codes. [b] These contacts are not shown in Figure 7.

BF₃⁻ contact is now to a second *o*-P*Ph*₃ proton (H18) instead of the second *o*-C*Ph*₂ proton. This subtle variation between the solution and crystal structures is caused by the additional interactions between BF₄⁻ and the other surrounding phosphonium ions in the crystal (Figure 7g and Table 7).

Benzhydryl triphenylphosphonium hexafluoroantimonate (2a SbF₆⁻): According to the calculations, the fluorine atoms of the SbF₆⁻ anions in the **2a** SbF₆⁻ ion pairs in CH₂Cl₂ solution also form multifurcated hydrogen bonds (Figure 7d and Table 6). The C(α)−H proton forms a short bifurcated hydrogen bond with two of the fluorine atoms (H13···F4 distance 2.28 Å and C13−H13···F4 angle 151°; H13···F5 distance 2.44 Å and C13−H13···F5 angle 141°). The same two fluorine atoms are also involved in a bifurcated hydrogen bond with one of the *o*-P*Ph*₃ protons (H2···F5 distance 2.30 Å and C2−H2···F5 angle 165°; H2···F4 distance 2.74 Å and C2−H2···F4 angle 122°), and each of them also has a weaker interaction with an *o*-C*Ph*₂ proton (H15 or H21) (Table 6). A further strong hydrogen bond is found between one of the *o*-C*Ph*₂ protons and a third fluorine atom (H21···F3 distance 2.44 Å and C21−H21···F3 angle 165°). Two weaker interactions are observed between the *o*-P*Ph*₃ (H2) and *m*-P*Ph*₃ (H3) protons and a fourth fluorine atom (F2) (Table 6).

The fluorine atoms of the SbF₆⁻ anions in the **2a** SbF₆⁻ crystal also form multifurcated hydrogen bonds (Figure 7h and Table 7), but the C−H···F interactions differ somewhat from those in CH₂Cl₂ solution. The closest C−H···F−SbF₅⁻

contact is between an *o*-P*Ph*₃ proton and one of the fluorine atoms (H2···F5 distance 2.42 Å and C2−H2···F5 angle 178°). This proton also has a second weaker interaction with another fluorine atom (F2), which also forms a hydrogen bond to the adjacent *m*-P*Ph*₃ proton (H3). The bifurcated hydrogen bonds between the C(α)−H proton and the SbF₆⁻ anion are significantly longer than in solution or in the crystals of

Ion-Pairing of Phosphonium Salts in Solution

FULL PAPER

the other salts (H13···F4 distance 2.67 Å and C13-H13···F4 angle 151°; H13···F5 distance 2.84 Å and C13-H13···F5 angle 153°), and the typical interaction with one or more o-CPh_2 protons is not found (Figure 7 h). Instead, the o-CPh_2 protons (H19 and H25) form hydrogen bonds to a second SbF_6^- anion which is located on the far side of the C(α)−H proton. The packing of the ions is also influenced by several other contacts between the protons of the PPh_3 groups and neighboring SbF_6^- anions (Figure 7 h and Table 7).

Benzyl triphenylphosphonium salts (1 X$^-$)

Halide and tetrafluoroborate salts: The calculated structures of **1a**Cl$^-$ and **1a**BF$_4^-$ in CH$_2$Cl$_2$ solution closely resemble those of the benzhydryl derivatives **2a**X$^-$ and are shown in Figure S2 in the Supporting Information. In each case, the anions form hydrogen bonds with three donors: one of the C(α)−H, one o-PPh_3 and one o-CPh proton. The crystal structures of these salts are worth discussing briefly because of the additional possibility of an interaction of the anion with the second C(α)−H proton of the benzyl group belonging to a second phosphonium ion.

The crystal structure of **1a**Cl$^-$ has been reported previously (Figure 8).[44] The shortest contact between cation and anion is the interaction of one C(α)−H proton with the chloride anion (H1···Cl distance 2.52 Å and C1−H1···Cl angle 170°), which forms a second hydrogen bond to one of the o-PPh_3 protons (H8···Cl distance 2.83 Å and C9−H8···Cl angle 176°) (Table 8). The second C(α)−H proton shows a weaker hydrogen bond to a second chloride anion (H2···Cl distance 2.66 Å, C1−H2···Cl angle 163°), which also has a very short contact to another o-PPh_3 proton (H13···Cl distance 2.57 Å, C15−H13···Cl angle 176°). These strong bidirectional interactions result in the formation of one-dimensional chains of alternating cations and anions in the crystal, which interact by weaker contacts between the chloride anions and some of the p- and m-PPh_3 protons.

The crystal structure of **1a**BF$_4^-$ with co-crystallized CH$_2$Cl$_2$ has previously been reported.[45] Figure 9 a and b

compare the structures of **1a**BF$_4^-$ with co-crystallized CH$_2$Cl$_2$[45] and co-crystallized CHCl$_3$, respectively. Both structures resemble that of **1a**Cl$^-$ (Figure 8), except that some of the hydrogen bonds are bifurcated towards two of the BF$_4^-$ anions' fluorine atoms (Figure 9 and Table 8). On each side of the benzyl moiety, there are strong interactions between the anion and the C(α)−H (H1/H2 in Figure 9a; H19 A/H19B in Figure 9b) and one p-PPh_3 proton (H10/H19 in Figure 9a; H18/H8 in Figure 9b). The larger size of the BF$_4^-$ anion and a slight rotation of the benzyl group's phenyl ring allow for an additional contact between one o-CPh proton and one of the BF$_4^-$ anions, as shown on the left side in Figure 9a (H5) and 9b (H21).

The second BF$_4^-$ anion (shown on the right side) cannot undergo such an interaction, because the phenyl ring of the benzyl moiety is already twisted in the wrong direction. Instead, this anion forms strong hydrogen bonds to a solvent molecule. In the case of **1a**BF$_4^-$·CH$_2$Cl$_2$ there is also a contact between an o-PPh_3 proton and a chlorine atom of CH$_2$Cl$_2$ (Figure 9a), but this interaction is rather weak (H20···Cl1 distance 2.84 Å, C22−H20···Cl1 angle 135°).

The tetraphenylborate salts: Like **2a**BPh$_4^-$, **1a**BPh$_4^-$ crystallizes as very long fine needles and we could not obtain

Figure 8. Crystal structure of **1a**Cl$^-$.[44b] All contacts with d(H···X$^-$) ≤2.90 Å are shown as orange lines. For C−H···X$^-$ bond lengths and angles, see Table 8.
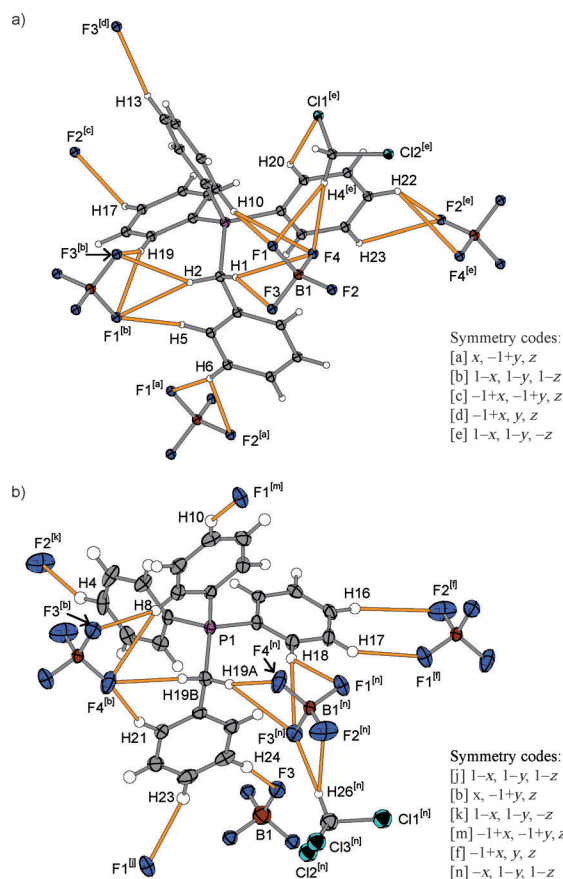
Figure 9. Crystal structures of a) **1a**BF$_4^-$·CH$_2$Cl$_2$ (ref. [45]) and b) **1a**BF$_4^-$·CHCl$_3$ (this work). All C−H···X$^-$ contacts with d(H···X$^-$) ≤2.90 Å are shown as orange lines. For C−H···X$^-$ bond lengths and angles, see Table 8.

J. Ammer, K. Karaghiosoff et al.

Table 8. Distances and angles of C–H···X⁻ contacts in crystals of ArCH₂-PPh₃⁺ X⁻.

Salt	Donor[a]	Accept-or[a]	Code[a]	d(H···X⁻) [Å]	d(C···X⁻) [Å]	∢(C–H···X⁻) [°]
1a Cl⁻[44b]	H1 (α-H)	Cl1	a	**2.52**	3.490(6)	**170**
	H8	Cl1	a	**2.83**	3.803(5)	**176**
	H2 (α-H)	Cl1	–	**2.66**	3.602(5)	**163**
	H13	Cl1	–	**2.57**	3.550(6)	**176**
	H15	Cl1	d	**2.76**	**3.424(6)**	123
	H16	Cl1	d	2.84	3.472(7)	123
	H11	Cl1	c	2.87	3.771(7)	153
	H20	Cl1	b	**2.81**	3.532(7)	132
1a BF₄⁻·CH₂Cl₂[45]	H1 (α-H)	F3	–	**2.52**	3.437(3)	158
	H1 (α-H)	F4	–	2.81	3.643(3)	145
	H10	F1	–	**2.49**	3.298(2)	146
	H10	F4	–	2.76	3.594(3)	150
	H4 (CH₂Cl₂)	F1	–	2.58	3.367(4)	139
	H4 (CH₂Cl₂)	F4	–	**2.52**	3.478(5)	169
	H2 (α-H)	F1	b	**2.51**	3.422(3)	157
	H2 (α-H)	F3	b	**2.54**	3.403(3)	148
	H19	F1	b	2.57	3.448(2)	157
	H19	F3	b	2.64	3.490(3)	152
	H5	F1	b	2.68	3.391(3)	134
	H6	F1	a	**2.56**	3.435(3)	158
	H6	F2	a	2.88	3.552(3)	130
	H17	F2	c	**2.52**	3.283(3)	140
	H13	F3	d	2.65	3.350(3)	133
	H22	F2	e	2.75	3.376(3)	125
	H22	F4	e	2.78	3.398(4)	125
	H23	F2	e	2.80	3.396(3)	123
	H20	Cl1	e	2.84	3.563(3)	135
1a BF₄⁻·CHCl₃	H19 A (α-H)	F4	n	**2.47**	3.390(3)	159
	H19 A (α-H)	F3	n	2.71	3.570(3)	149
	H18	F3	n	2.82	3.696(3)	154
	H18	F1	n	2.64	3.412(3)	139
	H26 (CHCl₃)	F3	n	**2.24(4)**	3.192(3)	**169(3)**
	H26 (CHCl₃)	F2	n	**2.50(3)**	3.250(3)	134(3)
	H19B (α-H)	F4	b	**2.53**	3.443(3)	157
	H8	F4	b	2.83	3.741(4)	**162**
	H8	F3	b	**2.49**	3.253(3)	138
	H21	F4	b	**2.51**	3.390(3)	154
	H24	F3	–	2.60	3.479(4)	153
	H23	F1	j	2.68	3.226(4)	117
	H4	F2	k	**2.54**	3.436(3)	157
	H10	F1	m	2.87	3.730(4)	151
	H17	F1	f	**2.41**	3.209(3)	141
	H16	F2	f	2.87	3.738(3)	152
1b BPh₄⁻	H1A (α-H)	phenyl[b]	–	2.80	3.633(2)	142
	H1B (α-H)	phenyl[c]	d	3.40	4.388(4)	**180**

[a] See Figures 8–10 for atom numbering and symmetry codes. [b] Center of six atoms C33, C34, C35, C36, C37, C38. [c] Center of six atoms C27, C28, C29, C30, C31, C32.

suitable material for X-ray structure analyses. We could, however, crystallize (p-CF₃-C₆H₄)CH₂–PPh₃⁺ BPh₄⁻ (**1b** BPh₄⁻) as platelets from CH₂Cl₂/Et₂O. Its crystal structure is shown in Figure 10; the CF₃ group is disordered.

Both C(α)–H bonds (C1–H1A and C1–H1B) point towards phenyl rings of the BPh₄⁻ anions. The nature of these C–H···π contacts can be characterized by the distances between the H (or C) atoms and the centers of the phenyl rings, as well as the angles between the C–H bonds and the lines connecting the H atom and the center of the phenyl ring (Table 8). One of the C(α)–H bonds (C1–H1B) points exactly at the center of the phenyl ring of one BPh₄⁻ anion (angle: 180°) (Figure 10), but the distance to the center of

the phenyl ring is relatively large (3.40 Å). The second C(α)–H proton (H1 A) forms a much closer contact to a phenyl ring of another BPh₄⁻ anion (distance: 2.80 Å, sum of C and H van der Waals radii: 2.79 Å[38]), but in this case the projection of the C(α)–H bond does not point exactly at the phenyl ring (angle 142°).

Comparison of calculated and experimental NMR spectra

We also calculated the ¹H NMR chemical shifts for the ion pairs in CD₂Cl₂ solution with the gauge-independent atomic orbital method (GIAO)[46] and the functional WP04[47] (Table 9). This method has been developed especially for the calculation of ¹H NMR data.[47a] For the calculation of the chemical shifts we additionally used pseudo potentials for all atoms from the third period on.[43] For a comparison with the experimental data, the δ_H values were averaged for both α-H of the benzyl systems, all o-CPh protons, or all six o-PPh₃ protons, respectively (Table 9). As the solvent certainly takes part in the hydrogen bond network (compare Figure 9 a), the implicit solvent continuum used for the calculations is a simplification. Further deviations may be caused by the fact that the calculations refer to the most stable conformation, while the experimental data reflect a statistical distribution of different conformations. Still, the experimentally observed trends are fairly well reproduced by the calculated ¹H NMR shifts of the optimized solution structures (Table 9).

Infrared Spectra

Hydrogen bonding is usually associated with red-shifts of the IR stretching frequencies for the involved bonds in the donor group.[8] Figure 11 shows the C–H stretching regions of the IR spectra of different phosphonium salts in CD₂Cl₂ solution, which were acquired under conditions where the phosphonium salts are mostly paired (3×10^{-2} M solutions).

The red-shifted C(α)–H stretch vibrations ($\bar{\nu} \approx 2831$ and 2791 cm⁻¹) in the benzhydryl triphenylphosphonium halides **2a** Cl⁻ and **2a** Br⁻ are clearly visible (Figure 11 a). The occurrence of two bands might be explained by couplings with lower-frequency modes, which is a common phenomenon in hydrogen bonding,[48] or by the existence of two conformations, which are discernible on the IR time scale but not on the NMR time scale. Further investigations are needed to resolve this issue. Unfortunately, direct calculations of the IR bands of ion pairs consisting of such large ions are beyond the scope of this work, since reliable calculations

Ion-Pairing of Phosphonium Salts in Solution
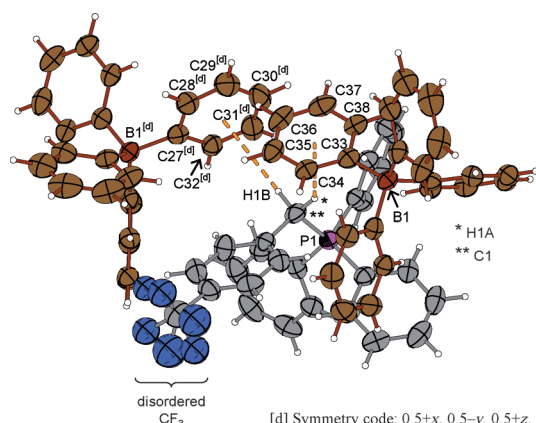
Figure 10. Crystal structure of **1b** BPh$_4^-$. For clarity, the carbon atoms of the BPh$_4^-$ anions are shown in brown color. The orange dashed lines indicate the distances between the α-protons and the centers of the phenyl groups. For C−H···X$^-$ bond lengths and angles, see Table 8.

Table 9. Comparison of calculated and experimental ^{1}H NMR chemical shifts δ_H for **2a** X$^-$ and **1a,b** X$^-$ in CD$_2$Cl$_2$ solution under conditions where the salts exist as ion pairs.

salt	δ_H(CHP$^+$)[a] [ppm]		δ_H(o-CPh)[a] [ppm]		δ_H(o-PPh$_3$)[a] [ppm]	
	calcd[b]	exptl	calcd[b]	exptl	calcd[b]	exptl
2a Cl$^-$	8.01	8.25	7.43	7.55–7.60	7.54	7.79–7.84
2a Br$^-$	7.71	8.10	7.61	7.53–7.61	7.34	7.74–7.79
2a BF$_4^-$	6.57	6.23	7.33	7.19–7.33	6.99	7.43–7.49
2a SbF$_6^-$	6.22	5.98	6.98	7.15–7.17	6.95	7.38–7.44
"free" **2a**[c]	5.84	5.77	6.74	7.09–7.11	6.71	7.33–7.37
1a Cl$^-$	6.33	5.42	7.39	7.07–7.10	7.76	7.70–7.76
1a BF$_4^-$	5.04	4.56	6.58	6.91–6.94	7.16	7.48–7.54
"free" **1a**[c]	4.09	~4.37	6.39	6.87–6.89	6.91	7.43–7.46
1b Br$^-$	5.07	5.78	7.19	7.36	7.33	7.76–7.82
1b BF$_4^-$	5.00	4.72	6.78	7.11	7.16	7.54–7.60
"free" **1b**[c]	4.10	~4.44	6.39	7.04	6.95	7.47–7.51

[a] Averaged δ_H of both α protons of the benzyl systems, all six o-PPh$_3$ protons, or all o-CPh protons, respectively. [b] From quantum chemical calculations (see text). [c] Experimental values determined from ^{1}H NMR (600 MHz) spectra of ca. 2×10^{-5} M solutions of the SbF$_6^-$, BF$_4^-$ and/or BPh$_4^-$ salts in CD$_2$Cl$_2$. At these concentrations, the phosphonium salts predominantly exist in the form of the free (unpaired) ions.

would require molecular dynamics simulations with the explicit inclusion of at least two solvent shells.

The intensities of the aliphatic C−H stretching bands in the other benzhydryl triphenylphosphonium salts **2a** X$^-$ with X$^-$ = BF$_4^-$, SbF$_6^-$, and BPh$_4^-$ are very weak (Figure 11 a). These bands can be better discerned in the IR spectra of the benzyl triphenylphosphonium salts **1a** X$^-$ (Figure 11 b) and **1b** X$^-$ (Figure 11 c). For the halides, we again observe pronounced red-shifts of the C(α)−H stretching bands ($\bar{\nu} \approx$ 2850 and 2777 cm^{-1}).

Interestingly, the C(α)−H bands of the tetrafluoroborates **1a,b** BF$_4^-$ ($\bar{\nu} \approx$ 2962 and 2919 cm^{-1}) in Figure 11 b and 11 c are located at *higher* wave numbers (i.e., blue-shifted) and have lower intensities than those of the corresponding tetraphenylborates **1a,b** BPh$_4^-$ ($\bar{\nu} \approx$ 2935 and 2899 cm^{-1}), although the dissociation constants K_D indicate stronger interactions of the phosphonium ions with the BF$_4^-$ anions than
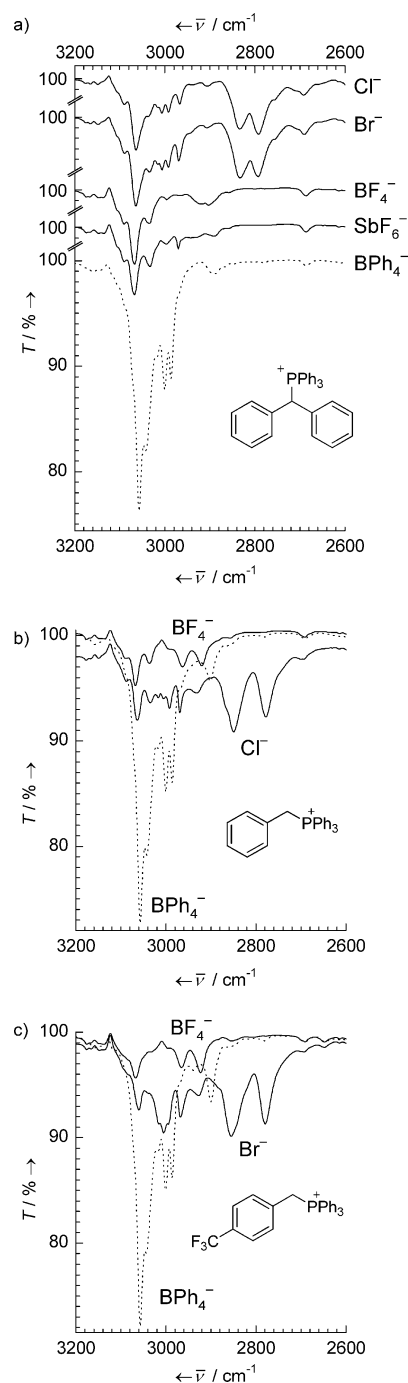
Figure 11. IR spectra of 3×10^{-2} M solutions of a) **2a** X$^-$ (vertical offset for visibility), b) **1a** X$^-$, or c) **1b** X$^-$ with X$^-$ = Cl$^-$, Br$^-$, BF$_4^-$, SbF$_6^-$, or BPh$_4^-$ in CD$_2$Cl$_2$.

with the BPh$_4^-$ anions (Table 4). This may indicate the existence of so-called blue-shifting hydrogen bonds between the phosphonium ions and the BF$_4^-$ anions (see below).

As both the NMR and X-ray data indicated hydrogen bonding between the counter-anions and aryl protons (see above), it is also interesting to compare the aromatic C−H stretching vibrations. Indeed, the C(aryl)−H stretching bands of the BF$_4^-$ salts are found above 3000 cm^{-1}, while those of the halides extend further into the red to well

below 3000 cm^{-1} (Figure 11 a–c). The IR spectra thus provide further evidence for C(aryl)−H···X$^-$ hydrogen bonds in CD$_2$Cl$_2$ solutions of the phosphonium halides.

C−H···X$^-$ Hydrogen Bonds: What Is Typical?

Bird's eye view of the whole data set

The NMR data of the phosphonium salts in CD$_2$Cl$_2$ solution show that ion pairing with the counteranion X$^-$ mainly affects the proton resonances of the C(α)−H, o-PPh$_3$, and o-CPh protons of **2a** (Table 1) or **1a** (Table 3), respectively. A comparison with the crystal structures of these salts reveals that these protons are also involved in the shortest and least bent C−H···X$^-$ contacts in the crystals (Figure 7–9; Tables 7 and 8). The presence of C−H···X$^-$ hydrogen bonds in solutions of **2**X$^-$ and **1**X$^-$ is consistent with the strong deshielding of the respective protons, as well as with the fact that the deshielding increases with increasing C−H acidity and with increasing basicity of the anions X$^-$ (SbF$_6^-$ < BF$_4^-$ < Br$^-$ < Cl$^-$).[34] Moreover, the IR spectra clearly show that the C−H stretch frequencies of the phosphonium salts in CD$_2$Cl$_2$ solution depend on the counter-anion (Figure 11). The results of our quantum chemical calculations also confirm C−H···X$^-$ hydrogen bonds for the C(α)−H, o-PPh$_3$, and o-CPh protons of **2a**X$^-$ and **1a,b**X$^-$ ion pairs in CH$_2$Cl$_2$ solution (Figure 7a–d; Tables 6 and 9). The relevant data for the C(α)−H···X$^-$ hydrogen bonds in dichloromethane solution are summarized again in Tables 10 and 11.

The data presented in the three previous Sections as a whole thus clearly support the existence of C−H···X$^-$ hydrogen bonds between the phosphonium ions and the anions (Tables 10 and 11). Some of these C−H···X$^-$ interactions, however, show spectroscopic characteristics which are worth discussing in greater detail in the following. Looking at

these pieces of evidence individually, one might not have recognized the hydrogen bonds clearly in some cases.

The nature of the "BPh$_4^-$ Effect" in benzyl triphenylphosphonium salts

While we did not find such interactions in **2a**BPh$_4^-$, the crystallographic data in Figure 10 reveal C−H···π interactions between **1b** and BPh$_4^-$, where the protons reside above the centers of the phenyl rings. Unlike the typical CH–π interaction, which is mainly based on dispersion interactions,[49] the interaction between **1b** and BPh$_4^-$ can be expected to have a strong electrostatic component due to the high acidity of the C−H bond and the negative charge on the phenyl rings of the BPh$_4^-$ anion. This notion is supported by the strong directionality of the C1−H1B···Ph interaction, since the electrostatic interaction is the main source of directionality in CH–π interactions.[49] Hence, the C(α)−H···Ph interactions in **1b** BPh$_4^-$ can be viewed as hydrogen bonds in which a phenyl ring of the tetraphenylborate anion acts as the hydrogen bond acceptor.[2,50] Similar C(α)−H···Ph hydrogen bonds have also been reported in the crystal structure of choline tetraphenylborate, Me$_3$N$^+$−C(α)H$_2$−CH$_2$OH BPh$_4^-$ (H···Ph distances 2.42 Å and 2.38 Å, C−H···Ph angles 168 and 159°).[50b]

A similar interaction between cation and anion in CD$_2$Cl$_2$ solution can explain the upfield shift of the C(α)−H resonances of **1a,b**BPh$_4^-$ in the ^{1}H NMR spectra (Figure 2): The resulting ring current effect[51] over-compensates any small downfield shift in the ^{1}H NMR spectrum that may be expected due to the formation of a weak hydrogen bond.

Blue-shifting hydrogen bonds with weak hydrogen bond acceptors

Blue-shifting hydrogen bonds show stretching vibrations at higher wave numbers, often accompanied by reduced inten-

Table 10. Summary of experimental and calculated data for the C(α)−H···X$^-$ hydrogen bonds of the benzhydryl triphenylphosphonium ion pairs **2a**X$^-$ in dichloromethane solution.
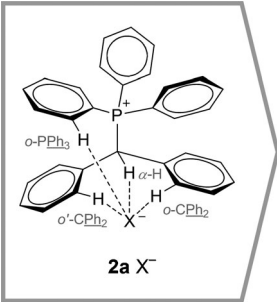
	X$^-$	Cl$^-$	Br$^-$	BF$_4^-$	SbF$_6^-$	BPh$_4^-$ ($\approx$ free ion)	free ion
	δ_H for C(α)−H [ppm]	8.25	8.10	6.23	5.98	5.72	5.77
	$^1J_{C,H}$ for C(α)−H [Hz]	131.3	131.1	130.2	129.3	128.7	n/a
	$\tilde{\nu}_{CH}$ [cm^{-1}]	2832 (s)	2829 (s)	2903 (w)	2889 (w)	2888 (w)	n/a
		2791 (s)	2791 (s)	2918 (w)			
	calcd d(C−H) [Å]	1.1022	1.1021	1.0968	1.0977	n/a	1.0977
	calcd d(H···X$^-$) [Å]	2.44	2.64	2.30/2.20	2.28/2.44	n/a	–
	calcd d(C···X$^-$) [Å]	3.54	3.74	3.24/3.23	3.28/3.37	n/a	–
	calcd ∡(C−H···X$^-$) [°]	176	177	142/156	151/141	n/a	–
	further H-bonds to… (also see Figure 7a–d)	H2 (o-PPh$_3$) H31 (o-CPh) H21 (o'-CPh$_2$)	H6 (o-PPh$_3$) H25 (o-CPh$_2$) H13 (o'-CPh$_2$)	H12 (o-PPh$_3$) H31 (o-CPh$_2$) H25 (o'-CPh$_2$)	H2 (o-PPh$_3$) H21 (o-CPh$_2$) H15 (o'-CPh$_2$) H3 (m-PPh$_3$)	n/a	–

Ion-Pairing of Phosphonium Salts in Solution

FULL PAPER

Table 11. Summary of experimental and calculated data for the C(α)−H···X$^-$ hydrogen bonds of the benzyl triphenylphosphonium ion pairs **1a,b**X$^-$ in dichloromethane solution.

	X$^-$	Cl$^-$	Br$^-$	BF$_4^-$		BPh$_4^-$		free ions	
	1a	**1b**	**1a**	**1a**	**1b**	**1a**	**1b**	**1a**	**1b**
δ_H for C(α)−H [ppm]		5.42	5.78	4.56	4.72	3.94	3.66	~4.37	~4.44
$^1J_{C,H}$ for C(α)−H [Hz]		134.6	134.6	134.2	134.9	133.9	134.6	n/a	n/a
$\tilde{\nu}_{CH}$ [cm^{-1}]		2852 (s)	2848 (s)	2960 (m)	2963 (m)	2899 (m)	2935 (w)	n/a	n/a
		2776 (s)	2778 (s)	2916 (m)	2921 (m)		2899 (m)		
calcd d(C−H)[a] [Å]		1.0983	1.0980	1.0929	1.0931	n/a	n/a	1.0941[b]	1.0940[b]
calcd d(H···X$^-$) [Å]		2.52	2.72	2.18/2.34	2.15/2.34	n/a	n/a	–	–
calcd d(C···X$^-$) [Å]		3.57	3.74	3.26/3.12	3.22/3.14	n/a	n/a	–	–
calcd ∢(C−H···X$^-$) [°]		159	154	172/126	168/128	n/a	n/a	–	–
further H-bonds to…		o-PPh_3	o-PPh_3	o-PPh_3	o-PPh_3	n/a	n/a	–	–
		o-CPh	o-CPh	o-CPh	o-CPh				

[a] Length of C(α)−H bond acting as hydrogen bond donor. [b] Average of two C(α)−H bonds of the free phosphonium ions **1a** ($\pm$0.0007 Å) or **1b** ($\pm$0.0008 Å), respectively.

sities of the IR bands,[52,53] which is the opposite behavior of normal hydrogen bonds.[8] The nature of blue-shifting hydrogen bonds has been discussed controversially,[52,53] but now there seems to be a general agreement that there is no fundamental difference between blue-shifting and normal red-shifting hydrogen bonds.[54]

According to Joseph and Jemmis,[53] there are two opposing effects, when the hydrogen bond acceptor X$^-$ approaches the C−H proton. On the one hand, there is an attractive interaction between the positive H and the negative X$^-$, which lengthens the C−H bond and reduces the force constant. On the other hand, the presence of X$^-$ induces a greater polarization of the C−H bond, because it compensates the resulting positive charge at H. As a result, the C−H bond is contracted and the force constant increases. If the former effect dominates, a classical red-shifting hydrogen bond is the result. If the latter dominates, a blue-shift of the frequency of the C−H stretch mode is observed.[53]

Compared to classical hydrogen bond donors such as O−H or N−H, the C−H bond is longer and less polar. An approach of the hydrogen bond acceptor X$^-$ will thus lead to a considerable polarization of the C−H bond. Whether the increased polarization causes a contraction of the C−H bond and a blue shift of its IR stretching band depends on the relative importance of the compensating attractive interaction between H and X$^-$. Increasing interaction energy between the hydrogen bond donor and acceptor causes a blue shift at relatively long equilibrium distances between H and X$^-$, which then decreases again and changes into a red shift as the equilibrium distance between H and X$^-$ becomes shorter.[53] For strong acceptors such as Cl$^-$ or Br$^-$, the attraction between H and X$^-$ clearly dominates and we observe the classical red-shifting hydrogen bonds (Figure 11, Tables 10 and 11). The hydrogen bond acceptor BF$_4^-$ seems to be of an intermediate strength, where we observe a blue shift with the C−H hydrogen bond donors **1a** and **1b** in CD$_2$Cl$_2$ solution (Figure 11 b and c, Table 11).

This interpretation of the IR spectra is supported by the quantum chemical calculations, which also show C(α)−H bond contractions (ca. −1 mÅ) relative to the unpaired phosphonium ions for the tetrafluoroborate salts and bond elongations (ca. +4 mÅ) for the halide salts (Tables 10 and 11). An experimental confirmation of the polarization of the C(α)−H bond, which is expected for both red- and blue-shifting hydrogen bonds (see above), is provided by the NMR data of **2a** X$^-$ (Table 1) and **1a** X$^-$ (Table 3): Compared to the free ions, the H atoms are deshielded (i.e., lower electron density around H) and the C atoms are shielded (i. e., higher electron density around C) in the hydrogen-bonded systems. While δ_H may reflect changes in the electron density caused by polarization of the C−H bond as well as by interaction with the acceptor X$^-$, changes in δ_C primarily reflect polarization effects. This polarization is observed in all studied systems and becomes more pronounced with increasing interaction between cation and anion (Tables 1 and 3).

Cooperativity or anti-cooperativity phenomena between the different types of hydrogen bonds may also play a role in controlling the strengths of the C−H···X$^-$ hydrogen bonds.[55] A point which may be relevant here is the fact that the hydrogen bonds involving the BF$_4^-$ and SbF$_6^-$ acceptors, which are characterized as blue-shifting in this work, are bifurcated hydrogen bonds (Figures 7 and 9). A theoretical study of linear and bifurcated hydrogen bonds between the proton donors H$_2$CZ (Z=O, S, Se) or H$_2$CZ$_2$ (Z=F, Cl, Br) and the halide ions Cl$^-$ and Br$^-$ found that all linear hydrogen bonds in the investigated systems were red-shifting, while all bifurcated hydrogen bonds were blue-shifting.[56]

The NMR data for the phosphonium ion pairs **2a**X$^-$ (Table 1) or **1a**X$^-$ (Table 3) do not show any qualitative differences between the blue-shifting and red-shifting hydrogen bonds. We note that in both the blue-shifting (**2a**BPh$_4^-$ ≈ "free" **2a** → **2a**BF$_4^-$) as well as the red-shifting series (**2a**Br$^-$ → **2a**Cl$^-$) of the benzhydryl triphenylphosphonium salts, the chemical shifts δ_C for the α-carbon atom of **2a** de-

crease (Table 1) and the coupling constants $^1J_{H,C}$ for the C(α)−H bond increase (Table 10) with increasing interaction energy. These parameters had previously been suggested as indicators for the transition between blue- and red-shifting hydrogen bonds, based on data for a series of single hydrogen bonds between fluoroform and various hydrogen bond acceptors.[57]

Implications for the identification of C−H···X$^-$ hydrogen bonds

In the course of this work, we have encountered many of the concepts that have been debated controversially in the field of hydrogen bonding during the last decades: hydrogen bonds involving C−H donors, bi- and multi-furcated hydrogen bonds, "aromatic" hydrogen bonds with phenyl groups as acceptors, and "improper" blue-shifting hydrogen bonds. It seems that these are widespread phenomena which should be considered when dealing with solutions of onium salts. As hydrogen bonding can lead to both downfield or upfield shifts in the ^1H NMR spectra, and both red- or blue-shifts in the IR stretching bands, none of these techniques alone is sufficient to unambiguously detect weak C−H···X$^-$ interactions in solution. The combination of these methods with variations of concentrations, C−H acidities, or X$^-$ basicities provides more detailed insights.

Conclusion

The remarkably large counterion-induced shifts in the ^1H NMR spectra of the phosphonium ion Ph$_2$CH−PPh$_3$$^+$ (**2a**) (e.g., C(α)−H signals of **2a**Cl$^-$: 8.25 ppm; **2a**BPh$_4$$^-$: 5.72 ppm in CD$_2Cl_2$) have previously been attributed mainly to the shielding by the ring current effect of the BPh$_4$$^-$ anions.[9] In contrast, we have now demonstrated that the ^1H NMR spectrum of the phosphonium ion **2a** is not affected by BPh$_4$$^-$ anions at all, and that the formation of ion pairs of **2a** with Cl$^-$ anions or other hydrogen bond acceptors is responsible for the large downfield shifts of the C(α)−H signals of **2a** in CD$_2$Cl$_2$ relative to that of the unpaired cation (Figure 1, Table 10). Even weakly coordinating anions such as SbF$_6$$^-$ or BF$_4$$^-$ induce a noticeable downfield shift of +0.2 to +0.4 ppm. In sterically less congested systems such as PhCH$_2$−PPh$_3$$^+$ (**1a**), the BPh$_4$$^-$ anion does induce a noticeable upfield shift, but its magnitude remains second to the deshielding effect of Cl$^-$ or Br$^-$ anions (Figure 2, Table 11).

The counterion-induced NMR shifts in quaternary phosphonium salts are caused by the formation of charge-assisted C−H···X$^-$ hydrogen bonds between the anion and the C(α)−H protons of the cation. The o-P*Ph$_3$* and o-C*Ph* protons are likewise involved in such C−H···X$^-$ hydrogen bonds. The strengths of the hydrogen bonds increase in the order BPh$_4$$^-$ < SbF$_6$$^-$ < BF$_4$$^-$ < Br$^-$ < Cl$^-$ and also increase with increasing C−H-acidities of the phosphonium ions. A C−H···π hydrogen bond between C(α)−H and the BPh$_4$$^-$

anion has also been observed in the crystal structure of **1b**BPh$_4$$^-$, and the NMR spectra indicate that a similar interaction is also relevant in dichloromethane solution. Ion pairing thus plays an important role in solutions of phosphonium salts even when weakly coordinating anions such as BF$_4$$^-$, SbF$_6$$^-$, or BPh$_4$$^-$ are employed in solvents such as CH$_2$Cl$_2$ or CHCl$_3$. In more polar solvents such as CH$_3$CN, only stronger hydrogen-bond acceptors such as Cl$^-$ or Br$^-$ form ion pairs with the phosphonium ions.

Similar C−H···X$^-$ hydrogen bonds probably also play a major role in solutions of other onium salts, as demonstrated by the large number of examples for the "BPh$_4$$^-$ effect" in phosphonium,[9, 10] ammonium,[14] anilinium,[11] pyridinium,[13] sulfonium,[15] arsonium,[12] and stibonium[12] salts, which were collected by Schiemenz and co-workers. Indeed, the crystal structures reported for tetraarylborate salts of other onium ions[50b,c] show similar cation–anion interactions as described for **1b**BPh$_4$$^-$ in this work (Figure 10). However, if the conclusions drawn for the benzyl triphenylphosphonium salts **1a,b**X$^-$ in this work are also applicable to these other onium salts, the strongest anion effect has to be expected for the "ordinary" halide salts and not the BPh$_4$$^-$ salts. The fact that red-shifts of the C(α)−H IR stretching bands in CHCl$_3$ solution were reported even for *alkyl* triphenylphosphonium halides[7] illustrates that hydrogen bonding also plays a role for substrates of lower C−H acidity.

This work once again demonstrates that the formation of weak hydrogen bonds does not always induce red-shifts of the C−H stretch vibrations. This may be a reason why the decisive role of hydrogen bonding for the structure of onium ion pairs has often been underappreciated in the past, although the structural features of the ion pairs control the spectroscopic characteristics and reactivities of the onium salts in solution.[59]

Experimental Section

Syntheses of the phosphonium salts ArCH$_2$−PPh$_3$$^+X^-$ (1X$^-$), Ar$_2$CH−PPh$_3$$^+X^-$ (2X$^-$), and Ar$_2$CH−P(*p*-Cl-C$_6$H$_4$)$_3$$^+X^-$ (3X$^-$): The benzyl triphenylphosphonium salts **1a**Cl$^-$ and **1a**BF$_4$$^-$ are commercially available; **1b**Br$^-$ was prepared by a literature method;[58] **1b**BF$_4$$^-$ and **1a,b**BPh$_4$$^-$ were prepared by anion exchange from **1a**Cl$^-$ or **1b**Br$^-$. The benzhydryl triphenylphosphonium tetrafluoroborates Ar$_2$CH−PPh$_3$$^+BF_4$$^-$ (**2**BF$_4$$^-$) and **2a**Cl$^-$ were synthesized by heating the benzhydrols Ar$_2$CH−OH (**4**) with Ph$_3$PH$^+$X$^-$ (X$^-$=BF$_4$$^-$ or Cl$^-$). The phosphonium bromides Ar$_2$CH−PAr$_3$$^+Br^-$ (**2**Br$^-$ and **3**Br$^-$) were obtained by reaction of the benzhydryl bromides Ar$_2$CH−Br (**5**) with PAr$_3$. Subsequent anion metathesis provided the phosphonium salts **2**SbF$_6$$^-$, **2**BPh$_4$$^-$, **3**BF$_4$$^-$, and **3**SbF$_6$$^-$. Details of the synthetic procedures are described in the Supporting Information.

Calculated structures of phosphonium salts in solution: The solution structures of the salts **1a,b**X$^-$ and **2a**X$^-$ were obtained by DFT calculations using the program package Gaussian09.[39] The solution structures of the BPh$_4$$^-$ salts were not calculated due to the large size of the ions. The geometries of the different ion pairs **1a,b**X$^-$ and **2a**X$^-$ were optimized and confirmed by frequency analysis showing no imaginary frequency. We used the recently developed hybrid meta-GGA functional M06-2X for all geometry optimizations,[40] which has been shown to describe intermolecular interactions adequately.[40] We included implicit sol-

Ion-Pairing of Phosphonium Salts in Solution

FULL PAPER

vent effects of dichloromethane using the integral equation formalism variant of the polarizable continuum model (IEFPCM).[41] The optimizations were calculated with the double ζ basis 6-31+G(d,p).[42] For all atoms in the fourth period and higher we used effective core potentials.[43] Details of the calculations and the calculated structures are given in Section S4 of the Supporting Information.

Crystal structure determinations: CCDC-916846 (**1a** BF_4^-·$CHCl_3$), -916530 (**1b** BPh_4^-), -916849 (**2a** Cl^-), -916848 (**2a** Br^-), -916847 (**2a** BF_4^-) and -916850 (**2a** SbF_6^-) contain the supplementary crystallographic data for this paper. These data can be obtained free of charge from The Cambridge Crystallographic Data Centre via www.ccdc.cam.ac.uk/data_request/cif.

[1] a) G. R. Desiraju, *Acc. Chem. Res.* **1991**, *24*, 290–296; b) G. R. Desiraju, *Acc. Chem. Res.* **1996**, *29*, 441–449; c) M. C. Wahl, M. Sundaralingam, *Trends Biochem. Sci.* **1997**, *22*, 97–102; d) R. K. Castellano, *Curr. Org. Chem.* **2004**, *8*, 845–865; e) H.-J. Schneider, *Angew. Chem.* **2009**, *121*, 3982–4036; *Angew. Chem. Int. Ed.* **2009**, *48*, 3924–3977; f) Y. Hua, A. H. Flood, *Chem. Soc. Rev.* **2010**, *39*, 1262–1271; g) J. J. Novoa, F. Mota, E. D'Oria, in *Hydrogen Bonding–New Insights* (Ed.: S. J. Grabowski), Springer, Dordrecht, **2006**, pp. 193–244; h) S. Scheiner, in *Hydrogen Bonding–New Insights* (Ed.: S. J. Grabowski), Springer, Dordrecht, **2006**, pp. 263–292; i) W. A. Herrebout, M. A. Suhm, *Phys. Chem. Chem. Phys.* **2011**, *13*, 13858–13859; j) S. Scheiner, *Phys. Chem. Chem. Phys.* **2011**, *13*, 13860–13872.

[2] a) M. Nishio, *CrystEngComm* **2004**, *6*, 130–158; b) M. Nishio, *Phys. Chem. Chem. Phys.* **2011**, *13*, 13873–13900.

[3] T. Steiner, *Angew. Chem.* **2002**, *114*, 50–80; *Angew. Chem. Int. Ed.* **2002**, *41*, 48–76.

[4] a) B. P. Hay, V. S. Bryantsev, *Chem. Commun.* **2008**, 2417–2428; b) L. Pedzisa, B. P. Hay, *J. Org. Chem.* **2009**, *74*, 2554–2560.

[5] Y. Fu, H.-J. Wang, S.-S. Chong, Q.-X. Guo, L. Liu, *J. Org. Chem.* **2009**, *74*, 810–819.

[6] J.-P. Cheng, B. Liu, Y. Zhao, Y. Sun, X.-M. Zhang, Y. Lu, *J. Org. Chem.* **1999**, *64*, 604–610.

[7] L. B. Senyavina, V. I. Sheichenko, Y. N. Sheinker, A. V. Dombrovskii, M. I. Shevchuk, L. I. Barsukov, L. D. Bergel'son, *Zh. Obshch. Khim.* **1967**, *37*, 499–506; *J. Gen. Chem. USSR* **1967**, *37*, 469–474.

[8] E. Arunan, G. R. Desiraju, R. A. Klein, J. Sadlej, S. Scheiner, I. Alkorta, D. C. Clary, R. H. Crabtree, J. J. Dannenberg, P. Hobza, H. G. Kjaergaard, A. C. Legon, B. Mennucci, D. J. Nesbitt, *Pure Appl. Chem.* **2011**, *83*, 1637–1641.

[9] G. P. Schiemenz, *J. Magn. Reson.* **1972**, *6*, 291–297.

[10] G. P. Schiemenz, E. Papageorgiou, *Phosphorus Sulfur* **1982**, *13*, 41–58.

[11] G. P. Schiemenz, *Org. Magn. Reson.* **1973**, *5*, 257–261.

[12] G. P. Schiemenz, *J. Organomet. Chem.* **1973**, *52*, 349–354.

[13] G. P. Schiemenz, *J. Mol. Struct.* **1973**, *16*, 99–102.

[14] G. P. Schiemenz, *Tetrahedron* **1973**, *29*, 741–745.

[15] G. P. Schiemenz, H. P. Hansen, *Angew. Chem.* **1973**, *85*, 404; *Angew. Chem. Int. Ed. Engl.* **1973**, *12*, 400.

[16] Recent examples where this view was expressed: a) G. P. Schiemenz, C. Näther, S. Pörksen, *Z. Naturforsch. B: Chem. Sci.* **2003**, *58*, 59–73; b) G. P. Schiemenz, *Magn. Reson. Chem.* **2010**, *48*, 261–269.

[17] Also see: R. P. Taylor, I. D. Kuntz, Jr., *J. Am. Chem. Soc.* **1970**, *92*, 4813–4823. In this study, an upfield shift of $\Delta\delta_H \approx -0.4$ ppm was observed for the methyl protons of $CH_3PPh_3^+$ X^- in $CDCl_3$ solution,

[18] a) G. P. Schiemenz, *Angew. Chem.* **1971**, *83*, 929–930; *Angew. Chem. Int. Ed. Engl.* **1971**, *10*, 855; b) G. P. Schiemenz, H. Rast, *Tetrahedron Lett.* **1972**, *13*, 1697–1700; c) G. P. Schiemenz, P. Klemm, *Org. Magn. Reson.* **1974**, *6*, 276–278.

[19] J. Ammer, C. F. Sailer, E. Riedle, H. Mayr, *J. Am. Chem. Soc.* **2012**, *134*, 11481–11494.

[20] J. Ammer, C. Nolte, H. Mayr, *J. Am. Chem. Soc.* **2012**, *134*, 13902–13911.

[21] a) C. K. Broder, M. G. Davidson, V. T. Forsyth, J. A. K. Howard, S. Lamb, S. A. Mason, *Cryst. Growth Des.* **2002**, *2*, 163–169; b) I. Ling, Y. Alias, A. N. Sobolev, C. L. Raston, *CrystEngComm* **2010**, *12*, 4321–4327.

[22] a) A. Hamdi, K. C. Nam, B. J. Ryu, J. S. Kim, J. Vicens, *Tetrahedron Lett.* **2004**, *45*, 4689–4692; b) H. M. Yeo, B. J. Ryu, K. C. Nam, *Org. Lett.* **2008**, *10*, 2931–2934; c) H. M. Yeo, N. J. Jeon, K. C. Nam, *Bull. Korean Chem. Soc.* **2011**, *32*, 3171–3174; d) W. Huang, H. Lin, H. Lin, *Sens. Actuators B* **2011**, *153*, 404–408.

[23] Ionic liquids: D. R. MacFarlane, M. Forsyth, E. I. Izgorodina, A. P. Abbott, G. Annat, K. Fraser, *Phys. Chem. Chem. Phys.* **2009**, *11*, 4962–4967.

[24] Deep eutectic solvents: a) M. A. Kareem, F. S. Mjalli, M. A. Hashim, I. M. AlNashef, *J. Chem. Eng. Data* **2010**, *55*, 4632–4637; b) K. Shahbaz, F. S. Mjalli, M. A. Hashim, I. M. AlNashef, *Energy Fuels* **2011**, *25*, 2671–2678.

[25] a) E. O. Alonso, L. J. Johnston, J. C. Scaiano, V. G. Toscano, *Can. J. Chem.* **1992**, *70*, 1784–1794; b) C. Imrie, T. A. Modro, E. R. Rohwer, C. C. P. Wagener, *J. Org. Chem.* **1993**, *58*, 5643–5649.

[26] a) G. P. Schiemenz, M. Sommerfeld, *Phosphorus Sulfur* **1979**, *6*, 273–274; b) G. P. Schiemenz, R. Hinz, *Phosphorus Sulfur* **1983**, 237–240; c) G. P. Schiemenz, R. Bukowski, L. Eckholtz, B. Varnskühler, *Z. Naturforsch. B Chem. Sci.* **2000**, *55*, 12–20; d) G. P. Schiemenz, C. Näther, S. Pörksen, *Z. Naturforsch. B Chem. Sci.* **2003**, *58*, 663–671.

[27] Counteranion effects in the Wittig reaction: a) H. Bandmann, T. Bartik, S. Bauckloh, A. Behler, F. Brille, P. Heimbach, J.-W. Louven, P. Ndalut, H.-G. Preis, E. Zeppenfeld, *Z. Chem.* **1990**, *30*, 193–204; b) H. Yung-Son, C.-F. Lee, *Tetrahedron* **2000**, *56*, 7893–7902.

[28] Reviews about phosphonium salts as organocatalysts: a) T. Werner, *Adv. Synth. Catal.* **2009**, *351*, 1469–1481; b) D. Enders, T. V. Nguyen, *Org. Biomol. Chem.* **2012**, *10*, 5327–5331; c) D. Uraguchi, T. Ooi, *Yuki Gosei Kagaku Kyokaishi* **2010**, *68*, 1185–1194.

[29] F. G. Bordwell, *Acc. Chem. Res.* **1988**, *21*, 456–463.

[30] Y. Marcus, *Pure Appl. Chem.* **1983**, *55*, 977–1021.

[31] H. Friebolin, *Basic One- and Two-Dimensional NMR Spectroscopy*, 5th ed., Wiley-VCH, Weinheim, **2011**, p. 97.

[32] R. H. Contreras, J. E. Peralta, *Prog. Nucl. Magn. Reson. Spectrosc.* **2000**, *37*, 321–425.

[33] R. K. Harris, in *Encyclopedia of Nuclear Magnetic Resonance, Vol. 5* (Eds.: D. M. Grant, R. K. Harris), Wiley, Chichester, **1996**, pp. 3301–3314.

[34] I. A. Koppel, P. Burk, I. Koppel, I. Leito, T. Sonoda, M. Mishima, *J. Am. Chem. Soc.* **2000**, *122*, 5114–5124.

[35] H. Mayr, A. R. Ofial, E.-U. Würthwein, N. C. Aust, *J. Am. Chem. Soc.* **1997**, *119*, 12727–12733.

[36] R. Schneider, H. Mayr, P. H. Plesch, *Ber. Bunsen-Ges.* **1987**, *91*, 1369–1374.

[37] C. Hansch, A. Leo, R. W. Taft, *Chem. Rev.* **1991**, *91*, 165–195.

[38] a) van der Waals radii of C (1.70 Å), F (1.47 Å), Cl (1.75 Å), Br (1.85 Å) taken from: A. Bondi, *J. Phys. Chem.* **1964**, *68*, 441–451; b) radius of hydrogen (1.09 Å) taken from: R. S. Rowland, R. Taylor, *J. Phys. Chem.* **1996**, *100*, 7384–7391.

[39] Gaussian 09, Revision A.02, M. J. Frisch, G. W. Trucks, H. B. Schlegel, G. E. Scuseria, M. A. Robb, J. R. Cheeseman, G. Scalmani, V.

J. Ammer, K. Karaghiosoff et al.

Barone, B. Mennucci, G. A. Petersson, H. Nakatsuji, M. Caricato, X. Li, H. P. Hratchian, A. F. Izmaylov, J. Bloino, G. Zheng, J. L. Sonnenberg, M. Hada, M. Ehara, K. Toyota, R. Fukuda, J. Hasegawa, M. Ishida, T. Nakajima, Y. Honda, O. Kitao, H. Nakai, T. Vreven, J. A. Montgomery Jr., J. E. Peralta, F. Ogliaro, M. Bearpark, J. J. Heyd, E. Brothers, K. N. Kudin, V. N. Staroverov, R. Kobayashi, J. Normand, K. Raghavachari, A. Rendell, J. C. Burant, S. S. Iyengar, J. Tomasi, M. Cossi, N. Rega, J. M. Millam, M. Klene, J. E. Knox, J. B. Cross, V. Bakken, C. Adamo, J. Jaramillo, R. Gomperts, R. E. Stratmann, O. Yazyev, J. Austin, R. Cammi, C. Pomelli, J. W. Ochterski, R. L. Martin, K. Morokuma, V. G. Zakrzewski, G. A. Voth, P. Salvador, J. J. Dannenberg, S. Dapprich, D. A. Daniels, O. Farkas, J. B. Foresman, J. V. Ortiz, J. Cioslowski, D. J. Fox, Gaussian, Inc., Wallingford CT, **2009**.

[40] Y. Zhao, D. G. Truhlar, *Theor. Chem. Acc.* **2008**, *120*, 215–241.

[41] a) M. Caricato, B. Mennucci, J. Tomasi, F. Ingrosso, R. Cammi, S. Corni, G. Scalmani, *J. Chem. Phys.* **2006**, *124*, 124520; b) R. Improta, V. Barone, G. Scalmani, M. J. Frisch, *J. Chem. Phys.* **2006**, *125*, 054103; c) G. Scalmani, M. J. Frisch, *J. Chem. Phys.* **2010**, *132*, 114110.

[42] a) R. Ditchfield, *J. Chem. Phys.* **1971**, *54*, 724–728; b) P. C. Hariharan, J. A. Pople, *Theor. Chim. Acta* **1973**, *28*, 213–222; c) V. A. Rassolov, M. A. Ratner, J. A. Pople, P. C. Redfern, L. A. Curtiss, *J. Comput. Chem.* **2001**, *22*, 976–984.

[43] a) A. Bergner, M. Dolg, W. Küchle, H. Stoll, H. Preuß, *Mol. Phys.* **1993**, *80*, 1431–1441; b) B. Metz, H. Stoll, M. Dolg, *J. Chem. Phys.* **2000**, *113*, 2563–2569.

[44] a) A. C. Skapski, F. A. Stephens, *J. Cryst. Mol. Struct.* **1974**, *4*, 77–85; b) A. Fischer, D. Wiebelhaus, *Z. Kristallogr. New Cryst. Struct.* **1997**, *212*, 335–336.

[45] M. C. Ramirez de Arellano, private communication, **1997**, CCDC-100328.

[46] a) R. Ditchfield, *Mol. Phys.* **1974**, *27*, 789–807; b) F. London, *J. Phys. Radium* **1937**, *8*, 397–409; c) K. Wolinski, J. F. Hinton, P. Pulay, *J. Am. Chem. Soc.* **1990**, *112*, 8251–8260.

[47] a) K. W. Wiitala, T. R. Hoye, C. J. Cramer, *J. Chem. Theory Comput.* **2006**, *2*, 1085–1092; b) R. Jain, T. Bally, P. R. Rablen, *J. Org. Chem.* **2009**, *74*, 4017–4023.

[48] W. O. George, R. Lewis, in *Handbook of Vibrational Spectroscopy* (Eds.: J. M. Chalmers, P. R. Griffiths), *Vol. 3*, Wiley, Chichester, **2002**, pp. 1919–1934.

[49] S. Tsuzuki, A. Fujii, *Phys. Chem. Chem. Phys.* **2008**, *10*, 2584–2594.

[50] a) T. Steiner, A. M. M. Schreurs, J. A. Kanters, J. Kroon, J. van der Maas, B. Lutz, *J. Mol. Struct.* **1997**, *436–437*, 181–187; b) T. Steiner, A. M. M. Schreurs, M. Lutz, J. Kroon, *New J. Chem.* **2001**, *25*, 174–178; c) T. Alaviuhkola, J. Bobacka, M. Nissinen, K. Rissanen, A. Ivaska, J. Pursiainen, *Chem. Eur. J.* **2005**, *11*, 2071–2080.

[51] a) J. A. N. F. Gomes, R. B. Mallion, *Chem. Rev.* **2001**, *101*, 1349–1383; b) G. Merino, T. Heine, G. Seifert, *Chem. Eur. J.* **2004**, *10*, 4367–4371.

[52] a) P. Hobza, Z. Havlas, *Chem. Rev.* **2000**, *100*, 4253–4264; b) A. Masunov, J. J. Dannenberg, R. H. Contreras, *J. Phys. Chem. A* **2001**, *105*, 4737–4740; c) K. Hermansson, *J. Phys. Chem. A* **2002**, *106*, 4695–4702; d) I. V. Alabugin, M. Manoharan, S. Peabody, F. Weinhold, *J. Am. Chem. Soc.* **2003**, *125*, 5973–5987; e) E. S. Kryachko, in *Hydrogen Bonding–New Insights* (Ed.: S. J. Grabowski), Springer, Dordrecht, **2006**, pp. 293–336; f) A. D. Buckingham, J. E. Del Bene, S. A. C. McDowell, *Chem. Phys. Lett.* **2008**, *463*, 1–10.

[53] J. Joseph, E. D. Jemmis, *J. Am. Chem. Soc.* **2007**, *129*, 4620–4632.

[54] E. Arunan, G. R. Desiraju, R. A. Klein, J. Sadlej, S. Scheiner, I. Alkorta, D. C. Clary, R. H. Crabtree, J. J. Dannenberg, P. Hobza, H. G. Kjaergaard, A. C. Legon, B. Mennucci, D. J. Nesbitt, *Pure Appl. Chem.* **2011**, *83*, 1619–1636.

[55] a) For a comparison of cooperativity in CH···O and in OH···O hydrogen bonds, see: T. Kar, S. Scheiner, *J. Phys. Chem. A* **2004**, *108*, 9161–9168; b) for cooperativity in bifurcated hydrogen bonds, see: R. D. Parra, J. Ohlssen, *J. Phys. Chem. A* **2008**, *112*, 3492–3498.

[56] A. Y. Li, *J. Mol. Struct.* **2008**, *862*, 21–27.

[57] N. S. Golubev, G. S. Denisov, S. Macholl, S. N. Smirnov, I. G. Shenderovich, P. M. Tolstoy, *Z. Phys. Chem. (Muenchen Ger.)* **2008**, *222*, 1225–1245.

[58] Z.-L. Zhou, J. F. W. Keana, *J. Org. Chem.* **1999**, *64*, 3763–3766.

[59] For example, the photochemistry of quaternary phosphonium salts cannot be understood without considering the nature of the anion and the concentration of the salt (ref. [19]).

3. Secondary processes subsequent to the initial bond cleavage: The interplay between electron transfer, recombination, and diffusion studied for diphenylmethylchloride

The group of diphenylmethyl derivatives exhibiting photochemical bond cleavage is large. The leaving group diversity ranges from cationic ones like the phosphonium leaving groups discussed so far [131–133,139,140,233] or ammonium leaving groups [234–236] over ethers like phenoxy [137,237] and esters [237–239] to simple halides, e.g. Cl [39,135,137] or Br [60,136,137]. The derivative with Cl as leaving group, Ph_2CH-Cl, is in the focus of the present chapter comprising the article "A Comprehensive Microscopic Picture of the Benzhydryl Radical and Cation Photogeneration and Interconversion through Electron Transfer" published in *A European Journal of Chemical Physics and Physical Chemistry* [39]. The article provides a quantitative femtosecond absorption study of selected substituted Ph_2CH-Cl derivatives in different solvents together with a combined Marcus-Smoluchowski model which describes the interplay between Marcus-type electron transfer, geminate recombination and diffusion. A 270 nm laser pulse (35 fs) triggers the initial bond cleavage on the hundreds of femtoseconds timescale [135, 136]. After the ensuing build-up of the absorption signals of $Ph_2CH^\bullet$ and Ph_2CH^+ in a period of about 300 fs [136, 233], the geminate radical or ion pairs are subject to electron transfer, recombination and diffusion. These secondary processes subsequent to the initial bond cleavage take place on a time interval ranging from a few picoseconds up to several nanoseconds after the optical excitation. A white light probe pulse facilitates the simultaneous observation of the well separated product bands and thus to investigate closely the interwoven secondary processes. From a chemists point of view, the relatively stable product distribution after several nanoseconds is particularly interesting because the then present products are available for subsequent, mostly bimolecular reactions [124,126,130,240–242]. Besides the choice of the leaving group, the properties of the solvent, the substitution pattern as well as the temperature play a substantial role for the nanosecond product yield. The major conclusions drawn in the article are as follows:

- After the excitation of Ph_2CH-Cl, the dominant bond cleavage channel leads to homolysis ($Ph_2CH^\bullet + Cl^\bullet$) while only a small amount of direct heterolysis products ($Ph_2CH^+ + Cl^-$) is observed. Both generated populations undergo geminate recombination and diffusional separation. For the radical pairs, electron transfer additionally comes into play. The major fraction of the ion pairs is generated from the radical pairs via this electron transfer from $Ph_2CH^\bullet$ to $Cl^\bullet$.

- Already the initial populations show a large variety of distances up to three solvent molecules between the Ph_2CH and the Cl fragment which is necessary to explain the observed population dynamics. Distinct species like contact ion pairs, solvent-separated ion pairs and free ions as well as geminate radical pairs and free radicals which are utilized in traditional interpretations [243–247] could not explain the observed population dynamics.

- Additionally, distance-dependent rates for electron transfer, geminate recombination and diffusion are essential to properly model the time-dependent behavior of the radical and ion

pair populations with the presented Marcus-Smoluchowski model. The interplay between the distance dependent electron transfer rate and the time-dependent radical pair population results in an effectively time-dependent electron transfer rate and in the observed stretched exponential behavior of the electron transfer.

- The interwoven processes can be influenced by the variation of the solvent polarity whereby three different regimes can be distinguished: Solvents with low polarity like cyclohexane or n-heptane prevent electron transfer due to the missing stabilization of the emerging ions. In moderately polar solvents like dichloromethane ion pairs are generated intermediately but they are totally depleted by geminate recombination. Only in highly polar solvents e.g. MeCN sufficient stabilization of the ions is provided to efficiently separate them. Furthermore electron-withdrawing substituents on the Ph_2CH moiety lower the electron transfer yield while electron-donating substituents enlarge it.

The joint experimental and theoretical work explicates the secondary processes within the first nanoseconds subsequent to the initial bond cleavage and gives a microscopic picture of the interplay between geminate recombination, electron transfer and diffusion. Particularly with regard to the photochemical bond cleavage of $Ph_2CH-PPh_3^+$ presented in chapter 1, the different time scales for the bond cleavage under the influence of the dynamic solvent effect and for the secondary processes discussed in the present chapter should be kept in mind. For both derivatives – $Ph_2CH-PPh_3^+$ and Ph_2CH-Cl – the initial bond cleavage takes place below 1 ps. In the case of $Ph_2CH-PPh_3^+$, the system relaxes to the ground state through a S_1/S_0 CoIn and thermodynamically stable Ph_2CH^+ cations are generated. Then the interplay between geminate recombination and diffusional separation determines the final carbocation yield. For Ph_2CH-Cl the situation changes because Cl is a neutral leaving group. After the homolytic bond cleavage, the primary photoproducts are $Ph_2CH^\bullet$ and $Cl^\bullet$. In polar and moderately polar solvents, the radicals are not thermodynamically stable. Electron transfer from $Ph_2CH^\bullet$ to $Cl^\bullet$ generates the ion pair and becomes an additional important player among the secondary processes. Their interplay determines the yield of the again thermodynamically stable Ph_2CH^+ ions.

In the following, the article "A Comprehensive Microscopic Picture of the Benzhydryl Radical and Cation Photogeneration and Interconversion through Electron Transfer" is reprinted with permission from *ChemPhysChem* **14**, 1423–1437 (2013); copyright 2013 John Wiley and Sons. In the context of the present work the combined Marcus-Smoluchowski model was set up and the corresponding simulations were performed as well as interpreted. Furthermore all quantum chemical calculations for the driving force of the electron transfer in MeCN, dichloromethane, and cyclohexane were performed. Thereto, the Gibbs free energy of the radical pairs and the corresponding ion pairs resulting from a C-Cl bond cleavage of Ph_2CH-Cl, $(tol)_2CH-Cl$, $tol(Ph)CH-Cl$, $mfp(Ph)CH-Cl$, and $dfp(mfp)CH-Cl$ was calculated. Selected parts of the supporting information of the article (chapters S4 and S8) are reprinted in appendix B.

CHEM**PHYS**CHEM
ARTICLES

ChemPubSoc
Europe

A Comprehensive Microscopic Picture of the Benzhydryl Radical and Cation Photogeneration and Interconversion through Electron Transfer

Christian F. Sailer,[a] Sebastian Thallmair,[a, b] Benjamin P. Fingerhut,[b] Christoph Nolte,[b] Johannes Ammer,[b] Herbert Mayr,[b] Igor Pugliesi,[a] Regina de Vivie-Riedle,[b] and Eberhard Riedle*[a]

Bond cleavage and bond formation are central to organic chemistry. Carbocations play a key role in our understanding of nucleophilic substitution reactions that involve both processes. The precise understanding of the mechanism and dynamics of the photogeneration of carbocations and carbon radicals is therefore an important quest. In particular, the role of electron transfer for the generation of carbocations from the radical pair is still unclear. A quantitative femtosecond absorption study is presented, with ultrabroad probing on selected donor and acceptor substituted benzhydryl chlorides irradiated with 270 nm (35 fs) pulses. The ultrafast bond cleavage within 300 fs is almost exclusively homolytic, thus leading to a radical pair. The carbocations observable in the nanosecond regime are generated from these radicals by electron transfer from the benzhydryl to the chlorine radical within the first tens of picoseconds. Their concentration is reduced by geminate recombination within hundreds of picoseconds. In moderately polar solvents this depletion almost extinguishes the cation population; in highly polar solvents free ions are still observable on the nanosecond timescale. The explanation of the experimental findings requires the microscopic realm of the intermediates to be accounted for, including their spatial and environmental distributions. The distance dependent electron transfer described by Marcus theory is combined with Smoluchowski diffusion. The depletion of the radical pair distribution at small distances causes a temporal increase of the mean distance and the observed stretched exponential electron transfer. A close accord with experiment can only be reached for a broad distribution of the nascent radical pairs. The increase in the inter-radical and inter-ion pair distance is measured directly as a shift of the UV/Vis absorption of the products. The results demonstrate that, at least for aprotic solvents, traditional descriptions of reaction mechanisms based on the concept of contact and solvent-separated pairs have to be reassessed.

1. Introduction

Carbocations are key intermediates in many organic reactions.[1–5] They can be generated by photoinduced heterolysis of organic halides such as R–Cl[6–22] or other precursors.[6–8,21,23–26] The photolysis of these precursors can also lead to the generation of carbon-centered radicals.[9–11,26] Photoinduced heterolysis and homolysis are ideal processes for the time-resolved investigation of bond cleavage and subsequent reactions involving the photogenerated ionic and radical intermediates through ultrafast pump–probe spectroscopy. Systems can be chosen for which no spectroscopically relevant fragment population is produced thermally. The photoinduced processes were previously investigated by the nanosecond pump–probe experiments of McClelland[6] as well as Miranda, Scaiano, and co-workers,[10] and by the product studies of Hilborn et al.[27] Their data have led researchers to propose that in addition to the direct generation of carbocations and carbon-centered radicals by photoinduced bond cleavage, there is a pathway by which initially generated radical pairs decay into ion pairs through electron transfer.[6,10,27] It was suggested that this pathway is the main source of carbocations.[27,28] However, the factors contributing to the electron transfer responsible for the interconversion of radicals to cations are not yet clear. Early work of Peters and co-workers on the photolysis of benzhydryl halides suggests that the interconversion occurs by electron transfer in the vicinity of a proposed radical and cation potential energy surface crossing.[11,29,30] The considered potential energy surfaces were only analytic model potentials reflecting covalent and ionic character and were not derived from quantum chemistry. In addition, it was shown by several groups that intermolecular electron transfer can occur on much larger donor–acceptor distances and is strongly affected by diffusion.[31–34] It is therefore conceivable that carbocations

[a] C. F. Sailer, S. Thallmair, Dr. I. Pugliesi, Prof. E. Riedle
Lehrstuhl für BioMolekulare Optik
Ludwig-Maximilians-Universität München
Oettingenstr. 67, 80538 München (Germany)
Fax: (+49) 089-2180-9202
E-mail: Riedle@physik.uni-muenchen.de

[b] S. Thallmair, Dr. B. P. Fingerhut, Dr. C. Nolte, J. Ammer, Prof. H. Mayr,
Prof. R. de Vivie-Riedle
Department Chemie
Ludwig-Maximilians-Universität München
Butenandtstr. 5–13, 81377 München (Germany)

Supporting information for this article is available on the WWW under
http://dx.doi.org/10.1002/cphc.201201057.
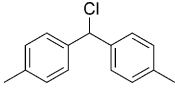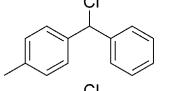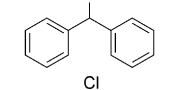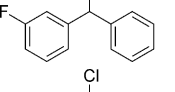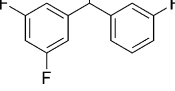
are not only generated from radical pairs in contact distance, but also from radical pairs separated by at least one solvent shell.

Furthermore, it is not clear how the carbocation yield is related to the electron transfer. It has been reported that the yield of the benzhydryl cations observable with nanosecond techniques is strongly solvent dependent and that in many solvents virtually no carbocations can be detected.[6–9] For example, moderately stabilized benzhydryl cations Ar_2CH^+ ($E \geq 0$, see Table 1) can be obtained by photolysis of the corresponding benzhydryl chlorides in CH_3CN but not in CH_2Cl_2[9] and the

Table 1. Benzhydryl chlorides investigated in this work and empirical electrophilicity parameters E[37] of the corresponding benzhydryl cations.[a]

Compound	Abbreviation[b]	E[c]
	(tol)$_2$CHCl	3.63
	tol(Ph)CHCl	4.43
	Ph$_2$CHCl	5.47
	mfp(Ph)CHCl	6.23
	dfp(mfp)CHCl	7.52

[a] $\Delta E \approx 4$ on the logarithmic E scale indicates that dfp(mfp)CH$^+$ is approximately 10 000 times more electrophilic than (tol)$_2$CH$^+$. [b] tol = toluene, Ph = phenyl, mfp = m-fluorophenyl, dfp = (3,5-)difluorophenyl. [c] From ref. [38].

photogeneration of these benzhydryl cations in CH_2Cl_2 requires other photoleaving groups, such as PPh_3.[25, 26] In view of the important role of photolytic techniques in the characterization of benzhydryl ions[19, 20, 25, 26, 35–37] and other reactive carbocations,[6–20, 21–24] it is desirable to find out whether an inhibition of the electron transfer or an efficient depletion of the ion pairs by geminate recombination is responsible for the negligible quantum yields in solvents of low polarity.

Herein, we present ultrafast broadband pump–probe experiments on the photolysis of a set of benzhydryl chlorides (shown in Table 1). The sub-100 fs time resolution and the ultrabroad probe (290–700 nm) allow for the observation of the dynamics of all evolving product bands and make even subtle effects visible, such as shifts of the maxima of the UV/Vis product absorption band (peak shifts) and deviations from the standard exponential kinetics that can elucidate the population dynamics in great detail. The wealth of data generated by the quantitative evaluation of the broadband measurements and the modifications in the substitution pattern are summarized

in Section 3. In Section 4 we develop a microscopic model that can reproduce and explain all the observations. Furthermore, we analyze the temporal shifts of the benzhydryl cation and radical absorption band to trace the microscopic changes in the solute environment. In Section 5 we study the influence of solvent and temperature variations on the dynamics and yields. A further dimension is gained by changing the nature of the substituents on the aryl groups. In Section 6 we finally compare our comprehensive microscopic picture to the previous kinetic model used to describe the photoinitiated carbocation formation.

2. Quantitative Femtosecond Pump–Probe Spectroscopy

2.1. Materials

Benzhydryl chloride (Ph$_2$CHCl) was purchased from Sigma–Aldrich and used without further purification. The derivatives (tol)$_2$CHCl (tol = toluene), tol(Ph)CHCl (Ph = phenyl), and mfp(Ph)CHCl (mfp = m-fluorophenyl) were prepared as described in refs. [39] and [40]. The details for the synthesis of 3,3′,5-trifluorobenzhydryl chloride, dfp(mfp)CHCl (dfp = (3,5-)difluorophenyl), are given in Section S6 of the Supporting Information. Structural formulae and abbreviations for the full names of the compounds are shown in Table 1. The solvents used were of the highest spectroscopic grade available.

2.2. Femtosecond Transient Absorption Measurements

The details of the femtosecond transient absorption setup have been described in ref. [41]. For the measurements presented herein, solutions of the precursors were pumped through a flow cell of 120 µm optical path length and excited at 270 nm, close to the maximum of the first absorption band. The pulses had an energy of about 200 nJ and a pulse duration of approximately 35 fs. They were focused down to a diameter of about 100 µm leading to a fraction of excited precursor molecules in the pumped volume of ≤1 % (see Section S1.2). A CaF$_2$ continuum spanning from 290 to 700 nm and polarized at the magic angle was used as probe light. The temporal resolution was about 100 fs, well below all observed decay rates.

Temperature-dependent measurements were carried out with a slightly modified flow cell system. The temperature of the sample, the pump, and the flow cell itself were kept at a constant temperature between 5 and 60 °C by a thermostat. The temperature of the sample solution was additionally monitored by a digital thermometer.

2.3. Conversion of Absorption Changes into Absolute Quantum Yields

Absolute quantum yields are an essential measure to gain detailed insight into the mechanism and dynamics of photochemical processes. Although the temporal dependence of the spectroscopic signatures gives information on the speed of a reaction, quantum yields give access to the efficiency of the

product formation on the sub-pico- to microsecond timescale. They often allow for the determination of competing processes that can otherwise not be resolved. The concentration of excited precursors can be derived from the pump pulse wavelength, energy, and full width at half maximum diameter as well as the molar absorption coefficient of the precursor. The molar absorption coefficients of the benzhydryl radicals and cations are well documented in the literature,[9] so we were able to calculate the time-dependent concentrations of photogenerated benzhydryl radicals and cations. By comparing the concentration of the photofragments to the concentration of excited precursors, one obtains the time-dependent quantum yields of benzhydryl cations and radicals. Final yields of specific subprocesses (e.g. electron transfer) are the limit to "infinite" time and technically determined from the preexponential factors in the fit. The details of the calculations of the yields are given in the Supporting Information (Sections S1 and S2). The resulting values are summarized in Table 3.

3. Photoinduced Dynamics of Benzhydryl Chloride and Its Photoproducts

Figure 1 b shows the evolution of the transient absorption spectrum after UV irradiation of benzhydryl chloride (Ph$_2$CHCl) in acetonitrile (CH$_3$CN): the probe wavelength is plotted on the horizontal axis and the pump–probe delay on the vertical axis. Blue color indicates low absorbance and red color high absorbance. The delay on the vertical axis is shown in a linear scale for the first picosecond and in a logarithmic scale afterwards.

After UV irradiation, we observe the appearance of two bands at 329 and 435 nm (see Figure 1 a for the spectrum observed after 40 ps). The two spectral signatures coincide with the product bands observed in nanosecond laser flash photolysis experiments on benzhydryl halides[9] and benzhydryl phos-

phonium ions.[26] In line with refs. [9] and [26] and other reports, we assign the band at 329 nm to the benzhydryl radical and the 435 nm band to the benzhydryl cation. After a fast initial rise, the radical band reaches its maximum at about 1 ps and subsequently decays within 100 ps to about half of its initial intensity and then remains constant on the nanosecond timescale. In contrast, the cation band reaches its maximum within 40 ps and subsequently decays within a few hundred picoseconds. The residue of the cation signal is stable on the nanosecond timescale (compare Figures 1 b and 2).
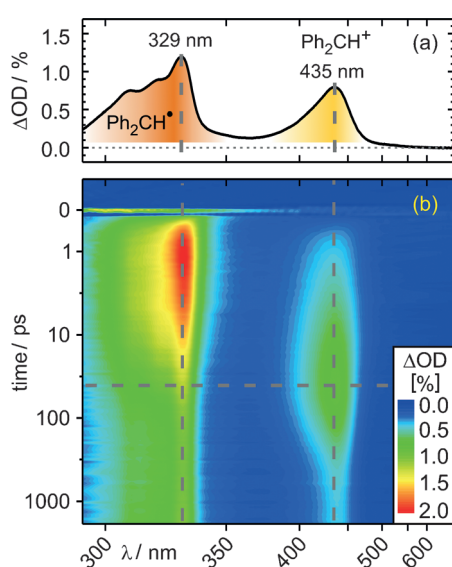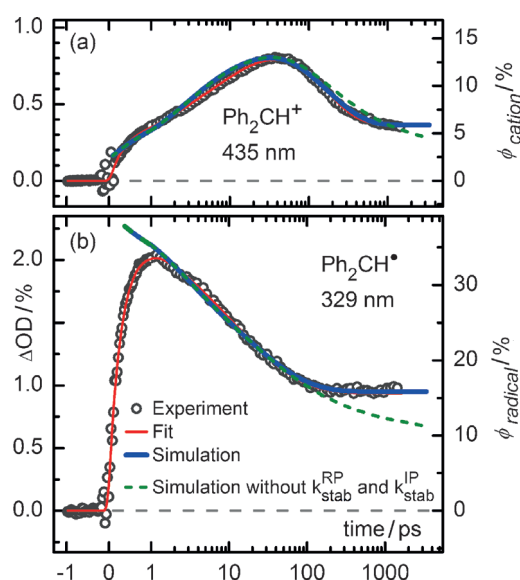
Figure 2. Temporal evolution of the signal (black circles) of a) the benzhydryl cation and b) the benzhydryl radical in CH$_3$CN. The corresponding cation and radical quantum yields Φ_{cation} and $\Phi_{radical}$ are indicated on the right vertical axes. Fits are shown in red. Results from the simulations, which combine Marcus-type electron transfer and Smoluchowski-type diffusion with and without the fragment stabilization rates k_{stab}^{RP} and k_{stab}^{IP} (RP = radical pair, IP = ion pair; see Section 4.1), are shown in blue and green. The calculated signals were normalized with respect to the radical population after the homolytic bond cleavage.

Neither product band displays a temporal evolution of the shape or position that would give any support to an initially excited electronic state of the fragments. Contrary to previous investigations at just one probe wavelength each,[29] our transient spectra show that both the benzhydryl radical and the small amount of nascent cation are produced in their electronic ground states.

The temporal evolution of the signal attributed to the cation and radical population along the vertical lines in Figure 1 b is shown in Figure 2 (gray circles). To quantify the product dynamics we employed fits on the band maxima of cation and radical (red lines): both products show a fast initial rise, which can be fitted with a 300 fs (radical)/260 fs (cation) exponential time constant.[42] These times are significantly faster than those in earlier reports, for which the temporal resolution was limited by the group velocity mismatch in the thick cuvette.[29] Although the fast rise of the radical signal is associated with a large increase of its population, the rise of the cation signal

Figure 1. a) Transient spectrum at a pump–probe delay of 40 ps and b) false color representation of the 2D transient absorption data matrix of Ph$_2$CHCl in CH$_3$CN after 270 nm UV excitation. The delay time axis is linear between −1 and 1 ps and logarithmic beyond 1 ps. OD = optical density.

amplitude is 20 times weaker. For the subsequent picosecond decay of the radical and the rise of the cation a satisfactory fit cannot be obtained with a single or double exponential. However, we obtained an excellent fit by employing a stretched-exponential function, namely $A(t) = A_{SE} \exp\left[-(t/\tau_{SE})^{\beta_{SE}}\right]$. A comparative monoexponential fit for the $Ph_2CH^\bullet$ radical is shown in Figure S2 (Supporting Information).

The inability of an exponential fit to reproduce the experimental data has already been reported by Peters and co-workers.[29] They did not, however, interpret this observation. We believe that it is the decisive evidence for the identification of the mechanism that transfers radical pairs into ion pairs.

It turns out that the dynamics of the large number of measurements with differing substituents, solvents, and temperatures reported below can all be well fitted with $\beta_{SE} = 0.5$. To confine the number of free fit parameters β_{SE} was therefore set to 0.5. For the decay of the radical and the rise of the cation we obtain the same time constant of $\tau_{SE} = 11.1$ ps. With this time constant the cation signal increases greatly and the cation population reaches its maximum. The radical population decreases with the same time constant and then remains unchanged for several nanoseconds. The magnitude of the population changes matches closely. At later times the cation absorption shows a further decay with a time constant of 140 ps before it reaches a sustained level after 1 ns. The need to include standard and stretched exponentials into a stable fit of the complete experimental data set is in distinct contradiction to earlier analyses.[29,30] The conclusions drawn from the earlier multiexponential fits of single-wavelength measurements, therefore, have to be viewed with care.

Based on the experimental data and fits presented so far, we developed a kinetic reaction scheme for the population dynamics of the photoproducts, which is shown in Scheme 1. We assign the 300/260 fs time constants to simultaneous photoinduced homolytic and heterolytic C–Cl bond cleavages and subsequent solvent and geometric relaxation of the benzhy-

dryl radical and cation. Details of this complex evolution of the earliest signals, which can also explain the slightly different times, are discussed elsewhere.[42] The homolysis proceeds through a first conical intersection close to the Franck–Condon point and leads to the radical pair $Ph_2CH^\bullet/Cl^\bullet$ (pathway ① in Scheme 1) with a quantum yield of $\Phi_{Hom} = 40\%$.[43] The heterolysis proceeds through a second conical intersection at slightly larger C–Cl distance and generates the ion pair Ph_2CH^+/Cl^- (pathway ② in Scheme 1) with $\Phi_{Het} = 2\%$ (see Figure 2 and Table 3).

The stretched exponential time constant $\tau_{SE} = 11.1$ ps is associated with a dramatic rise of the cation signal and a substantial decrease of the radical signal. This coordinated rise and fall indicates that the cations are formed from the radicals by an electron transfer from the benzhydryl radical to the Cl$^\bullet$ radical in close vicinity (pathway ③ in Scheme 1). As has been shown,[44,45] the fact that the electron transfer has to be fitted with a nonexponential function indicates that the observed ensemble kinetics is actually a superposition of dynamics in subensembles. It will be shown that a distribution of fragment distances is created by the bond cleavage, and diffusion is too slow to overcome the depletion of close $Ph_2CH^\bullet$ and Cl$^\bullet$ radicals by electron transfer (see Section 4). Consequently, the distance-dependent electron transfer rate translates to the time-dependent electron transfer rate seen in the experiment as stretched exponential decay. The mean electron transfer time is given by twice τ_{SE},[46] that is, $\tau_{ET} = 2\tau_{SE} = 22.2$ ps. This time is nearly two orders of magnitude slower than the electron transfer proposed recently for Ph_2CHCl in water.[47]

Electron transfer is the main process depleting the radical population. Still, a sizable part of the radical pairs can avoid electron transfer and also geminate recombination (pathway ⑤ in Scheme 1) and separate by diffusion leading to free radicals (pathway ④). A major part of the formed cations decays with an additional time constant of 138 ps whereas a smaller fraction remains unchanged for hundreds of nanoseconds or even longer. This behavior can be explained by competition between the geminate recombination of the ion pair and diffusional separation of the ions: after the photoinduced C–Cl bond cleavage, the ion pairs generated by heterolysis or electron transfer can either separate to give rise to long-lived free ions (pathway ⑥ in Scheme 1) or recombine to Ph_2CHCl (pathway ⑦). The geminate recombination can only occur as long as the fragments are in close vicinity and is terminated by diffusional separation. The observed cation decay time of 138 ps is therefore determined jointly by the geminate recombination and the cation separation. Characteristic times for the individual processes can be extracted from the data and are 198 ps for the recombination and 456 ps for the separation (see Supporting Information for details).

Scheme 1. Reaction mechanism (not to scale) with yields observed in CH₃CN. After UV excitation of Ph₂CHCl the molecules undergo predominantly homolytic bond cleavage ①. The heterolytic pathway ② is only of minor importance. An electron can be transferred within the radical pair ③, which leads to the major part of the observed cations. The simultaneously occurring diffusional separation of the radical pair ④ slows down the electron transfer (ET) and leads to free radicals. A minor fraction of the radicals recombines to Ph₂CHCl ⑤. The ion pairs in close vicinity either undergo geminate recombination ⑦ or diffuse apart ⑥ and form free ions.

4. Microscopic Picture of the Photoinduced Reactions in Time and Space

The mechanism in Scheme 1 is only a simplification to illustrate the fundamentals of the contributing processes. The temporal evolution and the final quantum yield of the photogenerated

radicals and cations are the result of a subtle interplay between the time-dependent electron transfer, the geminate recombination, and the diffusion. The nonexponential kinetics observed for the depletion of the radical population and the generation of cations cannot be modeled by reaction mechanisms based solely on a simple picture of transitions between intermediates with well-defined spatial and environmental conditions, such as contact pairs and solvent-separated pairs.[11,48] The generated radical and ion pairs actually span a range of distances, configurations, and environments leading to a varying behavior. Therefore, we replace the kinetic model used so far by a microscopic description that explicitly takes into account the distribution of intermediates involved in the processes. In the microscopic model, inter-radical and inter-ion distance-dependent rates (probabilities) for the electron transfer, the geminate recombination, and the separation are used. The spatial average of these rates over the time-dependent spatial distribution then renders the experimentally observable rates that actually correspond to the ensemble average.

4.1. Theory: Combined Marcus–Smoluchowski Model

The proposed reaction mechanism incorporates electron transfer and geminate recombination subject to diffusion. Based on Scheme 1, these concepts are used to simulate the population dynamics and the associated signals. We embed the two processes in a joint theoretical model by combining diffusion with distance-dependent electron transfer and geminate recombination of the photofragments (these processes are associated with steps ③ to ⑦ in Scheme 1). A similar approach has already been employed by Fayer and co-workers[49] for describing electron transfer processes in dyes and by Grampp and co-workers[33] for bimolecular fluorescence quenching. The bond cleavage and the initial solvation dynamics occur in the first hundreds of femtoseconds and are not topics of the present investigation. It suffices to start with the effective situation present after a few hundred femtoseconds. We begin the description with an overview of all relevant aspects and detail them later together with the results of the simulation.

Time-Dependent Population Distributions

We consider the time-dependent population distribution $P_{RP}(R,t)$ for the radical pairs and $P_{IP}(R,t)$ for the ion pairs. We assume spherical symmetry and R denotes the distance between the centers of the two species making up each pair. The two functions correspond to the probability that a radical or ion pair is separated by the distance R at time t. The diffusional evolution is described by the Smoluchowski formalism,[50] the distance-dependent electron transfer rate $k_{ET}(R)$ by Marcus theory,[51,52] and the geminate recombination rates $k_{rec}^{RP}(R)$ and $k_{rec}^{IP}(R)$ as well as the stabilization rates $k_{stab}^{RP}(R)$ and $k_{stab}^{IP}(R)$ by a distance-dependent rate each. Notably, the term rate refers to the original meaning of a probability per time interval and not necessarily to an exponential decay or increase. To obtain the overall population $P(t)$, which is proportional to the experimentally accessible product absorption, integration over the

distance coordinate starting from the hard-sphere contact distance $R_c = r_{benzhydryl} + r_{Cl} = 6.13$ Å is necessary [Eq. (1)]:

$$P(t) = \int_{R_c}^{\infty} P(R,t)dR \tag{1}$$

$r_{benzhydryl}$ and r_{Cl} are the radii of the fragment radicals deduced from the cavity volume found by a DFT calculation in a continuum solvation model.

$P_{RP}(R,t)$ and $P_{IP}(R,t)$ cannot be propagated directly; instead, underlying distribution functions $S_{RP}(R,t)$ and $S_{IP}(R,t)$ have to be used.[33,53] These are related to $P_{RP}(R,t)$ and $P_{IP}(R,t)$ by [Eqs. (2) and (3)]:[54–56]

$$P_{RP}(R,t) = 4\pi R^2 S_{RP}(R,t)\exp[-V_{RP}(R)/k_BT] \tag{2}$$

$$P_{IP}(R,t) = 4\pi R^2 S_{IP}(R,t)\exp[-V_{IP}(R)/k_BT] \tag{3}$$

with the intrapair potentials $V_{RP}(R)$ and $V_{IP}(R)$. The radial distribution function $g(R)$ modeling the partially ordered solvent shell is entering the description through the potentials. k_BT is the thermal energy. This step is needed to ensure that the Boltzmann distribution is an equilibrium solution of the model.

Differential Equations with Sink and Source Terms

The resulting set of coupled differential equations is [Eqs. (4) and (5)]:

$$\frac{\partial}{\partial t}S_{RP}(R,t) = L^+ S_{RP}(R,t) - k_{ET}(R)S_{RP}(R,t)$$
$$- k_{rec}^{RP}(R)S_{RP}(R,t) - k_{stab}^{RP}(R)S_{RP}(R,t) \tag{4}$$

$$\frac{\partial}{\partial t}S_{IP}(R,t) = L^+ S_{IP}(R,t)$$
$$+ k_{ET}(R)S_{RP}(R,t)\exp\left[-\frac{e^2}{4\pi\varepsilon_0\varepsilon_{st}k_BT}\frac{1}{R}\right]$$
$$- k_{rec}^{IP}(R)S_{IP}(R,t) - k_{stab}^{IP}(R)S_{IP}(R,t) \tag{5}$$

The exponential factor accompanying the source term in Equation (5) ensures that the population transfer between $P_{RP}(R,t)$ and $P_{IP}(R,t)$ is properly described by $S_{RP}(R,t)$ and $S_{IP}(R,t)$ within the Smoluchowski formalism. L^+ is the adjoint Smoluchowski operator in spherical coordinates. The exact form of L^+ together with further details of the calculations are given in Section S4 of the Supporting Information. The system of partial differential equations is solved numerically for a given set of parameters. Various input parameters were taken from the literature and others were fitted to the experiment. Particularly important values are discussed below, and all values are summarized in Table S1.

The electron transfer is a sink term for the radical distribution and a source term for the ion pairs. The back electron transfer pathway is neglected in our simulations, because it is highly endergonic in solvents such as CH_3CN or CH_2Cl_2 due to the ultrafast solvation of the cation. The driving force for the

electron transfer is given by the change in Gibbs free energy ΔG_{ET}. Values for ΔG_{ET} are known in some cases from measurements and a complete set has been calculated (see Section S4.3). An explicit distance dependence of $k_{ET}(R)$ is taken as $\exp[-\beta(R-R_c)]$ with $\beta = 0.7$ Å^{-1}.[52] The distance dependence of relevant quantities for the simulation of the phototriggered processes in Ph$_2$CHCl dissolved in CH$_3$CN is displayed in Figure S4.

Geminate recombination is a sink term for both the radicals and the ions. Within the model of colliding hard spheres it should only happen at contact. In reality the recombination probability is proportional to the square of the overlap of the electronic wave functions and the wave functions fall off exponentially with distance. Therefore the recombination probability also has to fall off smoothly with the interfragment distance. In accordance with ref. [57] we model it as $k_{rec}(R) = k_{rec}^0 \cdot \exp[-\alpha(R-R_c)]$ with $\alpha = 1.0$ Å^{-1}. k_{rec}^0 is the rate (probability) of recombination at contact distance. Finally, Equations (4) and (5) contain formal sink terms for a stabilization of the fragments. These terms refine the description of the solvent. The Marcus–Smoluchowski Equations (4) and (5) are based on a continuum solvation model in which the dielectric constant of the solvent remains invariant for the photofragment separation distance. In other words, the continuum model assumes that the fragments are surrounded by a complete solvation shell for all fragment distances. In actual fact, fully stabilizing solvation shells are only formed at distances large enough to accommodate two solvent molecules between the two ions. This leads to a sudden decrease of the energy of the system as the photofragments move apart and prevents them from re-encountering each other. We use a sigmoidal function with a 50% value at $R_c + 2d_{solv} = 13.3$ Å for $k_{stab}(R)$ to model the transfer from reactive (bound) radical/ion pairs to free ones. Here, d_{solv} denotes the solvent diameter. For the evaluation of the time-dependent populations [Eqs. (1)–(3)] we add the populations of the reactive species and the free ones to $P_R(R,t)$ and $P_I(R,t)$, since they contribute equally to the experimental signal.

Initial Conditions

In our model, the initial distribution of radical pairs is described by a Gaussian for $S_{RP}(t=0)$ centered at a mean benzhydryl radical–Cl$^\bullet$ radical distance larger than the contact distance R_c by half a solvent diameter d_{solv} and with a half width at half maximum of $1.8\,d_{solv}$. These values were obtained as best fit to the experimental data from simulation runs with varied distributions. A similar distance distribution has been found for electrons that have been photodetached from I$^-$ in aqueous solution.[58] The need for a nascent distribution that far exceeds direct contact of the radicals can be seen directly from the experimental data (Figure 2). The cation yield from electron transfer increases rapidly in the first 10 ps. This means that the electron transfer rate has to be quite significant, roughly $k_{ET}(R_c) = 10^{12}$ s^{-1}. If only pairs close to contact would be present, the same high rate would lead to a nearly complete depletion of the radical population. Only the rather wide nascent distribution used in our simulation can lead to the observed survival of roughly half the radicals. The stretched exponential behavior observed is a direct consequence of the evolution of the population distribution and the ensuing slowdown of the ensemble-averaged electron transfer rate. Notably, we effectively start to consider the evolution of the ion and radical pairs after a few hundred femtoseconds when the planarization and solvation is complete, and the distance distribution has become quasi-stationary. For distances smaller than R_c the distribution is set to zero. This mirrors the fact that fragments that are not ejected far enough are nearly instantaneously recombining. This is also seen in the total yield of fragments, which is far from quantitative.

Results of the Simulation

The time-dependent radical and ion distributions in CH$_3$CN for the best fit are shown in Figure 3 a and b. The calculated population dynamics for the benzhydryl radical and cation are compared to the experiment in Figure 2 (blue lines). For delay times above 1 ps there is an excellent agreement between the experimental and the simulated signal. For times below 1 ps the effective increase of optical signal strength by planarization and solvation of ion and radical pairs prevents the direct extraction of populations from the experiment.[42] A list of all the input parameters used in the model (taken from the literature) and the values determined for the best fit is given in Table S1.
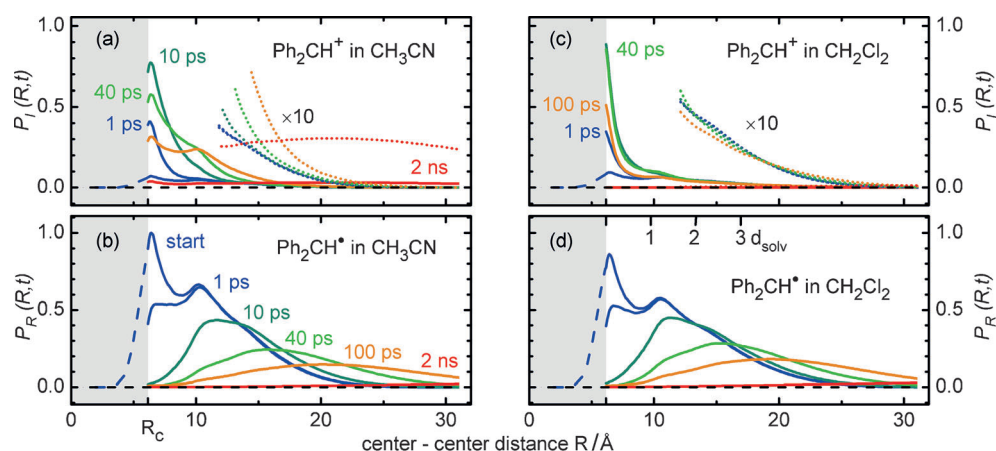
Figure 3. Simulated time dependence of the population distribution with CH$_3$CN as solvent for a) the sum of the bound and free ion pairs $P_I(R,t)$ and b) the sum of the bound and free radical pairs $P_R(R,t)$. Population distribution with CH$_2$Cl$_2$ as solvent for c) the ions and d) the radicals (see Section 5). The shaded area indicates distances smaller than the contact distance R_c. Nascent photofragments generated in this area (dashed lines) are assumed to recombine immediately.

The initial radical distribution $P_{RP}(R,t=0)$ shows some degree of structure due to the solvent shells. Within the first few picoseconds the closest radical pairs are converted to ion pairs or recombine. At $t=10$ ps the probability of finding radical pairs in the range from R_c to R_c+d_{solv} is already extremely small. Simultaneously the ion distribution $P_{IP}(R,t)$ rises from the small nascent values with a large distribution to sizable values close to R_c. At tens of picoseconds the radical distribution broadens due to diffusion and effectively shifts to larger average values, both due to diffusion and the still ongoing yet decreasingly important electron transfer and radical recombination at close distance. The ion pairs are held together by Coulomb attraction and therefore geminate recombination can compete with the diffusional separation. The value for the radical pair mutual diffusion coefficient D_F was taken from ref. [49]. The value for the ion pair was varied in the optimization of the model and the best value of $D_F(IP)=60$ Å^2 ns^{-1} is in the range of recently published values.[59,60] It is significantly smaller than the value for the radical pair, since the mobility of the ions is decreased by the stronger solvent–solute interactions and the resulting larger hydrodynamic radius.[61]

The distance-integrated radical population shows a pronounced decay and the cation population an increase with a stretched time constant of 10.8 ps (compare blue lines in Figure 2), nearly identical to the experimental value of 11.1 ps. The conversion of radicals to ions is slowed down from 20 ps on and ceases shortly after 100 ps due to the depletion of the radical distribution close to contact and the diffusional separation. The depletion is caused by both the electron transfer and the geminate recombination and in turn stops these processes eventually.

The cation population clearly decreases from the maximum achieved at 40 ps. This is due to the geminate recombination,

which we model with $k_{rec,0}^{IP}=25\times10^9$ s^{-1} at contact distance. The experimental value of $(198$ ps$)^{-1}=5\times10^9$ s^{-1} is five times smaller. This reflects directly the fact that the value in the simulation is distance dependent and only some of the ion pairs are in the range at which geminate recombination becomes effective, whereas the experimental value is the ensemble average. To obtain more comparable values, we calculated the recombination rate, that is, the ensemble-averaged probability, for selected times (see Table 2, second to last column). At 1 ps the calculated rate is nearly twice as fast as the experimental rate due to the large fraction of ion pairs with a small separation. At 40 ps it is roughly equal and at 2 ns it starts to become unimportant.

For the radical recombination a much faster value of $k_{rec,0}^{RP}=300\times10^9$ s^{-1} is found. This might seem surprising at first sight. We calculated the driving forces ΔG_{RP} and ΔG_{IP} and found the change in Gibbs free energy by 1.61 eV more exergonic for the radical recombination (see Table S2). This can readily explain the observed situation.

Without the consideration of stabilization for both the radicals and the ions (see above), we cannot reproduce the leveling of the radical population in the sub-nanosecond range, the recombination would keep going. This is shown in Figure 2 as green dashed lines. To reproduce the experimentally observed stable radical and cation population on the nanosecond timescale, equal stabilization rates $k_{stab,\infty}^{RP}=k_{stab,\infty}^{IP}=6.67\times10^9$ s^{-1} are used. Due to the sigmoidal function centered at two solvent diameters from contact distance, only pairs that have already been separated by diffusion are stabilized. The calculated rate (see Table 2, last column) at 1 ps shows little likelihood for the ions to stabilize, since they are still too close. At 40 ps the rate even decreases because the distance of the newly generated ions is even closer to R_c and only at 2 ns does it

Table 2. Experimental and theoretical (*italic*) driving forces ΔG and rate constants k of the electron transfer, geminate recombination, and separation/stabilization for different benzhydryl derivatives and solvents (see Supporting Information, Sections S1.4 and S4.2, for definitions).

Solvent	Derivative	ΔG_{ET}[a] [eV]	ΔG_{ET}[b] [eV]	τ_{SE}[c] [ps]	[ps]	k_{ET} [10^9 s^{-1}] ③[d]	k_{rec}^{IP} [10^9 s^{-1}] ⑦[e]	$k_{sep/stab}^{IP}$ [10^9 s^{-1}] ⑥[f]
	(tol)$_2$CHCl	−1.79	−1.82	17.6			3.57	1.98
	tol(Ph)CHCl	−1.69	−1.70	18.7			4.10	1.93
	Ph$_2$CHCl	−1.68	−1.61	11.1			5.05	2.19
					1	*66.7*	*7.87*	*0.86*
CH$_3$CN	*simulation*		*−1.71*	*10.8*	*40*	*3.77*	*5.81*	*0.46*
					2000	*0.13*	*1.33*	*3.23*
	mfp(Ph)CHCl		−1.48	8.4			5.13	2.52
	dfp(mfp)CHCl		−1.19	–			14.5	5.59
	(tol)$_2$CHCl		−1.45	19.3			4.08	<0.25
	tol(Ph)CHCl		−1.32	24.2			5.68	<0.25
CH$_2$Cl$_2$	Ph$_2$CHCl		−1.23	11.2			7.46	<0.25
					1	*35.7*	*7.30*	*0*
	simulation		*−1.13*	*12.3*	*40*	*2.31*	*10.0*	*0*
					2000	*0.004*	*0.37*	*0*
butyronitrile	Ph$_2$CHCl			27.3			6.06	1.12
chloroform	Ph$_2$CHCl			13.0			8.00	<0.25

[a] Experimental and [b] calculated Gibbs free reaction energy of the electron transfer within the radical pair. Experimental values from the one-electron reduction potentials for benzhydryl cations (from ref. [62]) and the Cl· radical (from ref. [63]). For calculation see Section S4.3. [c] Stretched exponential time constant assigned to the electron transfer ③. [d] Microscopic model ensemble average of the electron transfer rate at selected times. [e] Rate of the ion pair geminate recombination ⑦. [f] Rate for the cation diffusional separation (experiment)/stabilization (simulation) ⑥. One extra digit beyond the significance level is given in the last two columns to allow for a reproduction of the simulations/fits.

become quite sizable. The stabilization only has an effect in a distance range for which the electron transfer and the geminate recombination are no longer active.

Ensemble-Averaged Properties

The ability to calculate ensemble-averaged properties and in this way to link the microscopic picture with the experimental observables has been used for a number of further analyses. The results are summarized in Tables 2 and 3 and compared to the experimental values. The quantum yields Φ_{Hom} and Φ_{Het} as well as the yields Y_{ET} and Y_{rec}^{RP} rely on the knowledge of the molar absorption coefficients of benzhydryl radicals and cations. As the values reported in the literature vary to some extent,[9] Φ_{Hom}, Φ_{Het}, Y_{ET}, and Y_{rec}^{RP} can only be given with a relative precision of $\pm 20\%$. The other yields given in Table 3 are independent of the molar absorption coefficient and are therefore determined with a higher accuracy of about $\pm 5\%$.

The electron transfer rate is predominantly determined by ΔG_{ET} and the effective electronic coupling element V_{eff}. We calculated values for ΔG_{ET} (see Table S2) that compare favorably with the experimental values if available. For the simulations we allowed a variation within the known accuracy of the calculations of 0.1 eV. The value of $V_{eff} = 57$ cm^{-1} is within the range reported for these types of systems.[52,64] As a result an electron transfer rate of 667×10^9 s^{-1} is found on contact. The ensemble-averaged rate k_{ET} drops from 66.7×10^9 s^{-1} at 1 ps to 3.77×10^9 s^{-1} at 40 ps and finally practically vanishes at 2 ns when all remaining radical pairs have converted to free radicals. The theoretical model shows that the experimentally observed deviations from monoexponential decays are caused by the start-

ing distance distribution of the radical pairs and the distance dependence of the electron transfer rate. This leads to the effectively time-dependent electron transfer rate depicted in Figure S6.

The various yields clearly become time-dependent as the constituting processes evolve. By $t = 2$ ns the accumulated yields obtained from the simulation are all close to the experimental values. We mainly used the comparison with the optical signals, that is, the radical and cation population, for the adjustment of the model parameters, so the close match of all individual yields nicely confirms the consistency of our model.

In summary, the simulation highlights the importance of diffusion for the persistent generation of free ions and free radicals. The electron transfer predominantly happens in a narrow part of the distribution of benzhydryl–Cl$^{\cdot}$ inter-radical distances, even though a fairly wide range of distances arises from the photoinduced bond cleavage. This is a consequence of the electron transfer rate, which decays exponentially with increasing distance. The generated ion pairs still experience the Coulomb potential and cannot diffuse apart as easily as the uncharged radicals. This more than compensates the smaller driving force for recombination as compared to the radicals and leads to a higher overall recombination yield. These microscopic details are not considered by the kinetic model employed previously by Peters and co-workers in their extensive work on the photolysis of benzhydryl halides.[11,29,30] They invoke transitions between distinguishable species, that is, contact ion pairs (CIPs), solvent-separated ion pairs, and free ions as well as geminate radical pairs and free radicals, a model that renders at best a phenomenological description.

Table 3. Experimental and theoretical (*italic*) yields Y and quantum yields Φ of the electron transfer, geminate recombination, and separation/stabilization for different benzhydryl derivatives and solvents. See Supporting Information, Sections S1.3 and S4.2, for definitions. All values in %.

Solvent	Derivative	Φ_{Hom} ①[a]	Φ_{Het} ②[b]	[ps]	Y_{ET} ③[c]	Y_{rec}^{RP} ⑤[d]	$Y_{sep/stab}^{RP}$ ④[e]	Y_{rec}^{IP} ⑦[f]	$Y_{sep/stab}^{IP}$ ⑥[g]	Φ_{rad} [h]	Φ_{cat} [i]
	(tol)$_2$CHCl	46	2		75	0[j]	25[j]	64	36	19.3	11.4
	tol(Ph)CHCl	47	<1		73	0[j]	25[j]	68	32	17.7	11.0
	Ph$_2$CHCl	40	2		43	19	38	70	30	15.7	6.0
CH$_3$CN				*1*	*7*	*3*	*0*	*0*	*0*	*35.0*	*5.4*
	simulation			*40*	*36*	*14*	*9*	*20*	*1*	*19.5*	*13.2*
				2000	*43*	*17*	*40*	*69*	*31*	*(15.7)*	*6.0*
	mfp(Ph)CHCl	29	2		16	35	49	67	33	14.2	2.2
	dfp(mfp)CHCl	20	1		0	49	51	72	28	10.3	<1
	(tol)$_2$CHCl	27	2		60	0[j]	40[j]	>95	<5	12.3	1.3
	tol(Ph)CHCl	36	<1		56	2	42	>95	<5	15.4	<1
CH$_2$Cl$_2$	Ph$_2$CHCl	32	<1		27	28	45	>95	<5	14.5	<1
				1	*4*	*3*	*0*	*0*	*0*	*28.8*	*4.5*
	simulation			*40*	*21*	*20*	*9*	*29*	*0*	*18.1*	*7.2*
				2000	*27*	*26*	*47*	*99*	*0*	*(14.5)*	*0.3*
butyronitrile	Ph$_2$CHCl	25	<1		21	0[j]	79[j]	84	16	21.7	<1
chloroform	Ph$_2$CHCl	34	2		20	33	47	>95	<5	15.7	<1

[a] Quantum yield for direct homolytic bond cleavage. [b] Quantum yield for direct heterolytic bond cleavage. [c] Yield of the electron transfer (pathway ③ in Scheme 1). [d] Yield of recombination of the radical pair ⑤. [e] Yield of diffusional separation (experiment)/stabilization (simulation) of the radical pair ④. [f] Yield of the ion pair geminate recombination ⑦. [g] Yield of diffusional separation (experiment)/stabilization (simulation) of the ion pair ⑥. [h] Final (nanosecond) radical quantum yield for the experimental values, cumulative quantum yield up to the specific time for the simulation. [i] Final (nanosecond) cation quantum yield for the experimental values, cumulative quantum yield up to the specific time for the simulation. [j] Slightly more cations appear than radicals disappear. Therefore, Y_{rec}^{RP} was set to 0% and Y_{esc}^{RP} was set so that $Y_{ET} + Y_{rec}^{RP} = 100\%$. One extra digit beyond the significance level is given in the last two columns to allow for a reproduction of the simulations/fits.

4.2. Spectral Shifts Resolve Spatial Information

Due to the high signal-to-noise ratio and the sub-100 cm^{-1} (about 1 nm) resolution provided by our setup we are able to observe that the product bands shift in the sub-nanometer range. This observable has not been accessible previously as only two-color pump–probe experiments have been carried out on comparable systems. Due to electronic interactions the absorption band position of a single solute molecule is a sensitive probe for its immediate environment. With the ensemble averaging in our measurements the overall band position is given by the convolution of the time-dependent distance distribution and the distance-dependent spectral position of the absorption band. Therefore, temporal shifts of the absorption maximum (peak shift) reveal changes of the distance distribution and thereby the immediate surroundings in solution, specifically the leaving group and the solvent molecules.

Temporal shifts of the absorption band due to microscopic changes have already been observed in the infrared[32] as well as in the visible region.[65,66] In the first hundreds of femtoseconds the geometric relaxation of the nascent fragment can also contribute to the peak shift.[42] In the following we discuss the peak shift determined from the transient spectra (compare Figure 1) by an iterative procedure described in Section S3 of the Supporting Information.

The observed temporal evolution of the peak shifts (see Figure 4) shows a complex behavior that can only be fitted with a sum of exponential functions. After excitation, both the radical and the cation bands experience a pronounced initial blueshift. These shifts can be fitted with time constants of 170 fs for the radical and 250 fs for the cation.

The values compare well with the published solvation times of 140–500 fs of CH$_3$CN,[67–70] which indicates that the blueshift

is caused by the rearrangement of the solvation shell in the immediate vicinity of the photogenerated radical and ion pair.[42] The radical shows a further redshift within the first 2 ps. Although the initial dynamics up to 2 ps is caused by solvent rearrangement and by relaxation and planarization of the photofragments (light green range in Figure 4), the subsequent peak shifts shown in the light brown range of Figure 4 are caused by the interplay between the diffusional separation and the population dynamics of the cations and radicals.

The cation shows a redshift, which can be fitted with two exponential functions with time constants of 2.9 and 140 ps. At pump–probe delays larger than 500 ps the cation peak position reaches a wavelength of 436.1 nm and undergoes no further shift, thus indicating that free and fully solvated cations have been formed.

From a quantum chemical point of view it is reasonable that the absorption shifts to the red. For increasing inter-ion distances the energy of the ground state of the benzhydryl cation can be expected to increase slightly more than the energy of the excited state. Our observation also reproduces the findings of Schneider et al.[71] who observed that the absorption maximum of free (unpaired) benzhydryl cations (e.g. (tol)$_2$CH$^+$) is redshifted by approximately 2 nm relative to cations paired with BCl$_4^-$ anions.

The radical undergoes a blueshift from 2 to 30 ps—in contrast to the cation—which can be modeled with the 11.1 ps stretched exponential found in the kinetic analysis. After a further redshift from 30 to 100 ps with a time constant of 45 ps, the radical peak position reaches a stable wavelength of 328.4 nm.

Unlike for the cation, an increase in the inter-radical distance apparently leads to a blueshift. This can be rationalized by the fact that the exchange of the Cl$^\bullet$ radical by CH$_3$CN solvent molecules leads to a better stabilization of the radical ground state and thus a blueshift of the absorption band. By the observation of the peak shift we can trace the change in the inter-radical distance distribution, which is caused predominantly by the electron transfer.

The 140 ps time constant of the cation peak shift is equal within experimental precision to the 138 ps total decay time found in the analysis of the cation population. Together with the equality of the 11.1 ps stretched exponential for the radical peak shift and population kinetics, we find a reassuring match between the population and the peak shift evolution. We therefore arrive at the following microscopic picture for the reaction scheme: the individual photofragment pairs have a peak position dependent on their mutual distance. After photolysis a relatively broad distribution of distances exists leading to an inhomogeneous peak broadening additional to that caused by solvent interactions. Peak shifts are now caused by two mechanisms: 1) the tendency of the species to diffuse apart and hence to increase the mean distance; and 2) the efficient depletion of subensembles with small distances by electron transfer and geminate recombination. It is the second mechanism that mainly leads to the peak shifts that can be reproduced with time constants also found in the population dynamics.
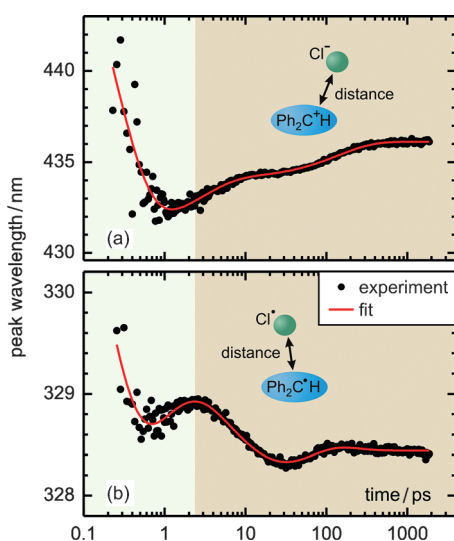
Figure 4. Measured (dots) and fitted (red lines) temporal evolution of the benzhydryl a) cation and b) radical peak position after photolysis of Ph$_2$CHCl in CH$_3$CN. The temporal regime in which the shift is dominated by the changes in the radical- and ion pair distance distributions caused by electron transfer, geminate recombination, and diffusion is highlighted in light brown.

In the model of Peters and co-workers[11, 29, 30] and in the concept of Winstein and Robinson,[72] distinguishable species denoted as contact ion/radical, solvent-separated, and free pairs are postulated. One might attempt to subdivide the distributions used in our simulation into these entities. Then the evolution of the distributions in our picture would transfer to decay from one species to the other. Spectroscopically this should yield isosbestic points in the evolution of the transient spectra. A careful analysis of our data clearly shows that these are not present. We therefore have to conclude that no well-defined subspecies exist and only the description by distributions is meaningful.

5. Effects of Temperature, Solvent Polarity, and Substitution on the Radical and Cation Yield

By a suitable variation of physical and chemical parameters we can influence the kinetics and the yields of the different pathways shown in Scheme 1. Although changes in temperature and solvent viscosity mainly affect the diffusional contribution, solvent polarity and redox potentials of the benzhydryl radicals and cations affect the driving force of the electron transfer. Control of the redox potential is achieved by attaching electron-donating or electron-withdrawing substituents to the phenyl rings of the benzhydryl chloride precursors (see Table 1).

5.1. Temperature Dependence of the Electron Transfer and Geminate Recombination

To verify the important role of diffusion experimentally, we carried out transient absorption measurements in a temperature interval from 5 to 60 °C. Figure 5 shows the temporal evolution of the radical and cation absorption at different temperatures normalized to the maximum. The curves for 22 °C have already been shown in Figure 2. The initial rise of the radical signal within the first 300 fs shows no significant variation with temperature and is therefore not shown in Figure 5b. Note that in Figure 5 the time axis is linear as compared to the combined linear/logarithmic scale in Figure 2. In contrast to the 300 fs increase, we observe a significant decrease of the stretched exponential time constant modeling the electron transfer from 11.5 ps at 5 °C to 9.4 ps at 60 °C. A consideration of the absolute amplitudes of the fit gives access to the efficiencies of the processes. Although at 5 °C only 37 % of the generated radicals do not undergo electron transfer and become free radicals, 44 % of the radicals survive at 60 °C (see Table S3 in the Supporting Information). Electron transfer quantum efficiencies Y_{ET} can be determined from the stretched exponential amplitudes of the cation and radical associated with the electron transfer. We observe a distinct decrease of the efficiency from 46 % at 5 °C to 38 % at 60 °C (see Figure 5b).

The lower efficiency and the smaller time constant of the electron transfer can be explained by the lowered viscosity of acetonitrile with increasing temperature.[73] At low temperatures the higher viscosity slows down the diffusional separa-
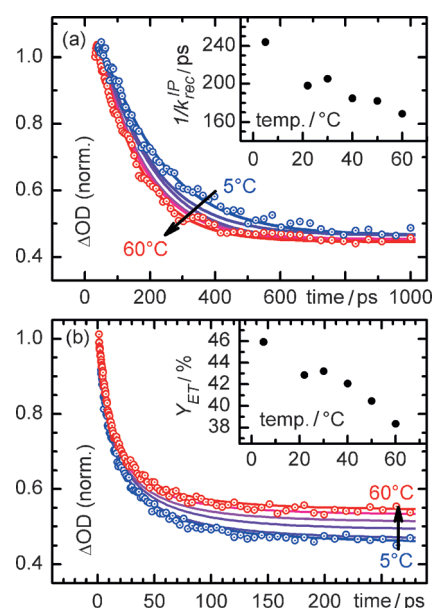
Figure 5. Temperature dependence of a) the geminate recombination of the cation and b) the radical absorption due to electron transfer after UV excitation of Ph_2CHCl in CH_3CN. Time traces are normalized to the maximum of the absorption. Fits are represented by solid lines. For clarity, only the data for the highest and lowest temperatures are shown. The initial rise of the radical signal within the first 300 fs as well as the rise of the cation signal within 40 ps are not shown.

tion of the radical pairs. Although the change in viscosity does not affect the electron transfer efficiency for radical pairs at small distances, it becomes important for radical pairs at the shoulder of the Gaussian distance distribution. Here the electron transfer rate is substantially lower relative to the center of the distribution. Therefore, an increase in the effective radical separation rate k_{sep}^{RP} due to a decrease of the viscosity lowers the overall efficiency of the electron transfer.

The temperature also has an impact on the geminate recombination of the cations (see Figure 5a; data before the cation maximum not shown). Raising the temperature from 5 to 60 °C leads to a faster decay of the cation population. The determination of the intrinsic rates for geminate recombination k_{rec}^{IP} and diffusional separation of the ion pair k_{sep}^{IP} reveals that both are strongly affected by the temperature (see Table S3). In analogy to the case of the radicals, the higher temperature leads to a faster diffusional separation and therefore the rate k_{sep}^{IP} rises from $1.78 \times 10^9 \text{ s}^{-1}$ at 5 °C to $2.40 \times 10^9 \text{ s}^{-1}$ at 60 °C. The higher temperature also facilitates the movement of the reactants towards each other and thus accelerates the geminate recombination reaction of the ion pair Ph_2CH^+/Cl^-. The rate constant for geminate recombination k_{rec}^{IP} therefore rises from $4.10 \times 10^9 \text{ s}^{-1}$ at 5 °C to $5.92 \times 10^9 \text{ s}^{-1}$ at 60 °C. However, the yield of the geminate recombination is hardly affected by the temperature as the faster geminate recombination is compensated by the faster diffusional separation.

5.2. Influence of Substitution and Solvent Polarity on the Intermediate (ps) and Final (ns) Quantum Yields of the Cation Generation

Figure 6a shows the experimental results obtained for Ar_2CHCl derivatives with different substituents attached to the phenyl rings in CH_3CN (Table 1). For the cation with the most electron-withdrawing substituents, $dfp(mfp)CH^+$, the observed carbocation population stems only from direct heterolysis. An in-
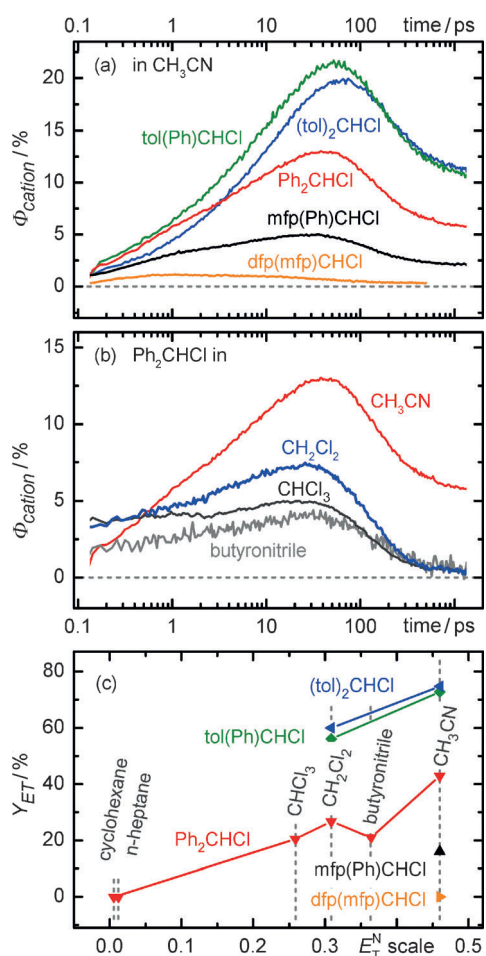
Figure 6. a) Substitution dependence of the transient cation quantum yield Φ_{cation} in CH_3CN. b) Solvent dependence of the transient cation quantum yield from Ph_2CHCl. c) Solvent dependence of the final electron transfer yield Y_{ET} for different benzhydryl chloride derivatives.

crease of the population due to electron transfer is not observed. For the less electrophilic cations, on varying the substituents at the aryl rings, we observe an increase in both the intermediate cation quantum yield Φ_{cation} on the picosecond timescale and the electron transfer yield Y_{ET} on going from electron-withdrawing to electron-donating substituents (see Figure 6a and c and Table 2).

Ofial et al.[62] have demonstrated that the oxidation potentials of benzhydryl radicals and hence the driving force ΔG_{ET} for electron transfer depend on the aryl substituents, but experimental data for the *m*-fluoro compounds are not available.

Ab initio calculations for the electron transfer reaction within the radical pair $Ar_2CH^\bullet/Cl^\bullet$ yielding the ion pair Ar_2CH^+/Cl^- at the M06-2X/6-311+G(d) level of theory with a polarizable continuum model (PCM) solvent for CH_3CN show a change in ΔG_{ET} from -1.82 eV for the reaction $(tol)_2CH^\bullet Cl^\bullet \rightarrow (tol)_2CH^+ Cl^-$ to -1.19 eV for the reaction $dfp(mfp)_2CH^\bullet Cl^\bullet \rightarrow dfp(mfp)CH^+ Cl^-$ (see Tables 2 and S2). Thus, the electron transfer becomes thermodynamically less favorable as we go from electron-donating to electron-withdrawing substituents. However, the electron transfer times observed in our experiments (Figure 6a and Table 2) increase with increasing driving force. This behavior indicates that the electron transfer already approaches the Marcus-inverted regime (see Table 2). As the reorganization energy $\lambda(R)$ changes with inter-radical distance, both the normal and the inverted regime can contribute to the effective electron transfer rate.

There is also a significant influence of the substituents on the geminate recombination of the ion pair. The rate of the geminate recombination k_{rec}^{IP} increases on going from the least electrophilic cation $(tol)_2CH^+$ ($E = 3.63$)[36] to the cation with the highest electrophilicity $dfp(mfp)CH^+$ ($E = 7.52$).[38] This behavior is reproduced by the ab initio free reaction energy for geminate recombination of the ion pair ΔG_{IP} shown in Table S2. An increase of the rate constants for activation-controlled reactions of benzhydryl ions with chloride anions was also reported for bimolecular reactions on the >10 ns timescale[74] and nicely matches the increasing rate k_{rec}^{IP} for increasing electrophilicity. Increasing electrophilicity of the benzhydryl cation leads to a distinct decrease of the nanosecond cation quantum yield $\Phi_{cat,\infty}$ as the yield of geminate recombination Y_{rec}^{IP} grows and the yield of the electron transfer Y_{ET} drops (see Figure 6a and Table 2).

As mentioned in the Introduction, the quantum yield of carbocations resulting from the photolysis of benzhydryl halides is negligibly small in many solvents on the nanosecond timescale.[6–9] Our femtosecond pump–probe measurements show that for Ph_2CHCl no electron transfer occurs in apolar solvents, such as cyclohexane ($E_T^N = 0.006$[75]) and *n*-heptane ($E_T^N = 0.012$; see Figure 6c). The ab initio Gibbs free reaction energy values ΔG_{ET} of the electron transfer indicate that in these solvents the electron transfer is an endergonic process (see Table S2). In contrast, in the moderately polar solvents dichloromethane ($E_T^N = 0.309$) and chloroform ($E_T^N = 0.259$) electron transfer does occur, with an electron transfer yield Y_{ET} of about 20% (see Figure 6b,c and Figure S9). As in CH_3CN ($Y_{ET} = 43\%$, $E_T^N = 0.460$) this leads to a significant intermediate cation quantum yield on the picosecond timescale. The large cation population is, however, quickly extinguished by an extremely efficient geminate recombination ($Y_{rec}^{IP} > 95\%$) with a rate of 7.46×10^9 s^{-1} in dichloromethane and 8.00×10^9 s^{-1} in chloroform (see Figure 6b and Table 2).

Only in the highly polar acetonitrile can a significant fraction of the ion pairs (≈ 30–35%) separate diffusionally to free ions, which are observable on the nanosecond timescale. This can be explained by the large difference in the relative permittivities of the solvents. Although in CH_3CN the large permittivity ($\varepsilon_r = 35.94$) promotes dissociation of ions, the moderate per-

mittivities of dichloromethane ($\varepsilon_r = 8.93$) and chloroform ($\varepsilon_r = 4.89$) do not allow for a shielding of the Coulomb attraction that is sufficient for the generation of free ions.[75] This leads to the pronounced decrease observed for the rate of cation separation on going from acetonitrile ($k_{sep}^{IP} = 2.19 \times 10^9$ s^{-1}) to dichloromethane or chloroform ($k_{sep}^{IP} < 0.25 \times 10^9$ s^{-1}).

An analogous behavior has been found for the solvent dependence of the cation generation from (tol)$_2$CHCl and tol(Ph)CHCl. Although a large intermediate cation quantum yield is observed in acetonitrile, as well as in dichloromethane and chloroform, only in acetonitrile does a significant fraction of the ion pairs separate diffusionally and give rise to free ions. In the moderately polar solvents CH$_2$Cl$_2$ and CHCl$_3$, the initially generated ion pairs again undergo highly efficient geminate recombination.

5.3. Simulation for CH$_2$Cl$_2$ as Solvent

To corroborate our microscopic model, we performed additional simulations for the photoinitiated processes of Ph$_2$CHCl in CH$_2$Cl$_2$. For the description of the reactions we had to use only slightly varied parameters compared to those for CH$_3$CN. The mutual diffusion coefficient D_F(RP) is lowered due to the larger cavity radius of both radical fragments in CH$_2$Cl$_2$. The slightly larger cavity radius in the larger and more spherical CH$_2$Cl$_2$ mirrors the definition of the cavity radius as an equivalent volume that cannot be accessed by the solvent. The optimum coefficient D_F(IP) is roughly doubled in accord with the much lower polarity and the subsequent decrease in solute–solvent association. The stabilization rate for the radicals could be left unchanged and this is reasonable because the uncharged radicals should not be influenced too strongly by the solvent polarity. In contrast, the stabilization rate for the ions has to be set very low, since the low polarity of CH$_2$Cl$_2$ does not stabilize the cation well. We therefore set the rate to zero. The electronic coupling for the electron transfer is only slightly changed. The main factor for the decreased yield is the decreased ΔG_{ET}. We also found the recombination rates to increase slightly. For the ion pairs this can be rationalized by the decreased stabilization of the ions in the less polar CH$_2$Cl$_2$. The resulting simulation of the distribution evolution (see Figure 3c and d) show nicely that the radicals evolve quite similarly in both solvents whereas the ions in CH$_2$Cl$_2$ never separate sufficiently to be eventually stabilized to free ions. The population kinetics are reproduced with high fidelity, as seen in Figure S5c and d.

6. Conclusions

We have presented sub-100 fs transient spectroscopy of the UV-initiated bond cleavage and reaction dynamics of benzhydryl chloride (Ph$_2$CHCl). The spectra fully cover the well-separated signatures of the radical and cation fragments. The extremely high sensitivity and spectral resolution allow the determination of the electronic state of the evolving product distributions and even small influences of the surroundings. The overall photolysis leading to the radical and ion pairs and the quantum yields observed on different timescales are the result

of several complex and interconnected processes. To decipher these processes and understand their interplay, the population dynamics obtained from transient spectroscopy is interpreted with a quantitative analysis of the species concentrations. This leads to absolute reaction quantum yields and is substantiated with a spectral peak shift analysis. The theoretical model reproduces faithfully the experimental findings on the Ph$_2$CHCl precursor and gives insight into decisive properties that are not accessible by experiment. We obtain a mechanism for the radical and cation generation that contains several unexpected aspects and goes far beyond the previously used kinetic model (Scheme 2).
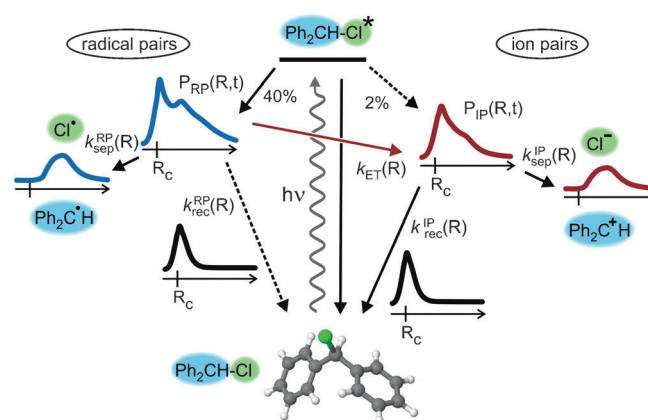
Scheme 2. Microscopic processes that add up to the overall heterogeneous reaction. After UV excitation of Ph$_2$CHCl the molecules undergo predominantly homolytic bond cleavage to a broad distribution of fragment distances symbolized by the inserted graphs. An electron can then be transferred within the radical pair for closely spaced radicals. The simultaneously occurring diffusional separation of the radical pair slows down the electron transfer and leads to free radicals. The ion pairs in close vicinity can undergo geminate recombination (see inserted black graphs). The ions at larger separation can diffuse apart and form free ions.

After excitation at 270 nm, Ph$_2$CHCl undergoes predominantly homolytic C–Cl bond cleavage (40%) in CH$_3$CN and relaxation into a radical pair within 300 fs. The direct photoinduced heterolytic C–Cl bond cleavage is a minor reaction channel (2%). The remaining 57% of the excited molecules do not contribute to the photofragment population and probably relax directly back into the ground state.

The radical pairs are generated in a wide distribution of distances due to the high kinetic energy induced by the bond cleavage. The previous assumption of exclusive occurrence of radical pairs at direct contact[11] cannot explain properly our observed signal evolutions. These can only be reproduced with a distribution out to about three interjacent solvent molecules.

The radical pairs with small inter-radical distances undergo electron transfer to form benzhydryl cations and Cl$^-$ anions (43%), geminate recombination (19%), or diffusional separation to free radicals (38%). The electron transfer generates the major part of the cation population.

As the electron transfer occurs from a distribution of distances between the benzhydryl and Cl· radical, the system exhibits a wide range of electron transfer rates leading to the observed stretched exponential with a mean electron transfer time of 22.2 ps. Contrary to the kinetic model of Lipson et al. that reported the same deviation from an exponential behavior but did not interpret it,[29] our model correctly reproduces this important feature.

Seventy percent of the generated ion pairs undergo geminate recombination in CH_3CN, whereas the competing diffusional separation leads to free ions for the remaining 30%. As shown by the combined Marcus–Smoluchowski model, the ion pairs generated by electron transfer at larger distances have a higher survival probability.

The previous kinetic model of the photolysis of benzhydryl halides invokes transitions between distinguishable species, that is, CIPs, solvent-separated ion pairs, and free ions as well as geminate radical pairs and free radicals.[11] From our comprehensive femtosecond broadband transient spectra we can deduce detailed and decisive information that could not be obtained from the former transients recorded at a single wavelength. The nascent radicals and cations are in the electronic ground state immediately after generation. This is seen unambiguously from their absorption spectrum. The evolution of the distance distributions is reflected in small but significant shifts of the bands. The time constants of the shifts match the kinetic time constants of the population evolution.

It turns out to be essential for the reaction modeling to consider explicitly the distance-dependent electron transfer acting on the radical distribution and to take diffusion into account for the later times. The resulting microscopic model does not rely on exponential transfer rates between well-defined species. Such rate-determined kinetics would lead to isosbestic points in the spectral evolution that are not seen. Rather a smooth shift of the band maximum is found. With the new model we are able to obtain an excellent agreement between the experimental findings and the simulation. A unified description of the population dynamics and diffusional separation to free radicals/ions results. It does not provide support for the distinct species considered in traditional descriptions.[48] Electron transfer not only happens in radical pairs at contact distance but also up to distances incorporating at least one solvent molecule.

The observed population dynamics can only be explained with a distance distribution of nascent radical pairs spanning out to as much as three solvent molecules in between the benzhydryl radical and the chlorine radical. Such a wide distribution allows efficient early generation of cations by electron transfer as well as sufficient survival of radicals at late times. The increase of the mean distance within the ion pairs in the first 100 ps is not dominated by the diffusional separation of the ions but results from the fact that the electron transfer at later times occurs in radical pairs, which are located further apart. Only at later times does diffusion become the main process increasing the mean distance and thus certainly generating free ions.

In the established description of bond heterolysis, the issue of nonequilibrium solvation was extensively discussed.[76] Analytic model potentials reflecting covalent and ionic character were used instead of potentials based on quantum chemistry.[77–79] As a result an excited geminate radical pair was postulated. The conversion to the ion pairs was then thought to proceed through a transition to the "ground-state surface" and subsequently to the CIP.[11] Similarly, in bimolecular photoinduced electron transfer the CIP was described as an exciplex.[80]

At least in aprotic solvents these descriptions cannot be supported in view of the present results and the existing quantum chemical calculations.[28,43] Interestingly, one of the few available quantum chemical calculations including solvent molecules could also not support the existence of CIPs.[81] After homolysis of benzhydryl chloride (Ph_2CHCl) in CH_3CN the benzhydryl radical is lower in energy than the unoccupied cation state. Only through fluctuations in the polar solvent environment and the radical geometry does the electron transfer from the benzhydryl to a neighboring chlorine radical become possible. A partial transfer is most likely able to stabilize the cation state below the radical state. Such a solvent-controlled electron transfer has been documented in crystal violet lactone.[82] We believe that the radical pair state is best described as metastable. Once the ion pair state is accessed it is immediately lowered sufficiently that back electron transfer is highly unlikely.

The dynamics and outcome of the interwoven processes can be steered by the variation of physical and chemical parameters. The investigation of the cation formation in a series of solvents with varying polarity unveiled the existence of three regimes. In apolar solvents, such as cyclohexane and n-heptane, the photogenerated radical pairs do not undergo electron transfer as the process is endergonic in these media. In moderately polar solvents, such as dichloromethane, electron transfer occurs but the carbocation population is almost totally extinguished by geminate recombination, as the low solvent permittivity does not allow for an efficient ion pair separation. The use of a neutral leaving group can avoid this problem and lead to a high benzhydryl cation yield.[26] Only in highly polar solvents (CH_3CN) is a large fraction of the ion pair population able to avoid geminate recombination and separates to free ions, which are detectable on the nanosecond timescale.

The complex dynamics of the photolysis of benzhydryl chlorides can also be modified by substitution at the phenyl rings. Electron-donating groups increase the primary homolysis yield, whereas electron-withdrawing groups decrease it by tens of percent. The electron transfer within the radical pair decreases in the same direction and even vanishes for dfp(mfp)CHCl in acetonitrile. With increasingly electron-withdrawing substituents the ion pair recombination rate and yield increases in line with the increasing electrophilicity.

Beyond the population kinetics, the benzhydryl chlorides allow for the observation of the temporal development of the distance distribution of the transient species through the analysis of the photoproduct quantum yields and the shifts of their peaks in the UV/Vis spectrum. This constitutes the basis for

more advanced multipulse nonlinear experiments that have been developed in recent years. For example, terahertz experiments[83] and 2D IR chemical exchange spectroscopy[84] allow for a more direct measurement of the Cl^- anion and $Cl^•$ radical displacement from the benzhydryl fragment. Furthermore, as recently shown by Baiz et al.,[85] vibrational Stark-effect spectroscopy can be employed to measure the solvent response during electron transfer between the radicals.

A major impetus of this study was the investigation of the reaction kinetics of photolytically generated benzhydryl cations with a variety of nucleophiles. As these bimolecular reactions occur on timescales longer than nanoseconds, the final quantum yields of the free carbocations are the aspect most important to the practical application of benzhydryl chlorides as precursors for benzhydryl cations. As many processes that increase or decrease the cation population occur on the femto- to picosecond timescale, their direct observation and understanding is crucial for the maximization of the final (nanosecond) cation quantum yield. The reported investigations show that this can be achieved if the radical pair sticks together as long as possible for an efficient electron transfer and the generated ions are separated efficiently with the aid of the solvent.

Acknowledgements

[1] *Reactive Intermediate Chemistry* (Eds.: R. A. Moss, M. S. Platz, M. Jones, Jr.), Wiley-Interscience, Hoboken, **2004**.
[2] *Carbonium Ions, Vols. I–V* (Eds.: G. A. Olah, P. v. R. Schleyer), Wiley, New York, **1968–1976**.
[3] G. A. Olah, *Angew. Chem.* **1973**, *85*, 183–234; *Angew. Chem. Int. Ed.* **1973**, *12*, 173—212.
[4] G. A. Olah, *J. Org. Chem.* **2001**, *66*, 5943–5957.
[5] *Carbocation Chemistry* (Eds.: G. A. Olah, G. K. S. Prakash), Wiley-Interscience, Hoboken, **2004**.
[6] R. A. McClelland, *Tetrahedron* **1996**, *52*, 6823–6858.
[7] R. A. McClelland in *Reactive Intermediate Chemistry* (Eds.: R. A. Moss, M. S. Platz, M. J. Jones), Wiley, Hoboken, **2004**, pp. 3–40.
[8] P. K. Das, *Chem. Rev.* **1993**, *93*, 119–144.
[9] J. Bartl, S. Steenken, H. Mayr, R. A. McClelland, *J. Am. Chem. Soc.* **1990**, *112*, 6918–6928.
[10] M. A. Miranda, J. Pérez-Prieto, E. Font-Sanchis, J. C. Scaiano, *Acc. Chem. Res.* **2001**, *34*, 717–726.
[11] K. S. Peters, *Chem. Rev.* **2007**, *107*, 859–873.
[12] P. J. Kropp in *CRC Handbook of Organic Photochemistry and Photobiology, 2nd ed.* (Eds.: W. Horspool, F. Lenci), CRC, Boca Raton, **2004**, pp. 1-1–1-32.
[13] T. Kitamura in *CRC Handbook of Organic Photochemistry and Photobiology, 2nd ed.* (Eds.: W. Horspool, F. Lenci), CRC, Boca Raton, **2004**, pp. 11-1–11-10.
[14] L. J. Johnston, P. Kwong, A. Shelemay, E. Lee-Ruff, *J. Am. Chem. Soc.* **1993**, *115*, 1664–1669.
[15] J. P. Sammes in *Chemistry of the Carbon–Halogen Bond* (Ed.: S. Patai), Wiley, New York, **1973**, chap. 11, pp. 747–794.
[16] G. Pohlers, J. C. Scaiano, E. Step, R. Sinta, *J. Am. Chem. Soc.* **1999**, *121*, 6167–6175.
[17] S. Kobayashi, Y. Hori, T. Hasako, K.-i. Koga, H. Yamataka, *J. Org. Chem.* **1996**, *61*, 5274–5279.
[18] J. Peon, D. Polshakov, B. Kohler, *J. Am. Chem. Soc.* **2002**, *124*, 6428–6438.
[19] M. Baidya, S. Kobayashi, F. Brotzel, U. Schmidhammer, E. Riedle, H. Mayr, *Angew. Chem.* **2007**, *119*, 6288–6292; *Angew. Chem. Int. Ed.* **2007**, *46*, 6176—6179.
[20] B. T. Phan, C. Nolte, S. Kobayashi, A. R. Ofial, H. Mayr, *J. Am. Chem. Soc.* **2009**, *131*, 11392–11401.
[21] G. Hallett-Tapley, F. L. Cozens, N. P. Schepp, *J. Phys. Org. Chem.* **2009**, *22*, 343–348.
[22] R. M. O'Ferrall, *Stabilities and Reactivities of Carbocations in Advances in Physical Organic Chemistry, Vol. 44* (Ed.: J. P. Richard), Amsterdam, **2010**, pp. 19–122.
[23] J. A. Pincock, *Acc. Chem. Res.* **1997**, *30*, 43–49.
[24] M. Dankowski in *The Chemistry of Organophosphorus Compounds, Vol. 3* (Ed.: F. R. Hartley), Wiley, Chichester, **1994**, pp. 325–343.
[25] J. Ammer, M. Baidya, S. Kobayashi, H. Mayr, *J. Phys. Org. Chem.* **2010**, *23*, 1029–1035.
[26] J. Ammer, C. F. Sailer, E. Riedle, H. Mayr, *J. Am. Chem. Soc.* **2012**, *134*, 11481–11494.
[27] J. W. Hilborn, E. MacKnight, J. A. Pincock, P. J. Wedge, *J. Am. Chem. Soc.* **1994**, *116*, 3337–3346.
[28] B. P. Fingerhut, D. Geppert, R. de Vivie-Riedle, *Chem. Phys.* **2008**, *343*, 329–339.
[29] M. Lipson, A. A. Deniz, K. S. Peters, *Chem. Phys. Lett.* **1998**, *288*, 781–784.
[30] L. R. Heeb, K. S. Peters, *J. Am. Chem. Soc.* **2008**, *130*, 1711–1717.
[31] E. Vauthey, *J. Photochem. Photobiol. A* **2006**, *179*, 1–12.
[32] O. F. Mohammed, K. Adamczyk, N. Banerji, J. Dreyer, B. Lang, E. T. J. Nibbering, E. Vauthey, *Angew. Chem.* **2008**, *120*, 9184–9188; *Angew. Chem. Int. Ed.* **2008**, *47*, 9044–9048.
[33] A. Rosspeintner, D. R. Kattnig, G. Angulo, S. Landgraf, G. Grampp, *Chem. Eur. J.* **2008**, *14*, 6213–6221.
[34] V. S. Gladkikh, A. I. Burshtein, H. L. Tavernier, M. D. Fayer, *J. Phys. Chem. A* **2002**, *106*, 6982–6990.
[35] H. Mayr, A. R. Ofial in *Carbocation Chemistry* (Eds.: G. A. Olah, G. K. S. Prakash), Wiley, Hoboken, **2004**, pp. 331–358.
[36] H. Mayr, T. Bug, M. F. Gotta, N. Hering, B. Irrgang, B. Janker, B. Kempf, R. Loos, A. R. Ofial, G. Remennikov, H. Schimmel, *J. Am. Chem. Soc.* **2001**, *123*, 9500–9512.
[37] H. Mayr, B. Kempf, A. R. Ofial, *Acc. Chem. Res.* **2003**, *36*, 66–77.
[38] J. Ammer, C. Nolte, H. Mayr, *J. Am. Chem. Soc.* **2012**, *134*, 13902–13911.
[39] B. Denegri, A. Streiter, S. Jurić, A. R. Ofial, O. Kronja, H. Mayr, *Chem. Eur. J.* **2006**, *12*, 1648–1656.
[40] C. Nolte, H. Mayr, *Eur. J. Org. Chem.* **2010**, 01435.
[41] U. Megerle, I. Pugliesi, C. Schriever, C. F. Sailer, E. Riedle, *Appl. Phys. B* **2009**, *96*, 215–231.
[42] B. P. Fingerhut, C. F. Sailer, J. Ammer, E. Riedle, R. de Vivie-Riedle, *J. Phys. Chem. A* **2012**, *116*, 11064–11074.
[43] C. F. Sailer, N. Krebs, B. P. Fingerhut, R. de Vivie-Riedle, E. Riedle, unpublished results.
[44] J. Li, Z. Liu, C. Tan, X. Guo, L. Wang, A. Sancar, D. Zhong, *Nature* **2010**, *466*, 887–891.
[45] Y.-T. Kao, X. Guo, Y. Yang, Z. Liu, A. Hassanali, Q.-H. Song, L. Wang, D. Zhong, *J. Phys. Chem. B* **2012**, *116*, 9130–9140.
[46] M. N. Berberan-Santos, E. N. Bodunov, B. Valeur, *Chem. Phys.* **2005**, *315*, 171–182.
[47] J. Friedrichs, D. J. Coughtrie, I. Frank, *Chem. Phys.* **2012**, *402*, 69–73.
[48] D. J. Raber, J. M. Harris, P. v. R. Schleyer, *Ions and Ion Pairs in Solvolysis Reactions in Ions and Ion Pairs in Organic Chemistry* (Ed.: M. Szwarc), Wiley, New York, **1974**, pp. 248–366.
[49] A. Goun, K. Glusac, M. D. Fayer, *J. Chem. Phys.* **2006**, *124*, 084504.
[50] S. A. Rice, *Diffusion-Limited Reactions* (Eds.: C. H. Bamford, C. F. H. Tipper, R. G. Compton), Elsevier, Amsterdam, **1985**.

[51] R. A. Marcus, N. Sutin, *Biochim. Biophys. Acta Rev. Bioenerg.* **1985**, *811*, 265–322.

[52] P. F. Barbara, T. J. Meyer, M. A. Ratner, *J. Phys. Chem.* **1996**, *100*, 13148–13168.

[53] K. Schulten, private communication.

[54] M. Tachiya, *Radiat. Phys. Chem.* **1983**, *21* 167–175.

[55] K. Weidemaier, H. L. Tavernier, S. F. Swallen, M. D. Fayer, *J. Phys. Chem. A* **1997**, *101*, 1887–1902.

[56] V. O. Saik, A. A. Goun, J. Nanda, K. Shirota, H. L. Tavernier, M. D. Fayer, *J. Phys. Chem. A* **2004**, *108*, 6696–6703.

[57] M. Wojcik, M. Tachiya, *Radiat. Phys. Chem.* **2005**, *74*, 132–138.

[58] J. A. Kloepfer, V. H. Vilchiz, V. A. Lenchenkov, A. C. Germaine, S. E. Bradforth, *J. Chem. Phys.* **2000**, *113*, 6288–6307.

[59] S. Zugmann, M. Fleischmann, M. Amereller, R. M. Gschwind, H. D. Wiemhöfer, H. J. Gores, *Electrochim. Acta* **2011**, *56*, 3926–3933.

[60] S. Zugmann, M. Fleischmann, M. Amereller, R. M. Gschwind, M. Winter, H. J. Gores, *J. Chem. Eng. Data* **2011**, *56*, 4786–4789.

[61] P. Atkins, J. de Paula, *Physical Chemistry, 9th ed.*, Oxford University Press, Oxford, **2009**.

[62] A. R. Ofial, K. Ohkubo, S. Fukuzumi, R. Lucius, H. Mayr, *J. Am. Chem. Soc.* **2003**, *125*, 10906–10912.

[63] A. A. Isse, C. Y. Lin, M. L. Coote, A. Gennaro, *J. Phys. Chem. B* **2011**, *115*, 678–684.

[64] V. O. Saik, A. A. Goun, M. D. Fayer, *J. Chem. Phys.* **2004**, *120*, 9601–9611.

[65] T. Bultmann, N. P. Ernsting, *J. Phys. Chem.* **1996**, *100*, 19417–19424.

[66] C. F. Sailer, R. B. Singh, J. Ammer, E. Riedle, I. Pugliesi, *Chem. Phys. Lett.* **2011**, *512*, 60–65.

[67] M. L. Horng, J. A. Gardecki, A. Papazyan, M. Maroncelli, *J. Phys. Chem.* **1995**, *99*, 17311–17337.

[68] B. M. Ladanyi, R. M. Stratt, *J. Phys. Chem.* **1995**, *99*, 2502–2511.

[69] W. P. de Boeij, M. S. Pshenichnikov, D. A. Wiersma, *J. Phys. Chem.* **1996**, *100*, 11806–11823.

[70] I. Eom, T. Joo, *J. Chem. Phys.* **2009**, *131*, 244507.

[71] R. Schneider, H. Mayr, P. H. Plesch, *Ber. Bunsenges. Phys. Chem.* **1987**, *91*, 1369–1374.

[72] S. Winstein, G. C. Robinson, *J. Am. Chem. Soc.* **1958**, *80*, 169–181.

[73] J. H. Dymond, M. A. Awan, N. F. Glen, J. D. Isdale, *Int. J. Thermophys.* **1991**, *12*, 433–447.

[74] S. Minegishi, R. Loos, S. Kobayashi, H. Mayr, *J. Am. Chem. Soc.* **2005**, *127*, 2641–2649.

[75] C. Reichardt, *Solvents and Solvent Effects in Organic Chemistry, 4th ed.*, Wiley-VCH, Weinheim, **2010**.

[76] H. J. Kim, J. T. Hynes, *J. Chem. Phys.* **1990**, *93*, 5194–5210.

[77] H. J. Kim, J. T. Hynes, *J. Am. Chem. Soc.* **1992**, *114*, 10508–10528.

[78] W. L. Jorgensen, J. K. Buckner, S. E. Huston, P. J. Rossky, *J. Am. Chem. Soc.* **1987**, *109*, 1891–1899.

[79] R. E. Westacott, K. P. Johnston, P. J. Rossky, *J. Am. Chem. Soc.* **2001**, *123*, 1006–1007.

[80] I. R. Gould, S. Farid, *Acc. Chem. Res.* **1996**, *29*, 522–528.

[81] S. Yamabe, N. Tsuchida, *J. Comput. Chem.* **2004**, *25*, 598–608.

[82] U. Schmidhammer, U. Megerle, S. Lochbrunner, E. Riedle, J. Karpiuk, *J. Phys. Chem. A* **2008**, *112*, 8487–8496.

[83] U. Heugen, G. Schwaab, E. Bründermann, M. Heyden, X. Yu, D. M. Leitner, M. Havenith, *Proc. Natl. Acad. Sci. USA* **2006**, *103*, 12301–12306.

[84] J. Zheng, K. Kwak, J. Asbury, X. Chen, I. R. Piletic, M. D. Fayer, *Science* **2005**, *309*, 1338–1343.

[85] C. R. Baiz, K. J. Kubarych, *J. Am. Chem. Soc.* **2010**, *132*, 12784–12785.

4. Summary and outlook

Bond cleavage and formation are key steps during chemical synthesis or biochemical reaction cascades. In the present work, the photoinduced bond cleavage of diphenylmethyl derivatives containing a cationic or neutral leaving group, namely $Ph_2CH-PPh_3^+$ and Ph_2CH-Cl, were investigated theoretically. To this, state-of-the-art quantum chemical and quantum dynamical methods as well as molecular dynamics simulations were applied. In the case of the charged precursor $Ph_2CH-PPh_3^+$, the focus was on the molecular mechanism of the bond cleavage and in particular on the impact of the environment. Secondary processes emerging after the initial bond cleavage, which are decisive for the chemically available amount of products, were in the focus of the Ph_2CH-Cl studies.

In the first part, a detailed microscopic description of the reaction mechanism of the excited state bond cleavage of $Ph_2CH-PPh_3^+$ in solution taking place on the hundreds of femtoseconds time scale is presented. The quantum chemical investigations of the model system $PhCH_2-PH_2Ph^+$ revealed that the first excited state S_1 offers the major relaxation pathway which involves a charge transfer state and results in a homolytic bond cleavage. Additionally, a S_1/S_0 CoIn was localized providing a connection to the heterolytic reaction channel of the ground state. Based on the knowledge about the model system, specially adapted reactive coordinates for the full system $Ph_2CH-PPh_3^+$ were designed. Together with the quantum chemical ONIOM method and the G-matrix method, they made QD simulations of the reaction process feasible. For the gas phase, these simulations showed $Ph_2CH^\bullet$ radical formation and thus a discrepancy from the experimental observations which exhibit the Ph_2CH^+ cation as the dominant reaction product. Electrostatic solvent effects could be excluded because both reaction channels comprise one positively charged and one neutral fragment in case of a charged precursor. Hence dynamic solvent effects – i.e. the mechanical influence of the solvent cage – were worth considering. In order to investigate closely the dynamic solvent effects, two methods with increasing complexity were developed to include the effects in the quantum mechanical formalism: The dynamic continuum ansatz and the combined QD/MD method. The first approach treats the solvent implicitly. It relies on the dynamic viscosity of the solvent together with quantum chemically and dynamically calculated values and does not require any fitting of parameters. The solvent cage decelerates the wave packet and the small gradient toward the CoIn comes into play. At the CoIn the population relaxes to the ground state where the spectroscopically observed Ph_2CH^+ cations are formed within a time window comparable to the experiment. To go one step further, classical MD simulations are used in the QD/MD method to explicitly describe the solvent environment. The MD simulations provide information about the arrangements of the solvent molecules around the precursor. On the basis of these arrangements a solvent potential can be calculated and included into the QD simulations. The total potentials for different MD snapshots comprising the molecular as well as the actual solvent potential exhibit two distinct reaction pathways. The main path which occurs in about two thirds of the considered potentials directs to the aforementioned S_1/S_0 CoIn, a minor route opens a dissociation opportunity in the excited state. The averaged quantum dynamics over 50 random snapshots display that 83% of the excited state population that leaves the FC region reaches the CoIn while 17% dissociates in the S_1 state. In summary, both approaches – the dynamic continuum ansatz as well as the QD/MD method – reveal the decisive role of the solvent environment. It guides the molecular wave packet to the CoIn where the excited state population relaxes into the ground state to generate Ph_2CH^+ cations.
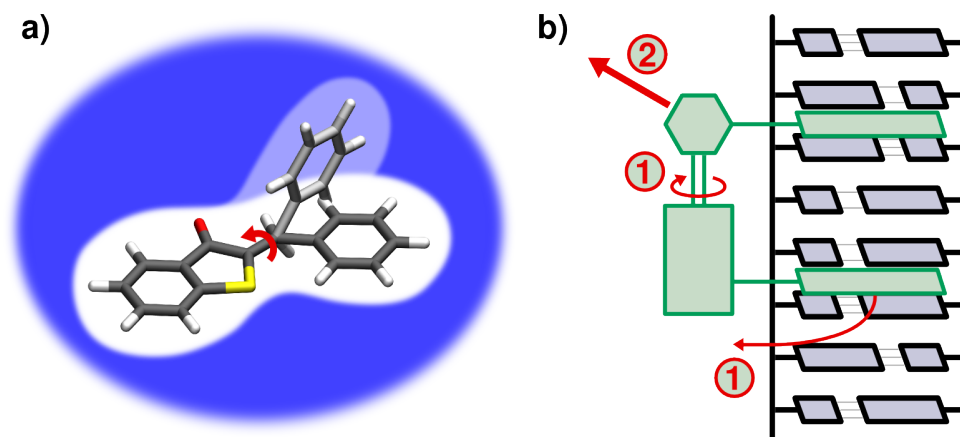
Figure 4.1.: a) (Z)-isomer of the molecular switch hemithioindigo-hemistilbene (dark gray structure) in its solvent cavity. The solvent is represented by blue color. The light gray phenyl ring indicates the necessary geometric deformation to reach a prominent CoIn (CoIn$_{Ac}$) which is important for the light-induced isomerization from (Z) to (E) [6, 248]. During the course of the isomerization the shape of the cavity changes. b) Schematic illustration of a molecular switch containing two anchor moieties which are intercalated in a DNA double helix. During the switching process ① one anchor is pulled out of the DNA ①. Subsequently, the whole molecular switch is released ②.

The development of the two approaches to describe the mechanic impact of the surrounding on the motion of a reactant opens a wide range of future applications. One obvious field of molecular applications are further dissociation reactions of other diphenylmethyl derivatives like Ph_2CH-Cl or Ph_2CH-Br. Another possibility would be for example a Wolff rearrangement of α-diazocarbonyl compounds which is initiated by a N_2 cleavage [15, 249–251]. Fig. 4.1 a) shows an additional potential application. The figure depicts the (Z)-isomer of the molecular switch hemithioindigo-hemistilbene in its solvent cavity. The light gray phenyl ring indicates the necessary geometric deformation to reach a prominent CoIn important for the light-induced isomerization from (Z) to (E) [6, 248]. During the course of the isomerization the shape of the cavity changes and consequently the molecular motion is decelerated. The resulting effect on the isomerization reaction could be simulated using the dynamic continuum ansatz. For the QD/MD approach several future projects are attractive as well. On the one side, an extension to include the feedback of the motion of the QD system on the behavior of the solvent environment is of interest. Then both systems could be propagated in parallel using e.g. an Ehrenfest ansatz [252]. On the other side, an extension with regard to the described surrounding is desirable. Not only different solvents but also more structured environments like DNA or active sites of proteins offer an enormous range of applications. One of those is depicted in fig. 4.1 b), where a molecular switch adheres to a DNA strand. The two anchor moieties of the molecular switch are intercalated in the DNA double helix. After the switching process one anchor is pulled out and thereon the whole molecular switch gets released.

The second part of this thesis deals with the ion pairing of $Ph_2CH-PPh_3^+ X^-$, $PhCH_2-PPh_3^+ X^-$, and $(p\text{-}CF_3\text{-}C_6H_4)CH_2-PPh_3^+ X^-$ in solution with X^- being Cl^-, Br^-, BF_4^-, SbF_6^- and BPh_4^-. In moderately polar solvents like dichloromethane, the initial bond cleavage of $Ph_2CH-PPh_3^+$ has been shown experimentally to be susceptible to the kind of counterion present [133]. The joint theoretical and experimental study presented in chapter 2 reports a counterion dependent deshielding effect of the protons of the three phosphonium ions by investigating ^1H NMR shifts. The observed deshielding effect increases according to $SbF_6^- < BF_4^-$

$\ll$ Br$^-$ < Cl$^-$. The structures of the ion pairs in solution have been determined by quantum chemical optimizations and confirmed by a good agreement between the experimental and the calculated ^{1}H NMR shifts. The optimized structures compare well with the experimentally determined crystal structures and reveal an important C(α)–H$\cdots$X$^-$ hydrogen bond. Its strength increases in the order of SbF$_6^-$ < BF$_4^-$ < Br$^-$ < Cl$^-$ reflecting the magnitude of the deshielding effect of the corresponding X$^-$.

The knowledge about the counterion position enables a future investigation of the experimentally observed changes of the photochemistry in case of Ph$_2$CH−PPh$_3^+$ ions with an easily oxidizable X$^-$ [133]. As a first step, quantum chemical calculations could give insights in the participation of the counterion in the excited state manifold. If the model system of the ONIOM calculations is extended by the X$^-$, e.g. Cl$^-$, a calculation of the excited state potentials would be feasible. On their basis, the differences in the product formation depending on the counterion could likely be explained.

In the focus of the last part are secondary processes subsequent to the initial bond cleavage using Ph$_2$CH−Cl as an example. They happen in a time window of a few picoseconds to several nanoseconds and are particularly of interest from a chemist's point of view, as they substantially determine the nanosecond yield which is available for further reactions. A combined Marcus-Smoluchowski model was set up interlinking geminate recombination, Marcus-type electron transfer and Smoluchowski-like diffusion. These competing processes are especially relevant for diphenylmethyl derivatives with neutral leaving groups, because there the electron transfer from the radical pair to the ion pair occurs frequently [39, 60, 133, 136]. The Marcus-Smoluchowski model allowed to derive a detailed microscopic picture of the interwoven processes and accurately reproduced the experimentally measured dynamics of the reaction products. A strict separation between species like contact ion pairs, solvent-separated ion pairs and free ions or geminate radical pairs and free radicals is not eligible here. In fact, rather continuous distributions of ion and radical pair populations are appropriate, which are subject to diffusion. The radical pair population is depleted by geminate recombination and electron transfer; the ion pair population mostly originates from electron transfer and is depleted by geminate recombination as well. Various physical and chemical properties shift the interplay between these processes, e.g. the temperature, the solvent polarity or the substitution pattern on the phenyl rings of the Ph$_2$CH moiety.

So far, the radical and ion pair populations resulting from the initial bond cleavage have been assumed being Gaussian shaped. With the dynamic continuum ansatz at hand (cf. chapter 1.2), it becomes feasible in the future to interlink QD calculations of the initial bond cleavage using ab-initio PESs [82, 138, 194] with the simulation of the ensuing secondary processes. Therefor the wave packets in the individual excited states have to be converted into population distributions required by the Marcus-Smoluchowski model. Besides this, the combined model could be employed for different neutral diphenylmethyl derivatives, e.g. Ph$_2$CH−Br and the results could be compared with the experimental observations [60, 136]. A further attractive application offers the opportunity to increase the Ph$_2$CH$^+$ yield by exciting the geminate radical pair population by a second laser pulse. This is expected to increase the driving force of the electron transfer. The changes in the time-dependent population distributions can be investigated with the help of the Marcus-Smoluchowski model. Especially if the electron transfer at larger inter-radical distances could be increased, the ion pair population is expected to rise because at larger distances the diffusional separation of the ions competing with the geminate recombination is more productive.

A. Supporting information for chapter 1.1.1

In the following, selected parts of the supporting information of the article "Ground and Excited State Surfaces for the Photochemical Bond Cleavage in Phenylmethylphenylphosphonium Ions" published in *The Journal of Physical Chemistry A* are reprinted with permission from *J. Phys. Chem A*, **117**, 10626–10633 (2013); copyright 2013 American Chemical Society.

Ground and Excited State Surfaces for the Photochemical Bond Cleavage in Phenylmethylphenylphosphonium Ions

Sebastian Thallmair,[†,‡] Benjamin P. Fingerhut,[†,¶] and Regina de Vivie-Riedle[*,†]

Department Chemie, Ludwig-Maximilians-Universität München, D-81377 München, Germany,

and Lehrstuhl für BioMolekulare Optik, Ludwig-Maximilians-Universität München, D-80538

München, Germany

E-mail: regina.de_vivie@cup.uni-muenchen.de

[*]To whom correspondence should be addressed

[†]Department Chemie, Ludwig-Maximilians-Universität München, D-81377 München, Germany

[‡]Lehrstuhl für BioMolekulare Optik, Ludwig-Maximilians-Universität München, D-80538 München, Germany

[¶]Current adress: Department of Chemistry, University of California, Irvine, California 92697-2025, USA

Supplementary information

Active space of the model system $PhCH_2–PH_2Ph^+$

For the CASSCF calculations we restricted the active space to four π-MOs of each phenyl ring of $PhCH_2–PH_2Ph^+$ and the σ_{CP}- and σ_{CP}^*-MO of the C-P bond (see Figure S1). The eight π-MOs are essential for the excitation process and the initial charge exchange whereas the bond cleavage process can only be described including the σ_{CP}- and σ_{CP}^*-MO of the C-P bond. The fully bonding and anti-bonding π-MOs are not contained in the active space. Their influence on the relative energies is taken into account by the MS-CASPT2 calculations.
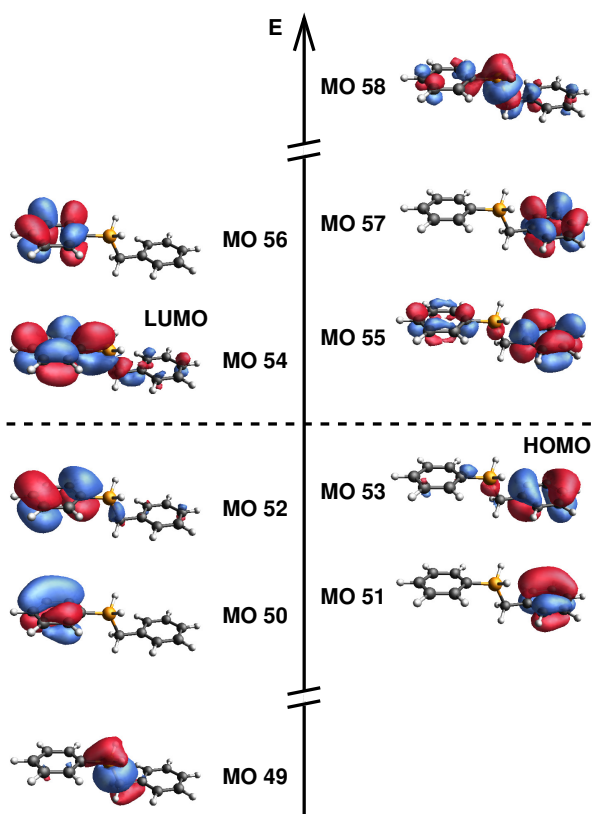
Figure S1: Active space used for the CASSCF(10,10) calculations. The molecular orbitals are shown for the ground state minimum geometry and are ordered corresponding to the orbital energies. The dashed line seperates the occupied orbitals (MO49 – MO53) from the virtual orbitals (MO54 – MO58).

Figure S2 shows the development of the active space along the reaction coordinate at three selected C-P distances. The breakup of the C-P bond as well as the subsequent linear combination of the resulting atomic p-orbitals with the π oritals of the phenyl rings can be clearly recognized.
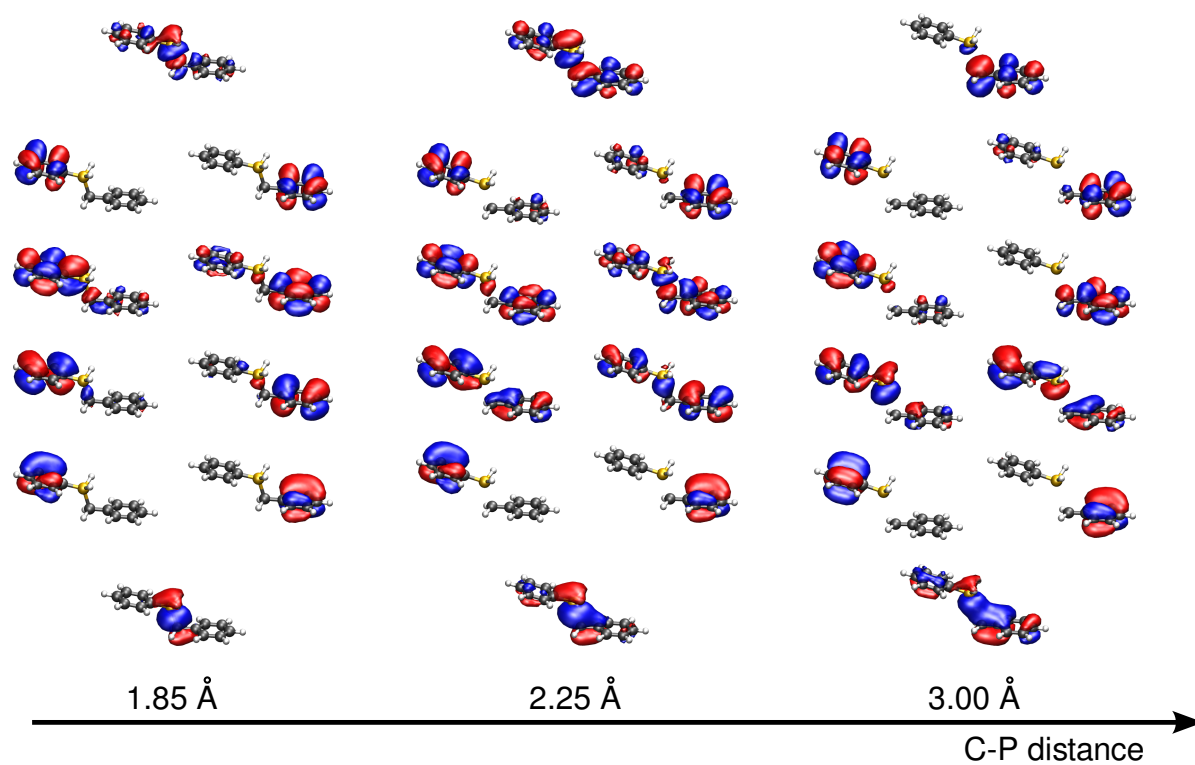
Figure S2: Development of the active space used for the CASSCF(10,10) calculations along the reaction coordinate at three selected C-P distances: 1.85 Å (ground state minimum), 2.25 Å and 3.00 Å.

Developing of the orbital energies

The interaction between the σ_{CP}^*- and the $1\pi^*$-orbital is shown in Figure S3. By symmetry reasons an interaction with the $2\pi^*$-, the $3\pi^*$- or the $4\pi^*$-orbitals is forbidden. The observed linear combination of both orbitals enables the π^*-σ_{CP}^* charge exchange between $2.10 - 2.20\,\text{Å}$.
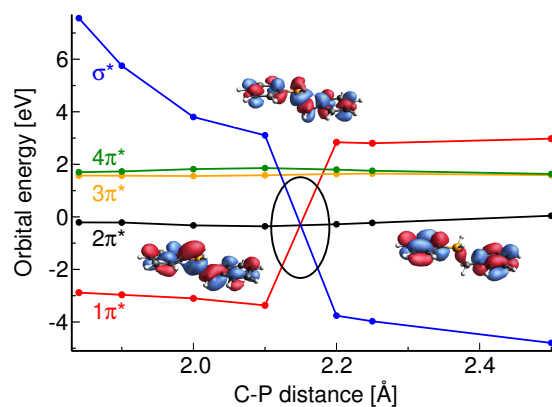
Figure S3: Developing of orbital energies along the ground state MEP for the C-P bond cleavage between $1.85 - 2.50\,\text{Å}$. The black ellipse indicates the region where a strong interaction between the $1\pi^*$ and the σ_{CP}^* orbitals occurs, which illustrates the change of the character of the key excited states. The shown orbitals visualize the linear combination of the $1\pi^*$ and σ_{CP}^* orbitals (top and bottom left) and the $2\pi^*$ orbital (bottom right) where the linear combination is forbidden by symmetry reasons.

B. Supporting information for chapter 1.3

In the following, the supporting information of the article "Quantum Dynamics in an Explicit Solvent Environment: A Photochemical Bond Cleavage Treated with a Combined QD/MD Approach" published in the *Journal of Chemical Theory and Computation* is reprinted with permission from *J. Chem. Theory Comput.*, DOI: 10.1021/acs.jctc.5b00046 (2015); copyright 2015 American Chemical Society.

Supporting information for:

Quantum Dynamics in an Explicit Solvent

Environment: A Photochemical Bond

Cleavage Treated with a Combined QD/MD

Approach

Sebastian Thallmair,[†,‡] Julius P. P. Zauleck,[†] and Regina de Vivie-Riedle[*,†]

Department Chemie, Ludwig-Maximilians-Universität München, D-81377 München, Germany, and Lehrstuhl für BioMolekulare Optik, Ludwig-Maximilians-Universität München, D-80538 München, Germany

E-mail: regina.de_vivie@cup.uni-muenchen.de

---

[*]To whom correspondence should be addressed
[†]Department Chemie, Ludwig-Maximilians-Universität München, D-81377 München, Germany
[‡]Lehrstuhl für BioMolekulare Optik, Ludwig-Maximilians-Universität München, D-80538 München, Germany

1 Partition of the coordinates to calculate the probability distributions $P(q_n)$

To analyze the standard deviation σ_{q_n} of the interaction energy, the probability distributions $P(q_n)$ for the angular coordinates in the orientation space have to be evaluated. To this, $P(q_n)$, calculated according to eq 6 in the manuscript, has to be smoothed. We Fourier transformed $P(q_n)$, applied a low-pass butterworth filter $F(\omega)$ and then performed an inverse

Table S1: Partition of the coordinates and relative deviation D of the normalized resulting probability distributions for the calculation of the standard deviation σ_{q_n} of the interaction energy with respect to the four angular coordinates α_s, β_s, α_f and β_f. The values are given for the two fragments PPh_3 and Ph_2CH in which $Ph_2CH-PPh_3^+$ is partitioned.

coordinate q_n	partition D	partition D	partition D	σ_{q_n} [au]
$\alpha_s(PPh_3)$	$\frac{\beta_s}{2}$ 0.038	$\frac{\alpha_f}{2}$ 0.047	$\frac{\beta_f}{2}$ 0.049	$1.58 \cdot 10^{-4}$
$\beta_s(PPh_3)$	$\frac{\alpha_s}{2}$ 0.044	$\frac{\alpha_f}{2}$ 0.032	$\frac{\beta_f}{2}$ 0.055	$7.61 \cdot 10^{-5}$
$\alpha_f(PPh_3)$	$\frac{\alpha_s}{2}$ 0.058	$\frac{\beta_s}{2}$ 0.039	$\frac{\beta_f}{2}$ 0.029	$1.62 \cdot 10^{-4}$
$\beta_f(PPh_3)$	$\frac{\alpha_s}{2}$ 0.095	$\frac{\beta_s}{2}$ 0.060	$\frac{\alpha_f}{4}$ 0.097 / 0.116	$2.71 \cdot 10^{-4}$
$\alpha_s(Ph_2CH)$	$\frac{\beta_s}{2}$ 0.020	$\frac{\alpha_f}{2}$ 0.035	$\frac{\beta_f}{2}$ 0.012	$1.28 \cdot 10^{-4}$
$\beta_s(Ph_2CH)$	$\frac{\alpha_s}{2}$ 0.047	$\frac{\alpha_f}{2}$ 0.059	$\frac{\beta_f}{2}$ 0.057	$7.21 \cdot 10^{-5}$
$\alpha_f(Ph_2CH)$	$\frac{\alpha_s}{2}$ 0.020	$\frac{\beta_s}{2}$ 0.021	$\frac{\beta_f}{2}$ 0.034	$1.03 \cdot 10^{-4}$
$\beta_f(Ph_2CH)$	$\frac{\alpha_s}{2}$ 0.085	$\frac{\beta_s}{2}$ 0.085	$\frac{\alpha_f}{2}$ 0.107	$1.34 \cdot 10^{-4}$

Fourier transformation. $F(\omega)$ reads

$$F(\omega) = \frac{1}{1 + \left(\frac{\omega}{\omega_0}\right)^n},$$ (1)

with the central frequency ω_0 and the order n. We used the values $\omega_0 = 0.1$ and $n = 100$. To ensure that no compensation of orientations occurs for the tested coordinate we divided the interval of the other angular coordinates in half and compared the shape of the obtained probability distributions of both parts with each other and with the initial shape. If they are similar enough no further dividing is necessary, if not the procedure is repeated for both halves. In Table S1 the relative deviation D, i.e. the integral of the absolute difference of the normalized probability distributions $P^j(q_n)$ for each interval j, for the final partitioning are given. All D values lie below 12% and are sufficiently small.

Figure S1 shows the normalized probability distributions $P(\alpha_s)$ for the PPh$_3$ fragment. The intervals of all remaining angular coordinates are divided into halves ((a) β_s; (b) α_f; (c) β_f). The corresponding relative deviations D are given in the second row of Table S1. In the depicted case the probability distributions are quite similar so no further partitioning of the coordinates is necessary.

To calculate the standard deviations σ_{q_n} for the interaction energy along the angular coordinates, the m standard deviations $\sigma_{q_n}^j$ for the partitions $j \in \{1, 2, \ldots, m\}$ have to be averaged according to eq 13 in the main text. Here we briefly want to explain the origin of the weighting factor $\frac{N_j}{N_0}$ in this equation.

The variance $\text{Var}_A(x) = (\sigma_{A,x})^2$ of the elements $x \in A$ of a set A is

$$\text{Var}_A(x) = \sum_{x \in A} (x - \overline{x_A})^2 \, P_A(x),$$ (2)

with the mean value of x in A being $\overline{x_A}$ and the discrete probability distribution $P_A(x)$ of the elements in A. The set A can now be divided into two subsets B and C. Each element
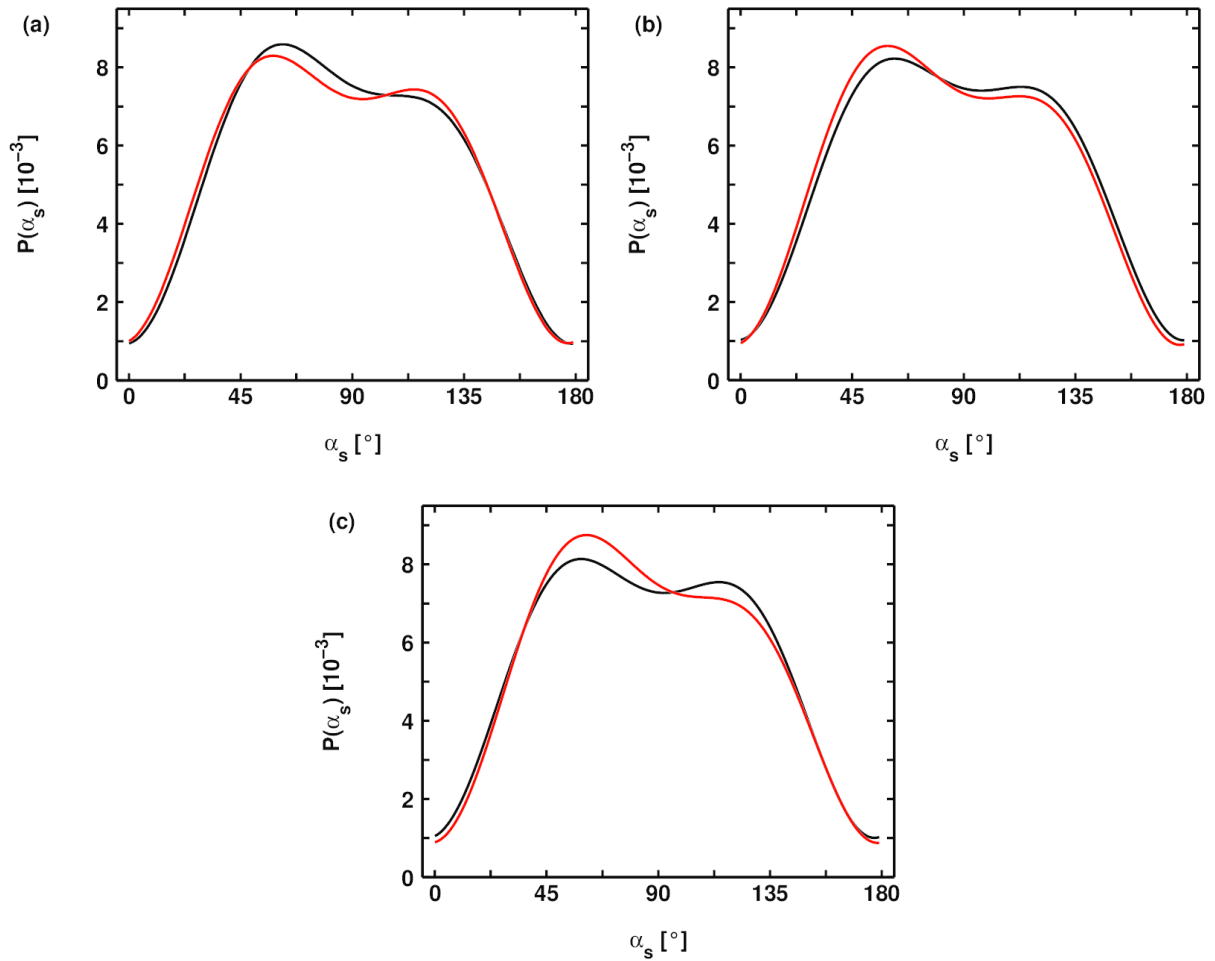
Figure S1: Normalized probability distributions $P(\alpha_s)$ evaluated for the halved interval of the remaining angular coordinates for the PPh$_3$ fragment. (a) Intervals for β_s: $[0; 180[$ (black) and $[180; 360[$ (red). (b) Intervals for α_f: $[0; 45[$ (black) and $[45; 90[$ (red). (c) Intervals for β_f: $[0; 180[$ (black) and $[180; 360[$ (red).

of A is either an element of B or of C. Thus eq 2 can be transformed to

$$\text{Var}_A(x) = \sum_{x \in B} (x - \overline{x_A})^2 \frac{N_B}{N_A} P_B(x) + \sum_{x \in C} (x - \overline{x_A})^2 \frac{N_C}{N_A} P_C(x). \tag{3}$$

Here N_A, N_B and N_C are the number of elements in the set A, B and C, respectively. In the case, the mean values in the subsets B and C ($\overline{x_B}$ and $\overline{x_C}$) are the same as $\overline{x_A}$ eq 3 can

be rewritten:

$$\text{Var}_A(x) = \frac{N_B}{N_A} \sum_{x \in B} (x - \overline{x_B})^2 \, P_B(x) + \frac{N_C}{N_A} \sum_{x \in C} (x - \overline{x_C})^2 \, P_C(x)$$
$$= \frac{N_B}{N_A} \text{Var}_B(x) + \frac{N_C}{N_A} \text{Var}_C(x). \tag{4}$$

In eq 13 in the main text we also use the proportion of elements in the each subset (here $\frac{N_B}{N_A}$ and $\frac{N_C}{N_A}$) as weighting factors for the squares of the standard deviations $\sigma_{q_n}^j$ like in eq 4 above.

2 Quantum dynamics

The quantum dynamics (QD) were performed on a regular space grid with 1024 points in r direction and 512 points in ϕ direction. The size of the spatial grid was $r \in [1.65 \, \text{Å}, 6.00 \, \text{Å}]$ and $\phi \in [40°, 140°]$. The time evolution of the system was calculated by solving the time-dependent Schrödinger equation numerically with the Chebychev propagation scheme.[S1] We used a time step of 100 au (1.42 fs). The vibrational ground state eigenfunction $v = 0$ of the electronic ground state was determined propagating in imaginary time.[S2] To express the kinetic operator $\hat{T}$ in the chosen two-dimensional coordinate space, the G-matrix method was used:[S3–S5]

$$\hat{T} = -\frac{1}{2} \sum_{r=1}^{M} \sum_{s=1}^{M} \frac{\partial}{\partial q_r} \left[G_{rs} \frac{\partial}{\partial q_s} \right] \tag{5}$$

$$\text{with} \quad G_{rs} = \sum_{i=1}^{3N} \frac{1}{m_i} \frac{\partial q_r}{\partial x_i} \frac{\partial q_s}{\partial x_i} \,. \tag{6}$$

Here M is the total number of internal coordinates and N is the number of atoms in the considered molecule.

The G-matrix method allows the use of arbitrary orthogonal coordinates for the quantum dynamical propagations. For details about the G-matrix elements see reference S6 and its supporting information.

3 Convergence of population dynamics
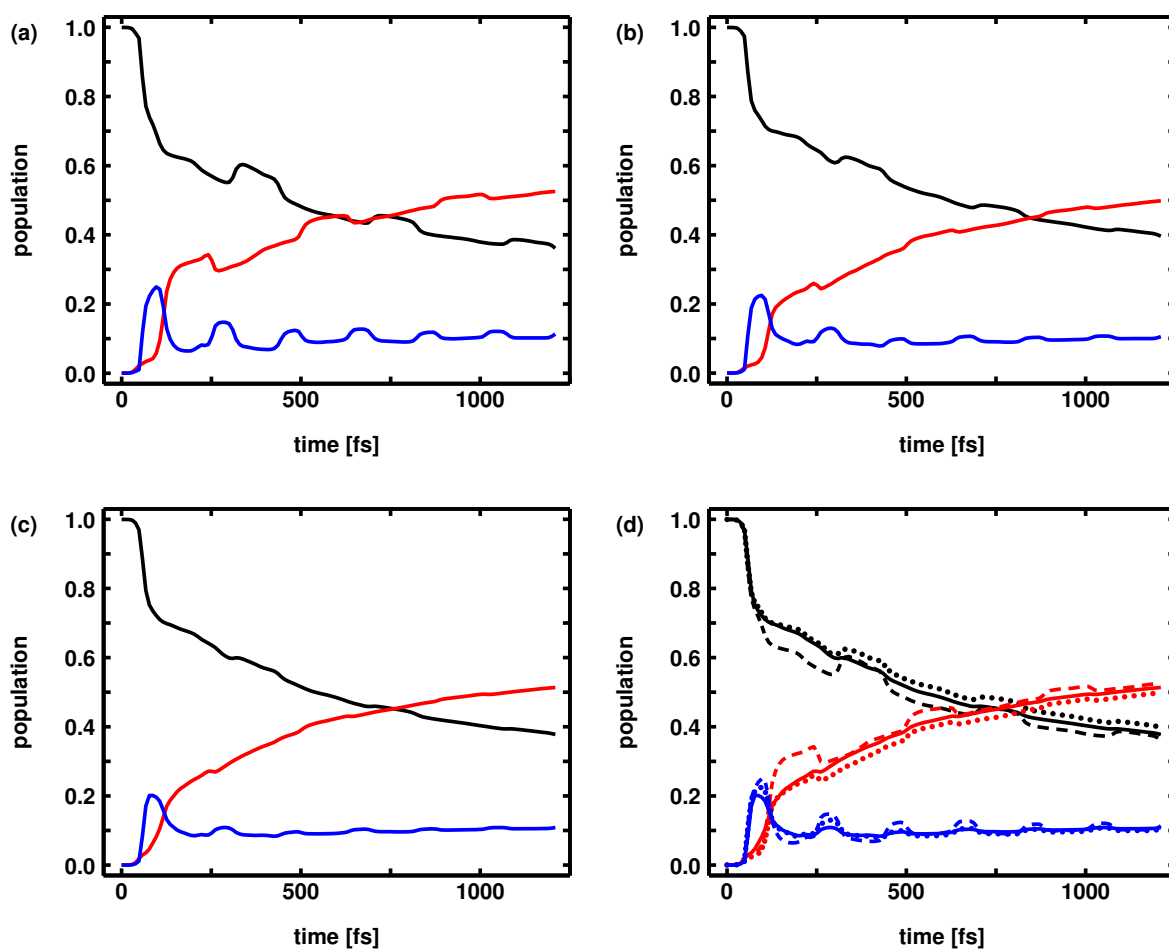
Figure S2: Population dynamics for the QD simulation of the bond cleavage of $Ph_2CH-PPh_3^+$ averaged over (a) 12, (b) 25 and (c) 50 different solvent arrangements taken from MD trajectories. The black line represents the population in the FC region, the blue line the population in the S_1 dissociation area and the red line the population around the CoIn. The three areas are depicted in the inlay in Figure 8 in the manuscript. (d) shows the overlay of the three graphs (dashed: 12 snapshots, dotted: 25, solid: 50).

A convenient way to cover the thermodynamically accessible configuration space of a solvent environment around a solute is to perform MD simulations of the system. From these a sufficient large number of snapshots along the trajectories represents the solvent surrounding. For an overall picture of the bond cleavage of $Ph_2CH-PPh_3^+$ we averaged the wave packet propagations in the different solvent surroundings according to eq 4 in the manuscript. Figure S2 shows the convergence in the population dynamics increasing the number of MD snapshots from $N_{snap} = 12$ (a) over $N_{snap} = 25$ (b) to $N_{snap} = 50$ (c). The black line represents the population in the FC region, the blue line the population in the S_1 dissociation area and the red line the population around the CoIn. In Figure S2(d) the three graphs of Figure S2(a)–(c) are overlaid (dashed line: 12 snapshots, dotted: 25, solid: 50). This showed 50 to be a sufficient large number of MD snapshots.

4   Qualitative comparison of the required computing time

The presented QD/MD approach requires several different computational steps to simulate the influence of the solvent environment on the QD of the solute. To estimate the effort behind the different computations table S2 lists the required computing time for the dif-

Table S2: Qualitative comparison of computing time for simulation of the photoinduced bond cleavage of $Ph_2CH-PPh_3^+$ using the presented QD/MD approach. The computing time is given for one CPU although some computations were performed parallel. Note that not all computations were performed on the same machine. The fourth column specifies how often the computation has been performed for the presented bond cleavage of $Ph_2CH-PPh_3^+$.

computation of	method	computing time [s]	number
$V_{mol}(r, \phi)$	QC (ONIOM)	$3.4 \cdot 10^6$	1
solvent dynamics	MD	$3.7 \cdot 10^4$	1
$P(q_n)$	evaluation of orientations	$3.2 \cdot 10^3$	1
$E_{sf}(|\vec{r_{sf}}|, \alpha_s, \alpha_f, \beta_f)$	QC (DFT)	$1.8 \cdot 10^7$	1
$V_{solv}(r, \phi)$	evaluation of orientations	$2.1 \cdot 10^2$	50
solute dynamics	QD	$4.4 \cdot 10^4$	50

ferent calculations in the case of the photoinduced bond cleavage of $Ph_2CH-PPh_3^+$. The computing time is given for one CPU although some computations were performed parallel. Note that not all computations were performed on the same machine. The fourth column specifies how often the corresponding computation has been performed for the investigation of the bond cleavage of $Ph_2CH-PPh_3^+$.

For the calculation of $V_{mol}(r, \phi)$ 483 single point calculations on the "our own n-layered integrated molecular orbital and molecular mechanics (ONIOM)" level of theory (CASSCF(10, 10)/M06-2X) were performed; for the quantum chemical database of $E_{sf}(|\overrightarrow{r_{sf}}|, \alpha_s, \alpha_f, \beta_f)$ 21 780 single points at the DFT level of theory (M06-2X).

5 Optimized geometries

In the following the optimized geometry of the ground state minimum of $Ph_2CH-PPh_3^+$ (DFT, B3LYP / 6-31g(d)) and the structure with the minimal energy difference between S_1 and S_0 at the ONIOM level of theory, where the S_1/S_0 CoIn is located, are given in xyz-format (all coordinates are given in Å):[S6]

S_0 minimum of $Ph_2CH-PPh_3^+$					
C	-0.857563	-0.363243	2.740120	C	-3.904048	1.193641	-1.825089
C	-0.857563	-0.363243	4.136624	C	-4.758800	0.209656	-1.326982
C	-0.857563	0.841154	4.841799	C	-4.361545	-0.552605	-0.227744
C	-0.856673	2.048881	4.142127	C	-3.115493	-0.342429	0.364361
C	-0.851032	2.049395	2.747461	H	-2.013596	2.184599	-1.623796
C	-0.853155	0.846224	2.026641	H	-4.209166	1.808742	-2.666574
C	-0.880912	0.923931	0.505055	H	-5.732204	0.049228	-1.780938
P	0.553877	-0.001046	-0.330103	H	-5.027687	-1.305911	0.182917
C	0.517185	0.439117	-2.096536	H	-2.843546	-0.924442	1.237017
C	0.599261	1.797043	-2.459860	C	-0.700253	-2.495806	-0.620834
C	0.592713	2.163352	-3.803077	C	-0.775043	-3.880705	-0.482911
C	0.506237	1.182728	-4.795959	C	0.270872	-4.586815	0.116795
C	0.437019	-0.164062	-4.442198	C	1.398748	-3.906729	0.577736
C	0.445454	-0.540090	-3.097451	C	1.485457	-2.520941	0.446454
H	-0.846940	-1.312929	2.215166	H	-1.519025	-1.963354	-1.091187
H	-0.859334	-1.308491	4.671702	H	-1.651438	-4.407711	-0.847813
H	-0.860511	0.838254	5.927692	H	0.207297	-5.665973	0.220175
H	-0.858520	2.992397	4.679905	H	2.216089	-4.452555	1.038998
H	-0.851139	2.996680	2.213670	H	2.367591	-2.003812	0.806828
H	-0.618846	1.954488	0.234810	C	2.399308	0.648467	1.716078
H	0.686844	2.570247	-1.701169	C	3.650060	1.051488	2.181513
H	0.658404	3.212488	-4.074981	C	4.669060	1.373368	1.283123
H	0.500526	1.470915	-5.842909	C	4.438939	1.285321	-0.090196
H	0.379884	-0.928828	-5.210685	C	3.191926	0.885547	-0.568494
H	0.401473	-1.591562	-2.837609	H	1.627922	0.392578	2.430697
C	-2.239750	0.631801	-0.138374	H	3.825451	1.112398	3.251277
C	0.433997	-1.804790	-0.150298	H	5.640696	1.687494	1.652754
C	2.156330	0.570647	0.331175	H	5.229081	1.526783	-0.794606
C	-2.658817	1.403261	-1.233867	H	3.031528	0.819900	-1.638206

S₁/S₀ CoIn of Ph₂CH−PPh₃⁺

C	0.294154	-1.602203	1.912734	C	-2.255969	-0.595800	-2.928832
C	0.621997	-1.826153	3.251610	C	-3.147218	-1.542878	-2.423208
C	1.007022	-0.763660	4.070578	C	-3.003787	-1.987426	-1.108301
C	1.063701	0.527240	3.542836	C	-1.971752	-1.498803	-0.306080
C	0.741769	0.750568	2.204326	H	-0.550484	0.641117	-2.531738
C	0.351269	-0.307908	1.371052	H	-2.368740	-0.225073	-3.943419
C	0.000000	0.000000	0.000000	H	-3.955918	-1.919045	-3.042749
P	2.819669	-0.677408	0.024219	H	-3.705104	-2.707433	-0.696474
C	2.782977	-0.237245	-1.742214	H	-1.901171	-1.834719	0.721734
C	2.865053	1.120681	-2.105538	C	1.565539	-3.172168	-0.266512
C	2.858505	1.486990	-3.448755	C	1.490749	-4.557067	-0.128589
C	2.772029	0.506366	-4.441637	C	2.536664	-5.263177	0.471117
C	2.702811	-0.840424	-4.087876	C	3.664540	-4.583091	0.932058
C	2.711246	-1.216452	-2.743129	C	3.751249	-3.197303	0.800776
H	0.007998	-2.446541	1.294024	H	0.746767	-2.639716	-0.736865
H	0.573669	-2.834330	3.652918	H	0.614354	-5.084073	-0.493491
H	1.258603	-0.940196	5.112078	H	2.473089	-6.342335	0.574497
H	1.360123	1.362210	4.170841	H	4.481881	-5.128917	1.393320
H	0.788979	1.760803	1.804978	H	4.633383	-2.680174	1.161150
H	0.355952	0.978807	-0.344955	C	4.665100	-0.027895	2.070400
H	2.952636	1.893885	-1.346847	C	5.915852	0.375126	2.535835
H	2.924196	2.536126	-3.720659	C	6.934852	0.697006	1.637445
H	2.766318	0.794553	-5.488587	C	6.704731	0.608959	0.264126
H	2.645676	-1.605190	-4.856363	C	5.457718	0.209185	-0.214172
H	2.667265	-2.267924	-2.483287	H	3.893714	-0.283784	2.785019
C	-1.058458	-0.559590	-0.808639	H	6.091243	0.436036	3.605599
C	2.699789	-2.481152	0.204024	H	7.906488	1.011132	2.007076
C	4.422122	-0.105715	0.685497	H	7.494873	0.850421	-0.440284
C	-1.224458	-0.108012	-2.127500	H	5.297320	0.143538	-1.283884

References

(S1) Tal-Ezer, H.; Kosloff, R. *J. Chem. Phys.* **1984**, *81*, 3967–3971.

(S2) Kosloff, R.; Tal-Ezer, H. *Chem. Phys. Lett.* **1986**, *127*, 223–230.

(S3) Wilson Jr., E. B.; Decius, J. C.; Cross, P. C. *Molecular Vibrations*; McGraw-Hill: New York, 1955.

(S4) Schaad, L.; Hu, J. *J. Mol. Struct.: THEOCHEM* **1989**, *185*, 203–215.

(S5) Kowalewski, M.; Mikosch, J.; Wester, R.; de Vivie-Riedle, R. *J. Phys. Chem. A* **2014**, *118*, 4661–4669.

(S6) Thallmair, S.; Kowalewski, M.; Zauleck, J. P. P.; Roos, M. K.; de Vivie-Riedle, R. *J. Phys. Chem. Lett.* **2014**, *5*, 3480–3485.

C. Supporting information for chapter 3

In the following, selected parts of the supporting information (chapters S4. and S8.) of the article "A Comprehensive Microscopic Picture of the Benzhydryl Radical and Cation Photogeneration and Interconversion through Electron Transfer" published in *A European Journal of Chemical Physics and Physical Chemistry* are reprinted with permission from *ChemPhysChem* **14**, 1423–1437 (2013); copyright 2013 John Wiley and Sons.

CHEMPHYSCHEM

Supporting Information

A Comprehensive Microscopic Picture of the Benzhydryl Radical and Cation Photogeneration and Interconversion through Electron Transfer

Christian F. Sailer,[a] Sebastian Thallmair,[a, b] Benjamin P. Fingerhut,[b] Christoph Nolte,[b] Johannes Ammer,[b] Herbert Mayr,[b] Igor Pugliesi,[a] Regina de Vivie-Riedle,[b] and Eberhard Riedle*[a]

cphc_201201057_sm_miscellaneous_information.pdf

Supporting Information

List of Contents

*Author to whom correspondence should be addressed.

Eberhard Riedle:

Tel: +49 (0)89 2180 9210

Fax: +49 (0)89 2180 9202

E-mail address: Eberhard.Riedle@physik.uni-muenchen.de

S4.   Theory

S4.1   Evolution of the radical and ion pair distribution: coupled electron transfer and diffusion

The transient absorption experiment measures the optical absorbance at selected wavelengths that correspond to the known absorption features of the species involved in the dynamic process. In the usual description given by the Lambert-Beer law the optical density is proportional to both the molar extinction coefficient and the concentration of a selected species. In recent work we were able to show that the extinction coefficient of the benzhydryl radical and the cation increase with about a 300 fs time constant after their optical generation due to planarization and solvation.[5] Therefore the measured optical signal can indeed be taken as a faithful measure of the concentrations from 1 ps on.

To model the evolution of the concentrations after UV excitation of benzhydryl chloride one would classically start with a nascent ratio of generated radicals and cations and then add a rate model in accord with Scheme 1. This model then includes the electron transfer that converts radical population to the cation, the geminate recombination and possibly a stabilization of species that prevents recombination and finally leads to free species. In Sec. 3 of the paper it was found that time dependent rates are needed to fit the data. This is not satisfactory from a chemical standpoint. Rather a microscopic insight into the reaction mechanism is sought.

For a proper treatment we therefore consider the time dependent population distribution $P_{RP}(R,t)$ for the radical pairs and $P_{IP}(R,t)$ for the ion pairs. We assume spherical symmetry and R denotes the distance between the centers of the two species making up each pair. The electron transfer rate $k_{ET}(R)$ is described by Marcus theory, the geminate recombination rates $k_{rec}^{RP}(R)$ and $k_{rec}^{IP}(R)$ as well as the stabilization rates $k_{stab}^{RP}(R)$ and $k_{stab}^{IP}(R)$ by a distance dependent rate each and the diffusional evolution is described in the frame work of the Smoluchowski formalism.

To obtain the overall population $P(t)$ which is proportional to the experimentally accessible product absorption, integration over the distance coordinate starting from the contact distance R_c is necessary

$$P(t) = \int_{R_c}^{\infty} P(R,t)\,dR \tag{S4.1}$$

It has been discussed that $P_{RP}(R,t)$ and $P_{IP}(R,t)$ cannot be directly propagated, instead underlying distribution functions $S_{RP}(R,t)$ and $S_{IP}(R,t)$ have to be used.[6,7] These are related to $P_{RP}(R,t)$ and $P_{IP}(R,t)$ by[8-10]

$$P_{RP}(R,t) = 4\pi R^2 \, S_{RP}(R,t)\exp\left[-V_{RP}(R)/k_B T\right] \tag{S4.2}$$

$$P_{IP}(R,t) = 4\pi R^2 \, S_{IP}(R,t)\exp\left[-V_{IP}(R)/k_B T\right] \tag{S4.3}$$

with the intrapair potentials $V_{RP}(R)$ and $V_{IP}(R)$. $k_B T$ is the thermal energy. This step is needed to ensure that the Boltzmann distribution is an equilibrium solution of the model.

The resulting set of coupled differential equations is

$$
\begin{aligned}
\frac{\partial}{\partial t} S_{RP}(R,t) = {}& L^+ S_{RP}(R,t) - k_{ET}(R) S_{RP}(R,t) \\
& - k_{rec}^{RP}(R) S_{RP}(R,t) - k_{stab}^{RP}(R) S_{RP}(R,t)
\end{aligned} \tag{S4.4}
$$

$$
\begin{aligned}
\frac{\partial}{\partial t} S_{IP}(R,t) = {}& L^+ S_{IP}(R,t) + k_{ET}(R) S_{RP}(R,t)\exp\left[-\frac{e^2}{4\pi\varepsilon_0\varepsilon_{st}k_B T}\frac{1}{R}\right] \\
& - k_{rec}^{IP}(R) S_{IP}(R,t) - k_{stab}^{IP}(R) S_{IP}(R,t)
\end{aligned} \tag{S4.5}
$$

L^+ is the adjoint Smoluchowski operator in spherical coordinates[8]

$$L^+ = \frac{1}{R^2}\exp\left[V(R)\right]\frac{\partial}{\partial R}\left(D(R)R^2\exp\left[-V(R)\right]\frac{\partial}{\partial R}\right). \tag{S4.6}$$

The electron transfer is a sink term for the radical distribution and a source term for the ion pairs. The back electron transfer pathway is neglected in our simulations since it is highly endergonic in polar solvents such as CH_3CN or CH_2Cl_2 due to the ultrafast solvation of the cation (see Section S4.3). The exponential factor accompanying the source term ensures that the population transfer between $P_{RP}(R,t)$ and $P_{IP}(R,t)$ is properly described by $S_{RP}(R,t)$ and $S_{IP}(R,t)$ within the Smoluchowski formalism. This can be understood as follows.

The intrapair potentials are given by

$$V_{RP}(R) = -\ln\left(g(R)\right)\cdot k_B T \tag{S4.7}$$

$$V_{IP}(R) = -\ln\left(g(R)\right)k_B T - \frac{e^2}{4\pi\varepsilon_0\varepsilon_{st}}\frac{1}{R} \tag{S4.8}$$

with e the elementary charge, ε_0 the vacuum permittivity, and ε_{st} the relative static permittivity (see Figure S4). $g(R)$ is the radial distribution function that describes the arrangement around the benzhydryl fragment in a solvent shell structure. For these potentials eqs (S4.2) and (S4.3) can be rewritten as

$$P_{RP}(R,t) = S_{RP}(R,t) \cdot g(R) \cdot 4\pi R^2 \tag{S4.9}$$

$$P_{IP}(R,t) = S_{IP}(R,t) \cdot g(R) \cdot \exp\left[\frac{e^2}{4\pi\varepsilon_0\varepsilon_{st}k_BT}\frac{1}{R}\right]4\pi R^2 \tag{S4.10}$$

and the factor accompanying the electron transfer source term in eq (S4.5) can be readily understood.

The radial distribution function $g(R)$ has been modeled by Monte-Carlo sampling[11] of the pure solvent. It resembles a partly ordered solvent structure with a maximum in probability at $R \approx d_{solv}$, $2\,d_{solv}$ and $3\,d_{solv}$, i.e. multiples of the solvent diameter d_{solv}. The solvent structure is transferred to the radical (ion) pair distribution by shifting $g(R)$ by $R_c - d_{solv}$. By this procedure we assume that the solvent structure around the benzhydryl radical or cation is similar to the one found around a selected solvent molecule. The chlorine radical or anion is thought to replace one of the solvent molecules. In the actual simulations we used the geometric mean $\sqrt{g(R)}$ between a fully structured ($g(R)$) and a random surrounding ($g(R)=1$) to mimic the deviation from spherical symmetry.

The fragments (benzhydryl radicals and cations, chlorine radicals and anions) are assumed to be spherical with radii $r_{benzhydryl}$ and r_{Cl}. The radii were deduced from the cavity volume determined by a DFT calculation in a continuum solvation model. The contact distance

$$R_c = r_{benzhydryl} + r_{Cl} \tag{S4.11}$$

is found to be practically identical for the radical pair and the ion pair.

In the Smoluchowski operator we use a distance dependent diffusion coefficient $D(R)$ which accounts for the hydrodynamic effects.[12] The diffusion is decelerated from the bulk value D_F when the two fragments are in close vicinity:

$$D(R) = D_F\left[1 - \frac{1}{2}\exp\left(-\frac{R - R_c}{d_{solv}}\right)\right] \tag{S4.12}$$

The rate for the geminate recombination of the radical and ion pairs is assumed to fall off exponentially ($\alpha \approx 1$ Å^{-1}) with distance, starting with a rate constant $k_{rec,0}$ when the pair is in contact at $R = R_c$[13]

$$k_{rec}(R) = k_{rec,0} \cdot \exp\left[-\alpha\left(R - R_c\right)\right] \tag{S4.13}$$

The electron transfer rate is described by Marcus theory[14,15]

$$k_{ET}(R) = \frac{2\pi}{\hbar} \cdot \frac{V_{eff}^2}{\sqrt{4\pi\lambda(R)k_B T}} \cdot \exp\left(-\frac{(\lambda(R)+\Delta G_{ET})^2}{4\lambda(R)k_B T}\right) \cdot \exp\left(-\beta(R-R_c)\right) \qquad (S4.14)$$

with V_{eff} the effective electronic coupling that incorporates the Franck-Condon factor and ΔG_{ET} the change in Gibbs free energy. The driving force ΔG_{ET} of the different benzhydryl systems ((tol)$_2$CH/Cl, tol(Ph)CH/Cl, Ph$_2$CH/Cl, mfp(Ph)CH/Cl, dfp(mfp)CH/Cl) are derived from quantum chemical calculations (see Section S4.4) and are given in Table S2.

The reorganization energy $\lambda(R)$ is given by

$$\lambda(R) = \lambda_{in} + \frac{e^2}{8\pi\varepsilon_0}\left(\frac{1}{\varepsilon_{op}} - \frac{1}{\varepsilon_{st}}\right) \cdot \left(\frac{1}{r_{benzhydryl}} + \frac{1}{r_{Cl}} - \frac{2}{R}\right) \qquad (S4.15)$$

with λ_{in} the internal reorganization energy and ε_{op} the relative optical permittivity. The last term in eq (S4.14) describes the fall-off of the ET rate with increasing distance from contact. β is around 1 Å^{-1}.[15] We do not use the density of states weighted Franck-Condon factor, since we find that it scales exponentially with R and cannot be distinguished at the constant temperature of our experiments from the $\exp(-\beta(R-R_c))$ factor. It just increases β by a small amount.

We model the distance-dependency of the stabilization rates with a sigmoid function (see Figure S4) which is essentially zero at contact distance R_c, reaches half its amplitude at a distance R_{sig} around the second solvation shell and provides for full stabilization with the rate $k_{stab,\infty}^{RP}$ or $k_{stab,\infty}^{IP}$ for larger distances

$$k_{stab}^{RP}(R) = k_{stab,\infty}^{RP} \cdot \frac{1}{1 + \exp\left[-2(R - R_{sig})\right]} \qquad (S4.16)$$

$$k_{stab}^{IP}(R) = k_{stab,\infty}^{IP} \cdot \frac{1}{1 + \exp\left[-2(R - R_{sig})\right]} \qquad (S4.17)$$

Stabilization rates are found to be necessary to reproduce the finite survival probability of radicals and cations found in the experiment. The introduction of k_{stab}^{RP} and k_{stab}^{IP} refine the description of the solvent. The Marcus-Smoluchowski equations (S4.4) and (S4.5) are based on a continuum solvation model where the dielectric constant of the solvent remains invariant for the photofragment separation distance. In other words, the continuum model assumes that the fragments are surrounded with a complete solvation shell for all fragment distances. In actual fact however, a fully stabilizing solvation shell is only formed at distances large enough to accommodate a solvent molecule between the two ions.

This leads to a sudden decrease of the energy of the system as the photofragments move apart and prevents them from reencounter. We model this solvation induced barrier by the introduction of the stabilization rates.

The stabilization rates transfer part of the radical (ion) distribution to distributions of nonreactive free radicals (ions). For a consistent description, the "free" distributions are propagated with the Smoluchowski formalism and result in population distributions $P_{FR}(R,t)$ and $P_{FI}(R,t)$ in analogy to eqs (S4.2) and (S4.3). The signals due to bound and free pairs are not differentiated in the experiment and therefore eq. (S4.1) transfers to

$$P_R(t) = \int_{R_c}^{\infty} \left(P_{RP}(R,t) + P_{FR}(R,t) \right) dR \tag{S4.18}$$

$$P_I(t) = \int_{R_c}^{\infty} \left(P_{IP}(R,t) + P_{FI}(R,t) \right) dR \tag{S4.19}$$

These two quantities are directly proportional to the experimental concentrations $c_{radical}(t)$ and $c_{cation}(t)$ as seen in eq. (S1.1). The two coupled differential equations (S4.4) and (S4.5) are solved numerically by the "pdepe"-solver[16] which is part of the MatLab suite. The numerical solution is hereby calculated on a restricted distance interval starting from the contact distance R_c up to a maximum distance $R_{max} = 80$ Å. Special care was taken to ensure that the outer limit is chosen large enough to assure an unperturbed diffusional separation of the photofragments.

As initial conditions we assume a Gaussian distribution for the radical pairs with a maximum at R_{Gauss} and a HWHM R_{HWHM} of the distribution. The Gaussian distribution is set to 0 for distances smaller than the contact distance R_c

$$S_{RP}(R, t = 0) = \begin{cases} A \exp\left(-\ln 2 \left(\dfrac{R - R_{Gauss}}{R_{HWHM}} \right)^2 \right) & , \text{ for } R \geq R_c \\ 0 & , \text{ for } R < R_c \end{cases} \tag{S4.20}$$

The latter assumption mirrors the experimental observation that not all optically excited molecules lead to radicals or ions. It effectively models the observed internal conversion that likely can be viewed as chlorine fragments bouncing off a solvent molecule to rapidly recombine.

The assumed initial distance distribution of the ion pair population $P_{IP}(R, t = 0)$ has the same shape as the radical pair population. The overall population ratio is set in agreement with the experimental findings.

We use reflecting boundary conditions for both species at contact distance R_c as well as at the maximum R_{max}. Since we treat the geminate recombination as explicit sink terms, the diffusion toward the inner boundary should not lead to an extra loss of population. This translates to[6,17]

$$\frac{dS_{RP}(t,R)}{dR}\bigg|_{R=R_c} = 0, \quad \frac{dS_{RP}(t,R)}{dR}\bigg|_{R=R_{max}} = 0$$

$$\frac{dS_{IP}(t,R)}{dR}\bigg|_{R=R_c} = 0, \quad \frac{dS_{IP}(t,R)}{dR}\bigg|_{R=R_{max}} = 0 \tag{S4.21}$$

Within the model we make several assumptions. First we assume a low radical pair concentration in order to neglect any crowding effects. This assumption is fully satisfied by the experimental conditions (concentration of excited precursors ≈ 100 μmol/L): together with the dissociation quantum yield ($\Phi_{Hom} \approx 40\%$) the radical pair concentration can be estimated as ~40 μmol/L. Second, our model starts just after the ultrafast bond cleavage process (300 fs).[18,19] As shown in Figure 1 and 2, radical pairs are the initially generated species in a ratio of 20 to 1. Finally, we assume that solvent stabilization occurs faster than the actually observed electron transfer rate $k_{ET}(R)$ ($\tau_{ET} = 1/k_{ET}(R) \gg \tau_{solv}$), which is justified for the investigated solvents acetonitrile and dichloromethane with typical relatively fast solvation times $\tau_{solv} = 140 - 500$ fs.[20-23] The focus of our model is on the limiting case of diffusion controlled electron transfer reactions. To investigate the opposite limit of the dielectric relaxation in solvents with slower solvation times (e.g., ethylene glycol or 1-4-dioxane), a straightforward approach within the Sumi-Marcus model would have to be applied.[24-26]
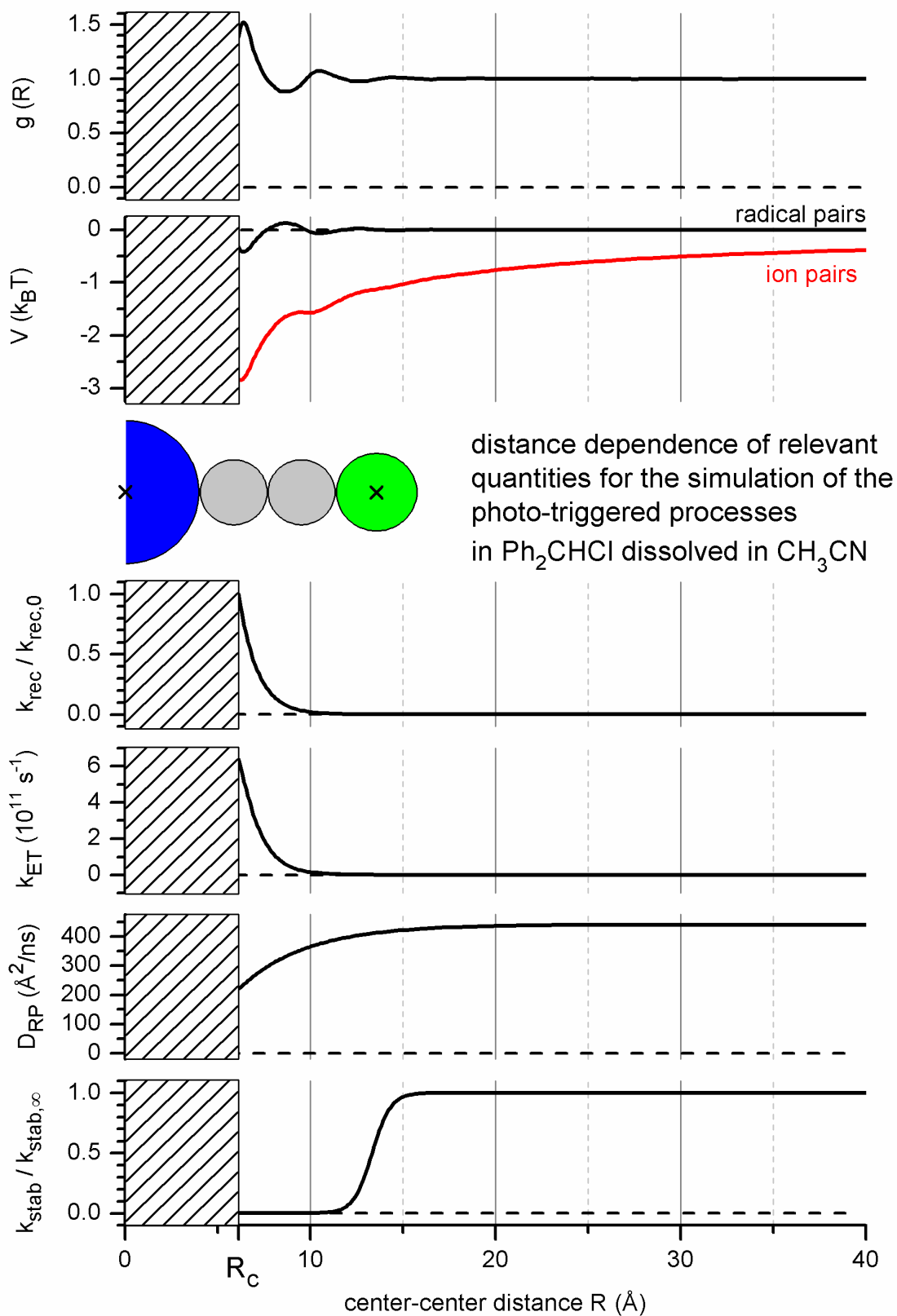
Figure S4   Distance dependence of relevant quantitites for the simulation of the photo-triggered processes in Ph$_2$CHCl dissolved in CH$_3$CN.

Table S1: Parameters used for the simulation of Scheme 1 according to the model described in S4.1.

parameter	CH$_3$CN	CH$_2$Cl$_2$	Ref.
solvent			
D_F (RP) (Å^2/ns)	440	342 [a]	27
D_F (IP) (Å^2/ns)	60	110	this work
d_{solv} (Å)	3.60	3.79	27,28 / this work
ε_{op}	1.80	2.02	
ε_{st}	36.6	8.93	
T (K)	298		
solute			
$R_c = r_{benzyhydryl} + r_{Cl}$ (Å)	3.96 + 2.17 = 6.13		this work
$k_{stab,\infty}^{RP}$ (10^9/s)	6.67	6.67	this work
$k_{stab,\infty}^{IP}$ (10^9/s)	6.67	0	this work
R_{Sig}	$R_c + 2\,d_{solv}$		this work
electron transfer			
ΔG_{ET} (eV) [b]	-1.71 (-1.61)	-1.13 (-1.23)	this work
V_{eff} (cm^{-1}) [c]	57	47	this work
β (Å^{-1})	0.7		29
λ_{in} (eV)	0.2		28
recombination			
$k_{rec,0}^{RP}$ (10^9/s)	300	370	this work
$k_{rec,0}^{IP}$ (10^9/s)	25	32	this work
α (Å^{-1})	1.0		13
starting distribution			
R_{Gauss}	$R_c + 0.5 d_{solv}$		this work
R_{HWHM}	1.8 d_{solv}	2.0 d_{solv}	this work

[a]) Estimated values from comparison of CH$_3$CN with CH$_2$Cl$_2$ [b]) Driving forces were derived by quantum chemical calculation and are given in parentheses. For details see Section S3.4 and Table S2. [c]) V_{eff} has been adopted by a fit to the experimental dynamics.

S4.2   Non-exponential processes: comparison between experiment and model calculations

S4.2.1 Transient absorption signal of benzhydryl radicals and cations

The model presented in Section S4.1 is used to investigate the electron transfer between benzhydryl radicals and chlorine radicals in CH_3CN and CH_2Cl_2 subsequent to ultrafast photolysis, the diffusional evolution and the partial recombinations. The input parameters used in the model (taken from literature) and the values determined for the best fit are given in Table S1. The model describes the experimentally observed evolution of the total radical and cation population very well despite the rather complex functional form. In addition, the microscopic model allows us to calculate experimental observables like the ensemble averaged (stretched exponential) electron transfer time τ_{SE} and the quantum yield of generated free radicals and ions.
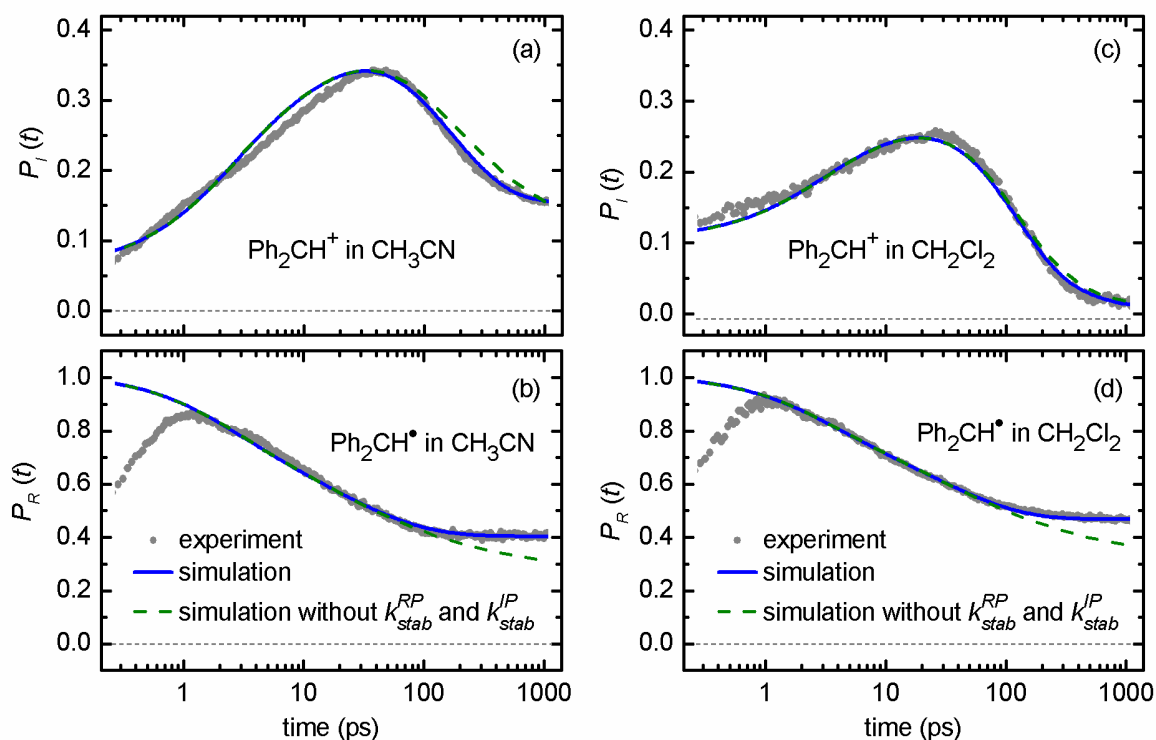
Fig S5:   Normalized simulated signals (blue and green) for (a) $P_I(t)$ for Ph_2CH^+ in CH_3CN, (b) $P_R(t)$ for $Ph_2CH^\bullet$ in CH_3CN, (c) $P_I(t)$ for Ph_2CH^+ in CH_2Cl_2 and (d) $P_R(t)$ for $Ph_2CH^\bullet$ in CH_2Cl_2 together with the respective experimental signals (grey dots).

The simulated time evolution of $P_R(t)$ and $P_I(t)$ for Ph_2CHCl in CH_3CN and CH_2Cl_2 is depicted in Figure S5 (blue line) as a semi-logarithmic plot. The experimentally observed evolution of the signals (grey dots) are well reproduced from about 1 ps up to the maximum delay time in the experiment. The deviation at the very earliest times can be readily explained by the 300 fs exponential increase in signal

strength due to planarization and solvation of the benzhydryl radicals and cations.[5] Clearly evident from Figure S5 is the non-exponential character of $P_R(t)$ and $P_I(t)$ caused by the diffusion controlled electron transfer from a non-equilibrium radical pair distribution. To illustrate the influence of the stabilization rates, we additionally ran the simulations without them. The result is shown as dashed green lines for comparison.

For a direct comparison between the simulation and the experimental dynamics we applied the same fit function (eq S2.1) to $P_R(t)$ and $P_I(t)$ as for the evaluation of the transient absorption data (see Section S2). The obtained electron transfer time constant for Ph_2CHCl in CH_3CN is $<\tau_{SE}> = 21.6$ ps; the decay of the ion signal can be fitted with a single exponential time constant of $\tau_{tot} = 1/k_{tot} = 137$ ps reflecting the geminate recombination and diffusion (see Section 3). Both derived lifetimes are in excellent agreement with the experimental results.

S4.2.2 Time dependent electron transfer rates $k_{ET}(t)$

The good agreement between simulations and experiment allows for a quantitative interpretation of the time and distance dependent populations $P_R(t,r)$ and $P_I(t,r)$ and thus to derive additional information which is not accessible from the experiment

The time dependent ensemble averaged electron transfer rate $k_{ET}(t)$, which is central to the complete reaction process, is determined from the microscopic model by

$$k_{ET}(t) = \frac{\int_{r_0}^{\infty} P_{RP}(t,r) \cdot k_{ET}(r)\, dr}{\int_{r_0}^{\infty} P_{RP}(t,r)\, dr} \qquad (S4.22)$$

$k_{ET}(t)$ is depicted in Figure S6. At very early times ($t < 1$ ps) $k_{ET}(t)$ is close to $(10\text{ ps})^{-1}$. This results from the combination of the on-contact rate of $667 \times 10^9\, s^{-1}$ and the initial fraction of slightly below 10% of radical pairs with a small enough distance for efficient ET. As close-to-contact pairs are quickly used up, $k_{ET}(t)$ drops to $10 \times 10^9\, s^{-1}$ at 10 ps. In the long time range diffusion cannot overcome the depletion of the radical distribution in the sub-10 Å range needed for further ET and the effective ET rate drops further to an insignificant level. Diffusion rather increases the average radical distance.
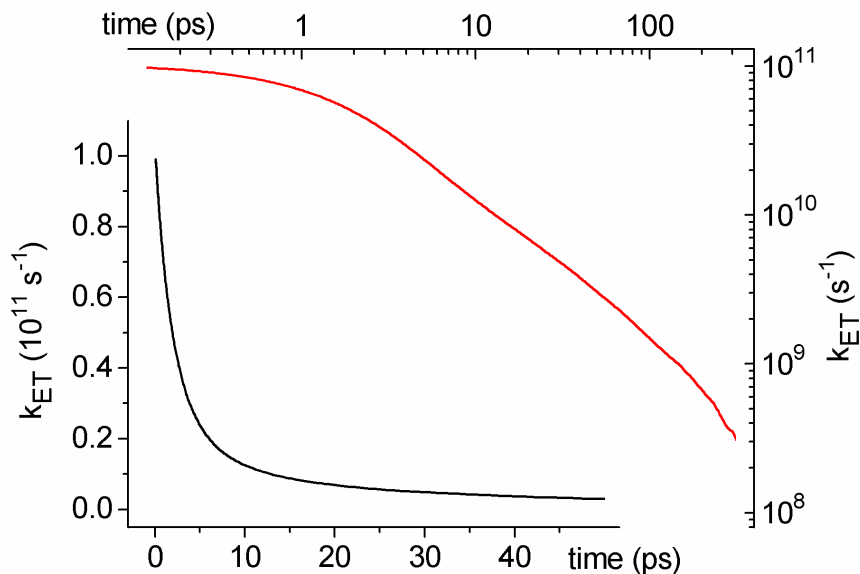
Fig S6: Time-dependent electron transfer rate $k_{ET}(t)$ calculated according to eq S4.15 and displayed once linearly (black curve) and once logarithmically (red curve).

S4.2.3 Evaluation of individual time-dependent rates and yields from the simulation

The ensemble averaged rates $k_{rec}^{IP}(t)$ and $k_{stab}^{IP}(t)$ are derived form the distance dependent rates given in eqs. S4.13 and S4.17 and the population distribution in analogy to the electron transfer rate (eq. S4.22).

The accumulative yield for various processes are determined in the following way. Each sink term in the differential equations S4.4 and S4.5 is added up during the numerical propagation and properly transformed into associated population distributions. To obtain the total yield Y_{ET} of electron transfer, Y_{stab}^{RP} of the stabilized radicals and Y_{rec}^{RP} of radical recombination, the distance dependent quantities are integrated over the full range.

The same procedure is used for the ion yields Y_{stab}^{IP} and Y_{rec}^{IP}. All the radical yields are reported in % of the originally generated radical pairs. The ion yields refer to the totally generated ion pairs up to a given time. This includes the small nascent contribution directly from the photoexcitation.

The quantum yields Φ_{rad} and Φ_{cat} are the ratio of the benzhydryl radicals / cations to the optically excited molecules at a given time. Since the model does not account for the finite probability of radical production, we had to fix the lasting radical yield in the model to the experimental values. The according values are shown in Table 2 in parentheses.

S19

S4.3 Quantum chemical calculations: Driving force ΔG_{ET} of the electron transfer

The quantum chemical calculations are performed with the program package Gaussian09.[30] All calculations rely on density functional theory, the geometries of the different precursors, benzhydryl cations and radicals are optimized and confirmed by frequency analysis showing no imaginary frequency. We use the recently developed hybrid meta-GGA functional M06-2X (see Table S2), which has proven to give accurate results for the study of main group thermochemistry.[31] Additionally we tested the popular hybrid functional B3LYP. Implicit solvent effects of acetonitrile, dichloromethane and cyclohexane are included using the integral equation formalism variant of the polarizable continuum model (IEFPCM).[32-34] The thermodynamic data are calculated with two different basis sets, the double ζ basis 6-31G(d) and the triple ζ basis 6-311+G(d). Values obtained with the functional M06-2X and the triple ζ basis (see Table S2) are used slightly adapted in the model of distance dependent electron transfer reactions (see Section S4.2). A further enlargement of the basis set (6-311++G(d,p)) does not improve the calculated Gibbs free reaction energies. The coordinates of the optimized geometries (functional M06-2X and basis set 6-311+G(d)) are given in Section S7 together with the absolute electronic energies.

The Gibbs free reaction energy for the electron transfer (ΔG_{ET}) as well as the driving force of recombination of the radical and ion pairs are calculated at standard conditions (298.15 K and 1.0 bar). The solvation energies for the benzhydryl cations and radicals in CH_3CN, CH_2Cl_2 and cyclohexane are calculated as the difference $\langle \Psi | H + V/2 | \Psi \rangle - \langle \Psi | H | \Psi \rangle$, where H is the electronic Hamiltonian and $V/2$ the perturbation by the solvent reaction field.

Table S2. Gibbs free reaction energy of the electron transfer within the radical pair ΔG_{ET}, of the geminate recombination of the radical pair ΔG_{RP} and the ion pair ΔG_{IP}, as well as the solvation energy of the benzhydryl radical $\Delta G_{solv,rad}$ and cation $\Delta G_{solv,cat}$. The Gibbs free energy values are calculated for different derivatives and solvents (IEFPCM) with DFT (functional M06-2X, basis set 6-311+G(d)). For comparison and validation ΔG_{ET} has also been calculated I with the functional M06-2X, basis set 6-31G(d) and II with functional B3LYP, basis set 6-31G(d).

solvent	Derivative	ΔG_{RP} (eV)	ΔG_{IP} (eV)	$\Delta G_{solv,rad}$ (eV)	$\Delta G_{solv,cat}$ (eV)	$\Delta G_{ET,exp}$ (eV) [a]	ΔG_{ET} (eV)		
								I	II
aceto-nitrile	(tol)$_2$CHCl	-2.539	-0.715	-0.199	-1.681	-1.79	-1.823	-1.707	-1.905
	tol(Ph)CHCl	-2.504	-0.806	-0.196	-1.738	-1.69	-1.698	-1.619	-1.756
	Ph$_2$CHCl	-2.536	-0.924	-0.191	-1.798	-1.68	-1.612	-1.507	-1.658
	mfp(Ph)CHCl	-2.552	-1.075	-0.200	-1.910		-1.477	-1.382	-1.532
	dfp(mfp)CHCl	-2.492	-1.307	-0.206	-2.096		-1.185	-1.106	-1.284
dichloro-methane	(tol)$_2$CHCl	-2.538	-1.087	-0.164	-1.527		-1.451	-1.319	-1.484
	tol(Ph)CHCl	-2.534	-1.218	-0.162	-1.580		-1.316	-1.197	-1.371
	Ph$_2$CHCl	-2.503	-1.271	-0.158	-1.634		-1.232	-1.110	-1.257
	mfp(Ph)CHCl	-2.506	-1.427	-0.168	-1.729		-1.079	-0.974	-1.120
	dfp(mfp)CHCl	-2.485	-1.719	-0.167	-1.887		-0.766	-0.680	-0.860
cyclo-hexane	(tol)$_2$CHCl	-2.575	-2.874	-0.064	-0.853		0.299	0.487	0.350
	tol(Ph)CHCl	-2.519	-2.959	-0.064	-0.884		0.440	0.632	0.478
	Ph$_2$CHCl	-2.571	-3.143	-0.063	-0.914		0.572	0.746	0.601
	mfp(Ph)CHCl	-2.531	-3.288	-0.070	-0.954		0.757	0.908	0.764
	dfp(mfp)CHCl	-2.509	-3.651	-0.078	-1.021		1.142	1.258	1.069

[a]) experimental values calculated via one electron reduction potentials in acetonitrile for the benzhydryl cations (from Ref. 35) and the Cl$^\bullet$ radical (from Ref. 36) vs. SCE.

S8.   References

(1)   Bartl, J.; Steenken, S.; Mayr, H.; McClelland, R. A. *J. Am. Chem. Soc.* **1990**, *112*, 6918-6928.

(2)   Megerle, U.; Pugliesi, I.; Schriever, C.; Sailer, C. F.; Riedle, E. *Appl. Phys. B* **2009**, *96*, 215-231.

(3)   Sailer, C. F.; Singh, R. B.; Ammer, J.; Riedle, E.; Pugliesi, I. *Chem. Phys. Lett.* **2011**, *512*, 60-65.

(4)   Lorenc, M.; Ziolek, M.; Naskrecki, R.; Karolczak, J.; Kubicki, J.; Maciejewski, A. *Appl. Phys. B* **2002**, *74*, 19-27.

(5)   Fingerhut, B. P.; Sailer, C. F.; Ammer, J.; Riedle, E.; de Vivie-Riedle, R. *J. Phys. Chem. A*, DOI: 10.1021/jp300986t

(6)   Rosspeintner, A.; Kattnig, D. R.; Angulo, G.; Landgraf, S.; Grampp, G. *Chem. Eur. J.* **2008**, *14*, 6213-6221.

(7)   Schulten, K. private communication

(8)   Saik, V. O.; Goun. A. A.; Nanda, J.; Shirota, K.; Tavernier, H. L.; Fayer, M. D. *J. Phys. Chem. A* **2004**, *108*, 6696-6703.

(9)   Weidemaier, K.; Tavernier, H. L.; Swallen, S. F.; Fayer, M. D. *J. Phys. Chem. A* **1997**, *101*, 1887-1902.

(10)   Tachiya, M. *Radiat. Phys. Chem.* **1983**, *21*, 167-175.

(11)   Metropolis, N.; Rosenbluth, A. W.; Rosenbluth, M. N.; Teller, A. H.; Teller, E. *J. Chem. Phys.* **1953**, *21*, 1087-1092.

(12)   Northrup. S. H.; Hynes, J. T. *J. Chem. Phys.* **1979**, *71*, 871-883.

(13)   Wojcik, M.; Tachiya, M. *Radiat. Phys. Chem.* **2005**, *74*, 132-138.

(14)   Marcus, R. A.; Sutin, N. *Biochim. Biophys. Acta* **1985**, *811*, 265-322.

(15)   Barbara, P. F.; Meyer, T. J.; Ratner, M. A. *J. Phys. Chem.* **1996**, *100*, 13148-13168.

(16)   Skeel, R. D.; Berzins, M. *SIAM J. Sci. Stat. Comp.* **1990**, *11*, 1-32.

(17)   Saik, V. O.; Goun, A. A.; Fayer, M. D. *J. Chem. Phys.* **2004**, *120*, 9601-9611.

(18)   Lipson, M.; Deniz, A. A.; Peters, K. S. *Chem. Phys. Lett.* **1998**, *288*, 781-784.

(19)   Fingerhut, B. P.; Geppert, D.; de Vivie-Riedle, R. *Chem. Phys.* **2008**, *343*, 329-339.

(20)   Horng, M. L.; Gardecki, J. A.; Papazyan, A.; Maroncelli, M. *J. Phys. Chem.* **1995**, *99*, 17311-

17337.

(21)   Ladanyi, B. M.; Stratt, R. M. *J. Phys. Chem.* **1995**, *99*, 2502-2511.

(22)   de Boeij, W. P.; Pshenichnikov, M. S.; Wiersma, D. A. *J. Phys. Chem.* **1996**, *100*, 11806-11823.

(23)   Eom, I.; Joo, T. *J. Chem.* Phys. **2009**, *131*, 244507.

(24)   Sumi, H.; Marcus, R. A. *J. Chem. Phys.* **1986**, *84*, 4272-4276.

(25)   Sumi, H.; Marcus, R. A. *J. Chem. Phys.* **1986**, *84*, 4894-4914.

(26)   Wang, H.; Lin, S.; Allen, J. P.; Williams, J. C.; Blankert, S.; Laser, C.; Woodbury, N. W. *Science*, **2007**, *316*, 747-750.

(27)   Goun, A.; Glusac, K.; Fayer, M. D. *J. Chem. Phys.* **2006**, *124*, 084504.

(28)   Tavernier, H. L.; Kalashnikov, M. M.; Fayer, M. D. *J. Chem. Phys.* **2000**, *113*, 10191-10201.

(29)   Page, C. C.; Moser, C. C.; Chen, X.; Dutton, P. L. *Nature* **1999**, *402*, 47.

(30)   Gaussian 09, Revision A.02, M. J. Frisch, G. W. Trucks, H. B. Schlegel, G. E. Scuseria, M. A. Robb, J. R. Cheeseman, G. Scalmani, V. Barone, B. Mennucci, G. A. Petersson, H. Nakatsuji, M. Caricato, X. Li, H. P. Hratchian, A. F. Izmaylov, J. Bloino, G. Zheng, J. L. Sonnenberg, M. Hada, M. Ehara, K. Toyota, R. Fukuda, J. Hasegawa, M. Ishida, T. Nakajima, Y. Honda, O. Kitao, H. Nakai, T. Vreven, J. A. Montgomery, Jr., J. E. Peralta, F. Ogliaro, M. Bearpark, J. J. Heyd, E. Brothers, K. N. Kudin, V. N. Staroverov, R. Kobayashi, J. Normand, K. Raghavachari, A. Rendell, J. C. Burant, S. S. Iyengar, J. Tomasi, M. Cossi, N. Rega, J. M. Millam, M. Klene, J. E. Knox, J. B. Cross, V. Bakken, C. Adamo, J. Jaramillo, R. Gomperts, R. E. Stratmann, O. Yazyev, A. J. Austin, R. Cammi, C. Pomelli, J. W. Ochterski, R. L. Martin, K. Morokuma, V. G. Zakrzewski, G. A. Voth, P. Salvador, J. J. Dannenberg, S. Dapprich, A. D. Daniels, O. Farkas, J. B. Foresman, J. V. Ortiz, J. Cioslowski, and D. J. Fox, Gaussian, Inc., Wallingford CT, 2009.

(31)   Zhao, Y.; Truhlar, D. G. *Theor. Chem. Account* **2008**, *120*, 215-241.

(32)   Caricato, M.; Mennucci, B.; Tomasi, J.; Ingrosso, F.; Cammi, R.; Corni, S.; Scalmani, G. *J. Chem. Phys.* **2006**, *124*, 124520.

(33)   Improta, R.; Barone, V.;Scalmani, G.; Frisch, M. J. *J. Chem. Phys.* **2006**, *125*, 054103.

(34)   Scalmani, G.; Frisch, M. J. *J. Chem. Phys.* **2010**, *132*, 114110.

(35)   Ofial, A. R.; Ohkubo, K.; Fukuzumi, S.; Lucius, R.; Mayr, H. *J. Am. Chem. Soc.* **2003**, *125*, 10906-10912.

(36)   Isse, A. A.; Lin, C. Y.; Coote, M. L.; Gennaro, A. *J. Phys. Chem. B* **2011**, *115*, 678-684.

(37)   Nolte, C.; Mayr, H. *Eur. J. Org. Chem.* **2010**, 1435-1439.

List of abbreviations

CASSCF	complete active space self consistent field
CASPT2	complete active space second-order perturbation theory
CC	coupled cluster
CC2	second-order approximate coupled cluster
cf.	compare
(p-CF$_3$-C$_6$H$_4$)CH$_2$−PPh$_3$$^+$	4-(trifluoromethyl)benzyltriphenylphosphonium ion
CI	configuration interactions
CLS	constraint low-level state
CoIn	conical intersection
COSMO	conductor-like screening model
CT	charge transfer
dfp(mfp)CH−Cl	(3,5-)difluorophenyl(3-fluorophenyl)methylchloride
DFT	density functional theory
DNA	deoxyribonucleic acid
e.g.	for example
eq.	equation
et al.	and others
FC	Franck-Condon
i.e.	that is
IR	infrared
MCTDH	multi configuration time dependent Hartree
MD	molecular dynamics
MeCN	acetonitrile
MEP	minimum energy path
mfp(Ph)CH−Cl	3-fluorophenyl(phenyl)methylchloride
MRCI	multi reference configuration interactions
NACME	non-adiabatic coupling matrix element

NMR	nuclear magnetic resonance
ONIOM	our own n-layered integrated molecular orbital and molecular mechanics
PCM	polarizable continuum model
PES	potential energy surface
Ph$_2$CH	diphenylmethyl
Ph$_2$CH$^+$	diphenylmethyl cation
Ph$_2$CH$^\bullet$	diphenylmethyl radical
Ph$_2$CH$-$Br	diphenylmethylbromide
Ph$_2$CH$-$Cl	diphenylmethylchloride
Ph$_2$CH$-$PPh$_3{}^+$	diphenylmethyltriphenylphosphonium ion
PhCH$_2$$-PH_2Ph^+$	phenylmethylphenylphosphonium ion
PhCH$_2$$-PPh_3{}^+$	benzyltriphenylphosphonium ion
QD	quantum dynamics
QM/MM	quantum mechanics / molecular mechanics
RMSD	root-mean-square deviation
tab.	table
TDDFT	time-dependent density functional theory
(tol)$_2$CH$-$Cl	di(4-tolyl)methylchloride
tol(Ph)CH$-$Cl	phenyl(4-tolyl)methylchloride
UV	ultraviolet

Bibliography

[1] N. J. Turro, V. Ramamurthy and J. C. Scaiano, *Modern Molecular Photochemistry of Organic Molecules*, University Science Books, Sausalito, California, USA (2010).

[2] B. L. Feringa and W. R. Browne (eds.), *Molecular Switches*, WILEY-VCH Verlag, Weinheim, Germany, second edn. (2011).

[3] N. Fuentes, A. Martin-Lasanta, L. Alvarez de Cienfuegos, M. Ribagorda, A. Parra and J. M. Cuerva, *Nanoscale* **3**, 4003 (2011).

[4] A. A. Beharry and G. A. Woolley, *Chem. Soc. Rev.* **40**, 4422 (2011).

[5] U. Al-Atar, R. Fernandes, B. Johnsen, D. Baillie and N. R. Branda, *J. Am. Chem. Soc.* **131**, 15966 (2009).

[6] A. Nenov, T. Cordes, T. T. Herzog, W. Zinth and R. d. Vivie-Riedle, *J. Phys. Chem. A* **114**, 13016 (2010).

[7] J. Broichhagen, M. Schönberger, S. C. Cork, J. A. Frank, P. Marchetti, M. Bugliani, A. M. J. Shapiro, S. Trapp, G. A. Rutter, D. J. Hodson and D. Trauner, *Nature Commun.* **5**, 5116 (2014).

[8] K. Takuma, T. Takata and T. Endo, *J. Photopolym. Sci. Tech.* **6**, 67 (1993).

[9] J. Shao, Y. Huang and Q. Fan, *Polym. Chem.* **5**, 4195 (2014).

[10] S. Chatani, C. J. Kloxin and C. N. Bowman, *Polym. Chem.* **5**, 2187 (2014).

[11] K. Fries and G. Finck, *Ber. Dtsch. Chem. Ges.* **41**, 4271 (1908).

[12] D. Belluč and P. Hrdlovič, *Chem. Rev.* **67**, 599 (1967).

[13] M. A. Miranda and F. Galindo, *The Photo-Fries Rearrangement*, in V. Ramamurthy and K. S. Schanze (eds.), *Photochemistry of Organic Molecules in Isotropic and Anisotropic Media*, vol. 9, pp. 43–131, CRC Press, New York, USA (2003).

[14] L. Kürti and B. Czakó, *Strategic Applications of Named Reactions in Organic Synthesis*, Elsevier Acadamic Press, Burlington, MA, USA (2005).

[15] L. Wolff, *Liebigs Ann. Chem.* **325**, 129 (1902).

[16] H. Meier and K.-P. Zeller, *Angew. Chem. Int. Ed.* **14**, 32 (1975).

[17] W. Kirmse, *Eur. J. Org. Chem.* **2002**, 2193 (2002).

[18] N. Nelson and A. Ben-Shem, *Nature Rev. Mol. Cell. Biol.* **5**, 971 (2004).

[19] S. Eberhard, G. Finazzi and F.-A. Wollman, *Annu. Rev. Genet.* **42**, 463 (2008).

[20] Y.-C. Cheng and G. R. Fleming, *Annu. Rev. Phys. Chem.* **60**, 241 (2009).

[21] E. Collini, C. Y. Wong, K. E. Wilk, P. M. G. Curmi, P. Brumer and G. D. Scholes, *Nature* **463**, 644 (2010).

[22] G. D. Scholes, G. R. Fleming, A. Olaya-Castro and R. van Grondelle, *Nature Chem.* **3**, 763 (2011).

[23] M. F. Hohmann-Marriott and R. E. Blankenship, *Annu. Rev. Plant Biol.* **62**, 515 (2011).

[24] E. Collini, *Chem. Soc. Rev.* **42**, 4932 (2013).

[25] A. Chenu and G. D. Scholes, *Annu. Rev. Phys. Chem.* **66**, 69 (2015).

[26] S. Hayashi, E. Tajkhorshid and K. Schulten, *Biophys. J.* **96**, 403 (2009).

[27] D. Polli, P. Altoe, O. Weingart, K. M. Spillane, C. Manzoni, D. Brida, G. Tomasello, G. Orlandi, P. Kukura, R. A. Mathies, M. Garavelli and G. Cerullo, *Nature* **467**, 440 (2010).

[28] I. Schapiro, M. N. Ryazantsev, L. M. Frutos, N. Ferré, R. Lindh and M. Olivucci, *J. Am. Chem. Soc.* **133**, 3354 (2011).

[29] O. P. Ernst, D. T. Lodowski, M. Elstner, P. Hegemann, L. S. Brown and H. Kandori, *Chem. Rev.* **114**, 126 (2014).

[30] J.-L. Ravanat, T. Douki and J. Cadet, *J. Photochem. Photobiol. B* **63**, 88 (2001).

[31] É. Sage, R. Drouin and M. Rouabhia (eds.), *From DNA Photolesions to Mutations, Skin Cancer and Cell Death*, Comprehensive Series in Photochemical & Photobiological Sciences, The Royal Society of Chemistry, Cambridge, UK (2005).

[32] K. Haiser, B. P. Fingerhut, K. Heil, A. Glas, T. T. Herzog, B. M. Pilles, W. J. Schreier, W. Zinth, R. de Vivie-Riedle and T. Carell, *Angew. Chem. Int. Ed.* **51**, 408 (2012).

[33] A. C. Kneuttinger, G. Kashiwazaki, S. Prill, K. Heil, M. Müller and T. Carell, *Photochem. Photobiol.* **90**, 1 (2014).

[34] W. J. Schreier, P. Gilch and W. Zinth, *Annu. Rev. Phys. Chem.* **66**, 497 (2015).

[35] J. Chen, Y. Zhang and B. Kohler, *Top. Curr. Chem.* **356**, 39 (2015).

[36] F. Borges and M. Pinto, *Helv. Chim. Acta* **75**, 1061 (1992).

[37] D. Stichnoth, P. Kölle, T. J. Kimbrough, E. Riedle, R. de Vivie-Riedle and D. Trauner, *Nature Commun.* **5**, 5597 (2014).

[38] A. Nenov, W. J. Schreier, F. O. Koller, M. Braun, R. de Vivie-Riedle, W. Zinth and I. Pugliesi, *J. Phys. Chem. A* **116**, 10518 (2012), PMID: 23020139.

[39] C. F. Sailer, S. Thallmair, B. P. Fingerhut, C. Nolte, J. Ammer, H. Mayr, I. Pugliesi, R. de Vivie-Riedle and E. Riedle, *ChemPhysChem* **14**, 1423 (2013).

[40] M. Dittmann, F. F. Graupner, B. Maerz, S. Oesterling, R. de Vivie-Riedle, W. Zinth, M. Engelhard and W. Lüttke, *Angew. Chem. Int. Ed.* **53**, 591 (2014).

[41] A. S. Alnaser, M. Kübel, R. Siemering, B. Bergues, N. G. Kling, K. J. Betsch, Y. Deng, J. Schmidt, Z. A. Alahmed, A. M. Azzeer, J. Ullrich, I. Ben-Itzhak, R. Moshammer, U. Kleineberg, F. Krausz, R. de Vivie-Riedle and M. F. Kling, *Nature Commun.* **5**, 3800 (2014).

[42] I. Tavernelli, *Acc. Chem. Res.* **48**, 792 (2015), PMID: 25647401.

[43] K. Sadeghian, D. Flaig, I. D. Blank, S. Schneider, R. Strasser, D. Stathis, M. Winnacker, T. Carell and C. Ochsenfeld, *Angew. Chem. Int. Ed.* **53**, 10044 (2014).

[44] D. Strickland and G. Mourou, *Opt. Commun.* **56**, 219 (1985).

[45] G. Cerullo, M. Nisoli and S. De Silvestri, *Appl. Phys. Lett.* **71**, 3616 (1997).

[46] E. Riedle, M. Beutter, S. Lochbrunner, J. Piel, S. Schenkl, S. Spörlein and W. Zinth, *Appl. Phys. B – Lasers O.* **71**, 457 (2000).

[47] G. Cerullo and S. De Silvestri, *Rev. Sci. Instrum.* **74**, 1 (2003).

[48] P. Baum, S. Lochbrunner and E. Riedle, *Appl. Phys. B – Lasers O.* **79**, 1027 (2004).

[49] N. Krebs, I. Pugliesi and E. Riedle, *Appl. Sci.* **3**, 153 (2013).

[50] M. Bradler and E. Riedle, *J. Opt. Soc. Am. B* **31**, 1465 (2014).

[51] V. Kandidov, O. Kosareva, I. Golubtsov, W. Liu, A. Becker, N. Akozbek, C. Bowden and S. Chin, *Appl. Phys. B – Lasers O.* **77**, 149 (2003).

[52] M. Bradler, P. Baum and E. Riedle, *Appl. Phys. B – Lasers O.* **97**, 561 (2009).

[53] M. J. Rosker, M. Dantus and A. H. Zewail, *J. Chem. Phys.* **89**, 6113 (1988).

[54] M. Dantus, M. J. Rosker and A. H. Zewail, *J. Chem. Phys.* **89**, 6128 (1988).

[55] A. H. Zewail, *Science* **242**, 1645 (1988).

[56] A. H. Zewail, *Angew. Chem. Int. Ed.* **39**, 2586 (2000).

[57] C. Manzoni, D. Polli and G. Cerullo, *Rev. Sci. Instrum.* **77**, 023103 (2006).

[58] D. Polli, M. Antognazza, D. Brida, G. Lanzani, G. Cerullo and S. D. Silvestri, *Chem. Phys.* **350**, 45 (2008).

[59] U. Megerle, I. Pugliesi, C. Schriever, C. Sailer and E. Riedle, *Appl. Phys. B – Lasers O.* **96**, 215 (2009).

[60] E. Riedle, M. Bradler, M. Wenninger, C. F. Sailer and I. Pugliesi, *Faraday Discuss.* **163**, 139 (2013).

[61] S. Mukamel, *Annu. Rev. Phys. Chem.* **51**, 691 (2000).

[62] D. M. Jonas, *Annu. Rev. Phys. Chem.* **54**, 425 (2003).

[63] T. Brixner, J. Stenger, H. M. Vaswani, M. Cho, R. E. Blankenship and G. R. Fleming, *Nature* **434**, 625 (2005).

[64] N. Krebs, I. Pugliesi, J. Hauer and E. Riedle, *New J. Phys.* **15**, 085016 (2013).

[65] I. Rivalta, A. Nenov, G. Cerullo, S. Mukamel and M. Garavelli, *Int. J. Quantum Chem.* **114**, 85 (2014).

[66] J. A. Pople, *Angew. Chem. Int. Ed.* **38**, 1894 (1999).

[67] W. Kohn, *Rev. Mod. Phys.* **71**, 1253 (1999).

[68] M. Karplus, *Angew. Chem. Int. Ed.* **53**, 9992 (2014).

[69] M. Levitt, *Angew. Chem. Int. Ed.* **53**, 10006 (2014).

[70] A. Warshel, *Angew. Chem. Int. Ed.* **53**, 10020 (2014).

[71] A. Szabo and N. S. Ostlund, *Modern Quantum Chemistry: Introduction to Advanced Electronic Structure Theory*, Macmillan Publishing Co., Inc., New York, USA (1982).

[72] T. Helgaker, P. Jorgensen and J. Olsen, *Molecular Electronic-Structure Theory*, John Wiley & Sons Ltd., Chichester, England (2013).

[73] M. K. Shukla and J. Leszczynski (eds.), *Radiation Induced Molecular Phenomena in Nucleic Acids*, vol. 5 of *Challenges and Advances In Computational Chemistry and Physics*, Springer Netherlands (2008).

[74] M. J. Bearpark, F. Ogliaro, T. Vreven, M. Boggio-Pasqua, M. J. Frisch, S. M. Larkin, M. Morrison and M. A. Robb, *J. Photochem. Photobiol. A* **190**, 207 (2007).

[75] A. Dreuw and M. Head-Gordon, *Chem. Rev.* **105**, 4009 (2005), PMID: 16277369.

[76] A. Dreuw, *ChemPhysChem* **7**, 2259 (2006).

[77] A. Dreuw, G. R. Fleming and M. Head-Gordon, *Phys. Chem. Chem. Phys.* **5**, 3247 (2003).

[78] M. Casida and M. Huix-Rotllant, *Annu. Rev. Phys. Chem.* **63**, 287 (2012), PMID: 22242728.

[79] C. Adamo and D. Jacquemin, *Chem. Soc. Rev.* **42**, 845 (2013).

[80] M. Svensson, S. Humbel, R. D. J. Froese, T. Matsubara, S. Sieber and K. Morokuma, *J. Phys. Chem.* **100**, 19357 (1996).

[81] M. J. Bearpark, S. M. Larkin and T. Vreven, *J. Phys. Chem. A* **112**, 7286 (2008).

[82] B. P. Fingerhut, *Optimale Photochemische Energiekonversion und Umgebungseffekte in Reaktiver Moleküldynamik*, Ph.D. thesis, Ludwig-Maximilians-Universität München (2011).

[83] B. P. Fingerhut, S. Oesterling, K. Haiser, K. Heil, A. Glas, W. J. Schreier, W. Zinth, T. Carell and R. de Vivie-Riedle, *J. Chem. Phys.* **136**, 204307 (2012).

[84] B. P. Fingerhut, T. T. Herzog, G. Ryseck, K. Haiser, F. F. Graupner, K. Heil, P. Gilch, W. J. Schreier, T. Carell, R. de Vivie-Riedle and W. Zinth, *New J. Phys.* **14**, 065006 (2012).

[85] C. J. Cramer, *Essentials of Computational Chemistry - Theories and Models*, John Wiley & Sons Ltd., Chichester, England (2004).

[86] J. Tomasi, B. Mennucci and R. Cammi, *Chem. Rev.* **105**, 2999 (2005).

[87] B. Mennucci and R. Cammi (eds.), *Continuum Solvation Models in Chemical Physics: From Theory to Applications*, John Wiley & Sons Ltd., Chichester, England (2007).

[88] S. Miertuš, E. Scrocco and J. Tomasi, *Chem. Phys.* **55**, 117 (1981).

[89] A. Klamt and G. Schüürmann, *J. Chem. Soc., Perkin Trans. 2* pp. 799–805 (1993).

[90] H. M. Senn and W. Thiel, *Angew. Chem. Int. Ed.* **48**, 1198 (2009).

[91] M. W. van der Kamp and A. J. Mulholland, *Biochemistry* **52**, 2708 (2013).

[92] B. Mennucci, *Phys. Chem. Chem. Phys.* **15**, 6583 (2013).

[93] C. Ochsenfeld, J. Kussmann and D. S. Lambrecht, *Linear-Scaling Methods in Quantum Chemistry*, in K. B. Lipkowitz and T. R. Cundari (eds.), *Reviews in Computational Chemistry*, pp. 1–82, John Wiley & Sons, Inc. (2007).

[94] R. Zaleśny, M. G. Papadopoulos, P. G. Mezey and J. Leszczynski (eds.), *Linear-Scaling Techniques in Computational Chemistry and Physics*, vol. 13 of *Challenges and Advances in Computational Chemistry and Physics*, Springer Netherlands (2011).

[95] J. Kussmann, M. Beer and C. Ochsenfeld, *WIREs Comput. Mol. Sci.* **3**, 614 (2013).

[96] C. Y. Yam, Q. Zhang, F. Wang and G. H. Chen, *Chem. Soc. Rev.* **41**, 3821 (2012).

[97] A. C. T. van Duin, S. Dasgupta, F. Lorant and W. A. Goddard, *J. Phys. Chem. A* **105**, 9396 (2001).

[98] H. M. Aktulga, S. A. Pandit, A. C. T. van Duin and A. Y. Grama, *SIAM J. Sci. Comput.* **34**, 1 (2012).

[99] T. Liang, Y. K. Shin, Y.-T. Cheng, D. E. Yilmaz, K. G. Vishnu, O. Verners, C. Zou, S. R. Phillpot, S. B. Sinnott and A. C. van Duin, *Annu. Rev. Mater. Res.* **43**, 109 (2013).

[100] J. P. Larentzos, B. M. Rice, E. F. C. Byrd, N. S. Weingarten and J. V. Lill, *J. Chem. Theory Comput.* **11**, 381 (2015).

[101] B. M. Rice, J. P. Larentzos, E. F. C. Byrd and N. S. Weingarten, *J. Chem. Theory Comput.* **11**, 392 (2015).

[102] M. Barbatti, G. Granucci, M. Persico, M. Ruckenbauer, M. Vazdar, M. Eckert-Maksić and H. Lischka, *J. Photochem. Photobiol. A* **190**, 228 (2007), Theoretical Aspects of Photoinduced Processes in Complex Systems.

[103] M. Barbatti, M. Ruckenbauer, F. Plasser, J. Pittner, G. Granucci, M. Persico and H. Lischka, *WIREs Comput. Mol. Sci.* **4**, 26 (2014).

[104] M. Richter, P. Marquetand, J. González-Vázquez, I. Sola and L. González, *J. Chem. Theory Comput.* **7**, 1253 (2011).

[105] S. Mai, P. Marquetand and L. González, *Int. J. Quantum Chem.* pp. n/a–n/a (2015).

[106] B. O. Roos, *Multiconfigurational quantum chemistry for ground and excited states*, in M. K. Shukla and J. Leszczynski (eds.), *Radiation Induced Molecular Phenomena in Nucleic Acids*, vol. 5 of *Challenges and Advances In Computational Chemistry and Physics*, pp. 125–156, Springer Netherlands (2008).

[107] J. C. Tully and R. K. Preston, *J. Chem. Phys.* **55**, 562 (1971).

[108] J. C. Tully, *J. Chem. Phys.* **93**, 1061 (1990).

[109] N. L. Doltsinis and D. Marx, *J. Theor. Comput. Chem.* **1**, 319 (2002).

[110] M. Barbatti, *WIREs Comput. Mol. Sci.* **1**, 620 (2011).

[111] J. P. Malhado, M. J. Bearpark and J. T. Hynes, *Front. Chem.* **2** (2014).

[112] M. Persico and G. Granucci, *Theor. Chem. Acc.* **133** (2014).

[113] D. J. Tannor, *Introduction to Quantum Mechanics: A Time-Dependent Perspective*, University Science Books, Sausalito, California, USA (2007).

[114] F. Gatti (ed.), *Molecular Quantum Dynamics – From Theory to Applications*, Springer-Verlag (2014).

[115] R. Marquardt, *ChemPhysChem* **14**, 1350 (2013).

[116] G. Nyman and H.-G. Yu, *Int. Rev. Phys. Chem.* **32**, 39 (2013).

[117] P. von den Hoff, S. Thallmair, M. Kowalewski, R. Siemering and R. d. Vivie-Riedle, *Phys. Chem. Chem. Phys.* **14**, 14460 (2012).

[118] S. Thallmair, R. Siemering, P. Kölle, M. Kling, M. Wollenhaupt, T. Baumert and R. de Vivie-Riedle, *The Interplay of Nuclear and Electron Wavepacket Motion in the Control of Molecular Processes: A Theoretical Perspective*, in F. Gatti (ed.), *Molecular Quantum Dynamics – From Theory to Applications*, pp. 213–248, Springer-Verlag (2014).

[119] A. Hofmann, *Ultraschnelle molekulare Quantendynamik durch konische Durchschneidungen*, Ph.D. thesis, Ludwig-Maximilians-Universität München (2001).

[120] A. Hofmann and R. de Vivie-Riedle, *Chem. Phys. Lett.* **346**, 299 (2001).

[121] M. Beck, A. Jäckle, G. Worth and H.-D. Meyer, *Phys. Rep.* **324**, 1 (2000).

[122] H.-D. Meyer, G. A. Worth and F. Gatti (eds.), *Multidimensional Quantum Dynamics: MCTDH Theory and Applications* , Wiley-VCH Verlag GmbH & Co. KGaA, Weinheim, Germany (2009).

[123] H.-D. Meyer, *WIREs Comput. Mol. Sci.* **2**, 351 (2012).

[124] H. Mayr and M. Patz, *Angew. Chem. Int. Ed.* **33**, 938 (1994).

[125] H. Mayr, T. Bug, M. F. Gotta, N. Hering, B. Irrgang, B. Janker, B. Kempf, R. Loos, A. R. Ofial, G. Remennikov and H. Schimmel, *J. Am. Chem. Soc.* **123**, 9500 (2001).

[126] H. Mayr, B. Kempf and A. R. Ofial, *Acc. Chem. Res.* **36**, 66 (2003).

[127] H. Mayr and A. R. Ofial, *Pure Appl. Chem.* **77**, 1807 (2005).

[128] H. Mayr and A. R. Ofial, *J. Phys. Org. Chem.* **21**, 584 (2008).

[129] H. Mayr and A. R. Ofial, *Nachr. Chem.* **56**, 871 (2008).

[130] H. Mayr, J. Ammer, M. Baidya, B. Maji, T. A. Nigst, A. R. Ofial and T. Singer, *J. Am. Chem. Soc.* **137**, 2580 (2015).

[131] J. Ammer, *Generation of carbocations by laser flash photolysis*, Ph.D. thesis, Ludwig-Maximilians-Universität München (2012).

[132] J. Ammer and H. Mayr, *J. Phys. Org. Chem.* **26**, 956 (2013).

[133] J. Ammer, C. F. Sailer, E. Riedle and H. Mayr, *J. Am. Chem. Soc.* **134**, 11481 (2012).

[134] C. F. Sailer, *Tracking the short life of highly reactive carbocations*, Ph.D. thesis, Ludwig-Maximilians-Universität München (2012).

[135] Sailer, C.F., Krebs, N., Fingerhut, B.P., de Vivie-Riedle, R. and Riedle, E., *EPJ Web of Conferences* **41**, 05042 (2013).

[136] C. F. Sailer and E. Riedle, *Pure Appl. Chem.* **85**, 1487 (2013).

[137] J. Bartl, S. Steenken, H. Mayr and R. A. McClelland, *J. Am. Chem. Soc.* **112**, 6918 (1990).

[138] B. P. Fingerhut, D. Geppert and R. de Vivie-Riedle, *Chem. Phys.* **343**, 329 (2008).

[139] S. Thallmair, *Ultraschnelle photochemische Dissoziation von Diarylmethan-Derivaten: Theorie und Experiment*, Master's thesis, Ludwig-Maximilians-Universität München (2010).

[140] C. F. Sailer, R. B. Singh, J. Ammer, E. Riedle and I. Pugliesi, *Chem. Phys. Lett.* **512**, 60 (2011).

[141] B. Podolsky, *Phys. Rev.* **32**, 812 (1928).

[142] E. B. Wilson Jr., J. C. Decius and P. C. Cross, *Molecular Vibrations*, McGraw-Hill, New York (1955).

[143] L. J. Schaad and J. Hu, *J. Mol. Struct.: THEOCHEM* **185**, 203 (1989).

[144] C. Reichardt and T. Welton, *Solvents and Solvent Effects in Organic Chemistry*, Wiley-VCH Verlag GmbH & Co. KGaA, Weinheim, Germany (2011).

[145] J. Clayden, N. Greeves and S. Warren, *Organic Chemistry*, Oxford University Press Ink., New York, USA, second edn. (2012).

[146] A. F. Holleman, N. Wiberg and E. Wiberg, *Lehrbuch der Anorganischen Chemie*, Walter de Gruyter, Berlin, Germany, 102nd edn. (2008).

[147] A. Melo, A. J. I. Alfaia, J. C. R. Reis and A. R. T. Calado, *J. Phys. Chem. B* **110**, 1877 (2006).

[148] V. D. Kiselev, I. I. Shakirova, D. A. Kornilov, H. A. Kashaeva, L. N. Potapova and A. I. Konovalov, *J. Phys. Org. Chem.* **26**, 47 (2013).

[149] H. Struebing, Z. Ganase, P. G. Karamertzanis, E. Siougkrou, P. Haycock, P. M. Piccione, A. Armstrong, A. Galindo and C. S. Adjiman, *Nature Chem.* **5**, 952 (2013).

[150] J. Tomasi and M. Persico, *Chem. Rev.* **94**, 2027 (1994).

[151] C. J. Cramer and D. G. Truhlar, *Chem. Rev.* **99**, 2161 (1999).

[152] C. Amovilli, *Chem. Phys. Lett.* **229**, 244 (1994).

[153] C. Amovilli and B. Mennucci, *J. Phys. Chem. B* **101**, 1051 (1997).

[154] R. A. Pierotti, *Chem. Rev.* **76**, 717 (1976).

[155] J. Langlet, P. Claverie, J. Caillet and A. Pullman, *J. Phys. Chem.* **92**, 1617 (1988).

[156] A. Ben-Naim, *Solvation thermodynamics*, Plenum Press, New York, USA (1987).

[157] R. A. Marcus, *J. Chem. Phys.* **24**, 966 (1956).

[158] R. Bonaccorsi, R. Cimiraglia and J. Tomasi, *Chem. Phys. Lett.* **99**, 77 (1983).

[159] R. Cammi, S. Corni, B. Mennucci and J. Tomasi, *J. Chem. Phys.* **122**, 104513 (2005).

[160] M. Caricato, B. Mennucci, J. Tomasi, F. Ingrosso, R. Cammi, S. Corni and G. Scalmani, *J. Chem. Phys.* **124**, 124520 (2006).

[161] B. Mennucci, C. Cappelli, C. A. Guido, R. Cammi and J. Tomasi, *J. Phys. Chem. A* **113**, 3009 (2009).

[162] J. Tomasi, *WIREs Comput. Mol. Sci.* **1**, 855 (2011).

[163] M. Orozco and F. J. Luque, *Chem. Rev.* **100**, 4187 (2000).

[164] A. Warshel and M. Levitt, *J. Mol. Biol.* **103**, 227 (1976).

[165] M. Maroncelli, J. MacInnis and G. R. Fleming, *Science* **243**, 1674 (1989).

[166] R. Jimenez, G. R. Fleming, P. V. Kumar and M. Maroncelli, *Nature Chem.* **369**, 471 (1994).

[167] F. Ingrosso, B. M. Ladanyi, B. Mennucci, M. D. Elola and J. Tomasi, *J. Phys. Chem. B* **109**, 3553 (2005).

[168] M. L. Horng, J. A. Gardecki, A. Papazyan and M. Maroncelli, *J. Phys. Chem.* **99**, 17311 (1995).

[169] I. Benjamin and K. R. Wilson, *J. Chem. Phys.* **90**, 4176 (1989).

[170] A. I. Krylov and R. B. Gerber, *J. Chem. Phys.* **100**, 4242 (1994).

[171] Y. Amatatsu and K. Morokuma, *Chem. Phys. Lett.* **245**, 469 (1995).

[172] N. Winter, I. Chorny, J. Vieceli and I. Benjamin, *J. Chem. Phys.* **119**, 2127 (2003).

[173] C. A. Rivera, N. Winter, R. V. Harper, I. Benjamin and S. E. Bradforth, *Phys. Chem. Chem. Phys.* **13**, 8269 (2011).

[174] E. M. Goldfield, P. L. Houston and G. S. Ezra, *J. Chem. Phys.* **84**, 3120 (1986).

[175] A. C. Moskun and S. E. Bradforth, *J. Chem. Phys.* **119**, 4500 (2003).

[176] A. C. Moskun, A. E. Jailaubekov, S. E. Bradforth, G. Tao and R. M. Stratt, *Science* **311**, 1907 (2006).

[177] D. Murdock, S. J. Harris, T. N. V. Karsili, G. M. Greetham, I. P. Clark, M. Towrie, A. J. Orr-Ewing and M. N. R. Ashfold, *J. Phys. Chem. Lett.* **3**, 3715 (2012).

[178] S. J. Harris, D. Murdock, Y. Zhang, T. A. A. Oliver, M. P. Grubb, A. J. Orr-Ewing, G. M. Greetham, I. P. Clark, M. Towrie, S. E. Bradforth and M. N. R. Ashfold, *Phys. Chem. Chem. Phys.* **15**, 6567 (2013).

[179] Y. Zhang, T. A. A. Oliver, S. Das, A. Roy, M. N. R. Ashfold and S. E. Bradforth, *J. Phys. Chem. A* **117**, 12125 (2013).

[180] T. S. Venkatesan, S. G. Ramesh, Z. Lan and W. Domcke, *J. Chem. Phys.* **136**, 174312 (2012).

[181] M. D. Kostin, *J. Chem. Phys.* **57**, 3589 (1972).

[182] K. Albrecht, *Phys. Lett. B* **56**, 127 (1975).

[183] R. W. Hasse, *J. Math. Phys.* **16**, 2005 (1975).

[184] M. Kostin, *J. Stat. Phys.* **12**, 145 (1975).

[185] R. W. Hasse, *Rep. Prog. Phys.* **41**, 1027 (1978).

[186] W. Stocker and K. Albrecht, *Ann. Phys.* **117**, 436 (1979).

[187] V. S. Batista and D. F. Coker, *J. Chem. Phys.* **106**, 6923 (1997).

[188] V. A. Apkarian and N. Schwentner, *Chem. Rev.* **99**, 1481 (1999).

[189] H. Ibrahim, M. Héjjas, M. Fushitani and N. Schwentner, *J. Phys. Chem. A* **113**, 7439 (2009).

[190] G. Nyman, *Int. J. Quantum Chem.* **114**, 1183 (2014).

[191] S. Thallmair, B. P. Fingerhut and R. de Vivie-Riedle, *J. Phys. Chem. A* **117**, 10626 (2013).

[192] M. Kowalewski, *Quantendynamik isolierter molekularer Systeme*, Ph.D. thesis, Ludwig-Maximilians-Universität München (2012).

[193] V. Alexandrov, D. M. A. Smith, H. Rostkowska, M. J. Nowak, L. Adamowicz and W. McCarthy, *J. Chem. Phys.* **108**, 9685 (1998).

[194] M. K. Roos, *Kombinierte interne Koordinaten für Diphenylmethylchlorid: Potentialflächen und kinetischer Hamiltonoperator*, Master's thesis, Ludwig-Maximilians-Universität München (2013).

[195] J. P. P. Zauleck, *Grundlagen der Implementierung quantendynamischer Rechnungen aus einer De-Broglie-Bohm-Perspektive*, Master's thesis, Ludwig-Maximilians-Universität München (2012).

[196] I. N. Bronstein, K. A. Semendjajew, G. Musiol and H. Mühlig, *Taschenbuch der Mathematik*, Verlag Europa-Lehrmittel, Haan-Gruiten, Germany, 9th edn. (2013).

[197] C. Eckart, *Phys. Rev.* **47**, 552 (1935).

[198] E. A. Coutsias, C. Seok and K. A. Dill, *J. Comput. Chem.* **25**, 1849 (2004).

[199] A. Y. Dymarsky and K. N. Kudin, *J. Chem. Phys.* **122**, 124103 (2005).

[200] K. N. Kudin and A. Y. Dymarsky, *J. Chem. Phys.* **122**, 224105 (2005).

[201] J. E. Hadder and J. H. Frederick, *J. Chem. Phys.* **97**, 3500 (1992).

[202] J. A. Pople and M. Gordon, *J. Am. Chem. Soc.* **89**, 4253 (1967).

[203] V. Brázdová and D. A. Bowler, *Atomistic Computer Simulations: A Practical Guide*, Wiley-VCH Verlag GmbH & Co. KGaA, Weinheim, Germany (2013).

[204] F. Bernardi, M. Olivucci, M. A. Robb and G. Tonachini, *J. Am. Chem. Soc.* **114**, 5805 (1992).

[205] S. Wilsey, K. N. Houk and A. H. Zewail, *J. Am. Chem. Soc.* **121**, 5772 (1999).

[206] T. Vreven, K. S. Byun, I. Komáromi, S. Dapprich, J. A. Montgomery, K. Morokuma and M. J. Frisch, *J. Chem. Theory Comput.* **2**, 815 (2006).

[207] S. Dapprich, I. Komáromi, K. Byun, K. Morokuma and M. J. Frisch, *J. Mol. Struct.: THEOCHEM* **461-462**, 1 (1999).

[208] H.-J. Werner, P. J. Knowles, G. Knizia, F. R. Manby, M. Schütz, P. Celani, T. Korona, R. Lindh, A. Mitrushenkov, G. Rauhut, K. R. Shamasundar, T. B. Adler, R. D. Amos, A. Bernhardsson, A. Berning, D. L. Cooper, M. J. O. Deegan, A. J. Dobbyn, F. Eckert, E. Goll, C. Hampel, A. Hesselmann, G. Hetzer, T. Hrenar, G. Jansen, C. Köppl, Y. Liu, A. W. Lloyd, R. A. Mata, A. J. May, S. J. McNicholas, W. Meyer, M. E. Mura, A. Nicklass, D. P. O'Neill, P. Palmieri, D. Peng, K. Pflüger, R. Pitzer, M. Reiher, T. Shiozaki, H. Stoll, A. J. Stone, R. Tarroni, T. Thorsteinsson and M. Wang, *MOLPRO, Version 2012.1, A Package of Ab Initio Programs* (2012).

[209] Y. Zhao and D. Truhlar, *Theor. Chem. Acc.* **120**, 215 (2008).

[210] Y. Zhao and D. G. Truhlar, *J. Chem. Theory Comput.* **4**, 1849 (2008).

[211] M. J. Frisch, G. W. Trucks, H. B. Schlegel, G. E. Scuseria, M. A. Robb, J. R. Cheeseman, G. Scalmani, V. Barone, B. Mennucci, G. A. Petersson, H. Nakatsuji, M. Caricato, X. Li, H. P. Hratchian, A. F. Izmaylov, J. Bloino, G. Zheng, J. L. Sonnenberg, M. Hada, M. Ehara, K. Toyota, R. Fukuda, J. Hasegawa, M. Ishida, T. Nakajima, Y. Honda, O. Kitao, H. Nakai, T. Vreven, J. J. A. Montgomery, J. E. Peralta, F. Ogliaro, M. Bearpark, J. J. Heyd, E. Brothers, K. N. Kudin, V. N. Staroverov, T. Keith, R. Kobayashi, J. Normand, K. Raghavachari, A. Rendell, J. C. Burant, S. S. Iyengar, J. Tomasi, M. Cossi, N. Rega, J. M. Millam, M. Klene, J. E. Knox, J. B. Cross, V. Bakken, C. Adamo, J. Jaramillo, R. Gomperts, R. E. Stratmann, O. Yazyev, A. J. Austin, R. Cammi, C. Pomelli, J. W. Ochterski, R. L. Martin, K. Morokuma, V. G. Zakrzewski, G. A. Voth, P. Salvador, J. J. Dannenberg, S. Dapprich, A. D. Daniels, O. Farkas, J. B. Foresman, J. V. Ortiz, J. Cioslowski and D. J. Fox, *Gaussian 09, Revision D.01, Inc., Wallingford C* (2013).

[212] R. Ditchfield, W. J. Hehre and J. A. Pople, *J. Chem. Phys.* **54**, 724 (1971).

[213] P. Hariharan and J. Pople, *Theor. Chim. Acta* **28**, 213 (1973).

[214] V. A. Rassolov, M. A. Ratner, J. A. Pople, P. C. Redfern and L. A. Curtiss, *J. Comput. Chem.* **22**, 976 (2001).

[215] S. Matsika and P. Krause, *Annu. Rev. Phys. Chem.* **62**, 621 (2011).

[216] D. R. Yarkony, *Chem. Rev.* **112**, 481 (2012).

[217] S. Thallmair, M. Kowalewski, J. P. P. Zauleck, M. K. Roos and R. de Vivie-Riedle, *J. Phys. Chem. Lett.* **5**, 3480 (2014).

[218] H. Tal-Ezer and R. Kosloff, *J. Chem. Phys.* **81**, 3967 (1984).

[219] R. Kosloff and H. Tal-Ezer, *Chem. Phys. Lett.* **127**, 223 (1986).

[220] H. Kuchling, *Taschenbuch der Physik*, Carl Hanser Verlag, München, Germany, 20th edn. (2010).

[221] Thallmair, S., Kowalewski, M., Fingerhut, B.P., Sailer, C.F. and de Vivie-Riedle, R., *EPJ Web of Conferences* **41**, 05043 (2013).

[222] S. Thallmair, J. P. P. Zauleck and R. de Vivie-Riedle, *J. Chem. Theory Comput.* **11**, 1987 (2015).

[223] E. Lindahl, B. Hess and D. van der Spoel, *J. Mol. Model.* **7**, 306 (2001).

[224] D. Van Der Spoel, E. Lindahl, B. Hess, G. Groenhof, A. E. Mark and H. J. C. Berendsen, *J. Comput. Chem.* **26**, 1701 (2005).

[225] B. Hess, C. Kutzner, D. van der Spoel and E. Lindahl, *J. Chem. Theory Comput.* **4**, 435 (2008).

[226] S. Thallmair, J. Zauleck and R. de Vivie-Riedle, *Quantum Dynamics of Molecular Reactions Directed by Explicit Solvent Environment*, in K. Yamanouchi, S. Cundiff, R. de Vivie-Riedle, M. Kuwata-Gonokami and L. DiMauro (eds.), *Ultrafast Phenomena XIX*, vol. 162 of *Springer Proceedings in Physics*, pp. 373–377, Springer International Publishing (2015).

[227] J. Ammer, C. Nolte, K. Karaghiosoff, S. Thallmair, P. Mayer, R. de Vivie-Riedle and H. Mayr, *Chem. Eur. J.* **19**, 14612 (2013).

[228] R. Improta, V. Barone, G. Scalmani and M. J. Frisch, *J. Chem. Phys.* **125**, (2006).

[229] G. Scalmani and M. J. Frisch, *J. Chem. Phys.* **132**, (2010).

[230] K. W. Wiitala, T. R. Hoye and C. J. Cramer, *J. Chem. Theory Comput.* **2**, 1085 (2006).

[231] R. Jain, T. Bally and P. R. Rablen, *J. Org. Chem.* **74**, 4017 (2009).

[232] G. Schiemenz, *J. Magn. Res.* **6**, 291 (1972).

[233] B. P. Fingerhut, C. F. Sailer, J. Ammer, E. Riedle and R. de Vivie-Riedle, *J. Phys. Chem. A* **116**, 11064 (2012).

[234] M. Baidya, S. Kobayashi, F. Brotzel, U. Schmidhammer, E. Riedle and H. Mayr, *Angew. Chem. Int. Ed.* **46**, 6176 (2007).

[235] J. Ammer, M. Baidya, S. Kobayashi and H. Mayr, *J. Phys. Org. Chem.* **23**, 1029 (2010).

[236] T. A. Nigst, J. Ammer and H. Mayr, *J. Phys. Chem. A* **116**, 8494 (2012).

[237] S. Minegishi, R. Loos, S. Kobayashi and H. Mayr, *J. Am. Chem. Soc.* **127**, 2641 (2005).

[238] K. S. Peters, S. Gasparrini and L. R. Heeb, *J. Am. Chem. Soc.* **127**, 13039 (2005).

[239] L. R. Heeb and K. S. Peters, *J. Am. Chem. Soc.* **130**, 1711 (2008).

[240] P. K. Das, *Chem. Rev.* **93**, 119 (1993).

[241] J. Ammer, C. Nolte and H. Mayr, *J. Am. Chem. Soc.* **134**, 13902 (2012).

[242] J. Ammer and H. Mayr, *J. Phys. Org. Chem.* **26**, 59 (2013).

[243] R. V. Slates and M. Szwarc, *J. Am. Chem. Soc.* **89**, 6043 (1967).

[244] D. J. Raber, J. M. Harris and P. v. R. Schleyer, *Ions and Ion Pairs in Solvolysis Reactions*, in M. Szwarc (ed.), *Ions and Ion Pairs in Organic Chemistry*, pp. 248–366, John Wiley & Sons, Ltd., New York (1974).

[245] M. Szwarc, *Pure Appl. Chem.* **48**, 247 (1976).

[246] K. S. Peters and B. Li, *J. Phys. Chem.* **98**, 401 (1994).

[247] K. S. Peters, *Chem. Rev.* **107**, 859 (2007).

[248] A. Nenov, *Relation between molecular structure and ultrafast photoreactivity with application to molecular switches*, Ph.D. thesis, Ludwig-Maximilians-Universität München (2012).

[249] Q. Li, A. Migani and L. Blancafort, *J. Phys. Chem. A* **113**, 9413 (2009).

[250] Q. Li, A. Migani and L. Blancafort, *J. Phys. Chem. Lett.* **3**, 1056 (2012).

[251] G. Cui and W. Thiel, *Angew. Chem. Int. Ed.* **52**, 433 (2013).

[252] J. C. Tully, *Faraday Discuss.* **110**, 407 (1998).

Danksagung

An dieser Stelle möchte ich allen danken, die in den vergangenen Jahren auf die eine oder andere Weise einen Beitrag zum Gelingen meiner Doktorarbeit geleistet haben.

Besonderer Dank gebührt Frau Prof. Regina de Vivie-Riedle für die Möglichkeit, in ihrer Gruppe meine Doktorarbeit anfertigen zu dürfen. Ihr persönliches Engagement sowie die Vielzahl an inspirierenden Diskussionen haben entscheidend zum Gelingen der Arbeit beigetragen. Die wissenschaftliche Freiheit, die ich in den vergangenen Jahren genießen durfte, und die daraus resultierende, große persönliche Verantwortung für spannende Forschungsprojekte haben viel Freude gemacht. Ich möchte mich auch für das Vertrauen bedanken, meine Arbeit auf vielen Konferenzen vorstellen zu dürfen.

Außerdem danke ich Herrn Prof. Eberhard Riedle für die Möglichkeit, einige Experimente zu den Phosphoniumsalzen in seiner Gruppe durchführen zu dürfen. Diese intensive Zusammenarbeit mit dem Experiment sowie die vielen gemeinsamen Diskussionen und das Interesse am Fortschritt der theoretischen Untersuchungen stellten einen großen Gewinn dar.

Des weiteren möchte ich Herrn Prof. Herbert Mayr sowie Johannes Ammer für die gute Zusammenarbeit und die zur Verfügung gestellten Diphenylmethanderivate danken.

Vielen Dank auch an meine momentanen und ehemaligen Kollegen im Arbeitskreis de Vivie-Riedle – Judith, Benni, Markus, Philipp, Artur, Patrick, Sven, Robert, Julius, Matthias, Daniel und Flo – für viele Knobeleien, Diskussionen und vor allem die gute und produktive Atmosphäre. Für die vielen übernommenen Administratoraufgaben geht ein zusätzliches Dankeschön an Markus und Sven. Auch Frau Prof. Spiridoula Matsika danke ich für die schöne und interessante Zusammenarbeit während ihres sechsmonatigen Aufenthalts in München. Außerdem möchte ich mich bei den Mitgliedern der Arbeitsgruppe Riedle am BMO bedanken – ganz besonders bei Christian Sailer und Roland Wilcken, mit denen ich eine wunderbare Zusammenarbeit genießen durfte. Stellvertretend für alle anderen seinen hier noch Igor, Max, Christian und Nils genannt. Nicht zu vergessen sind auch die vielen Bacheloranden, F-Praktikanten und Masteranden, die ich in den letzten Jahren allein oder gemeinsam mit Kollegen betreuen durfte: Matthias, Henry, Martin, Markus, Pascal, Matze, Andrea, Daniel, Flo und Bastien. Vielen Dank auch allen Korrekturlesern des Manuskripts!

Auch meinen langjährigen Freunden und Mitbewohnern Robert und Benjamin danke ich für die vielen Stunden gemeinsam verbrachter Freizeit, in denen wir jede Menge schöne und lustige Dinge unternommen haben, die ein guter Ausgleich zur Arbeit im Büro waren.

Für das bereits frühe Wecken und dauerhafte Fördern meines naturwissenschaftlichen Interesses und ihre großartige Unterstützung danke ich meinen Eltern ganz besonders. Und natürlich möchte ich auch meiner Schwester und meiner lieben Freundin Kathi für ihre tolle Unterstützung herzlich danken. Ohne Euch wären die letzten Jahre oft deutlich beschwerlicher und weniger schön gewesen!